The Origin and Timing of Quartz Cementation in Reservoir Sandstones: Evidence from in-situ Microanalysis of Oxygen Isotopes

Joseph Harwood

A thesis submitted to Newcastle University in partial fulfilment of the requirements for the degree of Doctor of Philosophy in the Faculty of Science

School of Civil Engineering and Geosciences

Newcastle University

February 2011

Declaration

I hereby certify that the work described in this thesis is my own work, except where otherwise acknowledged and has not been submitted previously for a degree at this, or any other University

Joseph Harwood

Acknowledgements

First and foremost I would like to thank my supervisor Andrew Aplin for his guidance and support throughout my PhD. In addition, the support and advice from Claire Fialips, James Illife (BP Exploration) and Kuncho Kurtev has been warmly received.

I would also like to extend my gratitude to Reinhard Kozdon, John Valley, Takayuki Ushikubo and all at the Wisc-SIMS lab (University of Wisconsin – Madison) who helped make my time in the States as fun as it was successful. I would like to thank Ruarri Day-Stirrat for supplying the Wilcox samples and their time – temperature histories. Thanks are also extended to Maggie White, Kath Liddell, Pauline Carrick and Grant Staines for their help with XRD and SEM analysis. I would also like to thank Phil Green, Trevor Whitfield, and Rob Hunter for their technical help in the lab and Yvonne Hall for always having the answers.

Ultimately I would like to thank my family and my partner Natasha for their unwavering support throughout.

Abstract

High precision oxygen isotope analyses of quartz cements, in combination with quantitative petrography and Quantitative X-Ray Diffraction (QXRD) as well as time-temperature history modelling, were employed to constrain the timing and source of porosity reducing quartz cement in the Jurassic Ness Formation (North Sea) and the Palaeocene Wilcox Group (Texas). Temperature history modelling indicates maximum burial temperatures in the chosen Ness samples to be 109 to 165^{o}C and 27 to 210^{o}C in the Wilcox samples. In both sample areas the volume of quartz cement is controlled by temperature and quartz surface area. The volume of quartz cement recorded ranges from 1.3 to 22.5 %bv in the Ness Formation and from 4.4 to 18.8 %bv in the Wilcox sandstone. With the notable exception of the hottest Wilcox samples (>143^{o}C), cement volume increases with temperature in both basins. In situ Secondary Ion Mass Spectrometry (SIMS) was performed at a spatial resolution of 12 µm and 2 µm on quartz overgrowths. $\delta^{18}O_{(cement)}$ measurements ranged from +27.7‰ to +19.3‰ in the Ness and +28.5‰ to +18.3‰ in the Wilcox. Precision for the 12 µm and 2 µm analysis was better than ±0.27‰ (2SD) and ±0.67‰ (2SD) respectively. $\delta^{18}O_{(cement)}$ measurements indicate that the initial 8% of cement in both the Ness and Wilcox sandstones precipitated below ~50^{o}C. The remaining 90% of cement observed in both basins precipitated above 60-80^{o}C in diagenetically evolving waters where $\delta^{18}O$ becomes heavier during burial. In all cases cementation appears to continue through to maximum burial temperatures, from 60 to 143^{o}C and can be accurately predicted using current cementation models. However, $\delta^{18}O_{(cement)}$ measurements in Wilcox sandstones sampled above 143^{o}C indicate that cementation may be inhibited at high temperatures as a response to the late precipitation of diagenetic minerals such as illite and ankerite which act to reduce available quartz surface area. Within the quartz cementation window (50-143^{o}C), silica producing reactions including the illitisation of kaolinite and smectite as well as the dissolution and albitisation of feldspars have been recorded in shale units adjoining both the Ness and the Wilcox sandstones. However, mass balance calculations indicate that insufficient silica is produced within these shale units to account for the total volume of cement quantified in the sandstone. These findings indicate that the majority of quartz precipitates above 60^{o}C and is sourced internally within the sandstone body.

Contents

List of Figures

List of Tables

1. Introduction to the Origin and Timing of Quartz Cementation in Reservoir Sandstones

Quartz cement is the most volumetrically significant diagenetic mineral observed in reservoir sandstones (Bjørlykke, 1979; McBride, 1989; Bjørlykke and Egeberg, 1993; Primmer et al., 1997; Worden and Morad, 2000). Precipitation of quartz during burial reduces porosity and is detrimental to reservoir quality. It is therefore important to accurately determine the extent and timing of cementation when considering the economical potential of a reservoir system and during the management of that reservoir. However, the exact timing and mechanism by which quartz cementation occurs has yet to be fully constrained.

This thesis describes a multi-analytical project that was undertaken to investigate and further constrain the timing of quartz cementation in the North Sea, Ness Formation and the Texas, Wilcox sandstones.

1.1.An Overview of Quartz Cementation in Reservoir Sandstones

There are three important factors to consider when evaluating the timing of quartz cementation: (i) the kinetics that control quartz precipitation; (ii) sources of silica; (iii) transportation of silica from source to precipitation site.

1.1.1. Quartz Precipitation Kinetics

Silica diagenesis and ultimately the precipitation of quartz is controlled by phase solubility (Williams and Crerar, 1985b).

$$SiO_2\ (s) + 2H_2O\ (l) \rightarrow H_4SiO_4\ (aq)$$

Equation 1.1 Silica dissolution

The solubility (K) of the most common phases of silica, including opal-A, opal-CT and quartz as a function of temperature are illustrated in Figure 1.1 taken from Bjørlykke and Egeberg (1993). Thermodynamic and kinetic controls dictate the phase of silica observed. At temperatures below 70^{o}C the rate of quartz precipitation is very slow. Less stable amorphous forms of silica dominate and pore waters remain supersaturated with respect to quartz (Williams and Crerar, 1985b). Progressive burial causes temperatures to rise and amorphous silica polymorphs become less stable; less soluble cristobalite-tridymite phase (opal-CT) then forms. This transformation is believed to occur below 50^{o}C (Pisciotto, 1981; Williams and Crerar, 1985b). Opal-CT later recrystallises to less soluble quartz. In the natural system this conversion is believed to occur above 31^{o}C but is poorly constrained (Murata and Larson, 1975; Williams and Crerar, 1985b). Both these transformations are time temperature dependant. Mituzatani (1970) showed that it takes 10 million year at 50^{o}C to transform 90% of cristobalite phase to quartz. However, metastable forms of silica are known to persist in deeply buried rocks of the Cretaceous (e.g.Gran, 1989); indicating other influences may be affecting precipitation kinetics.

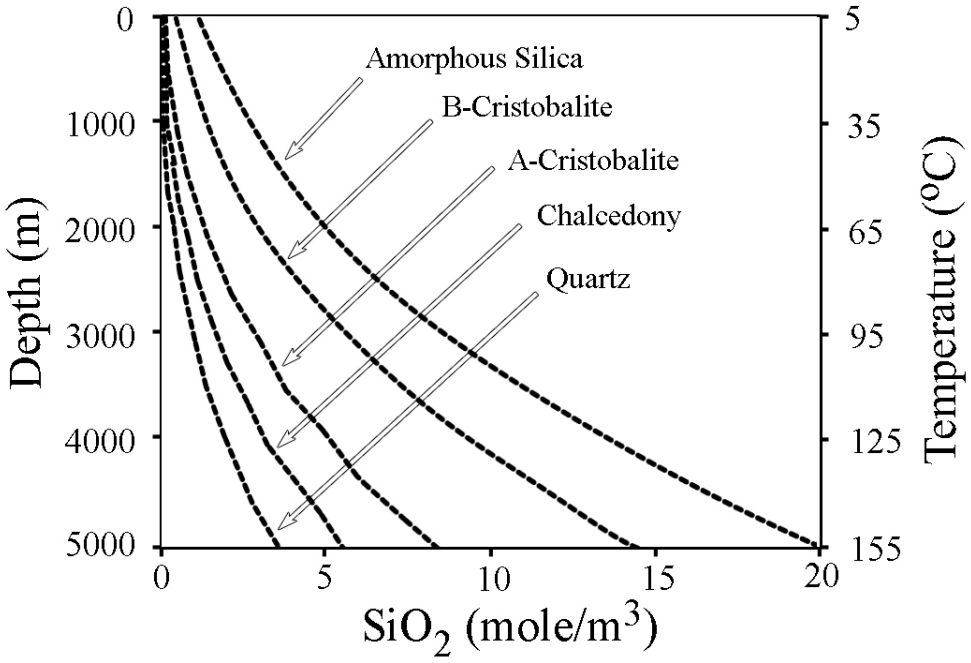

Figure 1.1 Concentration of silica$_{(aq)}$ in equilibrium with various silicates. At low burial temperatures the rate of quartz precipitation is slow and less stable forms of silica (amorphous and cristobalite) are metastable; causing formation waters to remain supersaturated with respect to quartz. At higher temperatures quartz precipitation rates increase and waters move towards equilibrium with quartz. Figure taken from Bjørlykke and Egeberg (1993).

The diagenetic sequence exhibited by silica (opal-A → opal-CT→ quartz) can be affected by pH, impurities, detrital surface area and silica diffusion (Williams et al., 1985a). Each affects the activity of H_4SiO_4 acting to reduce the supersaturation with respect to one of the silica polymorphs. For example if silica were to diffuse away from the system or be adsorbed by an impurity i.e. a high surface area clay mineral, then the overall concentration of silica [ΣSIO_2] would be reduced.

In summary the precipitation of quartz in sandstones can occur whenever the solubility product of quartz is exceeded and where detrital quartz grains have free and uninhibited surfaces. Indeed, most meteoric waters are supersaturated with respect to quartz (Bjørlykke and Egeberg, 1993). It is therefore feasible, under the right conditions that quartz may precipitate at surface temperatures.

1.1.2. Silica Sources

To accurately understand quartz cementation mechanisms suitable sources of silica must be identified. A full overview of potential silica sources can be found in McBride (1989) and Worden and Morad (2000). It is commonly accepted that quartz cement is derived from: (i) more soluble silica phases e.g. amorphous silica (biogenic or volcanic) and opal CT (Bjørlykke and Egeberg, 1993; Vagle et al., 1994; Aase et al., 1996; Weibel et al., 2010); (ii) dissolution of quartz by pressure solution, stylolitisation or grain fracturing (Heald, 1955; Gratier and Guiguet Irigm, 1986; Dewers and Ortoleva, 1990; Oelkers et al., 1996; Bjørkum et al., 1998; Fisher et al., 2000; Baron and Parnell, 2007); (iii) mineral reactions involving the release of silica from silicates (Saigal et al., 1988; Milliken, 1992; Thyne et al., 2001; Wilkinson et al., 2001; Lanson et al., 2002; van de Kamp, 2008). However the extent each reaction contributes to the overall quartz cement observed is unclear. Each of the above silica producing processes may take place 'internally' within the sandstone or 'externally' outside the sandstone unit. As around 70% of the sedimentary basin is formed of shale (MacQuaker and Adams, 2003), it is likely that external silica generation is related to reactions occurring in shale units.

1.1.2.1. Amorphous Silica Dissolution

At low temperatures, silica can precipitate from natural aqueous solutions as amorphous silica (Williams and Crerar, 1985b). This may occur either inorganically, as in silcretes (Smale, 1978; Thiry and Millot, 1987; Alexandre et al., 2004; Alexandre et al., 2006) or organically from diatoms, radiolarians, silicoflagellates, sponges and some terrestrial plants (Siever, 1957; Hurst and Irwin, 1982; McBride, 1989; Worden and Morad, 2000).

During burial, these metastable silica polymorphs undergo dissolution and recrystallise as quartz (Figure 1.1). The recrystallisation of amorphous silica leaves little direct trace. However, quartz cement precipitated from amorphous silica or opal-CT commonly has

a microcrystalline chert-like texture, which is related to the high degree of supersaturation during precipitation (Bjørlykke and Egeberg, 1993; Hendry and Trewin, 1995; Weibel et al., 2010). As biogenic silica predominates in marine sediment (Siever, 1962; Calvert, 1968; Bjørlykke and Egeberg, 1993) its dissolution may not be influential in either the fluvial/deltaic North Sea Ness or Texas Wilcox sandstones.

1.1.2.2. Quartz Dissolution: Stylolitisation and Grain Fracturing

It is widely recognized that some silica in quartz cement may be sourced by pressure solution (Weyl, 1959; Trurnit, 1968; Gratier and Guiguet Irigm, 1986; Tada and Siever, 1989; Bjørkum, 1996; Worden and Morad, 2000). Pressure solution is caused by a local increase in quartz solubility (Bjørlykke and Egeberg, 1993; Bjørkum, 1996; Oelkers et al., 1996). Pressure solution in sandstones is commonly divided into two types: intergranular pressure solution and stylolitisation.

Intergranular pressure solution (sometimes referred to as grain-to-grain stylolitisation) takes the form of adjacent detrital grains having interpenetrating sutured or smooth contacts (Trurnit, 1968; Renton et al., 1969; Robin, 1978; Houseknecht, 1984; Houseknecht, 1988; Tada and Siever, 1989). Early petrographic studies highlighted the presence of inter-locking quartz grains as a possible silica source in sandstones. These were believed to be regions in which dissolution of detrital quartz had been brought about by high pressures and temperatures. However, later use of luminescing microscopy indicated that much of what appeared to be evidence of pressure solution at the grain contacts were in fact boundaries between silica cement precipitated between adjacent grains (Sibley and Blatt, 1976; Walderhaug, 1994b; Oelkers et al., 1996; Walderhaug, 1996).

Stylolites are intergranular serrated surfaces that are lined by insoluble constituents of the enclosing rock (Heald, 1955; Heald, 1959; Park and Schot, 1968; Tada and Siever,

1989; Walderhaug and Bjørkum, 2003). Stylolites differ from intergranular pressure solution by scale. A number of factors are thought to influence stylolite formation in sandstones, including temperature, pressure, mineralogy of the sandstone host and the mineralogy of the stylolite. Although the presence of stylolites are commonly reported in reservoir sandstones (Heald, 1955; Heald, 1959; Oelkers et al., 1996; Walderhaug, 1996; Baron and Parnell, 2007) the minimum burial depth required for their development remains uncertain. However, Bjørkum (1996) highlighted that <10 bar of pressure is required for stylolite development; indicating low temperature stylolitisation may occur. Numerous studies have also shown that the presence of mica and/or illite clays promotes pressure solution in quartz (Bjørkum, 1996; Oelkers et al., 1996; Walderhaug et al., 2006). Indeed Greene et al (2009) highlighted that pressure solution/stylolitisation is promoted by the electrostatic difference between quartz and mica.

Numerous authors report considerably more quartz cement within reservoir sandstones than can be accounted for by intergranular pressure solution or stylolitisation within the same formation (Heald, 1955; Heald, 1959; Todd, 1963; Sibley and Blatt, 1976; McBride, 1987; Thomas et al., 1993). However few of these studies were quantitative. The few quantitative studies performed including Sibley and Blatt (1976) found that pressure solution accounted for about a third of the quartz cement. A similar figure was estimated by Thomas (1993). However, Sibley and Blatt's (1976) study ignored finer-grained sandstones. Finer sandstones usually undergo more severe pressure solution than coarser-grained beds (McBride, 1989; Oelkers et al., 1996). This is because of relative thermodynamic instability of mineral surfaces relative to mineral interiors. Ostwald ripening leads to the preferential dissolution of small grains and reprecipitation of the dissolved silica as a contribution to larger grains (Williams and Crerar, 1985b; Worden and Morad, 2000). Large-scale pressure dissolution of silica due to stylolite formation is also more common in siltstones and fine-grained sandstones that are rich in detrital mica (Oelkers et al., 1996).

During compaction grain fracturing has also been linked to quartz cementation. During early burial, mechanical compaction can fracture quartz grains. This process can cause the dissolution of detrital quartz, and will increase quartz surface area, promoting quartz precipitation (Chuhan et al., 2002; Makowitz et al., 2006).

Quantifying exactly how much silica can be produced by pressure solution is beyond the realm of this study. However, the above mentioned studies clearly indicate that stylolitisation and local intergranular grain contact can contribute towards the silica budget.

1.1.2.3. Silicate Reactions

The main rock-forming minerals in sandstones dissolve incongruently under natural porewater conditions with surface-reaction controlled dissolution rates (Berner and Holdren Jr, 1979; Hurst and Irwin, 1982). When considering reservoir quality silicate reactions in sandstones are important for three reasons: (i) silicate dissolution acts as a source of silica (ii) silicates provide a source of material for the genesis of authigenic clays; (iii) silicate dissolution produces secondary porosity.

Often early in the burial of sandstone the dissolution and kaolinisation of K-feldspar occurs (Bjørlykke, 1979; Holdren Jr and Berner, 1979; Bjørlykke and Egeberg, 1993; Lanson et al., 2002). The dissolution of K-feldspar has been reported in the North Sea Brent (Blanche and Whitaker, 1978; Bjørlykke et al., 1992; Giles, 1992; Harris, 1992; Morton et al., 1992) and in the Wilcox sandstone (Fisher and Land, 1986a; Day-Stirrat et al., 2010; Dutton and Loucks, 2010). Using end member chemical formulae and balanced equations it is possible to estimate the amount of silica produced during the kaolinisation of feldspars (Equation 1.2).

$$2KAlSi_3O_8 + 2H^+ + H_2O \rightarrow Al_2Si_2O_5(OH)_4 + 4SiO_2 + 2K^+$$

556.8g $\rightarrow$ 258.2g + 204.4g

Equation 1.2 Kaolinisation of K-feldspar (Worden and Morad, 2000)

The total molecular weight of reactants ($KAlSi_3O_8$) is 556.8g. This produces 204.4g of silica. Therefore the total silica released during the transformation is 43.2% that of the reactants. The reaction of 1 unit mass of K-feldspar produces 0.43 mass of quartz, assuming the reaction goes to 100% completion.

Although a viable source of silica the role the kaolinisation of K-feldspar may have on quartz cementation is disputed. Hurst and Irwin (1982) and later Bjørlykke and Egeberg (1993) demonstrate that for the reaction to take place protons must enter the system. The most likely source of these protons is by flushing the sandstone with meteoric water. This in turn is likely to remove any silica before precipitation can occur.

Later in the diagenetic process at higher temperatures any remaining K-feldspar may react with kaolinite to form illite (Equation 1.3) through a dissolution/precipitation mechanism (Lanson et al., 2002). This reaction is reported in many sedimentary basins including the North Sea (Bjørlykke et al., 1992; Lanson et al., 2002) and the Texas delta region (Land and Fisher, 1987). Using end member chemical formulae and balanced equations it is possible to estimate the mass of silica produced by the reaction of kaolinite and K-feldspar.

$$KAlSi_3O_8 + Al_2SiO_5(OH)_4 \rightarrow KAl_3Si_3O_{10}(OH)_2 + 2SiO_2 + H_2O$$

278.4g + 258.2g $\rightarrow$ 413.4g + 120.2g

Equation 1.3 Illitisation of kaolinite (Worden and Morad, 2000)

The total molecular weight of reactants is 536.5g, this produces 120.2g of silica. Therefore 22.4% of the total reactants are released as silica during this transformation; or for every single mass of reactants around 0.11 units of mass of silica are produced.

Feldspar albitisation is another common form of burial diagenetic alteration in sandstones of the North Sea (Saigal et al., 1988; Morad et al., 1990; Bjørlykke et al., 1992) and the Texas delta region (Land and Milliken, 1981; Day-Stirrat et al., 2010; Dutton and Loucks, 2010). The onset of feldspar albitisation may be at temperatures as low as 65°C, but wholesale albitisation occurs at temperatures of about ≥100–130°C (Saigal et al., 1988; Morad et al., 1990). The reaction of kaolinite and feldspar is shown in Equation 1.4 and occurs via a dissolution/precipitation mechanism (Perez and Boles, 2005) where silica is released from both reactants. Again, using end member chemical formulae and balanced equations it is possible to estimate the volume of silica produced by the reaction of K-feldspar to albite.

$$2KAlSi_3O_8 + 2.5Al_2Si_2O_5(OH)_4 + Na^+ \rightarrow NaAlSi_3O_8 + 2KAl_3Si_3O_{10}(OH)_2 + 2SiO_2 + H_2O + H^+$$

556.8g + 645.5g + 22.9g $\rightarrow$ 120.2g

Equation 1.4 Albitisation of feldspars (Worden and Morad, 2000)

The total weight of reactants is 1202.1g, the reaction can produce as much as 120.2g of silica. This equates to 10.0% of the total reactant being released as silica. Therefore, for each combined mass of reactant around 0.1 units of mass of quartz are produced, or for each unit mass of single reactant 0.05 unit mass of quartz are released.

A further high temperature silica source is the transformation of smectite to illite (Towe, 1962; Hower et al., 1976; Boles and Franks, 1979; Velde and Vasseur, 1992; Awwiller, 1993; Abercrombie et al., 1994; Berger et al., 1997; Lynch, 1997; Lanson et al., 2002; van de Kamp, 2008). This reaction (Equation 1.5) has been reported occurring within

reservoir sandstones (Morad et al., 2002; Worden and Morad, 2002) as well as external mudrocks (Bjørlykke, 1998; van de Kamp, 2008). Although widely disputed, it is argued that silica produced by the illitisation of smectite in external clay rich rocks may result in quartz cementation in adjacent reservoir sandstones (Gluyas et al., 2000; van de Kamp, 2008).

Where Equations 1.2 to 1.4 represent dissolution/precipitation reactions, the illitisation of smectite is thought to be a solid state transition (Lindgreen and Hanson 1991; Cuadros and Altaner, 1998) in which the transition of smectite to illite occurs as a response to temperature increases. Silica yields for this reaction are therefore estimated solely as a proportion of the reacting smectite, as outlined by van de Kamp (2008). Equation 1.5 illustrates that for every 1012.3g of smectite 197.7g of silica are produced, therefore for each unit mass of smectite undergoing illitisation 0.20 units of mass of silica are released.

$$1.308[(Al_{3.15}Mg_{0.85})(Si_8)O_{20}(OH)_4(Na_{0.85})2H_2O + (0.06Fe_2O_3 + 0.56K_2O + 0.02CaO) \rightarrow$$

Smectite (1012.3g)

$$[(Al_{4.12}Fe_{0.1}Mg_{0.56})(Si_{7.17})O_{20}(OH)_4(K_{1.47}Na_{0.01}Ca_{0.03})] + 3.29SiO_2 + 0.56Na_2O +$$

$$0.55MgO + 3.23H_2O$$ Silica (197.7g)

Equation 1.5 Smectite to illite transformation (van de Kamp, 2008)

The overall contribution of each of the above silicate reaction is summarised below in (Table 1.1). For the purposes of this investigation, the volume of quartz cement released from each of the above silicate reactions is assumed to be equal to the calculated mass of quartz produced (wt%).

Reaction / Process	Equation Number	Reactants (reacting ratio)	Silica Released per Single Mass of Reactants (g)
K-feldspar dissolution	1.2	K-feldspar	0.43
Illitisation of Kaolinite	1.3	K-feldspar + Kaolinite (1:1)	0.22
Albitisation of K-feldspar	1.4	K-feldspar + Kaolinite (4:5)	0.10
Illitisation of Smectite	1.5	Smectite	0.20

Table 1.1 Calculated silica yields from reaction involving commonly observed silicate minerals.

1.1.3. Silica Transport Mechanisms

Mass transport in sedimentary basins may occur by four basic processes; (i) Fluid flow in response to meteoric recharge; (ii) Fluid flow driven by compaction; (iii) Recycling of fluids by convection; (iv) Diffusion. However, although these processes have been widely discussed in previous studies (McBride, 1989; Bjørlykke and Egeberg, 1993; Aplin and Warren, 1994; Oelkers et al., 1996; Giles et al., 2000; Walderhaug et al., 2000) the exact mechanism by which silica is transported remains unclear.

By analysis of the composition and compositional heterogeneity of the mineralizing fluids Aplin and Warren (1994) were able to discount two, possibly three, of the above mechanisms. Firstly, transport by meteoric recharge was ruled out. Isotopic compositions measured in quartz overgrowths of the North Sea and Gulf of Mexico area tend to reflect formation in fluids diagenetically evolved such as basinal brines. However, in certain cases meteoric recharge may still be a plausible transport mechanisms; for example in regions where substantial uplift at the basin margins has caused exposure (Wilkinson et al., 2006).

Compaction-driven flow can also be discounted. Mass balance calculations show that around 10^4-10^6 pore volumes of water are require to precipitate 5 vol% quartz in a standard reservoir (Sibley and Blatt, 1976; Bjørlykke, 1979; Land and Dutton, 1979; Bjørlykke, 1983; Bjørlykke and Egeberg, 1993). This is far larger than the relatively small volumes of water expelled during the compaction of shales (McBride, 1989; Bjørlykke and Egeberg, 1993). If compaction was focused less water is required. Again, calculation (Aplin and Warren, 1994) show focusing is difficult to achieve. Furthermore, quartz cement is ubiquitous in most reservoir sandstones.

Recirculation or recycling of water by convective flow (Wood and Hewett, 1982) could theoretically overcome the ‘water problem’. However, large scale convection is likely to result in homogenous fluid compositions throughout the reservoir system (Leder and Park, 1986). Such compositions are rarely reported (Aplin and Warren, 1994).

The final possible transport mechanism proposed is diffusion. Wherever a concentration gradient is set up diffusion can occur. As the fluid simply acts as a transport medium, large volumes of water are not required. As demonstrated by Williams et al. (1985a) the solubility of quartz increases with temperature. This means that concentration gradients of dissolved silica should exist wherever there is a temperature gradient. However for diffusive transport to continue high regions of silica concentrations must be maintained. This is likely achieved by the reactions of silicates and stylolitisation. Calculation by Bjørlykke and Egeberg (1993) indicated diffusion is only possible over a few meters. This could potentially rule out external silica sources in large reservoir bodies.

1.2. Predicting the Timing of Quartz Cementation

Many analytical studies have attempted to evaluate the temperature and timing of the quartz 'cementation window', typically through the combined use of fluid inclusion (Haszeldine et al., 1984; Walderhaug, 1994b; Wilkinson et al., 1998), petrographic (Blanche and Whitaker, 1978; Hogg et al., 1992; Oelkers et al., 1996) and isotopic investigations (Brint et al., 1991; Aplin and Warren, 1994; Williams et al., 1997; Girard et al., 2001; Marchand et al., 2002).

By combining fluid inclusion and cement abundance data acquired from sandstones buried with well-defined thermal histories to a range of temperatures, Walderhaug (1994b) estimated the rate of quartz cementation as a function of time, temperature and quartz surface area. These data form the basis of commonly used predictive models for quartz cementation (Walderhaug, 1996; Lander and Walderhaug, 1999; Ajdukiewicz et al., 2010). Furthermore, since (a) quartz cement is infrequently observed below 80^{o}C and (b) fluid inclusions seldom reveal homogenisation temperatures below 80^{o}C, models commonly assume that quartz cementation has an effective threshold temperature of ~80^{o}C (Lander and Walderhaug, 1999; Walderhaug, 2000). Once cementation has been initiated, some authors (Walderhaug, 1996; Lander and Walderhaug, 1999; Wangen, 1999; Oelkers et al., 2000) suggest that cementation is a continuous process, with cement developing as a function of both temperature and quartz surface area, and with the majority of cement precipitating between 100-120^{o}C. Others (Girard et al., 2001; Marchand et al., 2002) propose a multi phase cementation process. Evidence supporting multi phase cementation includes measurements of isotopic and petrographic zonations. Indeed many authors, when viewing sandstones under cathodoluminescence report zonations within single quartz overgrowths (Hogg et al., 1992; Goldstein and Rossi, 2002). It is unclear what causes such striking textures, although it is believed it is caused by lattice defect created by varying concentrations of transition metals including aluminium and lithium (Demars et al., 1996; Götze et al., 2001; Boggs Jr et al., 2002). Changes in the concentrations of such impurities may be related to potential changes in the source and timing of cementation.

Until now, it has been impossible to validate these broadly based quartz-cementation models on the microscopic scale at which cement forms. In principle, detailed profiles of either or both fluid inclusion and oxygen isotopic data across single overgrowths can be used to constrain cementation history. However, fluid inclusions mainly occur close to the boundary of overgrowths and detrital grains, and thus constrain only the early phase of cementation (Osborne and Haszeldine, 1993). Oxygen isotopes have long been used as geothermometers to time precipitation reactions such as quartz cementation (Urey, 1947; Javoy, 1977; Blatt, 1987). The ratio of $\delta^{18}O$ to $\delta^{16}O$ within quartz is a function of the temperature and $\delta^{18}O_{(water)}$ in which it formed. Measurements of $\delta^{18}O_{(quartz)}$, as this study presents, facilitates the calculation of possible cementation temperatures. However, as $\delta^{18}O_{(water)}$ remains unknown and is likely to fluctuate during burial (Taylor, 1977; Morton and Land, 1987; Egeberg and Aagaard, 1989; Warren and Smalley, 1994) only constraints may be placed on true cementation histories.

Although oxygen isotope geothermometry applied to quartz cementation is not a new idea previous studies isolated whole overgrowths and could not generate temporal data (Lee and Savin, 1985; Brint et al., 1991; Aplin and Warren, 1994) whilst neither the resolution (20μm) nor the precision (±1-2‰; 1SD) of earlier *in situ* Secondary Ion Mass Spectrometry (SIMS) studies were sufficient to constrain growth histories (Graham et al., 1996; Williams et al., 1997; Girard et al., 2001; Marchand et al., 2002).

In summary previous attempts to constrain the timing of quartz cementation have suffered from a lack of high precision isotopic and quantitative mineralogical analyses. This has prevented full cementation histories and cementation kinetic from being determined. This in turn restricts our understanding of possible silica sources and transport mechanisms.

1.3.Scope and Purpose of Study

Although the mechanisms responsible for quartz cementation have been the subject of numerous studies (Heald, 1955; Bjørlykke, 1979; McBride, 1989; Primmer et al., 1997; Giles et al., 2000; Gluyas et al., 2000; Trewin and Fallick, 2000; Worden and Morad, 2000), key questions still remain. The main uncertainties are summarised below.

1.3.1. When does quartz cementation occur?

Many predictive quartz cementation models state a threshold temperature of 70-80^{o}C (Walderhaug, 1996; Walderhaug et al., 2000; Ajdukiewicz and Lander, 2010; Taylor et al., 2010). However this temperature has never been accurately tested on the scale at which cementation occurs. As highlighted above the spatial resolution of previous isotopic work made it physically impossible to perform high precision cement geothermometry on the scale required to examine all but the bulk of cement. Fluid inclusions, although a valuable source of geochemical data, may be subject to re-setting. Also, the sealing mechanisms required for inclusions to form imply that they can only reflect a temperature higher than the onset of cementation. It is also highly unlikely for fluid inclusions to be positioned across an entire overgrowth; therefore no details of cementation history can be extrapolated. Furthermore the 80^{o}C threshold is largely constrained by petrographic observations (Walderhaug, 1994a; Walderhaug, 1994b). However, more recent and detailed microscopy reports volumetrically important quantities of quartz cement forming below 80^{o}C (Vagle et al., 1994; Haddad et al., 2006; Dutton and Loucks, 2010; Marcussen et al., 2010) casting more doubt over this threshold temperature. It is also unclear if quartz cementation occurs within shales and if it is when does it take place? The timing of quartz cementation could signify the increase in silica concentrations within adjacent units and thus influence diffusive transport mechanisms.

1.3.2. Where is silica sourced? Internally or externally?

It is clear many reactions occurring within the sedimentary basin can chemically produce silica. However few studies have attempted to quantitatively examine these reactions with the aim of sourcing silica for quartz cementation. Furthermore, few studies have quantitatively examined any potential relationship there may be between sands and shale.

1.3.3. How is silica transported?

Unresolved issues concerning the timing and the source of silica result in further unknowns. For example, if cement is indeed sourced from a range of processes occurring across different temperatures how is silica transported at the reservoir scale?

1.4.Project Aims and Objectives

The specific aims of this project were twofold:

1. To constrain the onset of quartz cementation and resolve quartz cementation histories
2. To quantitatively evaluate potential silica sources internally within reservoir sands as well as externally in adjoining shale units.

The full objectives of this investigation were to:

- Quantify quartz cement in samples from a wide range of temperatures from the North Sea Ness Formation and Gulf of Mexico Wilcox Formation.
- Constrain quartz cement histories through
    - Isotopic analysis of quartz cements
    - Petrographic quantification of quartz cement
    - Time –Temperature history modelling
- Constrain potential silica sources through
    - Quantitative petrographic examination to evaluate internal sources
    - Quantification of mineralogical changes in adjoining shales
- Validate current quartz cementation modelling theory

1.5. Thesis Structure

This thesis is composed of 5 chapters:

1. Introduction to Quartz Cementation
2. Analytical Strategy and Methods
3. Quartz Cementation in the North Sea Ness Formation
4. Quartz Cementation in the Texas Wilcox Sandstone
5. Quartz Cementation Mechanisms in Reservoir Sandstones

In Chapter 1 a full literature review is presented and the project aims and objectives described. Chapter 2 describes the analytical strategy that was designed to fulfil these project aims. Two stand alone case studies are then presented in Chapters 3 and 4. Chapter 3 is a study of quartz cementation in the North Sea, Ness Formation. In this study petrographic, mineralogical and high precision oxygen isotope analysis are utilised to explore quartz cementation in a range of quartz rich sandstones as well as siltier sand deposits. Using the same techniques Chapter 4 then explores the timing and sources of quartz cementation in the Texas, Wilcox sandstone. Chapter 5 integrates the main findings of the Ness and Wilcox case studies to evaluate the timing and sources of quartz cementation in reservoir sandstones.

2. Methodology

This chapter describes a series of analytical methods designed to constrain the timing of quartz cementation in reservoir sandstones. Furthermore, this strategy was designed to examine possible silica sources and to test the validity of existing predictive cementation models. This analytical investigation is divided up into 6 stages as illustrated in Figure 2.1.

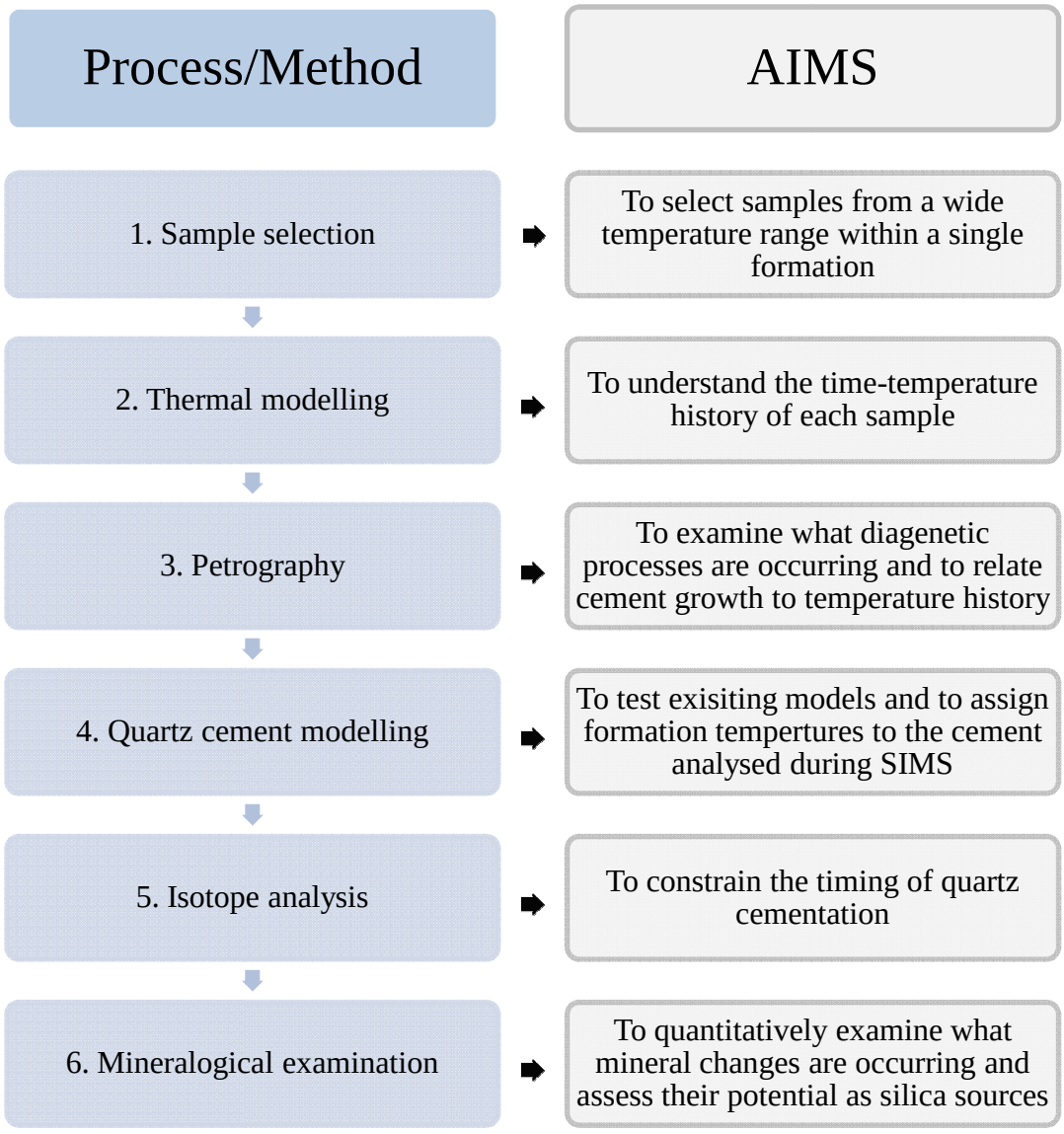

Figure 2.1 Analytical strategy designed to constrain the timing and mechanisms of quartz cementation in reservoir sands.

2.1.Sample Selection

Temperatures increase during burial; as a consequence diagenetic reactions occur. The overall aim of this project was to examine the effect of temperature on the rate and mechanisms by which quartz cementation occurs. To examine quartz cementation across a range of thermal and mineralogical conditions samples were selected from multiple wells in two study areas:

Study 1: Jurassic North Sea Ness Formation

Study 2: Early Eocene Texas Wilcox sandstone

2.1.1. The Ness Formation

The Ness Formation of the North Sea was chosen as it has been extensively cored at multiple burial temperatures. As part of the hydrocarbon rich Brent group the Ness Formation has been meticulously characterised in previous studies (Bjørlykke et al., 1992; Giles, 1992). Indeed, quartz cementation has been extensively investigated in the clean quartz rich sandstones of this formation (Burley et al., 1989; Walderhaug, 1994a; Walderhaug, 1994b; Primmer et al., 1997; Giles et al., 2000; Walderhaug et al., 2000; Girard et al., 2001). The Ness Formation was specifically chosen for its sands/silt/shale interlayers which provided scope for the examination of possible cementation in silt-rich units as well as sandstones. Furthermore, clay rich shale units were selected for investigation. Examination of these shale units was undertaken to assess if any silica migration has occurred between the Ness Formations distinct lithologies.

2.1.2. The Wilcox Group

As in the North Sea Study, a series of Wilcox sandstones were selected to examine quartz cementation and reservoir quality. Parallel to this a series of interlayered reservoir shales and silts were selected to examine the wider diagenesis in the system and to scrutinise possible silica sources. These onshore Wilcox samples are of specific interest as they may offer an insight into the reservoir quality of newly discovered deeply buried offshore potential plays. Similar Wilcox material has been extensively characterised by Fisher and Land (1986a), Land and Fisher (1987), Dutton and Loucks (2010) and Day-Stirrat *et al* (2010).

2.2. Time-Temperature History Modelling

This project deals with samples from multiple wells in two study areas. Each individual well has a separate burial and thermal history. Chemical diagenesis including quartz cementation (Bjørlykke, 1979; McBride, 1989; Walderhaug, 1996; Oelkers et al., 2000; Worden and Morad, 2000; Ajdukiewicz et al., 2010), the dissolution and albitisation of feldspars (Land and Milliken, 1981; Boles, 1982a; Hurst and Irwin, 1982; Saigal et al., 1988; Morad et al., 1990; Wilkinson et al., 2001) as well as some clay mineral transformations (Boles and Franks, 1979; Freed and Peacor, 1989; Berger et al., 1997; Lanson et al., 2002; van de Kamp, 2008) is driven by increasing temperatures during burial. It is therefore important to consider a sample's maximum burial temperature rather than its current burial depth. Furthermore, to constrain the timing of quartz cementation and related diagenetic processes it is important to understand the full temperature history of each sample.

In this investigation Genesis 4.92 (http://www.zetaware.com) was used to combine geological and geochemical data to produce time-temperature histories of each well. In the Wilcox study all temperature modelling was carried out and generously shared with us by R. Day-Stirrat working at the Bureau of Economic Geology, Texas. In both studies temperature histories were calibrated using measured temperature data and where available vitrinite reflectance. The modelling process is summarised in Figure 2.2.

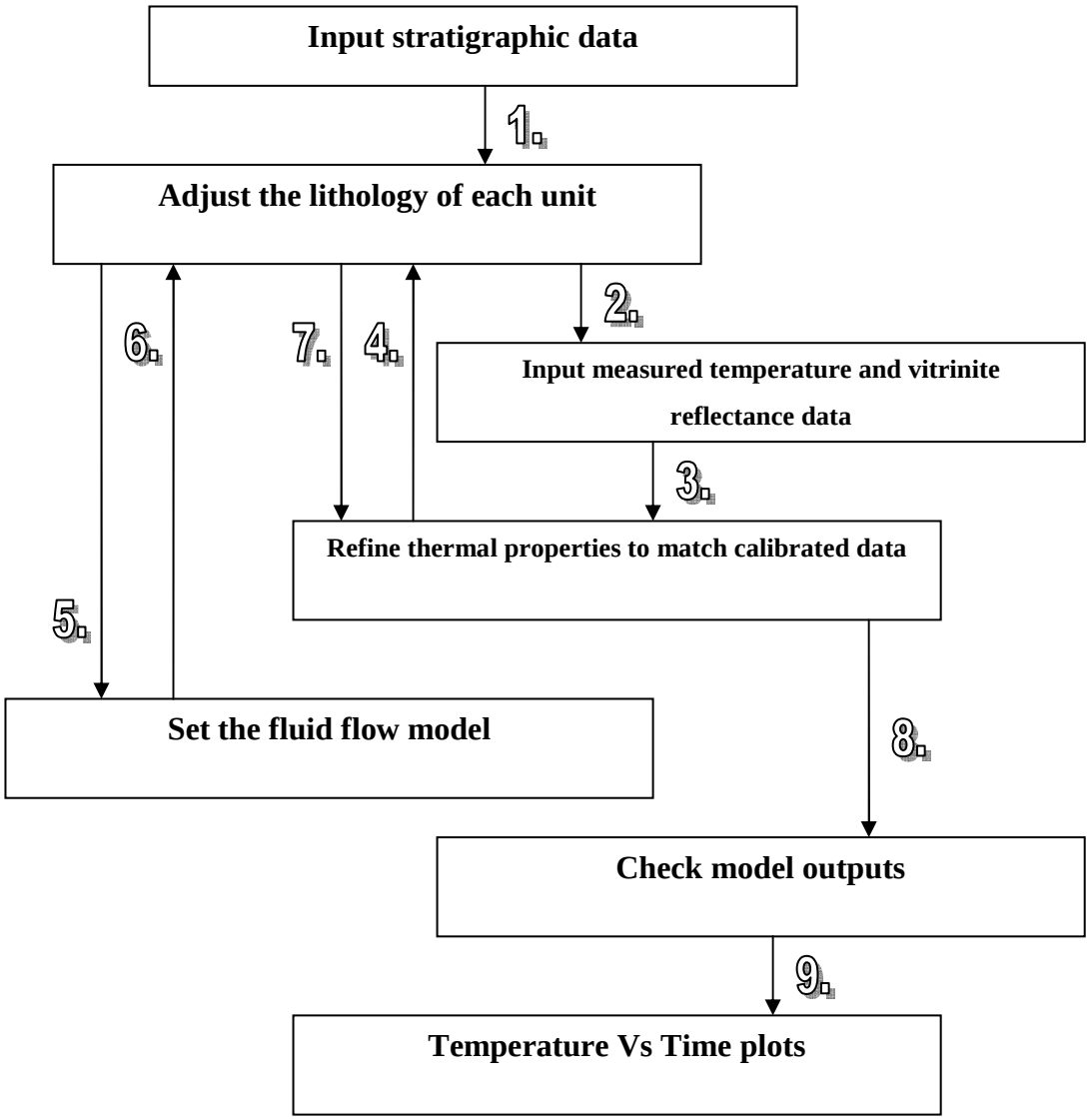

Figure 2.2 Workflow of the iterations required during Genesis modelling.

2.2.1. North Sea Time -Temperature Modelling

2.2.1.1. Geological Inputs

BP and the Norwegian Petroleum Directorate (NPD) supplied the geological information needed for thermal modelling. This information was obtained from production data and measurements made on core or cutting material in the laboratory. During the drilling of each well different down-hole measurements were made. Therefore, the available datasets vary slightly (Table 2.1).

Well	34/8-7	211/27-A2	211/11a-3	30/3-4	30/9-12
Lithology	•	•	•	•	•
Age	•	•	•	•	•
Temperature	•	•	•	•	•
Vitrinite Reflectance	•		•	•	
Tmax	•			•	

Table 2.1 Geological inputs required for Genesis modelling

2.2.1.2. Stratigraphy and Lithology

Table 2.2 gives the name and ages of the formations observed in the North Sea sample area. The lithology of each formation was individually determined for each well using composite logs.

Formation	Age (my)	Formation	Age (my)
Nordland	5.33	Tarbert	167
Hordaland	50	Ness	170
Rogaland	62	Etive	176
Shetland	91	Rannoch	178
Cromer Knoll	140	Broom	182
Kimmeridge	160	Dunlin	200
Heather	165	Hegre	203.6

Table 2.2 North Sea formation/group names and geological ages

2.2.1.3. Thermal Parameters

The thermal properties were set to transient, fixed at base of lithosphere. This implies that heating is fixed at the base of the lithosphere. Heating is therefore affected by any change in the type or amount of sediment in the basin. The temperature at the base of the lithosphere is taken to be fixed at 1330 ^{o}C. The total thickness of the mantle lid + lower crust + upper crust is always taken to be 120 km. A surface temperature of 10^{o}C was used, this is a standard setting used by BP in this region, based on work including Prentice and Mathews (1988). Advective heat transport and radioactive heat production were also activated allowing for the model to generate additional heat within the basin and not solely from aesthenosphere heating.

2.2.1.4. Temperature Calibration

Modelled temperatures were calibrated either using direct measurements of temperature or using a temperature proxy such as vitrinite reflectance. In this North Sea study direct temperature measurements were taken from drill stem tests. Only final stabilised temperatures were used. Additionally Bottom Hole Temperature (BHT), the maximum recorded temperature measured during a logging run, were used. However, as BHT recordings may not be stabilised these datum were added with a 5% error. In three wells vitrinite reflectance, the measure of the thermal maturity of organic matter, was also available for calibration (Table 2.1).

The calibration process required a series of iterations to be run. During these iterations the lithology was slightly adjusted within geological reason (determined by composite logs). Changes in the lithology altered the weight and thermal properties of the rocks, thus changing the heat flow within a well. However, changing lithologies alone has a minor effect on the modelled output. In situations where the modelled output remained far from the measured data it was necessary to alter the crustal thickness.

Altering the thickness of the crust will allow more or less heat to transfer into the sediment column and will thus affect the modelled temperature history. A number of iterations were run to match modelled to measured data using Chadwick and Pharaoh's (1998) geophysical study of the Moho in the North Sea as a guide. In general the total thickness of the mantle lid + lower crust + upper crust is taken to be 120km. Furthermore, the upper and lower crust have a similar thickness and in practice the mantle lid will be no less than 90km for continental crust.

2.2.1.5. Thermal Modelling: Uncertainties

Temperature calibrations using proxies such as vitrinite reflectance are made using calibration curves. Within Genesis four vitrinite reflectance calibration curves are

available. These curves are based on maturity kinetics formulated using different datasets. Two of these curves are supplied by BP (BP max and BP min), one from ARCO and finally the LL model. The kinetics controlling each curve are slightly different. In this study we calibrated the model output to within the min and max BP curves. Overall it must be recognised that a modelled output is only one interpretation of the calibration process. All effort was therefore made to keep the model simple to maintain a sense of geological reality.

2.3. Sandstone Petrography

A petrographic investigation by means of Scanning Electron Microscopy (SEM) was carried out on a selection of rock thin sections and rock chips. Since this study (a) aimed to understand the timing and temperature of any diagenetic processes, (b) was designed to evaluate basic reservoir quality and (c) will provide the input data required for cementation modelling, the total cement was quantified along with the total porosity, non-quartz minerals, detrital quartz and the average detrital grain size.

All petrographic analyses were carried out at Newcastle University using a Philips/FEI XL30 Environmental Scanning Electron microscope - Field Emission Gun (XL30 ESEM-FEG). The XL30 ESEM-FEG was chosen for its interchangeable Backscattered Scanning Electron (BSE), SEM-Cathodoluminescence (SEM-CL) and Secondary Electron (SE) capabilities. Full analytical conditions are given in Table 2.3.

SEM	kV	Spot size	Working distance (mm)	Magnification
BSEM	20	4	10-15	80 – 200x
SEM-CL	15	4	10-15	80 – 200x
SE	15	4	10-15	100-500x

Table 2.3 XL30 ESEM-FEG at Newcastle University, operating conditions

The XL30 ESEM-FEG at Newcastle is also fitted with an energy dispersive X-ray analyser, from EDAX capable of analysing elements with Z >4 (B to U). Alongside BSE imaging the EDAX system allowed for the analysis of all constituent mineral phases.

2.3.1. Rock Chip Examination

To examine the nature and relationship of diagenetic and detrital minerals SEM analysis of rock chips in Secondary Electron (Table 2.3) was carried out. Rock chips were mounted on a SEM pins and gold coated.

2.3.2. Thin Section Examination

Quantitative petrography designed to ascertain basic reservoir quality was carried out on thin sections. Thin sections were left slightly thicker than the standard 30µm, allowing for the possible addition of the UWQ-1 quartz standard required for isotope analysis. To remove all grease and dirt each thin section was thoroughly cleaned using ethanol followed by water under ultrasonification. All samples were carbon coated prior to SEM imaging. The carbon was applied to remove any charge that may build up.

2.3.2.1. Image Acquisition

Before image acquisition suitable magnifications were selected for each sample. A suitable magnification should be high enough to allow for all mineral phases to be recognised but low enough to suit the largest grain size. For most samples magnifications between x80 and x200 were sufficient, this allowed for between 30-50 grains to be viewed per image. The number of images acquired for quantification was pre-determined based on the magnification, grain size and inhomogeneity of each sample; Evans *et al* (1994) gives a strategy for determining this. Usually between 6 and 10 areas were sufficient, allowing around 150 grains to be examined. Areas were randomly selected from each thin section using Microsoft Excel to generate 6 to 10 random X and Y coordinates. The coordinates were then logged into the XL30 ESEM-FEG motorised stage.

Complimentary BSE and SEM-CL images were acquired using the operating conditions shown in Table 2.3; examples are given in Figure 2.3. The differences in the luminescing properties of detrital and authigenic quartz (Demars et al., 1996; Götze et al., 2001; Boggs Jr et al., 2002) facilitated the fast and efficient recognition and quantification of quartz cement.

Using these images, point counting and image analysis were utilised to carry out a quantitative petrographic study. Initially in the North Sea case study a 300 spot point count was performed, this was later followed by an image analysis strategy design to improve the efficiency of the quantification process. In the second study, Wilcox sandstones were examined using only the image analysis method.

2.3.2.2. Quartz Cement and Mineral Quantification: Point Count

Using Microsoft PowerPoint each SEM-CL (Figure 2.3b) image was overlain by its coupled BSE image (Figure 2.3a). Using Microsoft Excel 50 random X and Y coordinates were generated, graphed and placed above each image pair in PowerPoint. A fade out option was used to interchange between each image/graph.

Following standard practice in sedimentary petrography, the composition of each sample was estimated by a 300 spot point count (50 points per image pair) undertaken according to the Glagolev–Chayes method (Chayes, 1949; Chayes and Fairbairn, 1951; Weltje, 2002). When using standard light microscopy each point is represented by a cross hair on a randomly moving stage; here, these spots were replaced with randomly generated points. Initially the mineralogy of each of these points was resolved using the BSE image. Then fading between the BSE and SEM-CL images the nature of quartz, detrital or authigenic, was determined.

2.3.2.3. Quartz Cement and Mineral Quantification: Image Analysis

Image analysis involves a number of stages using the same images acquired for the point count method (Figure 2.3). This method was adapted from that formulated by Evans (1994) and Cooper (2000). This modified process makes use of Adobe Photoshop to manually select different areas of the digital BSE and SEM-CL images.

Stage 1: Using the magic wand tool in Photoshop all areas of porosity were selected in the acquired BSE image. Once selected all areas of porosity were coloured black, the remaining material made up of quartz and all other minerals was coloured white (Figure 2.4a).

Stage 2: Again, using the magic wand tool in Photoshop all areas that represent non-quartz were selected from the original BSE image and coloured white (Figure 2.4b).

Stage 3: Using a high contrast SEM-CL image the lighter detrital regions are easily distinguished from the darker cement material. Initially the porosity and non quartz mineral templates (stage 1 and 2) was superimposed onto the SEM-CL image. Using the magic wand tool in Photoshop the detrital quartz was selected and added to these templates. The remaining material representing authigenic quartz was coloured black (Figure 2.4c).

Stage 4: Using a Python code a simple image analysis tool was written by M. Drews (Newcastle University). This code scans each pixel in the modified BSE and SEM-CL images and assigns it a RGB colour value. These RGB values range from 255 (white) through to 0 (black). As each constituent was modified to be either black or white in the various images the Python code allows for the quantification, as outlined in Table 2.4.

Ref	Unknown	Image	Counter
1	All minerals	BSE (A)	White
2	Porosity	BSE (A)	Black
3	Non-quartz	BSE (B)	White
4	Quartz	BSE (A) BSE (B)	(Ref 1) –(Ref 3)
5	Quartz Cement	SEM-CL	Black
6	Detrital Quartz	SEM-CL, BSE	(Ref 4) –(Ref 5)

Table 2.4 Strategy for determining the quantity of each mineral phase during image analysis.

2.3.2.4. Identification of Non Quartz Minerals by X-Ray Diffraction

X-ray Diffraction (XRD) of powdered samples was used to determine the mineralogy of the non-quartz constituents. All X-Ray Diffraction analyses were carried out at Newcastle University using a Panalytical X'Pert Pro MPD, fitted with an X'Celerator and a secondary monochromator. A Cu anode was supplied with 40 kV and a current of 40 mA to generate Cu-Kα radiation (λ = 1.54180 Å). All analyses were run over a range of 2-70^{o}2θ with a nominal step size of 0.0167^{o}2θ and time per step of 100 seconds. Anti-scatter and divergence slits were both set to 1/4^{o} and a beam mask of 10mm was used. All scans were carried out in 'continuous' mode using the X'Celerator RTMS detector.

2.3.2.5. SEM-Cl Grain Size Analysis

Grain size is an important input parameter when utilising cementation models as it is the primary control on quartz surface area (Walderhaug, 1994b; Walderhaug, 1996; Taylor et al., 2010). Furthermore grain sizes also supply information about the depositional setting of a sample and allow for a direct comparison between samples to be made. Average detrital quartz grain size was determined during SEM-CL imaging. In each sample a minimum of 50 quartz grains were randomly selected. Grain size is taken as an

average of the long axis measured in accordance with the method described by Walderhaug (1994a)

2.3.2.6. Calculation of Detrital Quartz Surface Area

The detrital surface area of a sample reflects the potential free surface available for cementation to occur. Detrital quartz surface area can be calculated from the information gathered from the above petrographic analysis. Following Lasaga (1984) the initial quartz surface area can be estimated as the cumulative surface area of spheres with a fixed diameter D, equal to the measured average grain size with the total volume equal to the fraction of detrital quartz, f, in a fixed volume of sandstone. Here we assume a volume of sandstone, V, equal to $1cm^3$. This gives the equation:

$$A_0 = \frac{6fV}{D}$$

Equation 2.1

2.3.3. Statistical Analysis

All petrographic analyses were made on a selection of 6-10 images that represent the thin section. The standard deviation (%) of each mineral, phase or grain size was determined; the standard deviation is a measure of how widely values are dispersed from the mean value. In this investigation the standard deviation is determined by comparing results from each set of 6 to 10 image pairs. Also reported is the 95% confidence value. This value indicates that statistically 95% of the population (cement quantity, porosity…) fall plus or minus from the mean. Again this is calculated across the 6-10 images.

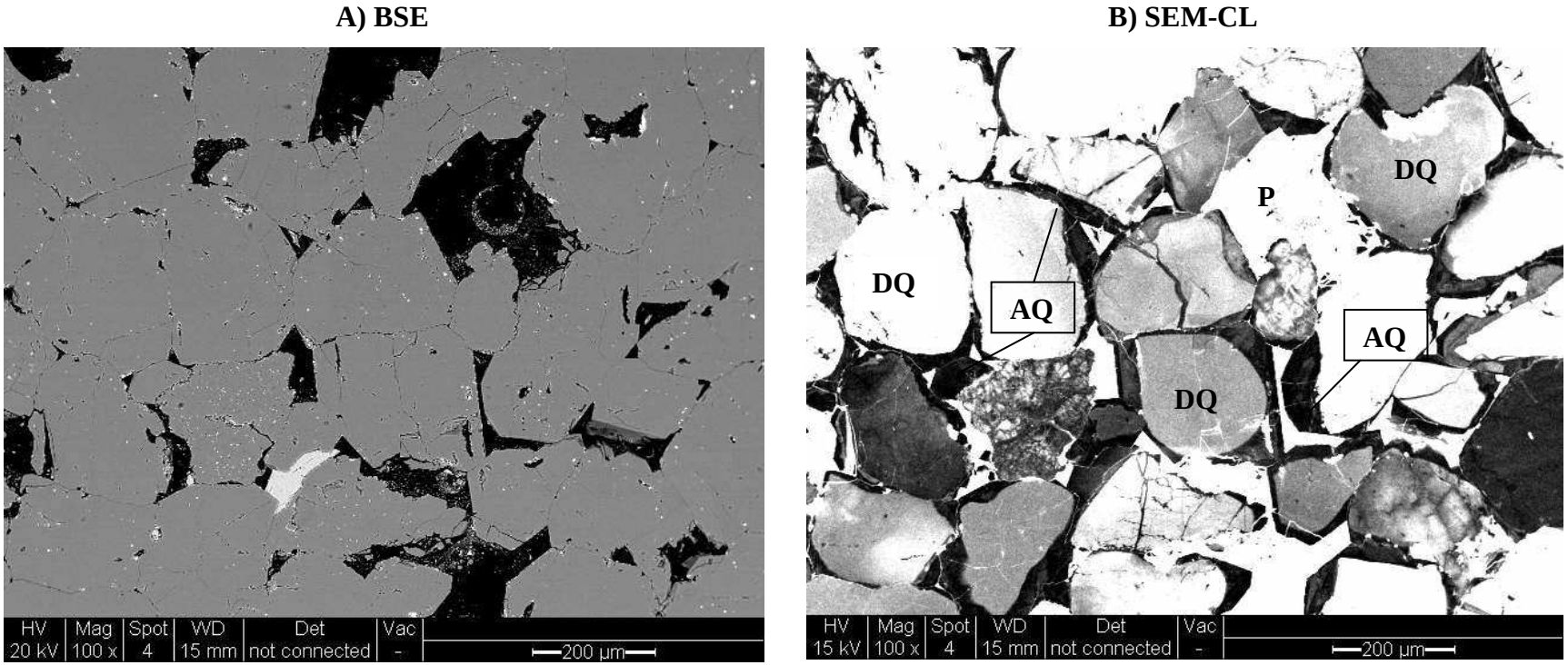

Figure 2.3 Complementary SEM images of Wilcox sandstone GOM6. A) Backscattered Scanning Electron Microscopy (BSE) image, the majority of the grey material is quartz, the darker areas represent porosity. **B)** Scanning Electron Microscopy – Cathodoluminescence (SEM-CL) image, darker non-luminescing areas highlight quartz overgrowth (AQ). Lighter areas represent either detrital grains (DQ) or porosity (P).

A) Stage 1 – BSE (i) **B) Stage 2 – BSE (ii)** **C) Stage 3 – SEM-CL**

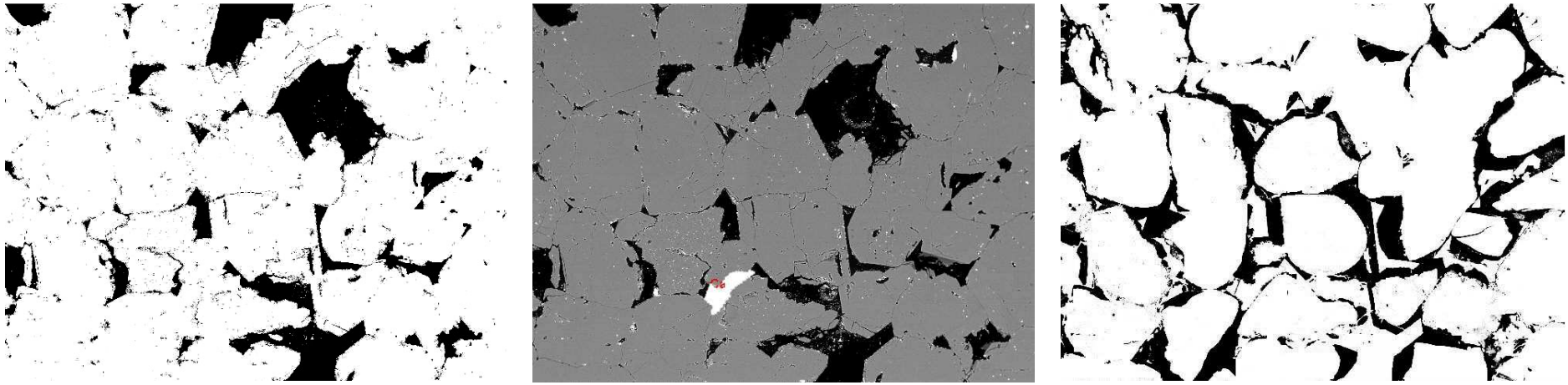

Figure 2.4 Image analysis images. A) Modified BSE image, black = porosity, white = all minerals, **B)** Modified BSE image, white = non quartz minerals, **C)** Modified SEM-CL image, black = quartz cement. See Figure 2.3 for scale bar.

2.4.Modelling of Quartz Cementation

Quartz cementation models are routinely used to determine sandstone porosity and reservoir quality (Taylor et al., 2010). A number of models have been proposed, some source silica from pressure solution (Ramm, 1992) others from concentrated stylolites (Canals and Meunier, 1995; Oelkers et al., 1996; Walderhaug, 1996; Bjørkum et al., 1998; Lander and Walderhaug, 1999; Wangen, 1999; Walderhaug et al., 2000). In recent years two commercial packages have been derived, Exemplar as described in Lander (1999) and Walderhaug (1996) and Touchstone as described in Makowitz and Lander (2010). Both models use quartz precipitation kinetics based largely on those experimental observation made in Walderhaug (1994b).

2.4.1. Quartz Cementation Models: Kinetics

Walderhaug (1996) used the data from his earlier studies (Walderhaug, 1994a; Walderhaug, 1994b) to show that at constant temperature, the volume of quartz cement Vq (cm^3) precipitated in a 1 cm^3 volume of sandstone with a quartz surface area A (cm^2) during time t (s) can be expressed as:

$$Vq = \frac{MrAt}{\rho}$$

Equation 2.2

where M is the molar mass of quartz (60.09 g/mole), r is the rate of quartz precipitation in moles/cm^2s, and ρ is the density of quartz (2.65 g/cm^3). The precipitation rate r is a function of temperature and, at diagenetic temperatures, the temperature dependence can be approximated by the equation (Walderhaug, 1994a)

$$r = a10^{bT}$$

Equation 2.3

where *T* is temperature (°C) and *a* and *b* are constants with units of moles/cm^{2}s and 1/°C, respectively. The constants *a* and *b* are analogous to the pre-exponential factor and activation energy, respectively, in an Arrhenius equation. For a linear temperature change, *T* can be expressed as a function of time in the following manner (Walderhaug, 1996):

$$r = a10^{b(ct+d)}$$

Equation 2.4

where *c* is heating rate (°C/s), *d* is the initial temperature (°C), and *t* is time (s). Combining Equation 2.2 and Equation 2.4 Walderhaug 1996 formulated an equation to predict quartz cement growth as a series of linear time-temperature segments;

$$V_{q2} = \phi_0 - (\phi_0 - V_{q1})\exp\frac{-MaA_0}{\rho\phi_0 bcln10}(10^{bT_2} - 10^{bT_1})$$

Equation 2.5 Walderhaug's (1996) Quartz Cementation Model

Where V_{q2} is the amount of quartz cement (cm^3) precipitated from temperature T_1 to T_2, and V_{q1} is the amount of quartz cement present at T_1. φ_0 is porosity at T_1, M is the molar mass of quartz, A is detrital quartz surface area (Equation 2.1) and ρ is the density of quartz.

As Walderhaug (1996) demonstrates, temperature is by far the most important parameter in the above model, although quartz surface area and original porosity must also be considered. As little cement has been petrographically observed below 80^{o}C and few fluid inclusions reveal homogenisation temperatures below 80^{o}C it is assumed this is a threshold temperature (T_1) at which cementation begins (Oelkers et al., 1996; Walderhaug, 1996; Lander and Walderhaug, 1999).

In this thesis Walderhaug's (1996) cementation model described by Equation 2.5 was used to model quartz cement growth in each of the sampled silts and sandstones examined during the above petrographic study. The aim of this modelling process was twofold. Firstly, the modelled response was compared to the petrographic data in an attempt to validate current predictive models. Secondly, this study aimed to use the Walderhaug model to assign formation temperatures to specific locations across individual overgrowths, thereby allowing the material analysed during later in-situ isotopic experiments to be assigned a formation temperature.

2.4.2. Cementation Modelling: Model Parameters

The values of the pre-exponential *a* and the exponential constant *b* were set to 1.98 × 10^{-22} moles/cm^{2}s and 0.022^{o}C respectively (Walderhaug 1994b). These values are determined from a measurement performed on North Sea sandstones, many of which are Jurassic in age (Walderhaug, 1994b). Walderhaug (2000) highlights that the pre-exponential constant *a* has much less influence on the modelled results than the exponential constant *b*. Walderhaug (2000) indicates that the exponential constant *b* can be modified for different basins in order to identify the values that gives the best fit between observations and simulations.

Walderhaug's (1996) cementation model was run on a 1cm^3 volume of sandstone. The fraction of detrital quartz, porosity and grain size were all determined from quantitative petrographic analysis. Heating rates were determined from time temperature histories

generated in Genesis 4.92. However, in the North Sea well 25/2-4 no geochemical or thermal data were available to construct a thermal model and so a linear time temperature history was assumed.

2.4.2.1. Temperatures Histories for Quartz Cementation Modelling

Above the threshold of 80°C each time temperature history could be separated in to a series of separate linear stages of heating, S1, S2, S3…. Walderhaug's (1996) model was run from 80°C and continued through to the maximum burial temperature. Cement volume increase was calculated every 0.1 million years. Effectively, cement was modelled as a series of linear steps 0.1 million years in length. The temperature increase [(T_2-T_1) Equation 2.5] during each time step is determined by the larger linear heating stages determined during Genesis modelling.

2.4.3. Cementation Growth: Radial Increase in Overgrowth Size

To use Walderhaug's (1996) model to attribute a formation temperature to each SIMS pit it is necessary to understand the growth of each individual overgrowth. The growth of each overgrowth was assumed to be equal to the radial growth of each grain; effectively this model builds up cement around detrital quartz spheres like layers of an onion. This assumes that total cement precipitated during each 0.1 million year time step is divided equally between all quartz grains. Overall, overgrowth thickness can be calculated by:

$$r_{growth} = \sqrt[3]{\frac{V_0 + (V_{q2} - V_{q1})/N_0}{\frac{3}{4}\pi}} - \sqrt[3]{\frac{V_o / N_o}{\frac{3}{4}\pi}}$$

Equation 2.6

Where V_0 is the initial grain volume in cm^3, VQ_1 is the initial volume of quartz cement, VQ_2 is the volume of quartz cement after 0.1 million years and N_0 is the number of quartz grains in the system.

To create a temperature profile across each overgrowth it was assumed cementation has occurred concentrically away from the detrital grain. It is also assumed that each overgrowth represents the full cementation history. Using the growth rates calculated above it was possible to measure out away from the detrital grain and estimate formation temperatures.

2.5. Secondary Ion Mass Spectrometry

Stable isotope abundances are measured as differences in the isotopic ratio of two isotopes. Stable isotopes are reported using δ (delta), in which the isotope ratio of a sample is expressed in terms of its deviation, in parts per thousand ($^{0}/_{00}$), from the same ratio in an internationally accepted standard, Standard Mean Ocean Water (V-SMOW).

$$\delta_A=[(R_A-R_{stnd})/R_{stnd}].10^3$$

Equation 2.7

Where R_A is the ratio of the heavy isotope to the light isotope ($^{18}O/^{16}O$).

The fractionation of ^{18}O between phases containing oxygen, such as quartz and water, at equilibrium is temperature-dependant as a result of the difference in the mass and mechanical properties of the isotopes ^{16}O, ^{17}O and ^{18}O with increasing temperature (Urey, 1947). The oxygen isotope fractionation between two coexisting phases forms the basis of oxygen isotope geothermometry (Javoy, 1977).

In this investigation high precision SIMS was utilised to examine quartz cement growth in Ness Formation and Wilcox sandstones. This SIMS study was designed to measure oxygen isotope ratios across individual overgrowth with the aim of constraining the formation temperatures of the cement. This isotope investigation is formed of four parts:

1. Sample and overgrowth selection
2. SIMS analysis
3. SIMS spot characterisation
4. Temperature estimates

2.5.1. Sample and Overgrowth Selection

Using the images made during the petrographic study a selection of sand and silt samples were selected for SIMS analysis. The sands all presented large (>30 µm) clean overgrowths. In the North Sea study, to examine possible precipitation in finer grain silt material a selection of sites was chosen in more silt rich material. Overgrowths in these silt samples were often <15 µm wide.

In the Wilcox study a selection of sandstone samples were chosen. Theses samples were selected as they represented a wide temperature variation and presented sufficiently large quartz overgrowths suitable for SIMS analysis. Due to complications associated with the earlier North Sea isotope study, no silts were selected for analysis, only sandstones with clean overgrowths.

2.5.2. SIMS Analysis

In situ oxygen isotope data were acquired in the WiscSIMS Laboratory at the University of Wisconsin-Madison using a CAMECA ims-1280 large radius multicollector ion microprobe (Kita et al., 2009; Valley and Kita, 2009). Quartz overgrowths were analysed during three sessions. In the first session, carried out in May 2008, only Ness samples were analysed. Initially the spot size was aligned to 20 µm reduced to 12 µm after just 10 sample measurements. During the second session, performed in June 2009 using a 12 µm beam, 3 Wilcox sandstones were examined. Finally in a third session in June 2009 a 2µm spot was used. In the first two sessions the $^{133}Cs^{+}$ primary ion beam was aligned to 20 then 12 µm with ~1.3 nA intensity. The typical secondary $^{16}O^{-}$ ion intensity was ~$1.5x10^{9}$ cps for analyses using the 1.3 nA beam. Measurements were performed in multicollector Faraday Cup mode and with conditions similar to those reported by Kelly *et al*(2007). In the third analytical session, a $^{133}Cs^{+}$primary ion beam with an intensity of ~25 pA was focused to a size of approximately 2x3 µm. General

conditions of the analyses are similar to those reported in Kozdon *et al*. (2009). The secondary O^- ions were detected by a Faraday cup ($^{16}O^-$) and a miniature Hamamatsu electron multiplier ($^{18}O^-$). The typical secondary $^{16}O^-$ ion intensity was ~$3x10^7$ cps. Charging of the sample surface was compensated by Au-coating and an electron flood gun. Grains of the University of Wisconsin quartz standard, UWQ-1, ($\delta^{18}O$ = 12.33‰ [SMOW];(Kelly *et al*., 2007)) were mounted in the center of each thin section. Four consecutive measurements of UWQ-1 quartz standard were performed before and after every set of 8-22 sample analyses. The precision (reproducibility) of a set of bracketing standard analyses is assigned as uncertainty of unknown samples. Detailed analytical protocols are described in Kita *et al.*(2009).

2.5.3. Examination of SIMS Pits

To gain an understanding of how quartz cement is growing as a function of time and temperature it is necessary to relate each SIMS site spatially within a single overgrowth. In the absence of sector zoning it has been assumed that cementation has occurred in an essentially concentric fashion outwards from the edge of detrital quartz grains. Measurements were therefore made from the boundary between the detrital quartz and initial cement, out to the center of each SIMS pit as shown by the blue lines in Figure 2.5. Additionally, to normalize measurements across a sample, calculations of percentage distance across the overgrowth were made. This required a further measurement to be made out to the edge of the cement as illustrated by the red line in Figure 2.5.

It is important to realise that cementation may not occur concentrically away from a detrital quartz grain. In reality the spatial variations that we may witness in the isotopic data are affected by a number of factors including; the cut of the thin section; crystal growth mechanisms and the late initiation or early termination of cementation related to pore opening and blocking.

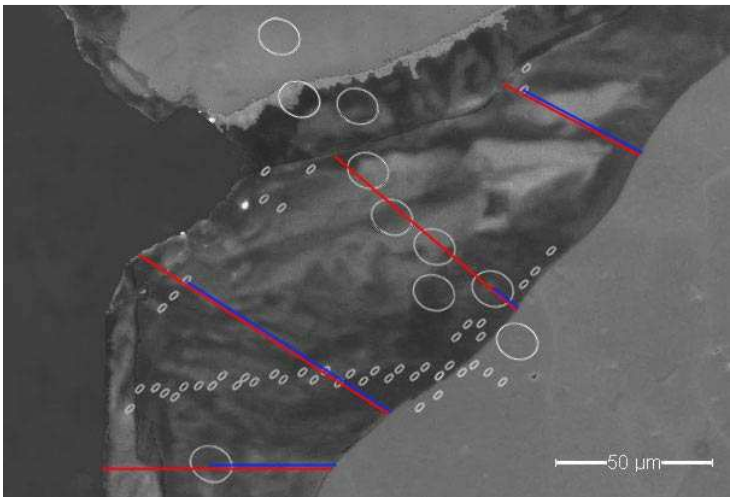

Figure 2.5 SEM-CL image showing the technique used to measure the relative distance of each SIMS pit away from the detrital grain. Blue line = distance to SIMS pit, red line = Total width of overgrowth.

2.5.4. Isotope Geothermometry

The stable isotope fractionation factor between two phases, A and B, is defined as:

$$\alpha = (1+10^{-3}\,\delta^{18}O_A)/(1+10^{-3}\,\delta^{18}O_B)$$

Equation 2.8

Above 0^oC , in most mineral – water systems, the natural logarithm of the isotopic fractionation between phases A and B ($\ln\alpha_{A\text{-}B}$) varies as an approximately linear function of $1/T^2$, where T is in Kelvin. Where A and B are constant the following equation is true;

$$10^3\ln\alpha = A.10^6/T^2+B$$

Equation 2.9

Many studies have approached the magnitude and temperature dependence of the ^{18}O fractionation through experimental calibration (Clayton et al., 1972; Matsuhisa et al., 1979; Matthews and Beckinsale, 1979; Zhang et al., 1989; Hu and Clayton, 2003). However, significant discrepancies exist amongst fractionation calibrations for individual quartz-water systems. Furthermore, because quartz precipitation rates are extremely slow at the relatively low temperatures relevant to diagenetic conditions, few calibrations exist below 200^{o}C. Table 2.5 summarises a number of fractionation equations that have been experimentally derived for the quartz-water system. Figure 2.6 shows a comparison of all the analyses made in the experiments highlighted in Table 2.5.

In this investigation all geothermometric interpretations were made using Clayton *et al.*'s (1972) fractionation equation (Equation 2.10). Clayton *et al.*'s (1972) quartz-water experiments yielded data from 100% exchange as well as partial exchange across a temperature range of 195 to 750^{o}C. The lower temperature experiments that resulted in partial exchange allowed Clayton *et al.*'s (1972) to derive a fractionation equation for systems between 200-500^{o}C. The inset in Figure 2.6 shows the fit of Clayton et al.'s (1972) fractionation equation with the raw data taken from fractionation experiments in the past 40 years. Clayton *et al.*'s (1972) equation fits all the data well and was derived from experimental conditions closer to that observed within the basins examined in this study. Kelly et al. (2007) has also shown that extrapolation of Clayton *et al.*'s (1972) equation to 10°C yields good agreement with Labeyrie (1974) empirical estimates of oxygen fractionation based on diatoms.

$$1000 \ln\alpha_{q\text{-}w} = 3.38 (10^{6} T^{-2}) - 3.40$$

Equation 2.10

Author	Experiment temperature range (^{o}C)	Lowest temperature exchange (^{o}C)	Experimental reactants	Fractionation Equations
Clayton *et al.* (1972)	200-500	195*	Natural quartz and silica gel	$1000\ \ln\alpha_{q\text{-}w} = 3.38\ (10^{6}\ T^{-2}) - 3.40$
Matthews and Beckinsale (1979)	200-500	265	Silicic acid	$1000\ \ln\alpha_{q\text{-}w} = 3.05\ (10^{6}\ T^{-2}) - 2.90$
Matsuhisa *et al.* (1979)	200-500	250	Natural and synthesised quartz	$1000\ \ln\alpha_{q\text{-}w} = 3.40\ (10^{6}\ T^{-2}) - 3.31$
Zhang *et al.* (1989)	200-500	180	Silica gel	$1000\ \ln\alpha_{q\text{-}w} = 3.306\ (10^{6}\ T^{-2}) - 2.71$
Hu and Clayton (2003)	400-750	400	Natural quartz	$1000\ \ln\alpha_{q\text{-}w} = 2.35\ (10^{6}\ T^{-2}) - 1.16$

Table 2.5 Summary of the experimental conditions used to determine of quartz – water fractionation equations. The data from each investigation is shown in Figure 2.6. *partial exchange.

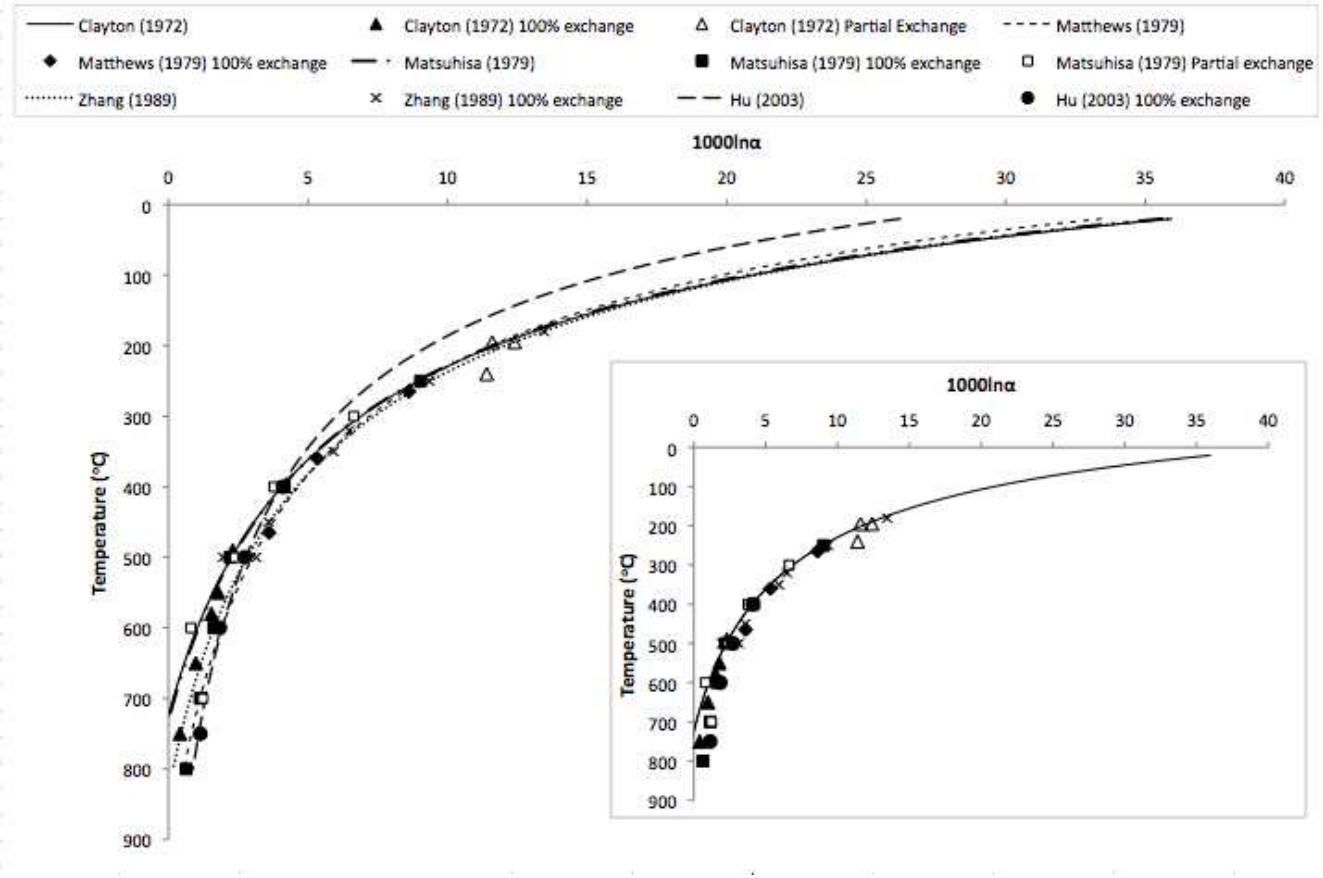

Figure 2.6 Quartz-water isotopic fractionations as a function of temperature. The inset graph illustrates the fit Clayton et al.'s (1972) fractionation equation to all the experiments summarized in Table 2.5.

2.6.Mineralogical Examination by X-Ray Diffraction

During diagenesis mineralogical reactions such as the dissolution and albitisation of feldspar as well as the transformation of illite to smectite and chlorite to smectite may produce silica. Many of these reactions occur within sandstone reservoirs as well as in interlayered silt and shale units. Using X-Ray diffraction techniques mineralogical examination was undertaken to study the overall diagenesis across both the Ness and Wilcox Formations. This mineralogical study is composed of two parts:

1. Quantitative X-Ray Diffraction (QXRD) of the bulk samples
2. XRD of the <2 µm clay fraction

The overall aim of this investigation is to quantify what potential there is for any diagenetic reactions to produce silica and to investigate any potential silica movement between adjacent sands and silts.

In the North Sea project, QXRD was used to quantify and explore mineralogical changes occurring in the clay rich shale and siltstone units across a range of burial temperatures. Whereas in the Wilcox study, in which abundant sandstone material was available, QXRD was performed in both the sandstone and shale units.

Furthermore, in both studies fine fraction XRD analyses were performed on shale material to investigate any changes in the clay mineral type and abundances as well as examining the maturity of mixed layered clays. Specifically, fine fraction analysis was concerned with quantifying the potential for the illite-smectite reaction to act as a silica source.

2.6.1. Preparation of Bulk Quantitative X-Ray Diffraction Samples

A full account of the preparation of randomly orientated X-Ray Diffraction (XRD) material is given by Hillier (2003). For quantitative analysis all XRD samples were prepared with an internal standard. To reduce mineral alignment samples were spray dried. After XRD all diffractograms were then analysed using Fullpat, a full pattern mineral quantification package developed by Bish and Chipera (2002).

2.6.2. QXRD Running Conditions

All X-ray Diffraction was carried out at Newcastle University using a PANalytical X'Pert Pro MPD, fitted with an X'Celerator and a secondary monochromator. A Cu anode was supplied with 40 kV and a current of 40 mA to generate Cu-Kα radiation (λ = 1.54180 Å). All analyses were run over a range of 2-70^{o}2θ with a nominal step size of 0.0167^{o}2θ and time per step of 100 seconds. Anti-scatter and divergence slits were both set to 1/4^{o} and a beam mask of 10mm was used. All scans were carried out in 'continuous' mode using the X'Celerator RTMS detector.

2.6.3. Fullpat

Quantitative X-ray diffraction (QXRD) using Fullpat is based on the fact that the intensities of each diffraction peak of a given mineral relates to its abundance. However absorption effects prevent us from directly comparing peaks to determine relative abundance. The use of internal standards, first recognised by Clark and Reynolds (1936), can correct for absorption matrix effects. Fullpat (Chipera and Bish, 2002) is a quantitative X-ray diffraction methodology that uses an internal standard (corundum) as well as matching to the entire diffraction pattern including the background.

2.6.3.1. Mineral Standards

At Newcastle University a library of 38 minerals has been established. Each library standard has a sample to standard weight ratio of 80:20. Each of these standards has also been spray dried. 20% corundum allows for a strong recognisable intensity without diluting which could lead to inaccuracies. All the library standards were then run at Newcastle University, using the identical operation conditions given above. Library standards are then normalised to equal corundum intensities.

2.6.3.2. Mineral Standard Uncertainties

Mixed layer clay minerals represent a transition stage between two clay mineral types for example smectite and illite (I/S). The proportion of each clay mineral in the mixed layer is temperature dependant (Hower et al., 1976; Boles and Franks, 1979; Ahn and Peacor, 1986; Velde and Vasseur, 1992; Berger et al., 1997; van de Kamp, 2008). In this investigation samples were selected from a range of different temperatures, therefore it is likely mixed layers are present in a variety of maturity states. This makes it difficult to match mixed layer standards to mixed layer samples in Fullpat. In an ideal world to overcome this issue multiple standards of each mixed layer clay would be available. In this study 5 mixed layer standards were available in the mineral library. Of these the I/S transition is most associated with silica production. However, only three I/S types were available for matching.

Quartz rich samples also proved problematic to match. Three quartz standards were available in the library. However, the crystallography of the quartz standards varies little compared to the variation observed in the samples; as a result in sand-rich samples quartz is often over estimated.

2.6.4. Application of Fullpat

Once XRD diffraction patterns were acquired the identity of each peak was identified manually using d-spacings listed in Brindley and Brown (1980, Table 5.18).

The most abundant phase in the sample was then used to scale the corundum intensities of the library in Fullpat, removing instrumental and sample related effects. Fullpat then varies the portion of individual pure components using the least squares minimisation to produce the best fit between the observed patterns and the simulated patterns produced by summing together patterns of individual components. The amount of each phase in the unknown mixture is equal to the amount by which the library standard must be scaled to match that phase portion in the unknown pattern:

$$I_{phase} = I_{std} \,.\, X\%$$

Equation 2.11

Where I is the intensity of the mineral phase (phase) or standard (std).

2.6.5. <2 µm Fine Fraction Clay Preparation

Clay mineral analysis required orientated clay mineral aggregates. Once the <2µm fraction was separated all samples were prepared following the 'evaporation' method outlined in Moore and Reynolds (1997).

Using the freeze-thaw technique described by Yang and Aplin (1997), each sample underwent a series of disaggregation cycles. From the resulting material the <64µm was sieved out and the remaining material suspended in water in preparation for sedimentation using the gravity settling method (Tanner and Jackson, 1947). Carrying out gravity sedimentation prior to centrifugation improves the accuracy of the particle

size separation as it encourages layer dispersion. Gravity sedimentation utilises Stokes Law to separate different sized particles. This sedimentation process was carried out using 150ml De-Ionised Water (DIW) in 200 ml beakers at 20^{o}C over a 5 cm distance. A series of cycles were run, at each stage larger material was removed out of solution. The following settling times were calculated using Tanner and Jackson (1947), Table 2.6.

Stage	Particle size (µm)	Sedimentation time
1	10	10m 30s
2	5	42m 00s
3	2	4h 20m

Table 2.6 Settling times used during gravity sedimentation over 5cm

For the analysis of clay minerals, specifically mixed layer illite-smectite, it is important to have a common inter-layer cation. Each sample was treated with 1M NaCl to saturate with the Na^{+} ion. A small amount of the clay sample was dropped on to a 2 cm round glass slide; the solution was then allowed to evaporate forming an orientated clay mount.

2.6.5.1. < 2 µm X-Ray Diffraction Running Conditions

Each slide was analysed air dried, after ethylene glycol saturation (60^{o}C for 24hours) and after two heat treatments, one to 375^{o}C (1-2 hours) the second to 550^{o}C (1-2 hours). All X-Ray Diffraction was performed at Newcastle University using the PANalytical X'Pert Pro MPD described above. Samples were run under identical conditions to that of the bulk fraction, except that each mount was not rotated and each run was only measured from 2 to 40^{o} 2θ.

2.6.6. Quantifying the Percentage Illite in Illite/Smectite

The percentage of illite within the illite/smectite mixed layers (I/S) was determined using the methodology of Moore and Reynolds (1997):

1. I/S is identified using air dried, glycolated and 375^{o}C treatments
2. The Reichweite or ordering type is determined by the position of reflections between 5 and 8.5^{o} 2θ for ethylene glycol saturated samples.
3. The percent of illite can be determined using the values of $^{o}\Delta 2\theta$ which are given in Table 8.3 of Moore and Reynolds (1997), which varies between 9.01 and 10.31 $^{o}\Delta 2\theta$ for 001/002 reflections and 15.80 and 17.39 $^{o}\Delta 2\theta$ for 002/003 reflections.

2.6.6.1. Decomposition of Diffractograms : Grams AI

Grams AI is a software package developed by ThermoScientific for the decomposition of diffractograms. In many of the <2 µm XRD analyses the I/S signal was not strong and was mixed with other reflections. To overcome this Grams AI was used to resolve the I/S 001/002 and 002/003 reflections in the glycolated <2 µm fine fraction diffractogram. Once resolved quantification of illite in the I/S mixed layers is possible. The process involves two stages:

1. Determination of the baseline and background correction (Figure 2.7 and Figure 2.9)
2. Decomposition of peaks(Figure 2.8 and Figure 2.10)

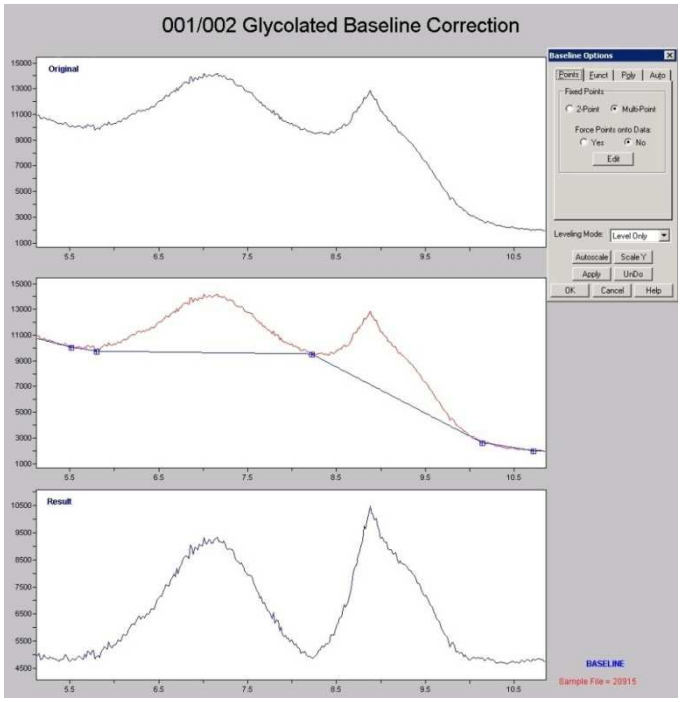

Figure 2.7 Grams AI001/002 baseline correction (Stage 1a)

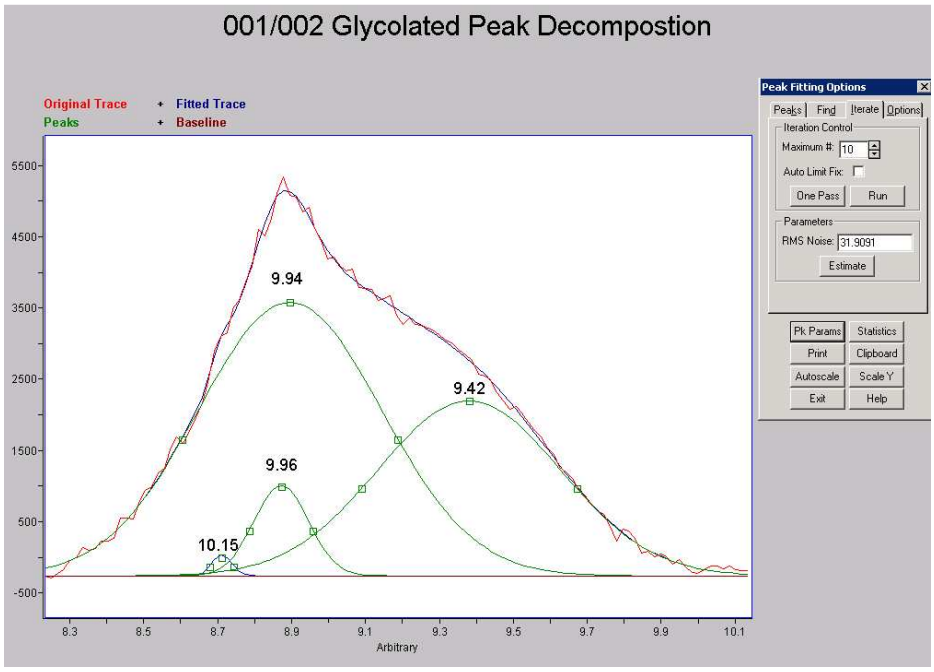

Figure 2.8 Decomposition of the 001/002 I/S reflection using Grams AI. Bold numbers indicate the d-spacing of each peak (Stage 2a)

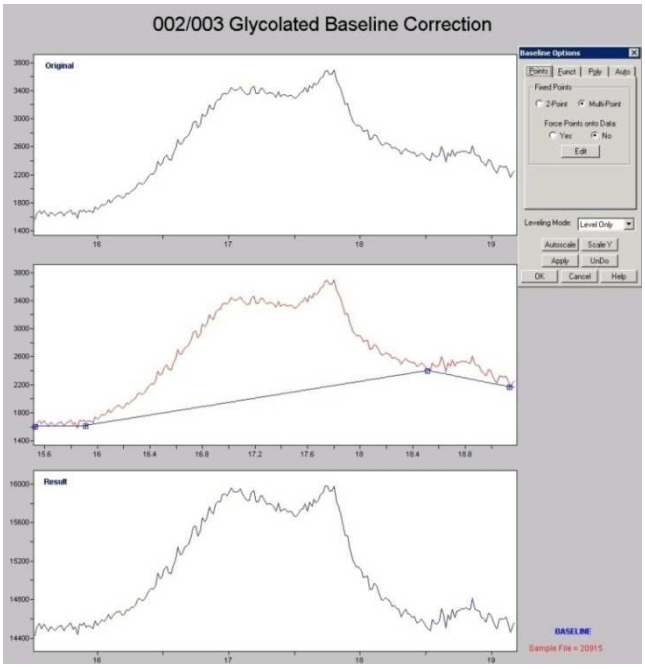

Figure 2.9 Grams AI 002/003 baseline correction (Stage 1b)

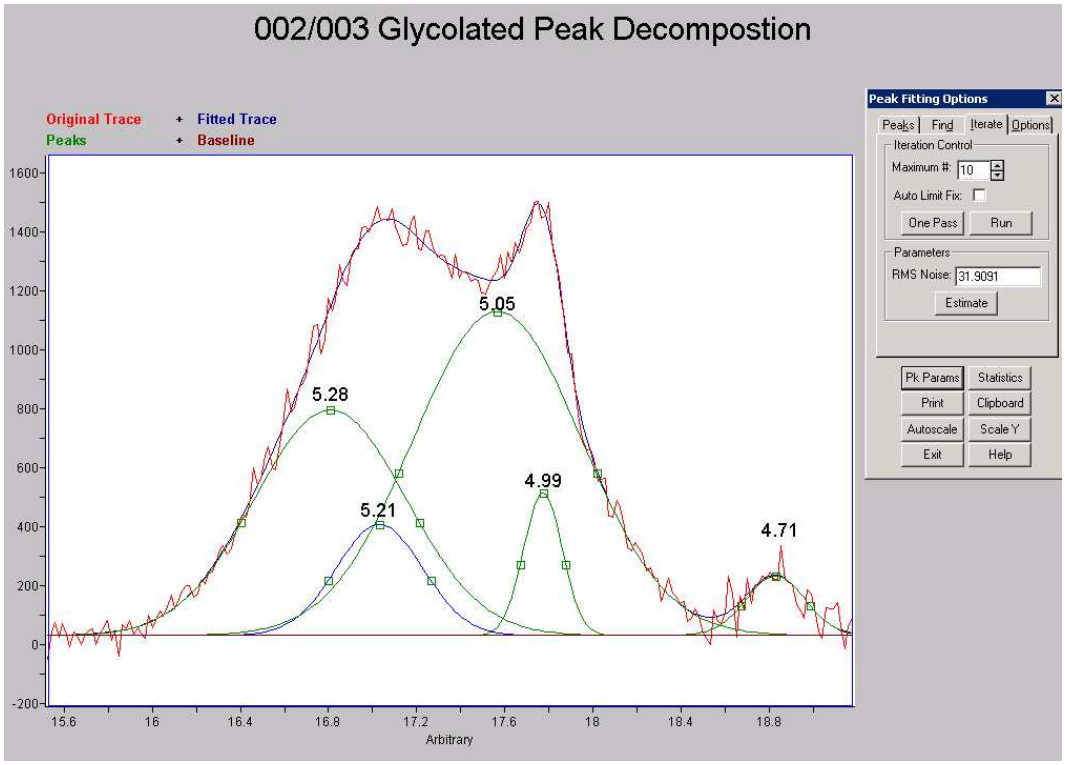

Figure 2.10 Decomposition of the 002/003 I/S reflection using Grams AI. Bold numbers indicate the d-spacing of each decomposed peak (Stage 2b)

3. Quartz Cementation and Diagenesis in the North Sea Ness Formation

The following chapter describes the diagenesis of the Jurassic Ness Formation in the northern North Sea. The aim of this study is to constrain the timing of quartz cementation in the Ness Formation. Furthermore, this multi-analytical investigation aimed to examine potential silica sources internally within the Ness sandstones as well as externally within neighbouring silt and shale units.

3.1. Introduction to the Ness Formation

Deposited on supra- or intertidal flats the deltaic Ness Formation comprises silty channelled sands with silts, muds and occasional thin coals (Blackbourn, 1984; NPD, 2011). Its mixed grain size, wide abundance, sand/shale inter-layering, and position at various temperatures in the North Sea basin provide an excellent material for this diagenetic study.

Many studies have recorded the diagenetic history of the Brent group (Scotchman et al., 1989; Glasmann et al., 1989a; Glasmann et al., 1989b; Bjørlykke et al., 1992; Giles, 1992; Harris, 1992; Haszeldine et al., 1992; Hogg et al., 1995; Wilkinson et al., 1998; Girard et al., 2001; Brosse et al., 2002; Girard et al., 2002). Results show that early carbonate cementation preceded a phase of quartz overgrowth, which continued during burial (Blackbourn, 1984). Alongside this occurred the continued dissolution of feldspars (Glasmann, 1992; Ehrenberg and Jakobsen, 2001) and the formation of illite and kaolinite (Harris, 1992; Hassouta et al., 1999).

Understanding the mechanisms by which quartz cementation is occurring in the Brent is vital for accurate prediction of reservoir quality. Many studies have attempted to evaluate the temperature and timing of the quartz 'cementation window', typically through the combined use of fluid inclusion (Haszeldine et al., 1984; Walderhaug, 1994b; Wilkinson et al., 1998), petrographic (Blanche and Whitaker, 1978; Hogg et al., 1992; Oelkers et al., 1996) and isotopic investigations (Brint et al., 1991; Aplin and Warren, 1994; Williams et al., 1997; Girard et al., 2001; Marchand et al., 2002). These largely macroscopic analyses indicate that quartz cementation has a threshold temperature around 80^{o}C (Walderhaug, 1994a; Walderhaug, 1994b; Primmer et al., 1997; Giles et al., 2000). However, although current predictive quartz cementation models initiate quartz precipitation from this 80^{o}C approximation (Ajdukiewicz and Lander, 2010), it has never been tested at the microscopic level at which quartz cement forms.

Furthermore it is unclear from where the necessary silica is sourced. Internally within the Ness sandstone there is evidence of feldspar dissolution (Bjørlykke et al., 1992; Morton et al., 1992) and stylolitisation (Bjørkum, 1996; Walderhaug, 1996). Whilst externally, in the expansive shale deposits of the Ness Formation and Brent Group, further silica producing reactions have also been documented including the transition of illite to smectite, the dissolution of feldspars and the albitisation of feldspars (Bjørlykke, 1998; Wilkinson et al., 2006).

3.2. The Ness Formation Study: Aims and Objectives

The specific aims of the Ness study were three fold:

1. To constrain the onset of quartz cementation and resolve quartz cementation histories in the Ness sandstone
2. To identify and constrain the onset of quartz cementation in the finer grained silts and shale units of the Ness Formation
3. To quantitatively evaluate potential silica sources internally within reservoir sands as well as externally in adjoining shale units.

The full objectives of this study were to:

- Quantify quartz cement in sand and shale samples from a wide range of temperatures from the North Sea Ness Formation.
- Constrain the quartz cementation histories through
    - Isotopic analysis of quartz cements
    - Petrographic quantification of quartz cement
    - Time-temperature modelling
- Constrain potential silica sources through
    - Quantitative petrographic examination to identify internal sources
    - Quantification of mineralogical changes in adjoining shales
- Validate current quartz cementation modelling theory

3.3. Sample Selection

Samples were selected from the Ness Formation of 7 wells across the North Sea (Figure 3.1). A brief description of each sample is given in Table 3.1. Observation made from hand specimens show Ness sandstones appearing dirty orange in colour and being fine to medium grained. Sand samples often contain various degrees of silt /clay grade matrix material. Some samples react with hydrochloric acid, indicating the possible presence of carbonate material. Dark grey to black siltstones occur as beds of varying thickness throughout the Ness. Occasional sand pockets are found in both the silt and the finer mudstone units. These mudstone/shale layers appear at various stages of lithification in hand specimen, from brittle, light brown claystones through to darker, rigid shales. Occasional silty laminations can be observed running through such units. Some pyritic veins were also noted.

Using well composite logs acquired from BP and the Norwegian Petroleum Directorate (NPD) an estimate of the shale to sand ratio was made across the Ness in the sampled wells. Assuming that a high gamma response represents a clay rich region (i.e. silts and shales), it is estimated that the sand to shale ratio is around 50:48 (the remaining material being made up of coal seams). However, previous studies have highlighted the Ness Formation can contain highly micaceous sandstones. The gamma signal of these units may be more akin to a shale material. This would result in an underestimation of the sand quantity.

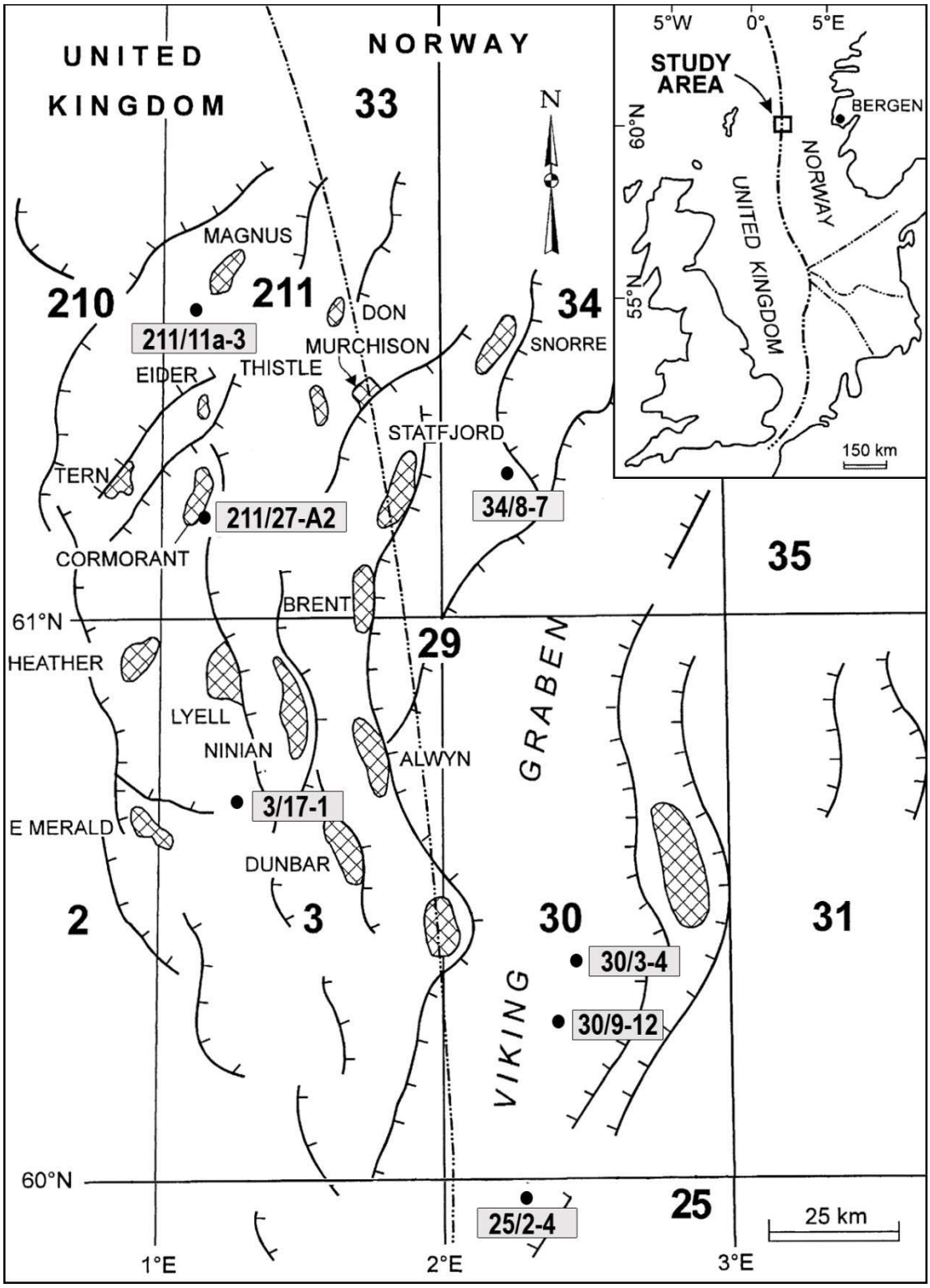

Figure 3.1 Map of North Sea study area, 7 wells were sampled.

Sample Overview						Analytical				
Sample reference	**Well**	**Depth (m)**	**Temperature (°C)**	**Description**	**Genesis 4.92**	**Point Count**	**Image Analysis**	**QXRD**	**< 2µm XRD**	**Ion Microprobe**
	30/9-12	2638.4	109	Sh Lam	•				•	
	30/9-12	2673.3	109	Sl	•			•		
NS 6	30/9-12	2673.7	109	Sl	•			•	•	12 µm
	30/9-12	2678.1	109	SlSa	•			•		
NS 4	30/9-12	2678.8	109	Sa	•	•				
	30/3-4	2831.8	118	Sh	•			•	•	
NS 11	30/3-4	2845.8	118	SlSa	•	•	•	•	•	12 µm
NS 10	30/3-4	2846.0	118	Sa	•	•	•			
	30/3-4	2846.1	118	Sh	•			•	•	
	3/17-1	3322.9	120	Sh					•	
	211/11a-3	3419.9	122	SlSh	•			•	•	
NS 23	211/11a-3	3420.8	122	Sa	•	•	•			

Sample Overview						Analytical					
Sample reference	**Well**	**Depth (m)**	**Temperature (^{o}C)**	**Description**	**Genesis 4.8**	**Point Count**	**Image Analysis**	**QXRD**	**<2 µm XRD**	**Ion Microprobe**
NS 1	211/11a-3	3462.2	122	Sa (Ca)	•	•				12 µm
	211/11a-3	3463.7	122	Sl	•				•	
	211/11a-3	3484.8	122	Sl	•			•		
	211/11a-3	3488.7	122	Sl	•			•	•	
	211/11a-3	3493.0	122	Sl	•			•	•	
	25/2-4	3817.7	137	Sh						
	25/2-4	3818.4	137	SlSh Lam				•	•	
NS 14	25/2-4	3831.4	137	Sa		•				
	211/27-A2	4292.2	133	Sh OM	•			•		
	211/27-A2	4311.1	133	Sh	•			•	•	
NS 25	211/27-A2	4313.5	133	Sa	•	•	•			
	211/27-A2	4319.0	133	Sh	•			•	•	

Sample Overview						Analytical				
Sample reference	**Well**	**Depth (m)**	**Temperature (^{o}C)**	**Description**	**Genesis 4.8**	**Point Count**	**Image Analysis**	**QXRD**	**<2 µm XRD**	**Ion Microprobe**
NS 17	211/27-A2	4332.7	133	Sa	•	•	•			
	211/27-A2	4337.0	133	Sh Lam	•			•	•	
	211/27-A2	4342.5	133	Sl Lam	•			•	•	
NS 20	211/27-A2	4343.4	133	Sa	•	•	•			12 µm
NS 19	211/27-A2	4344.3	133	Sa	•	•	•			12 + 2 µm
NS 26	34/8-7	4649.5	167	SlSa	•					
	34/8-7	4650.4	167	SlSa	•					
	34/8-7	4653	167	SlSa	•			•		
NS 12	34/8-7	4653.8	167	SlSa	•	•			•	12 µm
	34/8-7	4655.9	167	SlSh	•			•	•	
	34/8-7	4656.3	167	SlSh	•					

Table 3.1 Summary of the Ness Formation samples, including hand specimen descriptions and analytical techniques used to characterise each sample. Simple sample descriptions were made on each hand specimen using the following abbreviations; Sh (shale), Sa (sand), Sl (silt), ShSa (shaley sand), SlSh (silty shale), SlSa (silty sand) Lm (limestone), Ca… (carbonate rich ...), OM (organic rich, coal etc), Lam (laminations).

3.4. Time - Temperature Histories

Understanding the time temperature history of each individual well and sample is vitally important when constraining any diagenetic process including quartz cementation. In this project Genesis 4.92 was used to integrate geochemical and geophysical data to generate thermal histories for 5 of the 7 North Sea wells. Figure 3.2 to Figure 3.7 show the stratigraphic logs that were built up from composite logs and other well data. Temperature calibrations using measured temperature and vitrinite reflectance (VR) data are also shown. However, the VR data was fitted to in-house BP curves that cannot be published here. From these burial histories, a time vs. temperature history of each well was devised (Figure 3.8). Overall the temperature calibrations fit the measured data well, however again it must be emphasised that this is only one modelled output and may not be the true temperature histories.

For later cementation modelling, each time temperature history was subdivided into two or three distinct linear temperature gradients above the commonly accepted 80^{o}C cementation threshold. Details of these time-temperature segments are given in Table 3.2.

Figure 3.2 Genesis 4.92 lithological key

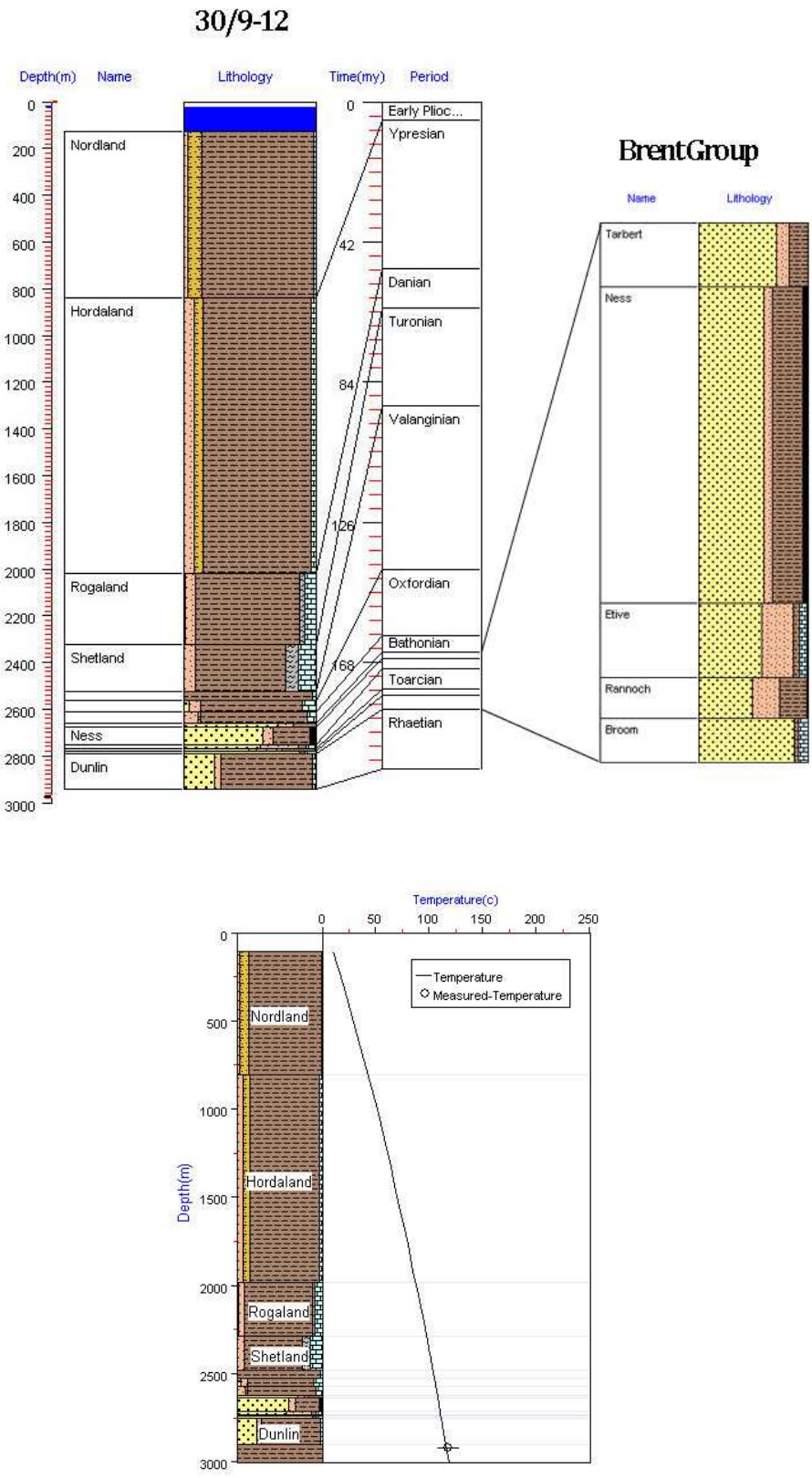

Figure 3.3 Stratigraphic log and temperature calibration of well 30/9-12

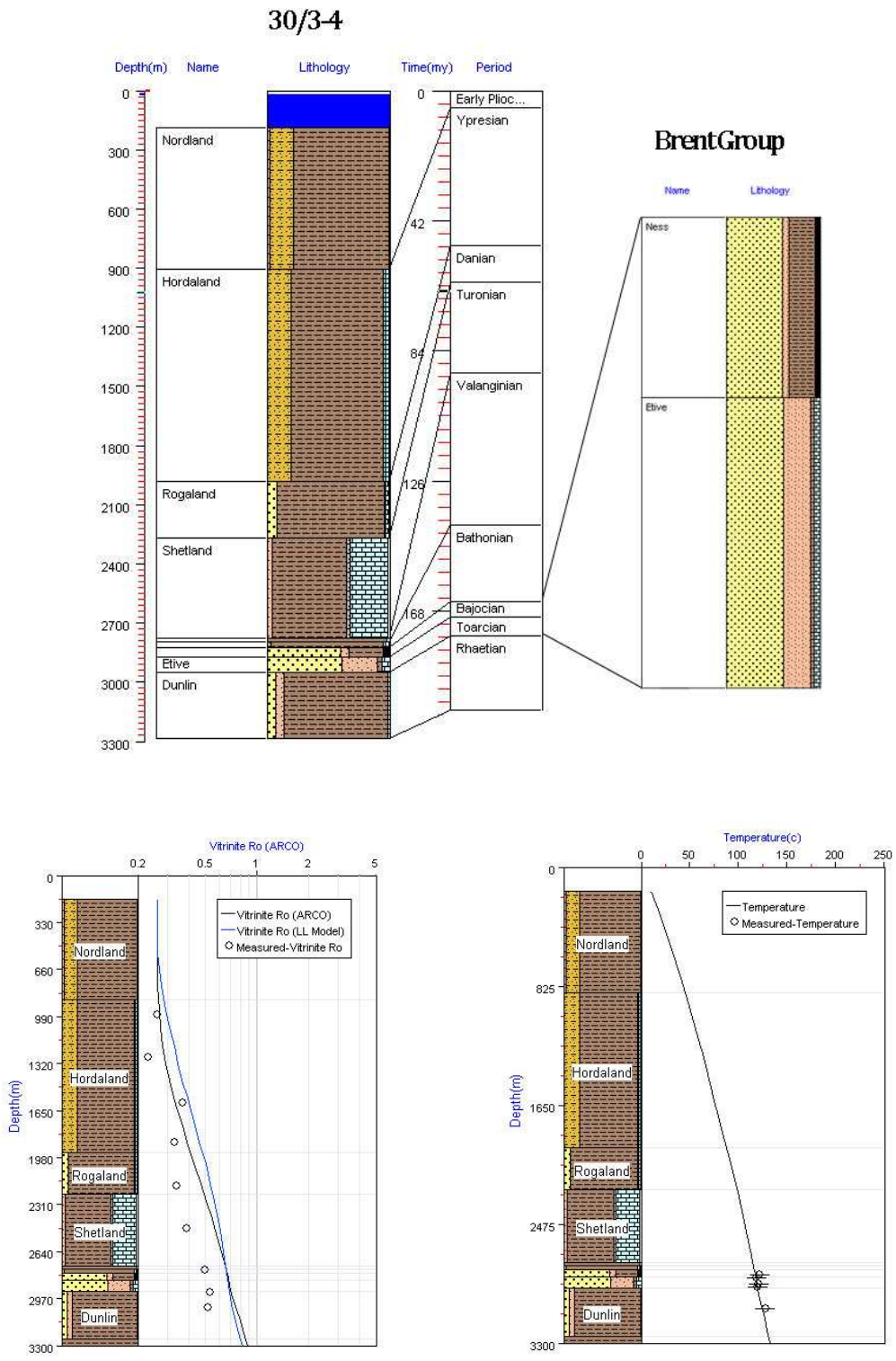

Figure 3.4 Stratigraphic log and temperature calibrations of well 30/3-4. Ro was fitted to BP curves not shown. The measured Ro data show a good fit to these curves.

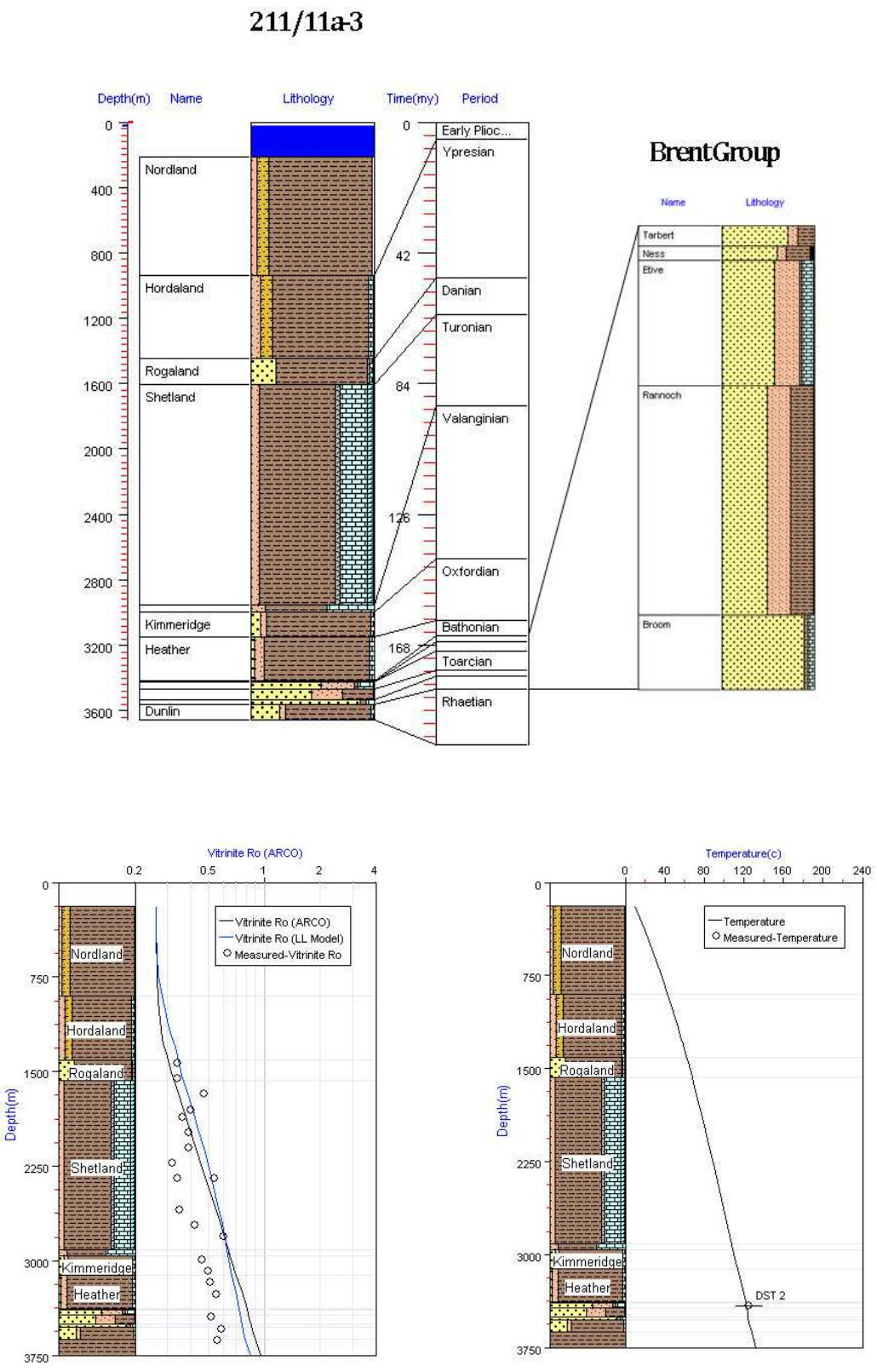

Figure 3.5 Stratigraphic log and temperature calibrations of well 211/11a-3. Ro shows a good fit to BP derived kinetics.

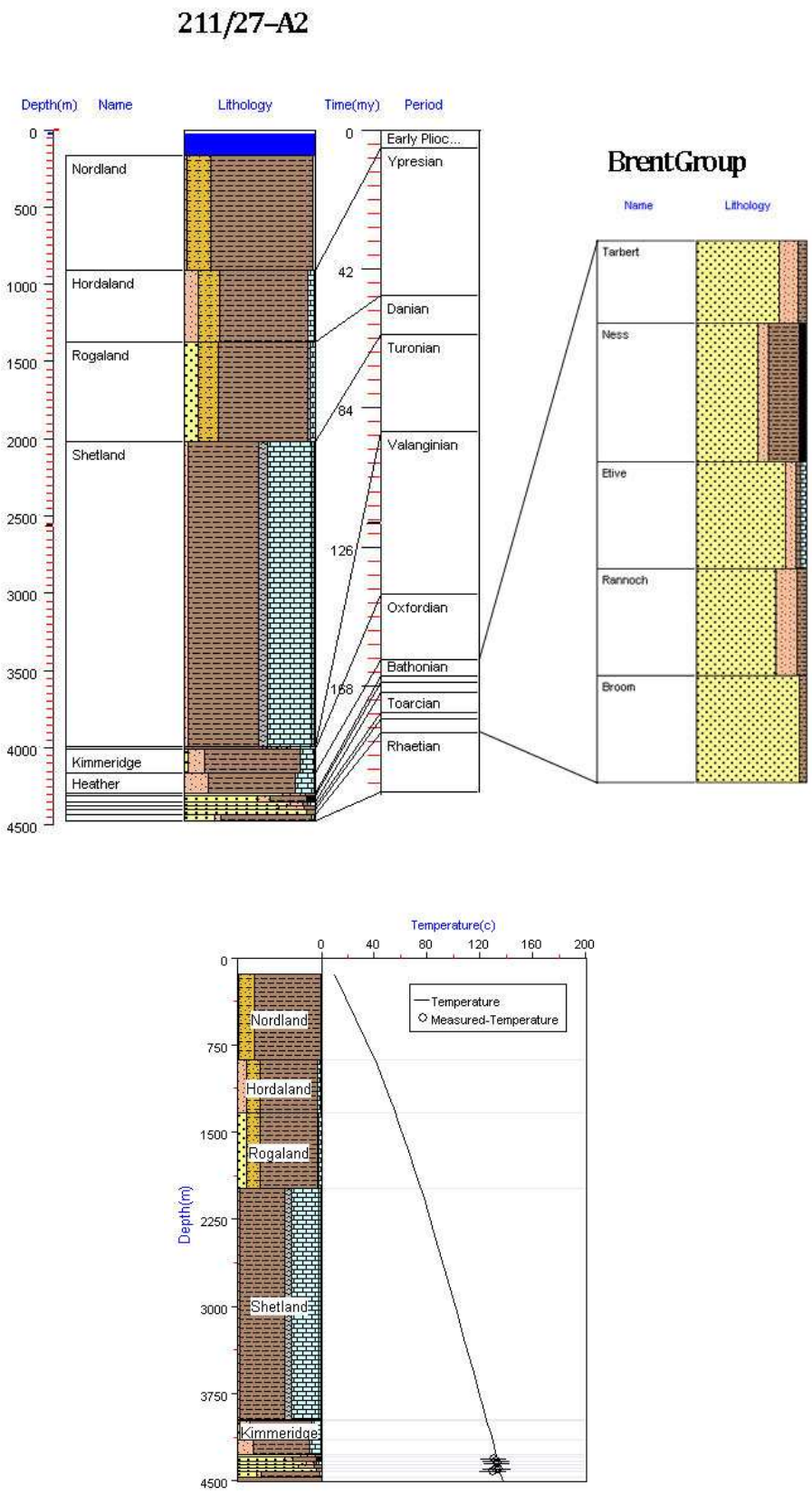

Figure 3.6 Stratigraphic log and temperature calibration of well 211/27-A2

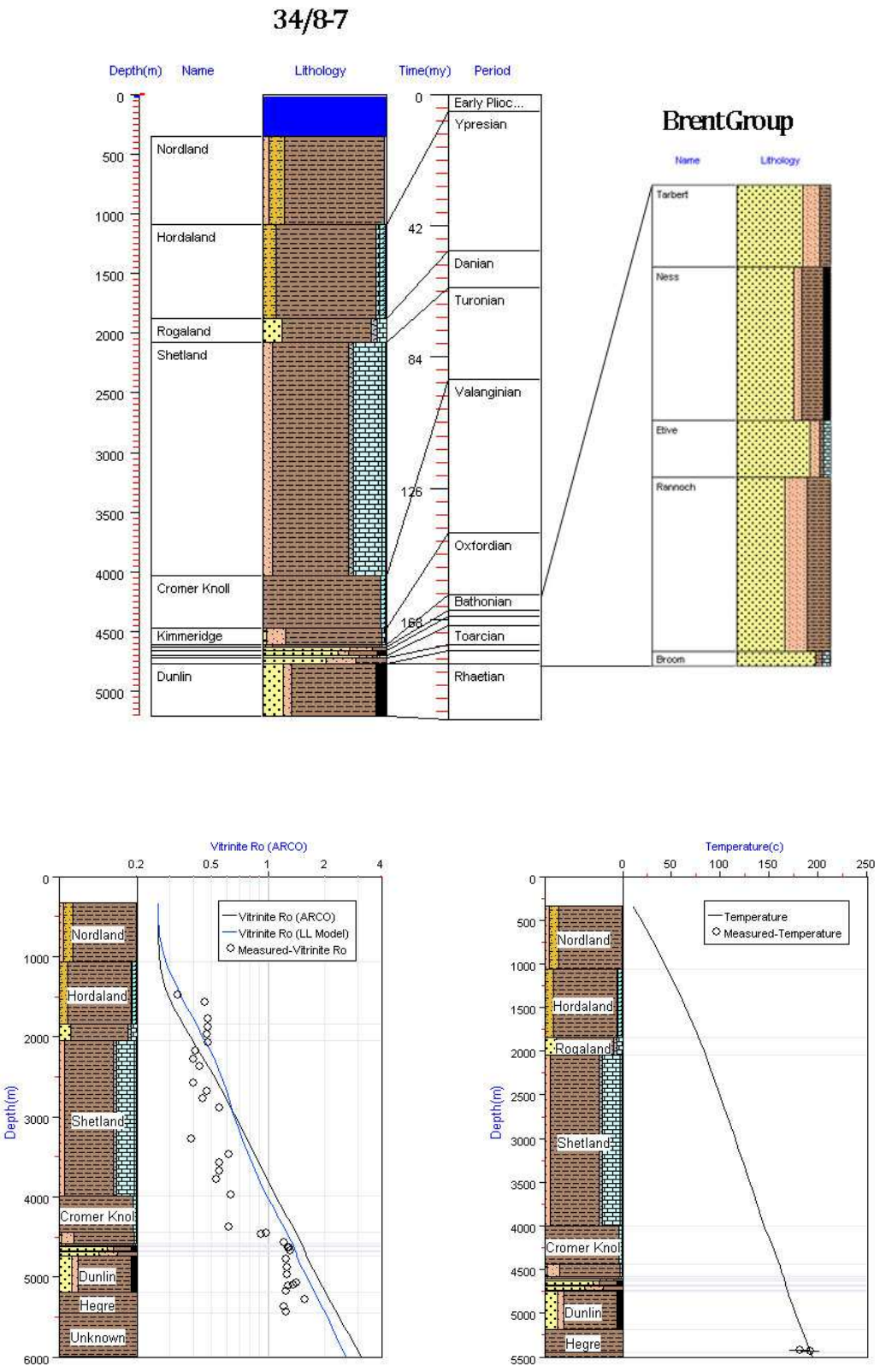

Figure 3.7 Stratigraphic log and temperature calibrations of well 34/8-7. Ro shows a good fit to BP derived kinetics.

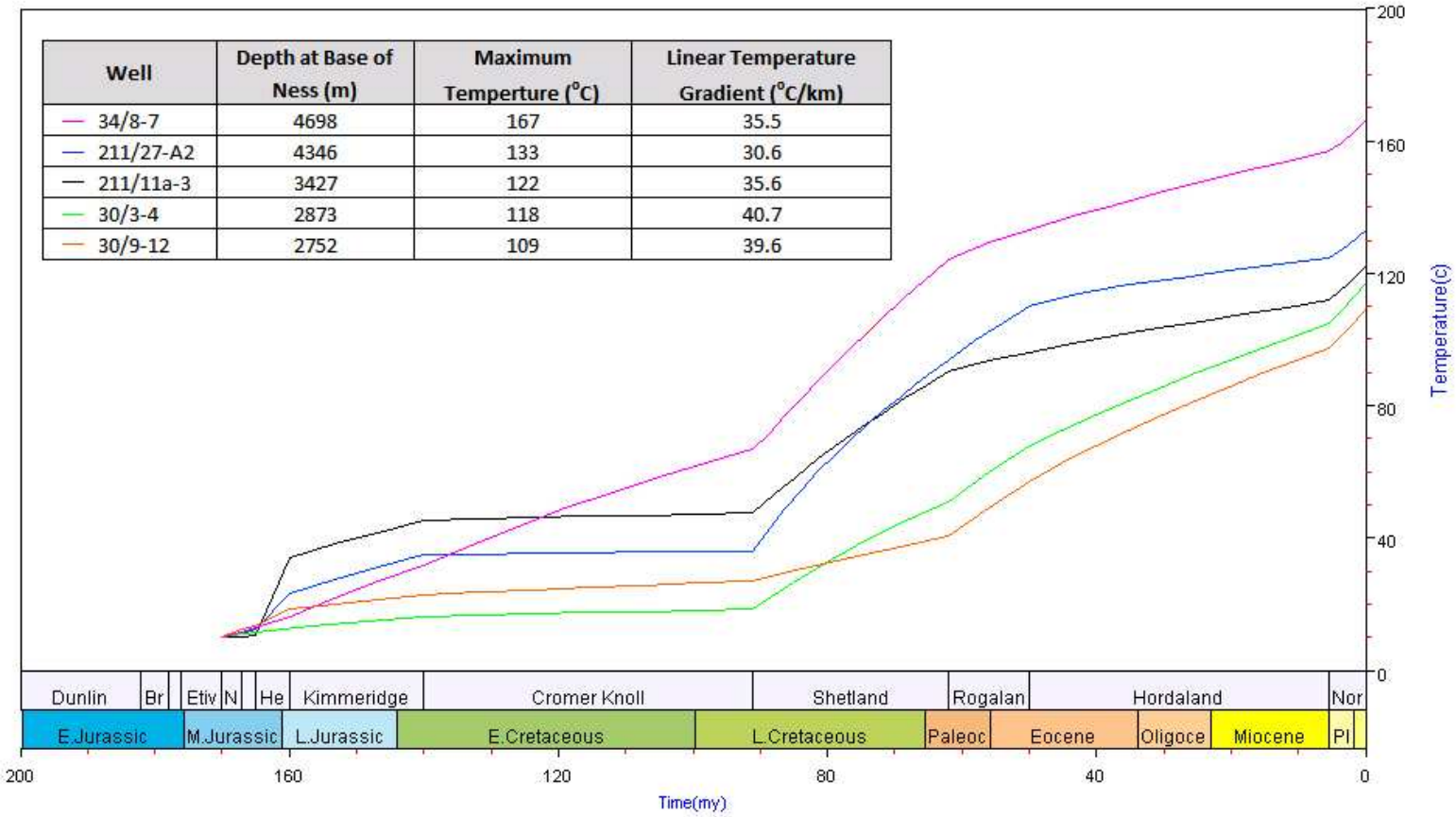

Figure 3.8 Time vs. Temperature histories generated in Genesis 4.92 of the North Sea study wells.

Well	S1		S2		S3	
	t (my)	^{o}C/my	t (my)	^{o}C/my	t (my)	^{o}C/my
30/9-12	-	-	22.9	0.76	5.2	2.20
30/3-4	-	-	31.5	0.78	5.5	2.21
211/11a-3	8.4	1.25	56.3	0.37	5.5	1.96
211/27-A2	21.3	1.46	44.2	0.32	5.5	1.52
34/8-7	24.0	1.88	55.7	0.57	5.2	1.79
25/2-4	70.0	1.21	-	-	-	-

Table 3.2 Calculated heating rates in the sampled North Sea wells (^{o}C/my). S1, S2 and S3 refer to linear time-temperature segments of each well above 80^{o}C. The low temperature wells (30/9-12 and 30/3-4) only contain 2 distinguishable linear heating segments.

3.5. Petrography of the Ness Formation

In total 11 North Sea samples were prepared for analysis under the Scanning Electron Microscope (SEM). An overview of these samples is given in Table 3.1. The samples range from clean quartz rich sandstones through to finer grained silts rich in clay minerals. The following images and data illustrate the key diagenetic processes occurring in the Ness Formations as well as quantifying the volume of quartz cement and porosity.

3.5.1. Petrographic Overview of Silica Releasing Processes

During SEM analysis a number of textures and mineral alterations were observed, these are outlined below in Figure 3.9 to Figure 3.19. These images highlight a number of key silica producing processes occurring in the Ness Formation; chemical processes such as the dissolution (Figure 3.9 to Figure 3.11) and albitisation of feldspars (Figure 3.12 Figure 3.13) and the formation of illite (Figure 3.14 and Figure 3.15) were observed; mechanical processes such as quartz grain fracturing were also recorded (Figure 3.18). The precipitation of quartz cement was recorded in the sandstones of the Ness (Figure 3.19) as well as the siltier deposits (Figure 3.20). Although the timing of quartz cementation cannot be accurately constrained from this petrographic study it appears that it does supersede the formation of kaolinite (Figure 3.17).

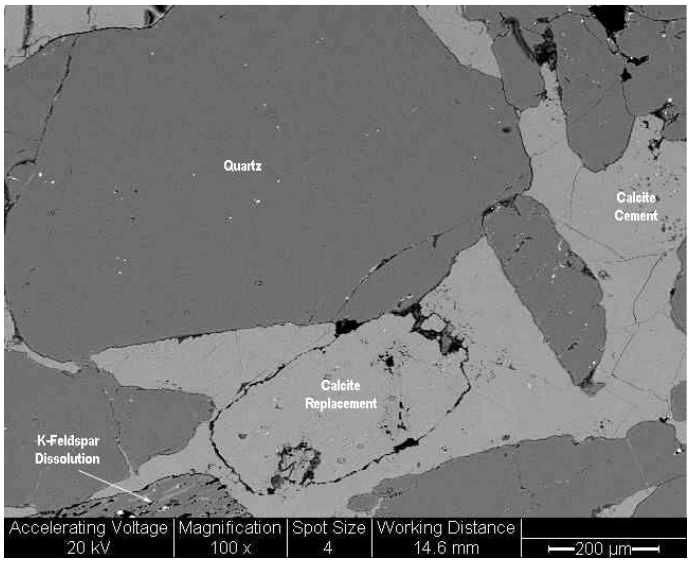

Figure 3.9 Backscattered Scanning Electron image of sample NS1 (118^{o}C), abundant calcite cement is observed filling pore space between quartz grains. K-feldspar dissolution a silica releasing process is observed as well as calcite replacement of a relic primary grain.

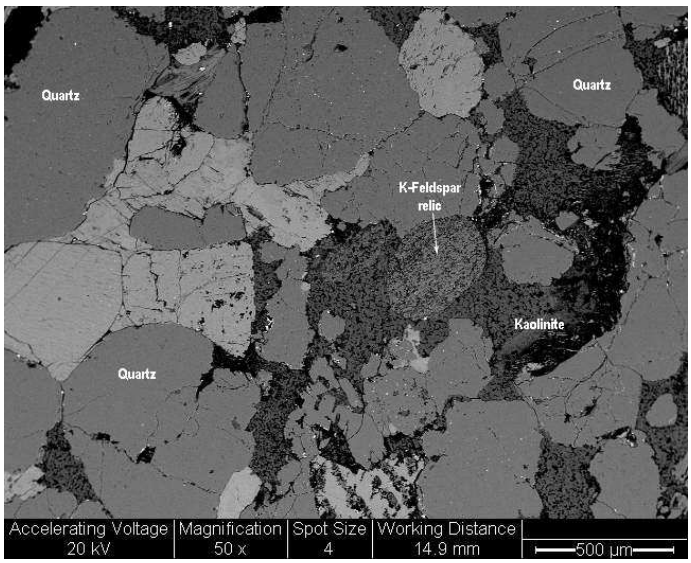

Figure 3.10 Backscattered Scanning Electron image of sample NS1 (118^{o}C). Abundant calcite cement is observed filling pore space between quartz grains. Illite is replacing K-feldspar (relic), and kaolinite is also abundant.

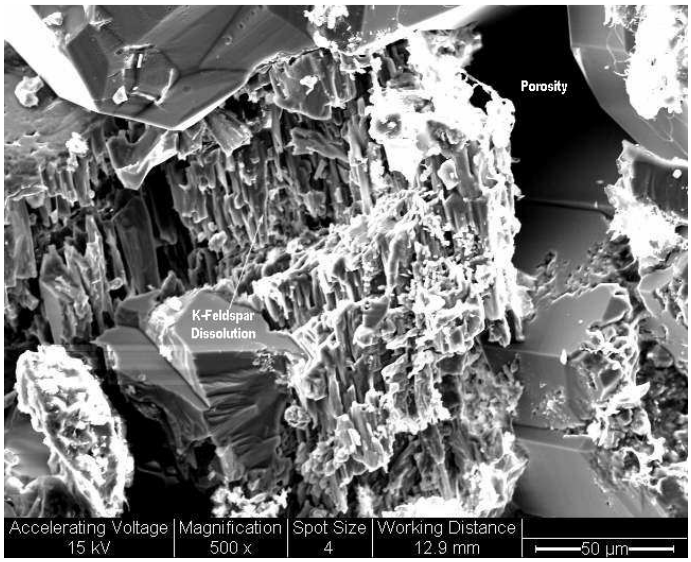

Figure 3.11 Secondary Electron image from a fresh rock stub taken from sample NS20 (133^{o}C) showing the dissolution of a K-feldspar grain.

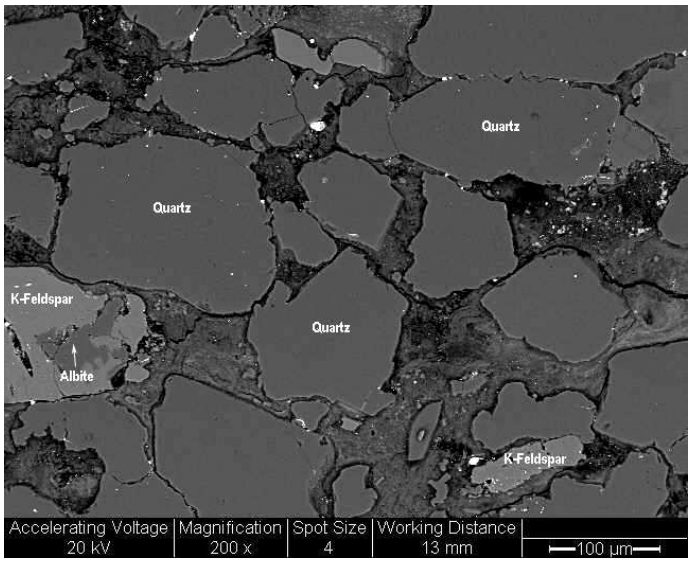

Figure 3.12 Backscattered Scanning Electron image of sample NS10 (122^{o}C), showing quartz and K-feldspar grains supported in a clay matrix. Albitisation of K-feldspar a silica producing reaction is apparent.

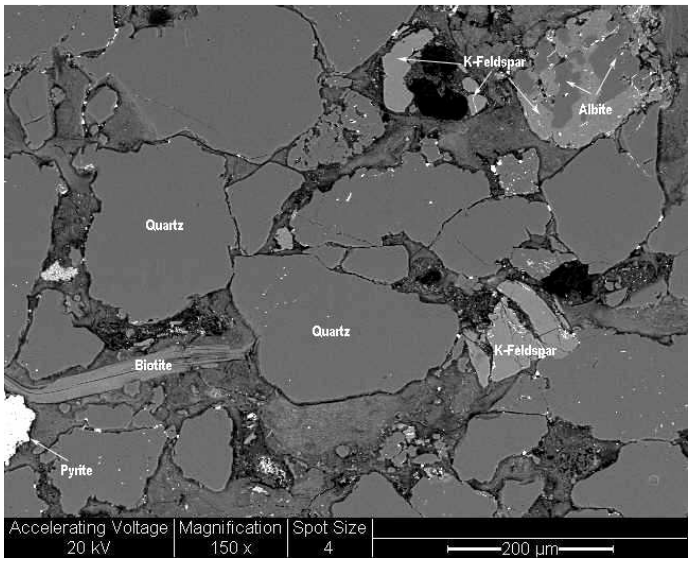

Figure 3.13 Backscattered Scanning Electron Image of sample NS11 (122^{o}C), showing quartz and K-feldspar grains supported in a clay matrix. Albitisation of K-feldspar can be seen as well as biotite and pyrite. Darker areas may be the result of grains being lifted or gouged during thin section preparation.

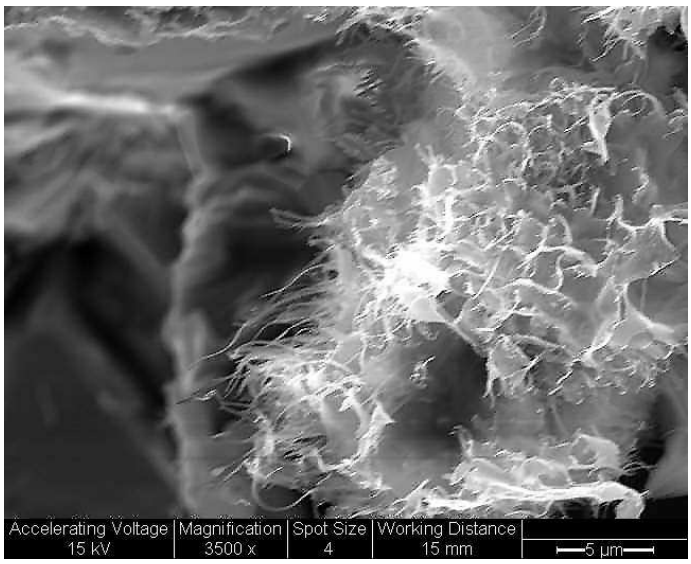

Figure 3.14 Secondary Electron image from a fresh rock stub of sample NS23 (118^{o}C) showing the growth of laths and fibrous illite.

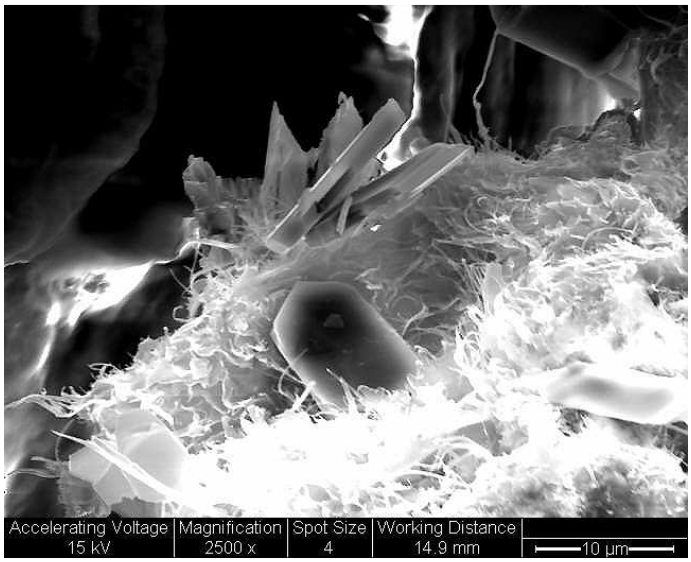

Figure 3.15 Secondary Electron image of fresh rock stub (NS19, 133^{o}C) showing the growth of fibrous illite.

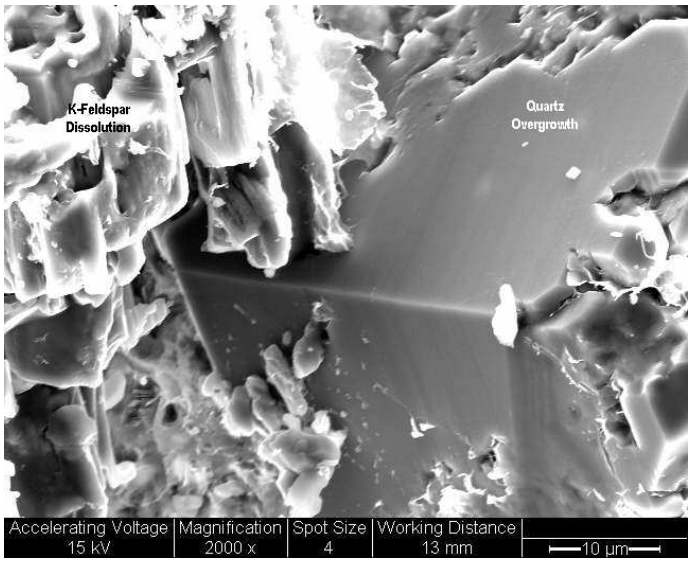

Figure 3.16 Secondary Electron image from a fresh rock stub taken from sample NS1 (118^{o}C), showing the growth of a quartz overgrowth consuming K-feldspar that is undergoing dissolution.

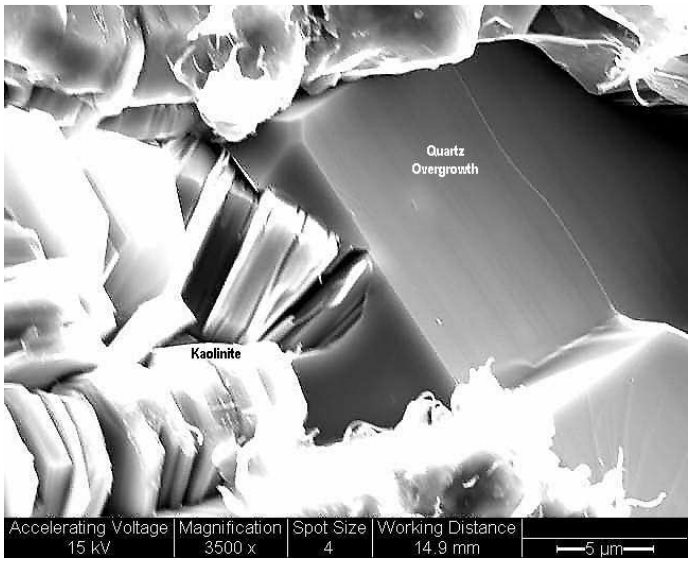

Figure 3.17 Secondary Electron image from a fresh rock stub taken from sample NS1 (118^{o}C), showing the growth of a quartz overgrowth consuming kaolinite.

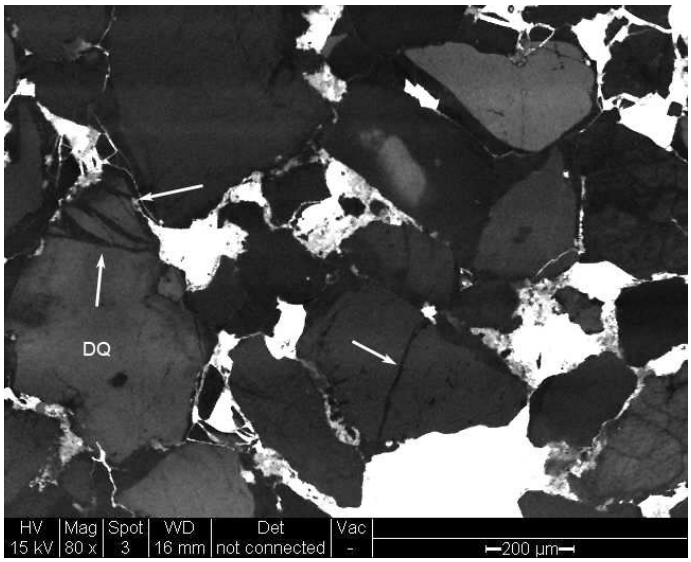

Figure 3.18 SEM-CL image of NS25 (133^{o}C) showing fracturing (white arrows) of detrital quartz grains (DQ) and subsequent quartz cementation.

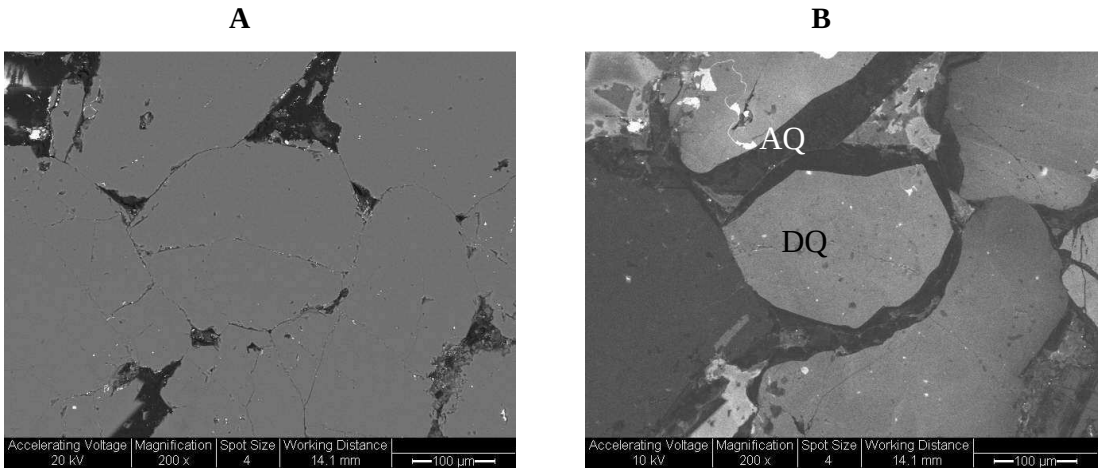

Figure 3.19 **A)** BSE image of quartz rich Ness reservoir sandstone NS19 (133^{o}C), **B)** SEM-CL image showing darker authigenic quartz (AQ) around grey detrital grains (DQ).

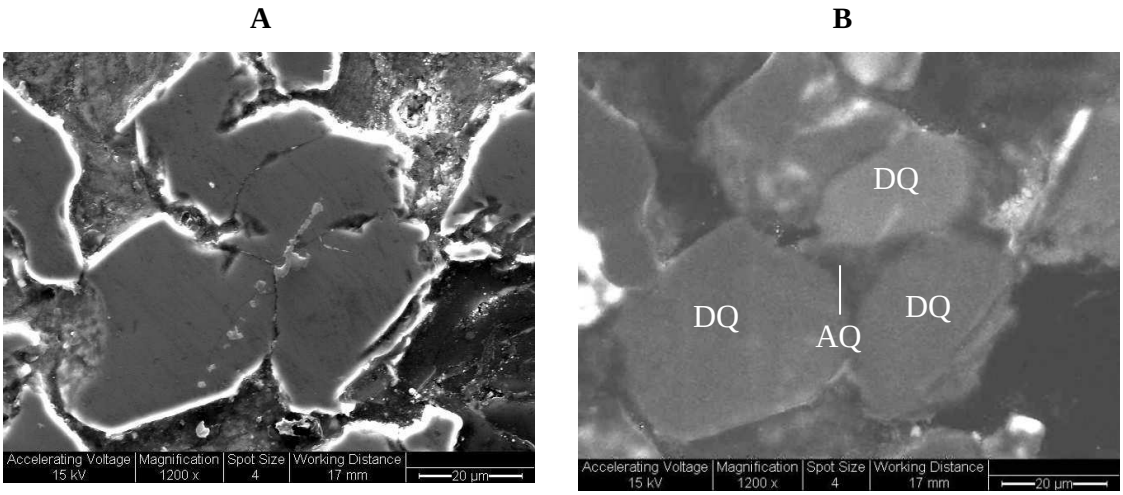

Figure 3.20 **A)** Secondary Electron image of clay rich sample NS6 (109^{o}C) showing silt sized quartz grains. **B)** SEM-CL image showing growth of authigenic quartz cement (AQ) between silt grains (DQ).

3.5.2. Quartz Cement Quantification

In this study both standard point counting and image analysis were used to quantify mineral, porosity and quartz cement volumes in the samples shown in Figure 3.21. However, samples NS1, NS4 and NS12 were only analysed using the point count method. In these three samples the acquired SEM-CL images contained glare caused by sample charging and carbonate luminescence, making computerised pixel differentiation of authigenic and detrital material impossible. The remaining eight samples were analysed using both the point count and image analysis method. Full point count and image analysis results are given in Appendix 1. In each sample a minimum of 6 image pairs were analysed. The standard deviation and 95% confidence levels between the image pairs are also reported.

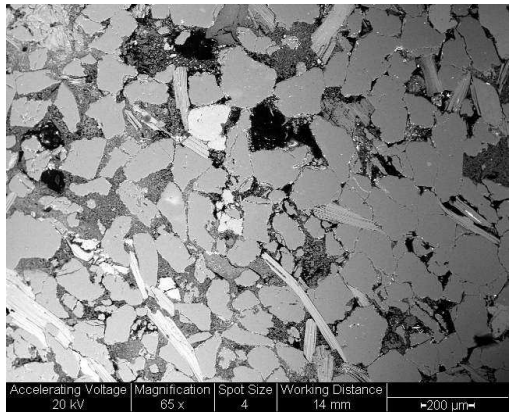

NS4 (109°C). Micaceous sandstone with minor feldspar and clay material

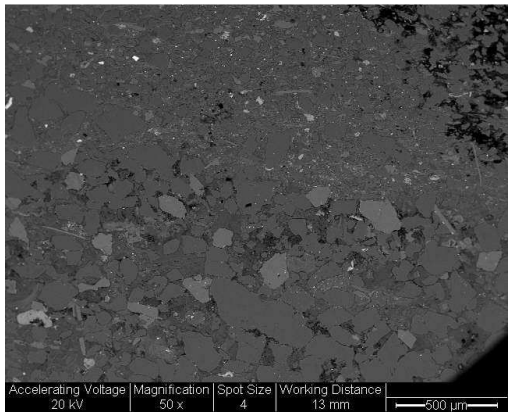

NS11 (118°C). Fine grained sandstone containing feldspar, illite and kaolinite.

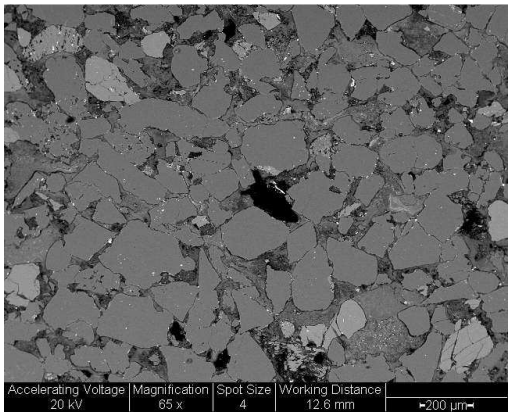

NS10 (118°C). Medium grained sandstone containing feldspars, kaolinite and illite.

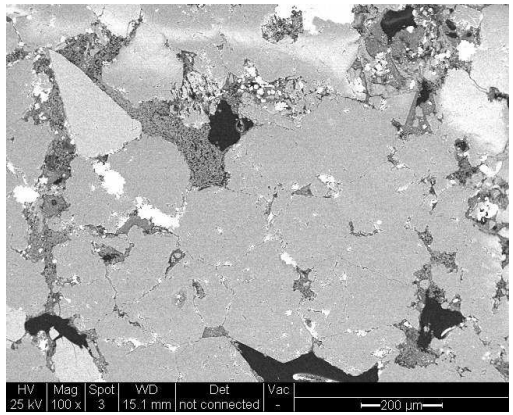

NS23 (122°C). Medium grained sandstone contain illite, kaolinite, siderite and feldspar.

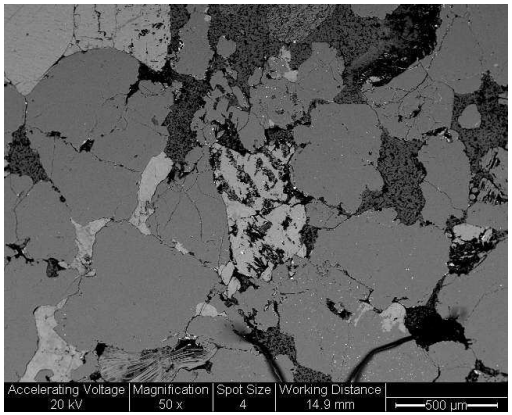

NS1 (122°C). Coarse grained sandstone. K-feldspar dissolution and calcite cement are observed.

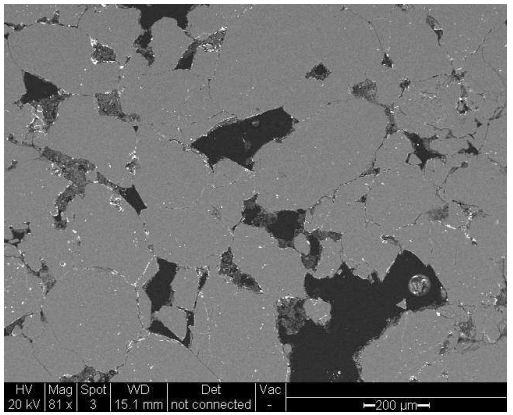

NS25 (133°C). Clean quartz rich sandstone containing trace kaolinite.

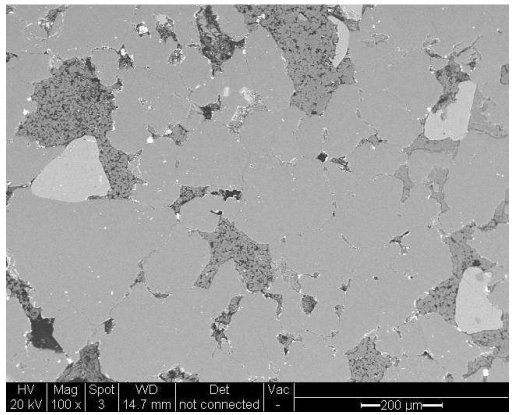

NS17 (133°C). Medium grained sandstone contain illite, kaolinite and feldspar, plus minor chlorite.

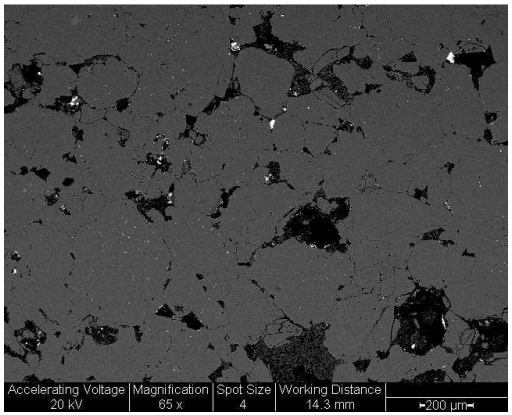

NS20 (133°C). Clean quartz rich sandstone containing trace feldspar and illite

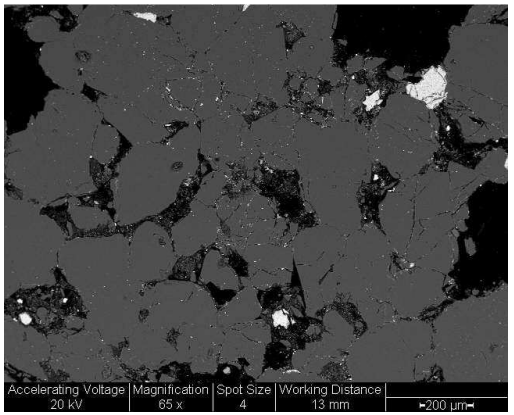

NS19 (133°C). Clean quartz rich sandstone containing trace feldspar, illite and siderite

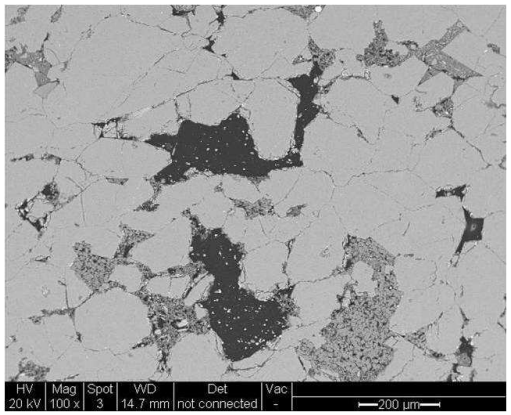

NS14 (137°C). Medium grained sandstone containing kaolinite and illite.

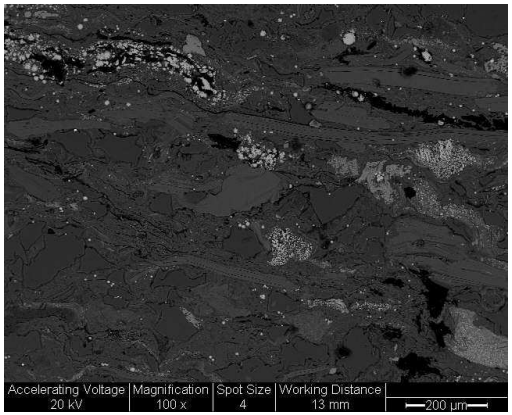

NS12 (167°C). Micaceous silt containing feldspar, illite, chlorite, and pyrite

Figure 3.21 BSE image of sandstones analysed during quantitative petrography

Quartz cement volumes are plotted against modelled maximum burial temperature in Figure 3.22. Quartz cement abundance increases with increased maximum burial temperature from 1.3 %bv at 109^{o}C to a maximum of 22.5 %bv at 133^{o}C. One exception was observed in the highest temperature silt rich sample analysed, NS12 (Figure 3.21), where cement was measured at 2.3 %bv at 167^{o}C.

Bulk porosity was determined in all samples and varies between 0.3 %bv and 18.3 %bv. However, as illustrates in Figure 3.23 there is no relationship between porosity and increasing burial temperature.

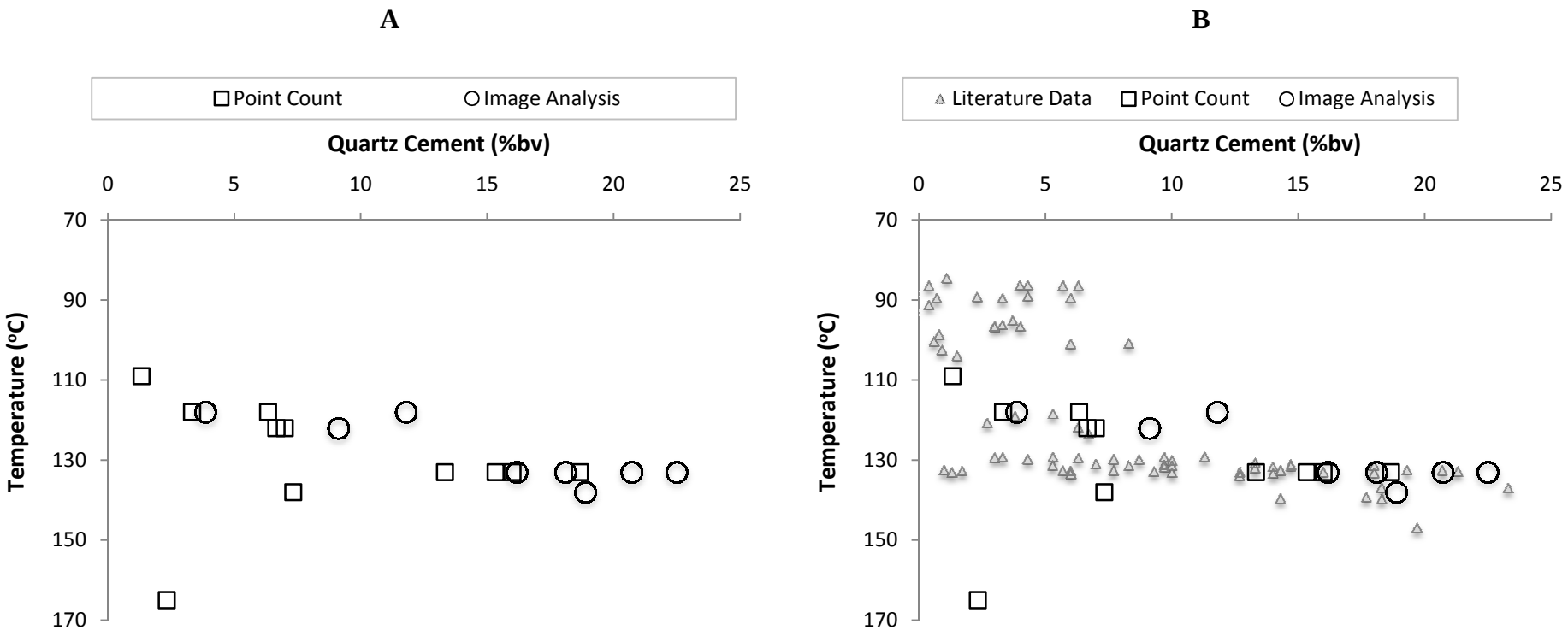

Figure 3.22 Quantitative petrographic analysis of quartz cement in the North Sea Ness Formation. A) Point count and image analysis measurements made in the studied Ness Formation samples. B) Quartz cement measured in this study compared to results recorded in similar Brent sandstones by (Harris, 1992; Walderhaug, 1994a; Walderhaug, 2000)

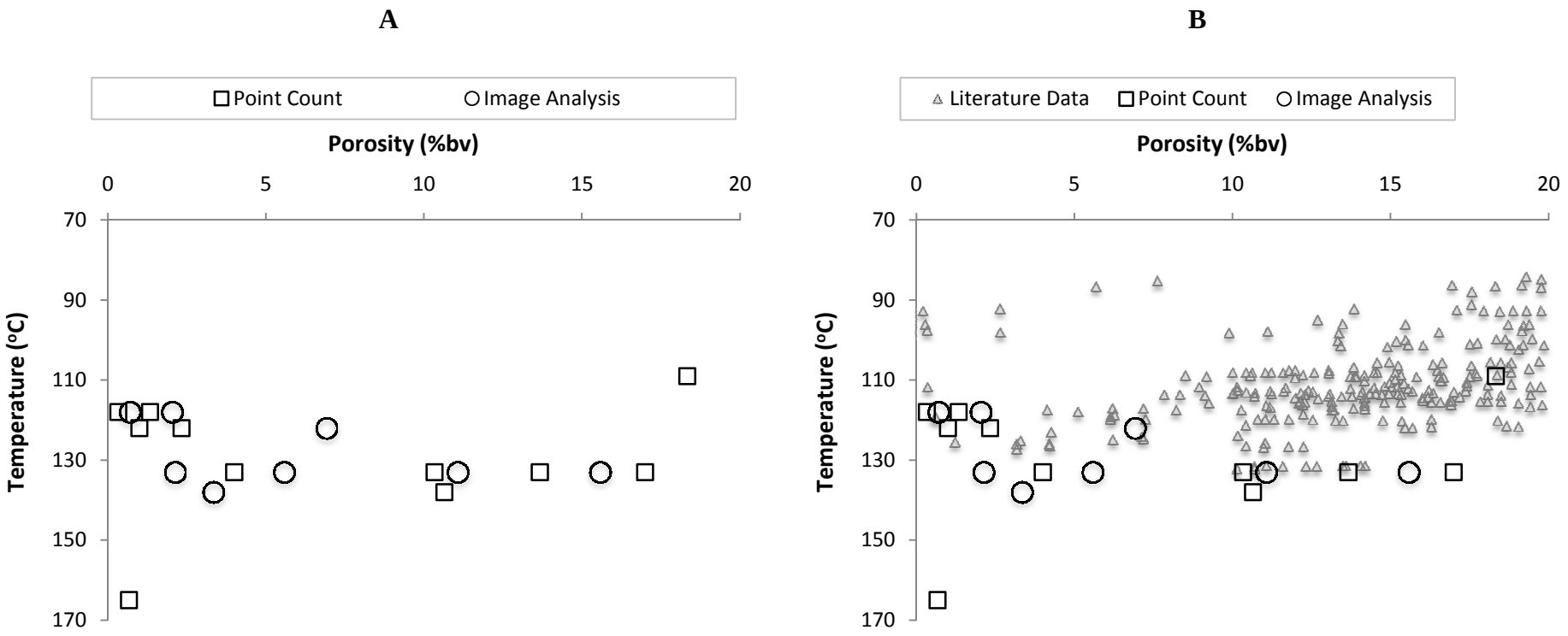

Figure 3.23 Quantitative petrographic analysis of porosity in the North Sea Ness Formation. A) Point count and image analysis measurements made in the studied Ness Formation samples. B) Porosity measured in this study compared to results recorded in similar Brent sandstones by Giles (1992) and Harris (1992)

In this investigation silt rich as well as clean quartz rich sandstone samples was selected for examination and quartz cement quantification. This selection was made in an attempt to examine possible quartz cementation within interlayered silt units. This petrographic study illustrates the mineralogical and physical diversity of the samples selected from the Ness (Appendix 1). Detrital quartz abundance varies from 36.2 %bv in the silt samples to 68.7 %bv in the quartz rich sands. Non-quartz mineral abundance including kaolinite, K-feldspar and illite/mica (Table 3.3) varies from 59 %bv to 5 %bv.

In many studies the growth of quartz cement is assumed to be the largest factor causing the loss of porosity in reservoir sandstones (Ramm, 1992; Robinson and Gluyas, 1992; Walderhaug, 1996; Ajdukiewicz et al., 2010). However, no such relationship is apparent in this investigation as is demonstrated in Figure 3.24. However, porosity is related to the abundance of non-quartz material (Figure 3.25).

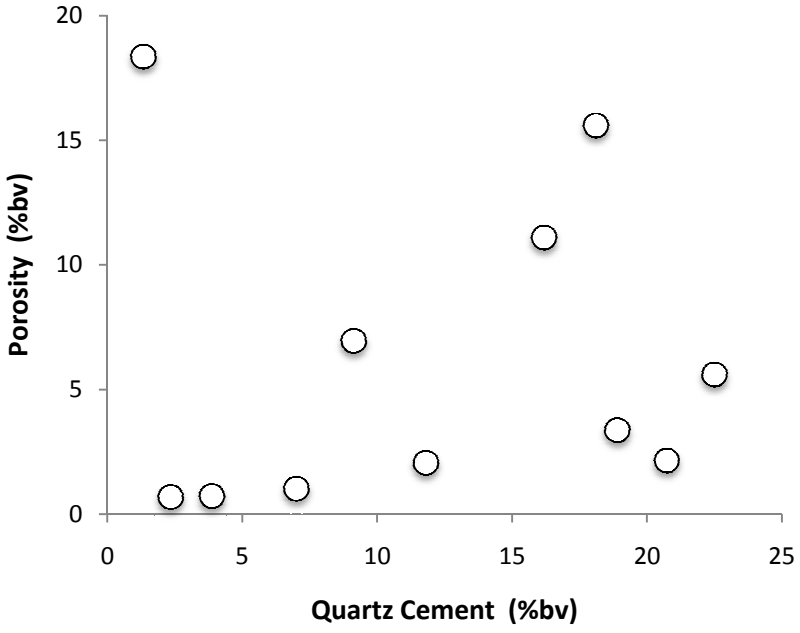

Figure 3.24 Cross-plot of measured quartz cement versus measured porosity abundance.

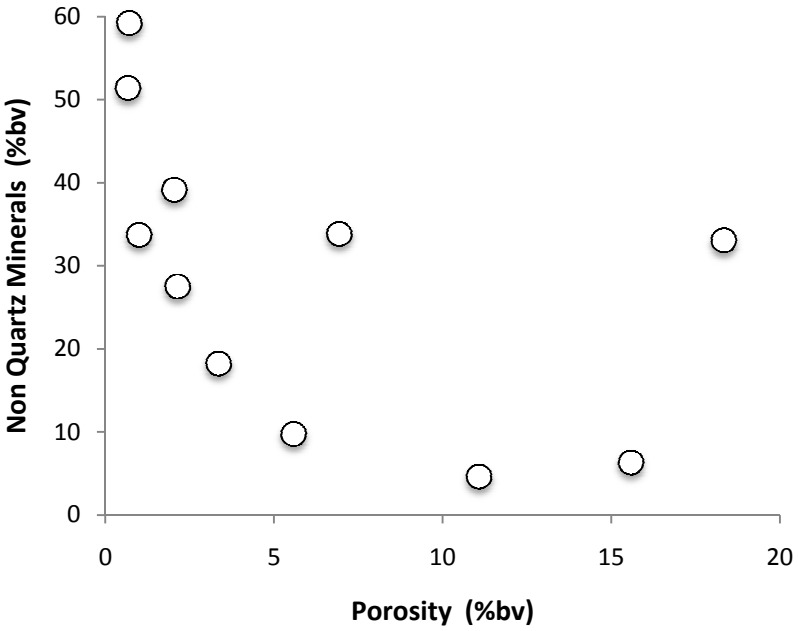

Figure 3.25 Cross-plot of measured porosity versus measured non-quartz mineral abundance.

Sample	Depth (m)	Temperature (^{o}C)	Ave. Grain Size (µm)	Non Quartz Minerals (%bv)
NS4	2678.80	109	125	**(33%)** M/I, K-F
NS11	2845.75	118	94	**(59%)** M/I, Ka, K-F, Na-F
NS10	2845.95	118	193	**(39%)** M/I, Ka, K-F, Na-F
NS23	3420.7	122	173	**(34%)** K-F, Ka, M/I, Si
NS1	3462.22	122	398	**(34%)** M/I, Ka, K-F, Na-F, Ca
NS25	4313.53	133	367	**(5%)** Na
NS17	4332.73	133	162	**(28%)** M/I, Ka, K-F, Na-F, Ch
NS20	4343.40	133	244	**(10%)** M/I, Ka, K-F, Ch
NS19	4344.31	133	323	**(7%)** Al, Ch, Si
NS14	3831.35	137	141	**(18%)** M/I, Ka
NS12	4653.80	167	103	**(51%)** Ch, M/I, Ka, Na-F, K-F

Table 3.3 Summary of North Sea Ness Formation grain size and non-quartz mineral components. Mineralogy determined by powdered XRD, M/I = Mica/Illite, Ka = Kaolinite, K-F = K-Feldspar, NA-F = Na-Feldspar, Na = Nacrite, Ch = Chlorite, Al = Albite, Si = Siderite, Ca = Calcite

3.5.2.1. Image Analysis vs. Point Count

Image analysis is used to improve the efficiency of quartz cement recognition and quantification. Cross plots of point count measurements against image analysis measurements for quartz cement (Figure 3.26) and porosity (Figure 3.27) agree well. In both techniques the standard deviation between different areas of the thin section are high, suggesting inhomogeneity across each thin section. Overall, the image analysis technique benefits from being faster and more efficient.

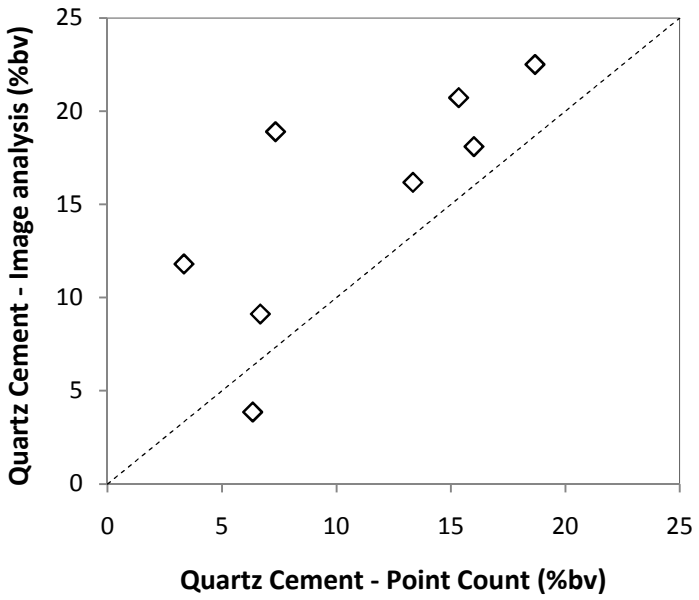

Figure 3.26 Cross-plot of total quartz cement measured using the SEM point count method versus total quartz cement measured using the image analysis method, the dotted line represents 100% agreement.

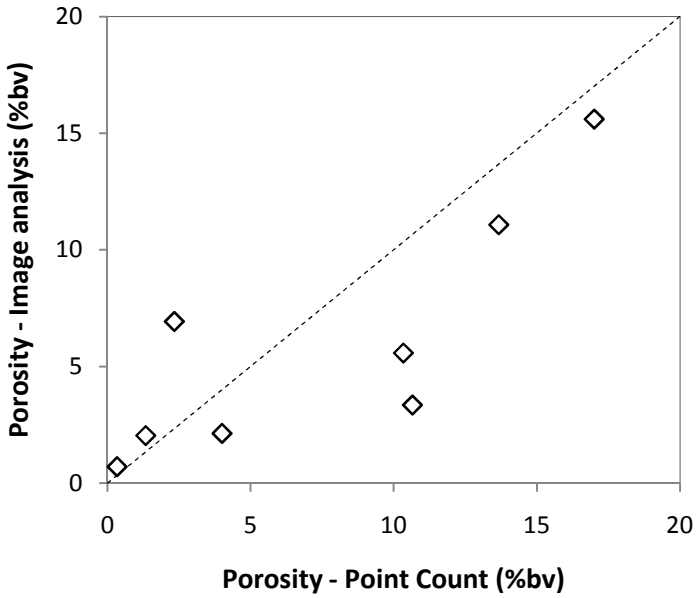

Figure 3.27 Cross-plot of total porosity measured using the SEM point count method versus total porosity measured using the image analysis method, the dotted line represents 100% agreement.

3.6. Quartz Cement Modelling

All quartz cementation modelling was undertaken using Walderhaug's (1996) kinetic model (Equation 2.5). Initial mineralogy, grain size and porosity needed for modelling were determined during petrographic analysis (Appendix 1). Initial porosity is assumed to be equal to the minus cement porosity. Thermal histories were derived from Genesis modelling (Table 3.2).

In total ten sandstone samples were modelled from 6 different North Sea wells. Table 3.4 gives details of the modelled final porosities and volume of cement precipitated. Measured quartz cement in these Ness samples was shown to vary from 1.3 to 22.5 %bv, increasing with increasing burial temperature (Figure 3.28). Porosity is between 0.7 and 18.3 %bv (Figure 3.29). Modelled quartz cement and porosity both show similar overall trends, with cement abundance ranging from 4.7 to 23.7 %bv and porosity from 0.2 to 13.7 %bv. Cross-plots of measured quartz cement against modelled quartz cement fit well (Figure 3.30), indicating Walderhaug's (1996) equation can be used to predict quartz cement growth. However, cross-plots of measured and modelled porosity data show a poor fit. The measured porosity is often higher than the modelled value (Figure 3.31).

Walderhaug's (1996) model predicts the volume of cement that precipitates across a specified volume of sandstone, not at the overgrowth level observed in this study. As an estimate, modelled overgrowth thickness was calculated as the radial increase observed in each quartz grain or model "sphere". However, this assumes equal growth around each grain and no grain contact, both of which are geologically unrealistic scenarios. Calculated values of overgrowth thickness are therefore much lower than petrographic measurements (Figure 3.32). However, this model does provide information concerning overall cement growth rates. In this investigation these rates were used to normalise growth across individual overgrowths, allowing possible precipitation temperatures to be estimated (Figure 3.33). Normalised growth rates assume that:

1. Growth occurs in concentric manner away from the detrital grain

2. Growth begins at 80^{o}C

3. Growth continues to the maximum burial temperature

Sample	NS4	NS11	NS10	NS23	NS 1	NS25	NS17	NS20	NS19	NS14
Depth (m)	2678.8	2845.8	2846.0	3420.8	3462.2	4313.5	4332.7	4343.4	4344.3	3831.4
Temperature (^{o}C)	109	118	118	122	122	133	133	133	133	137
Modelled Quartz Cement (%bv)	7.8	4.7	7.4	13.0	6.8	15.9	21.4	23.7	21.8	21.7
Measured Quartz Cement (%bv)	1.3	3.9	11.8	9.1	7.0	16.2	20.7	22.5	16.1	18.9
Modelled Porosity (%bv)	11.9	0.2	6.6	1.8	1.2	2.0	1.5	4.4	15.1	0.5
Measured Porosity (%bv)	18.3	0.7	2.0	6.9	1.0	11.1	2.1	5.6	6.8	3.3
Max Modelled Overgrowth Thickness (µm)	3.3	2.0	4.8	6.8	7.5	12.9	10.3	13.9	10.1	8.1
Max Measured Overgrowth Thickness (µm)	20.3	34.2	35.5	56.8	118.5	45.6	60.5	80.6	118.9	110.4

Table 3.4 Measured and modelled bulk volume cement, porosity and overgrowth thickness

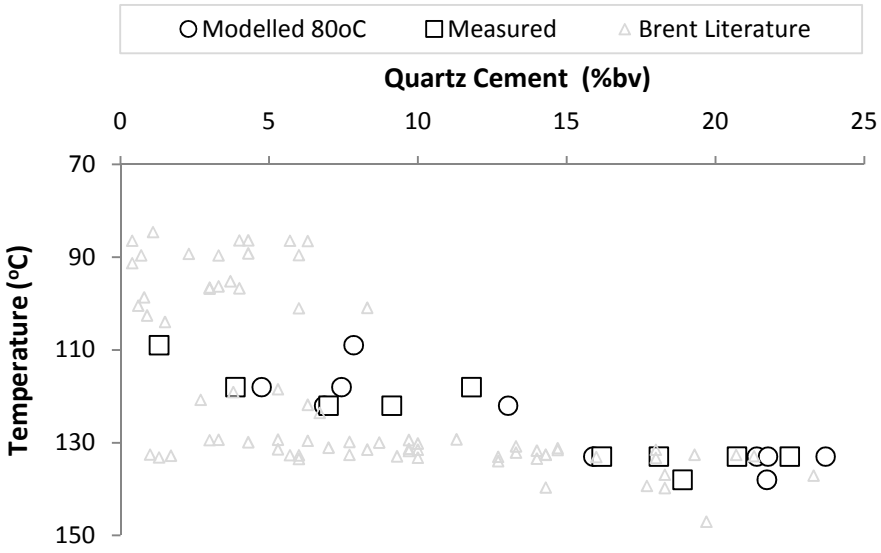

Figure 3.28 Modelled quartz cement abundance compared to petrographically measured Ness Formation and Brent literature values (Harris, 1992; Walderhaug, 1994a; Walderhaug, 2000).

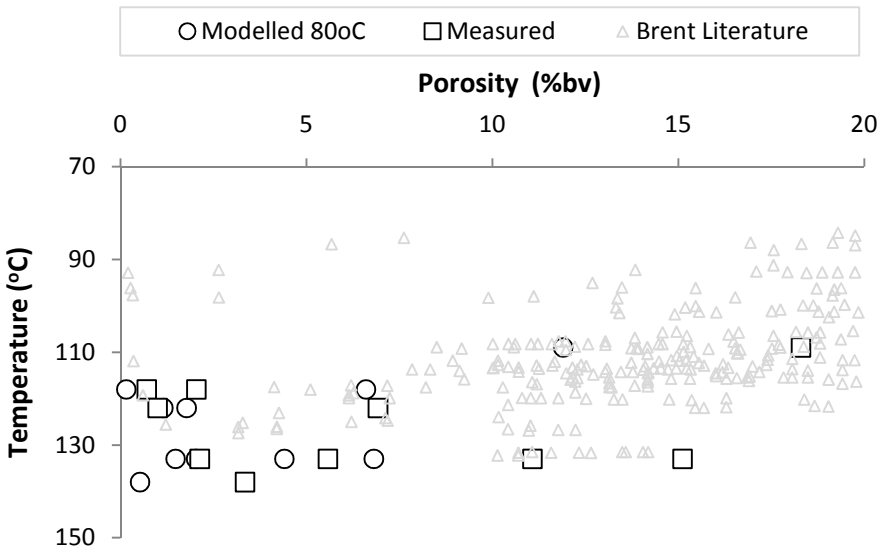

Figure 3.29 Modelled porosity abundance compared to petrographically measured Ness Formation and Brent literature values (Giles, 1992; Harris, 1992).

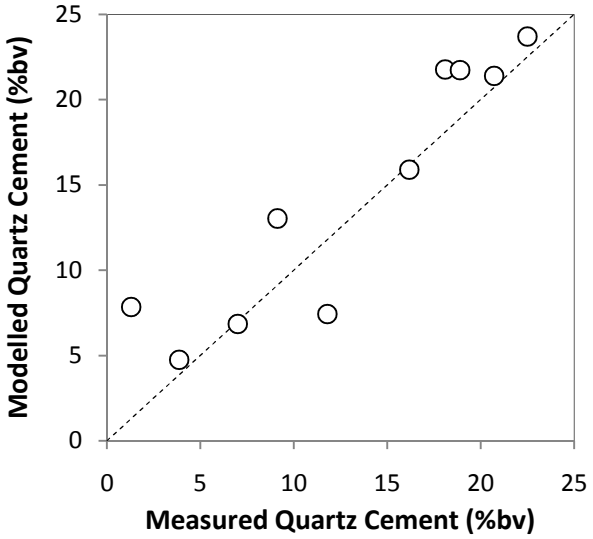

Figure 3.30 A cross-plot of measured quartz cement versus the volume of quartz cement predicted during cementation modelling using Walderhaug's (1996) model, the dotted line represents 100% agreement.

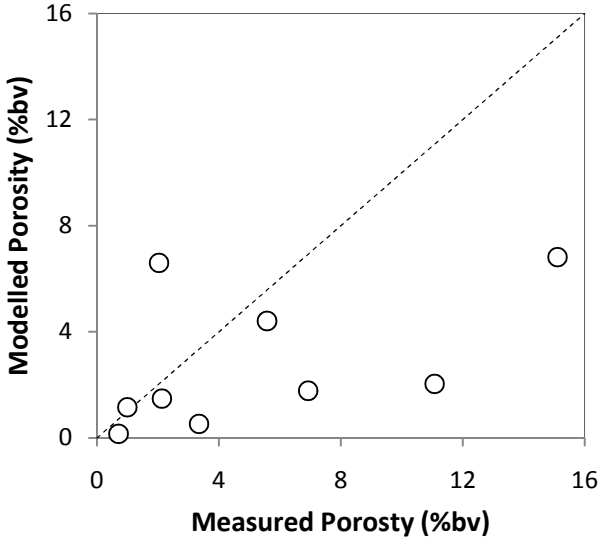

Figure 3.31 A cross-plot of measured porosity versus the volume of porosity predicted using Walderhaug's (1996) cementation model, the dotted line represents 100% agreement.

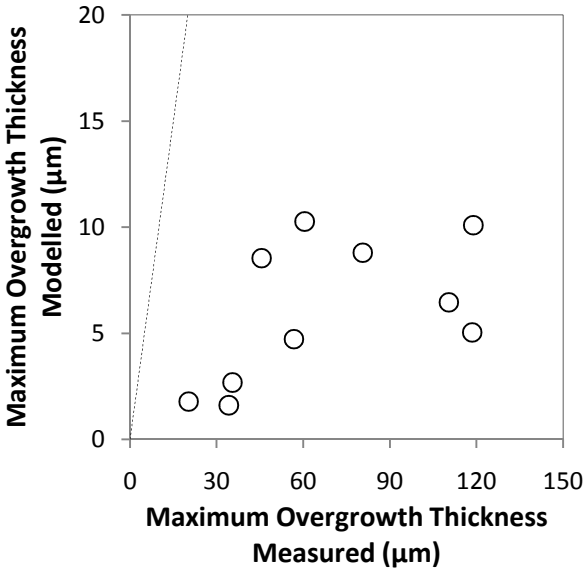

Figure 3.32 A cross-plot of measured maximum overgrowth thickness versus maximum overgrowth thickness as calculated from modelled cement volumes using Walderhaug's (1996) cementation model, the dotted line represents 100% agreement.

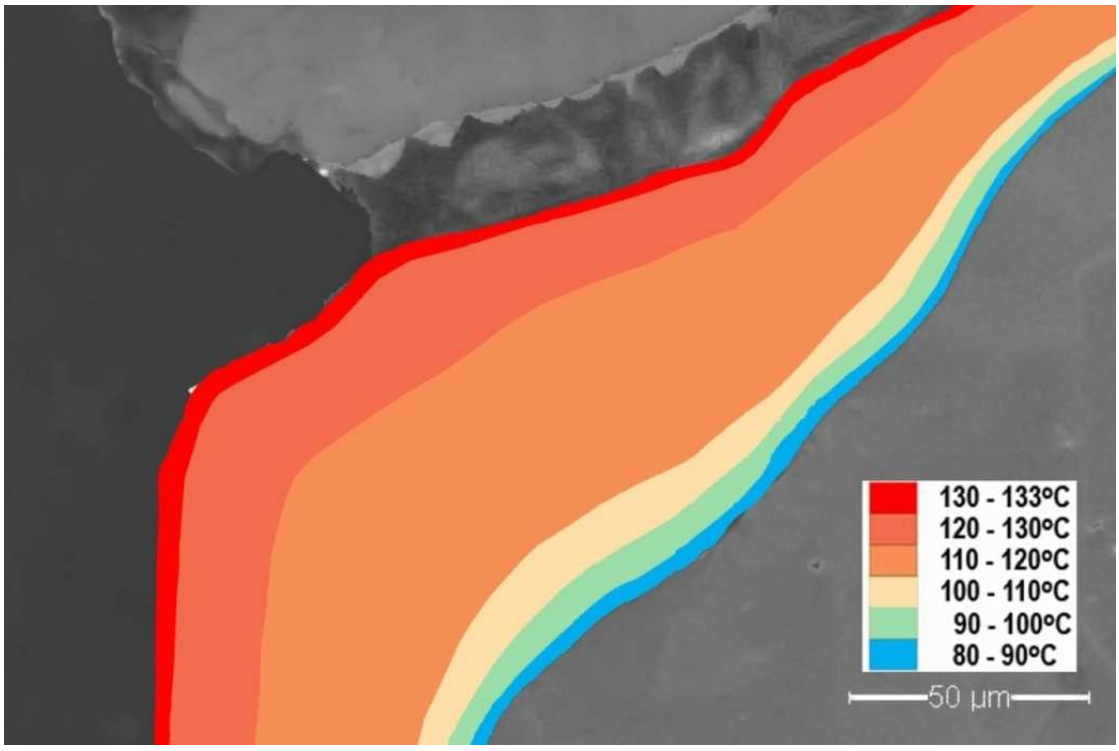

Figure 3.33 Image showing quartz cement growth modelled using Walderhaug's (1996) Exemplar kinetics (Equation 2.5) in sample NS19, maximum burial temperature was 133°C. Precipitation commences at 80°C.

3.7. Isotope Analysis

3.7.1. Ness Formation SIMS Samples

Seven samples from five wells were selected for SIMS investigation. A full description of the SIMS samples, NS6 through to NS12, can be found in Table 3.1. Quantitative petrology, XRD and Genesis 1-D modelling measurements are summarised in Table 3.5.

Sample	Well	Depth (m)	Max Burial Temp (°C)	Total Quartz (%bv)	Minor minerals (%bv)	Porosity (%bv)	Quartz Cement (%bv)	Grain Size (µm)
NS6	30/9-12	2673.7	109	-	-	-	-	-
NS10	30/3-4	3420.8	118	59	39% (I/M,Ka,Kf,Naf)	2	12	193
NS23	211/11a-3	3462.2	122	59	34% (I/M,Ka,Kf,Naf, Si)	7	9	173
NS1	211/11a-3	2846.0	122	65	34% (I/M,Ka,Kf,Naf, Ca)	1	7	334
NS20	211/27-A2	4343.4	133	84	10% (I/M,Ka,Kf,Ch)	6	23	244
NS19	211/27-A2	4344.3	133	78	7% (Al,Ch,Si)	15	18	323
NS12	34/8-7	4653.8	167	48	51% (I/M,Ka,Kf,Naf,Ch)	<1	2	104

Table 3.5 North Sea Ness Formation SIMS sample suite (I=illite, M=Mica, Ka= Kaolinite, Kf=K-Feldspar, Naf= Na-Feldspar, Ch=Chlorite, Al= Albite, Si=Siderite, Ca=Calcite)

3.7.2. SIMS Analysis

During a 34 hour period between the 8th and 9th of May, 2008, 404 oxygen isotope analyses were made at the WiscSIMS lab, University of Wisconsin-Madison. 271 measurements were made on the Ness samples and 121 on the internal quartz standard (UWQ-1). In June 2009 a second session took place in which 77 measurements were made. In the later session 49 analyses were made on a single grain from sample NS19 and a further 28 measurements of the UWQ-1 standard were made.

3.7.2.1. UWQ-1 Analysis

External precision is calculated using the method described by Kita (2009). This method required a single grain of the University of Wisconsin quartz standard, UWQ-1, to be mounted within 5 mm of each mount. UWQ-1 is extremely homogenous and analysis by laser fluorination yielded a $\delta^{18}O$ value of 12.33 ± 0.07‰ (1SD, n= 29; 1SE = ±0.01‰; (Kelly et al., 2007). Between every 8-22 sample measurements 4 analyses of the standard were performed. The spot to spot reproducibility of each bracket of 8 standard analyses (4 before and 4 after each 8-22 sample analyses) is then used to calculate external precision and instrument bias.

Figure 3.34 shows the reproducibility of UWQ-1 in the first session carried out during the North Sea investigation. Initially the SIMS beam was aligned to 20 μm; this was reduced after one bracket to 12 μm. The reproducibility during day one (02/05/08) falls slightly after the 20 μm beam is realigned down to a 12 μm spot. However, during both stages the reproducibility is very good (Table 3.6). Furthermore, during each session a number of sample changes were made but no discernable changes occurred in the UWQ-1 measurements.

Session/ spot size (μm)	n	Average $\delta^{18}O$ (‰)	Min $\delta^{18}O$ (‰)	Max $\delta^{18}O$ (‰)	Instrument bias (‰)
Day 1 / 20μm	8	7.03 ±0.22(2SD)	6.90	7.48	-5.30
Day 1 / 12μm	44	6.78 ±0.33(2SD)	6.20	7.44	-5.55
Day 2 / 12μm	62	7.47 ±0.34(2SD)	7.01	8.01	-4.86

Table 3.6 Summary of UWQ-1 standard measurements made during the 12 μm North Sea SIMS investigation.

Each measurement is subject to instrumental bias according to differences in the ionisation efficiency of individual isotopes, in the transmission through the mass spectrometer and efficiency of individual detectors (Kita et al., 2009). Therefore the measured ratios are always biased compared to the true value and must be corrected to the V-SMOW scale. True values are calculated using the deviation of the standard measurements by SIMS away from that determined by laser fluorination (Kelly et al., 2007).

In 2009 a second series of analyses were made in which the spot size was reduced down to 2 μm (Figure 3.35). Again spot to spot reproducibility is good, although instrument bias is much higher (Table 3.7).

Session/ spot size (μm)	n	Average $\delta^{18}O$ (‰)	Min $\delta^{18}O$ (‰)	Max $\delta^{18}O$ (‰)	Instrument bias (‰)
Day 1 / 2 μm	28	0.18 ±0.22(2SD)	-0.78	0.71	-12.15

Table 3.7 Summary of UWQ-1 standard measurements made during the 2 μm North Sea SIMS investigation.

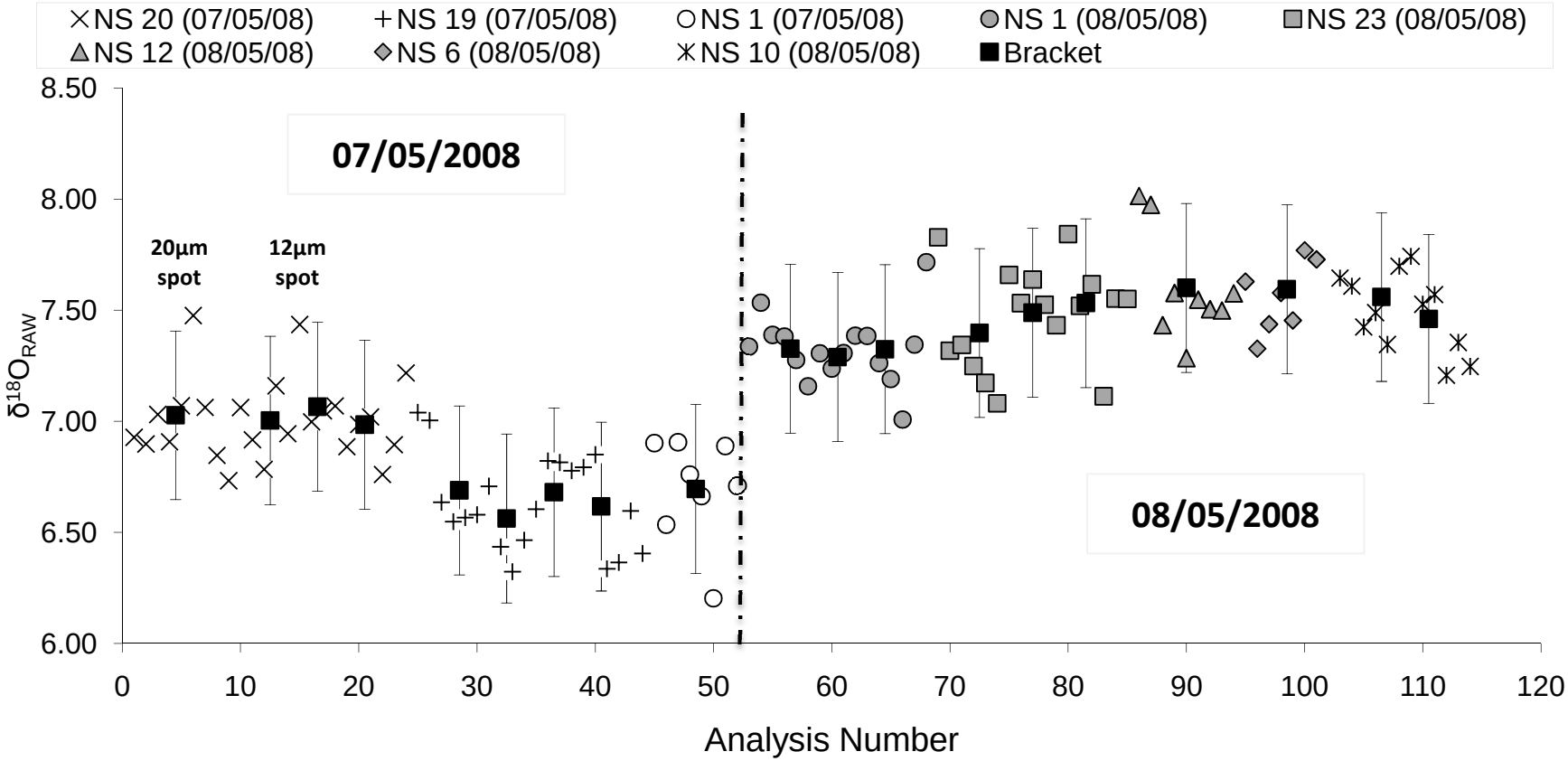

Figure 3.34 UWQ-1 standard analysis, brackets are average of 8 or 9 individual measurements made before and after each set of sample measurements. The error bars indicate the average error of each set of bracket analyses. The initial primary SIMS beam measured 20 µm (first bracket), thereafter all measurements were carried out with a 12 µm spot.

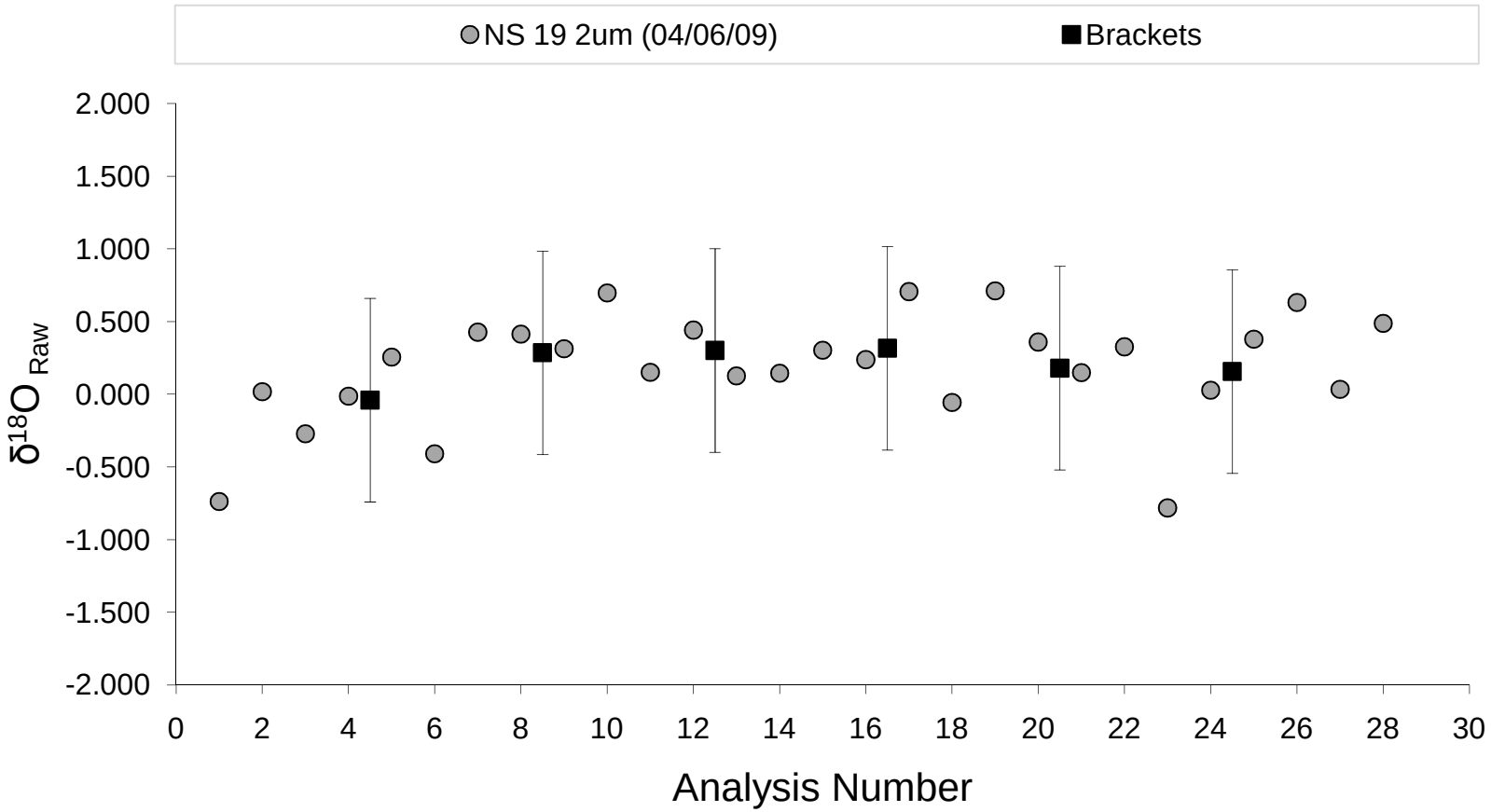

Figure 3.35 UWQ-1 standard analyses performed during the 2 μm high precision SIMS investigation. Each bracket contains 8 measurements of UWQ-1, 4 made prior to the sample analysis and 4 after. Error bars show the average bracket error that consists of 8 standard measurements.

3.7.2.2. SIMS Pit Characterisation

After the completion of the SIMS investigation a combination of Secondary Electron (SE), Back Scattered (BSE) and Cathodoluminescence (SEM-CL) microscopy was used to relocate and characterise each individual pit. Appendix 3 give a full account of how each pit was interpreted with reasoning for each pit's inclusion or exclusion from this study.

3.7.2.3. SIMS Analysis of Authigenic Quartz

Seven samples from the Ness were analysed from 5 separate wells (Table 3.1), although only 5 samples produced isotopic data from quartz cement ($\delta^{18}O_{(cement)}$). One sample (NS10) was taken from well 30/3-4, two samples (NS23, NS1) from well 211/11a-3 and two samples (NS19 and NS20) from well 211/27-A2. Current burial temperatures for the three wells are at 118^{o}C, 122^{o}C and 133^{o}C, respectively. No single SIMS pit fell in the quartz cement of two silt grade samples, NS6 and NS12 (Appendix 3).

A summary of all $\delta^{18}O_{(cement)}$ measurements made across these Ness samples is given in Table 3.8. A histogram of all the data gathered in the 2008 12 µm beam analysis are shown in Figure 3.36. Using straight-line measurements as described in Figure 2.5, Figure 3.37 illustrates how $\delta^{18}O_{(cement)}$ varies across individual overgrowths within each well. In all cases, $\delta^{18}O_{(cement)}$ becomes less positive away from the detrital quartz/overgrowth boundary. However, it is clear no measurements were made in the first 10% of any overgrowth at this 12 µm resolution.

Well	Samples	Temperature (^{o}C)	Quartz Cement Analysis			
			n	Min (‰)	Max (‰)	Precision (±2SD)
30/3-4	NS10	118	12	+19.3	+24.2	0.3
211/11a-3	NS23, NS1	122	42	+19.5	+27.7	0.4
211/27-A2	NS20*, NS19	133	59	+19.4	+26.3	0.4

Table 3.8 Summary of $\delta^{18}O_{(cement)}$ measurements made during 2008 SIMS investigation. *Initially the SIMS beam was aligned to 20 µm, this was realigned down to 12 µm after one bracket of measurements.

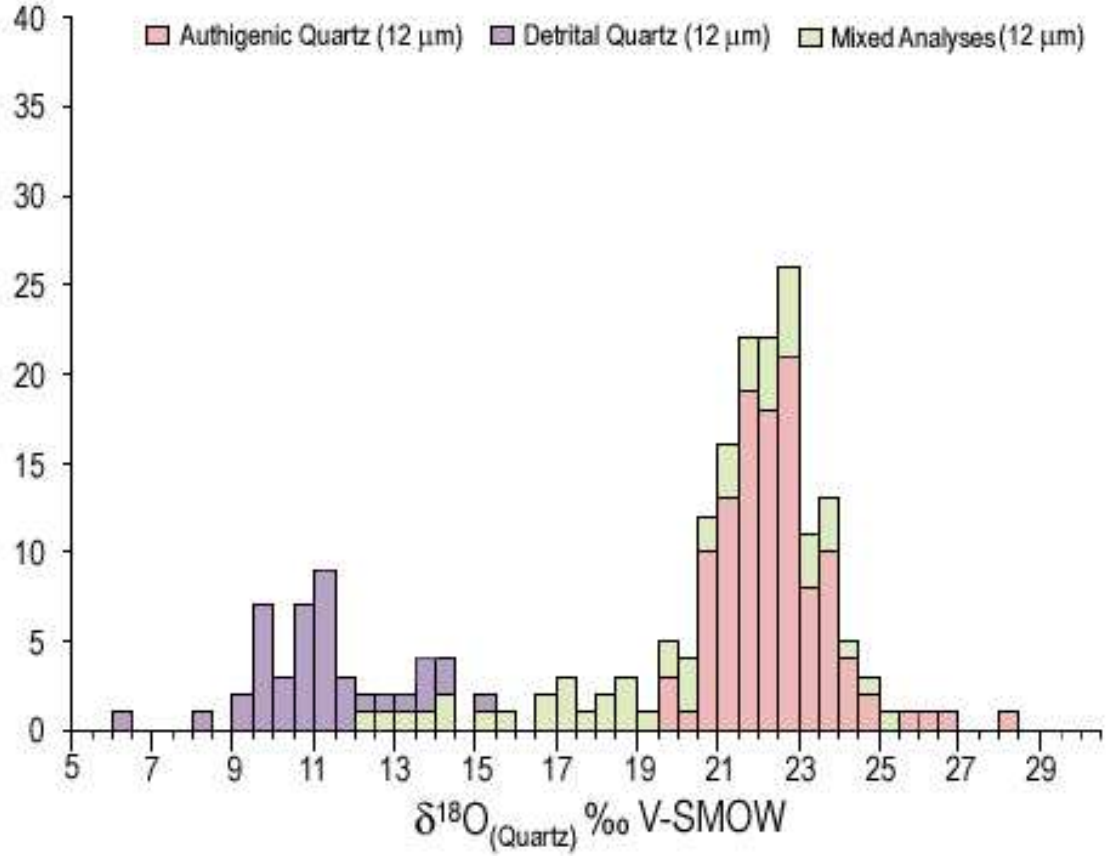

Figure 3.36 Histogram showing the frequency of $\delta^{18}O_{(quartz)}$ from 12 µm-sized spots by SIMS in the Ness Formation. Mixed analyses are on the boundary of detrital quartz and quartz overgrowths.

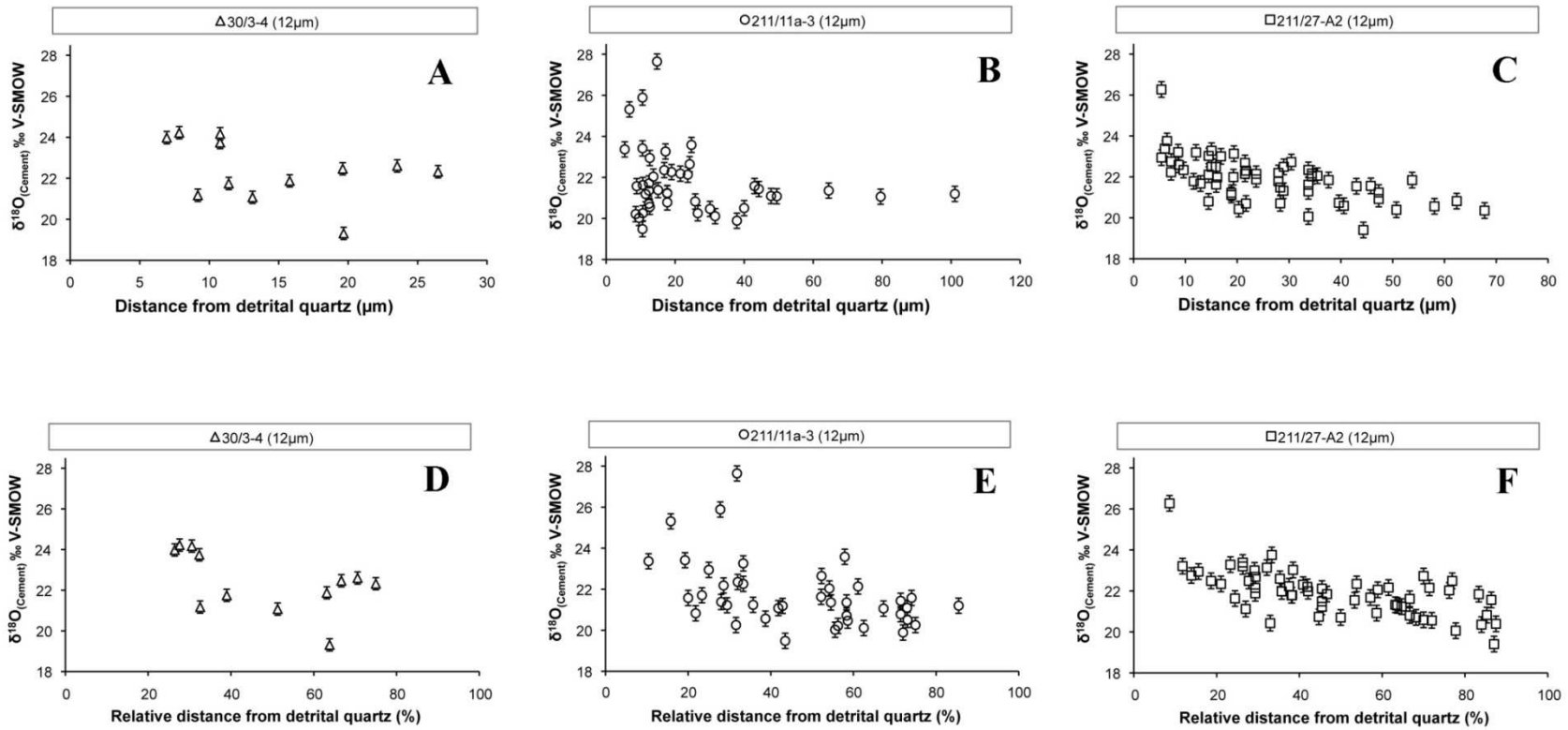

Figure 3.37 12 µm SIMS analysis of quartz cement in the Ness Formation. Plots of $\delta^{18}O_{(cement)}$vs. Distance from detrital quartz grain (µm), **A)** Well 30/3-4 118°C, **B)** Well 211/11a-3 122°C, **C)** Well 211/27-A2 133°C. Plots of $\delta^{18}O_{(cement)}$vs. Relative distance from detrital quartz grain (%), **D)** Well 30/3-4 118°C, **E)** Well 211/11a-3 122°C, **F)** Well 211/27-A2 133°C.

In 2009, a second series of measurements were performed at the WiscSIMS lab. This later investigation was designed to reduce the SIMS spot size below 12 µm in an attempt to target the precipitate closest to detrital grain 2 of NS19 Area5 (Figure 3.38B). Previous studies at the WiscSIMS lab have shown spot sizes can be reduced to the sub micron scale with a precision of ±2‰ (2SD) (Page et al., 2007). NS19 Area 5 was selected for further micron scale investigation after the 2008 analysis highlighted a >4‰ range in $\delta^{18}O_{(cement)}$ across the large, clean overgrowth. Any variation in $\delta^{18}O_{(cement)}$ would therefore be recognised within the analytical error using the reduced spot size.

In total a further 49 analyses were made, composing 1 mixed analysis, 6 detrital, 1 unusable pit and 41 authigenic. All data and spot interpretations are given in Appendix and Figure 3.38. Using the 2 µm it was possible to make SIMS measurements in the first 10% (~9 µm) of the overgrowth closest to the detrital grain that was unattainable using the larger 12 µm spot size. $\delta^{18}O_{(cement)}$ ranged from +27.7‰ close to the detrital grain to +20.9‰ at the edge of the grain.

Six 2 µm spots taken within the initial 8% of the cement on grain 2 (Figure 3.38b) have $\delta^{18}O_{(cement)}$ values of +24.5‰ to +27.7‰, values which were also hinted at by the 12 µm data Figure 3.38E. It is unclear however if the two values between +24.5‰ and +25.2‰ represent a mixed analysis of two isotopically distinct zones or represent part of a continuous isotopic profile.

In total 248 useable SIMS measurements were performed in 7 Ness sand and siltstones using a 20, 12 and 2 µm SIMS beams (Figure 3.39). 154 analyses were performed in quartz cement material. $\delta^{18}O_{(cement)}$ ranged from +19.3 to +27.7‰. Figure 3.40 illustrates the total range of $\delta^{18}O_{(cement)}$ measured in each well.

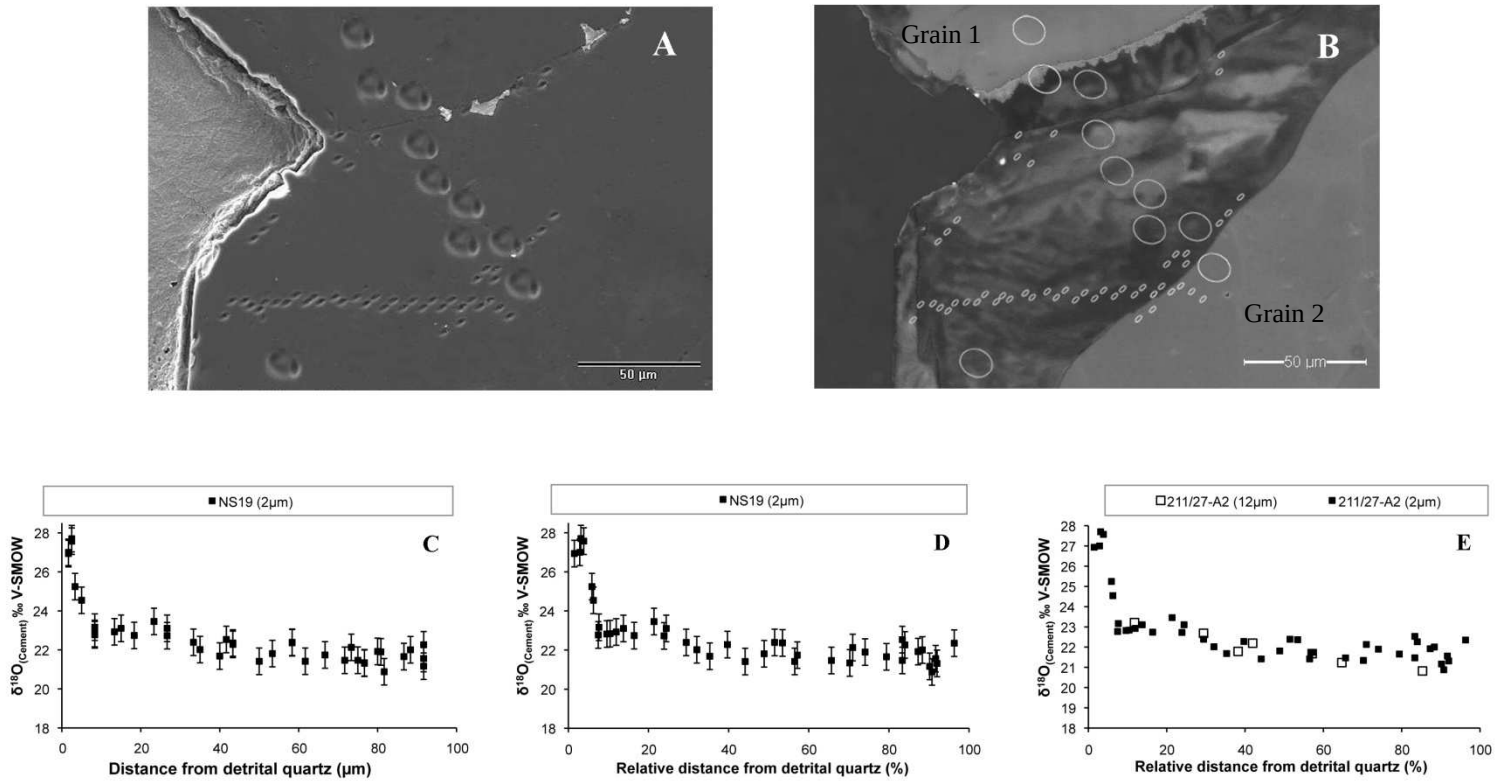

Figure 3.38 2 µm SIMS analysis of quartz cement. **A)** BSE image of area NS19_A5 (133°C) showing both 12 and 2 µm SIMS pits, **B)** SEM-CL image showing quartz cement and detrital quartz, the locations of the SIMS pits are highlighted with white circles. **C)** Plot of 2 µm $\delta^{18}O_{(cement)}$ analyses vs. distance from detrital quartz grain (µm). **D)** Plot of 2 µm $\delta^{18}O_{(cement)}$ analyses vs. Relative distance from detrital quartz grain (%). **E)** Plot of 2 µm and 12 µm $\delta^{18}O_{(cement)}$ analyses vs. relative distance from detrital quartz grain (%).

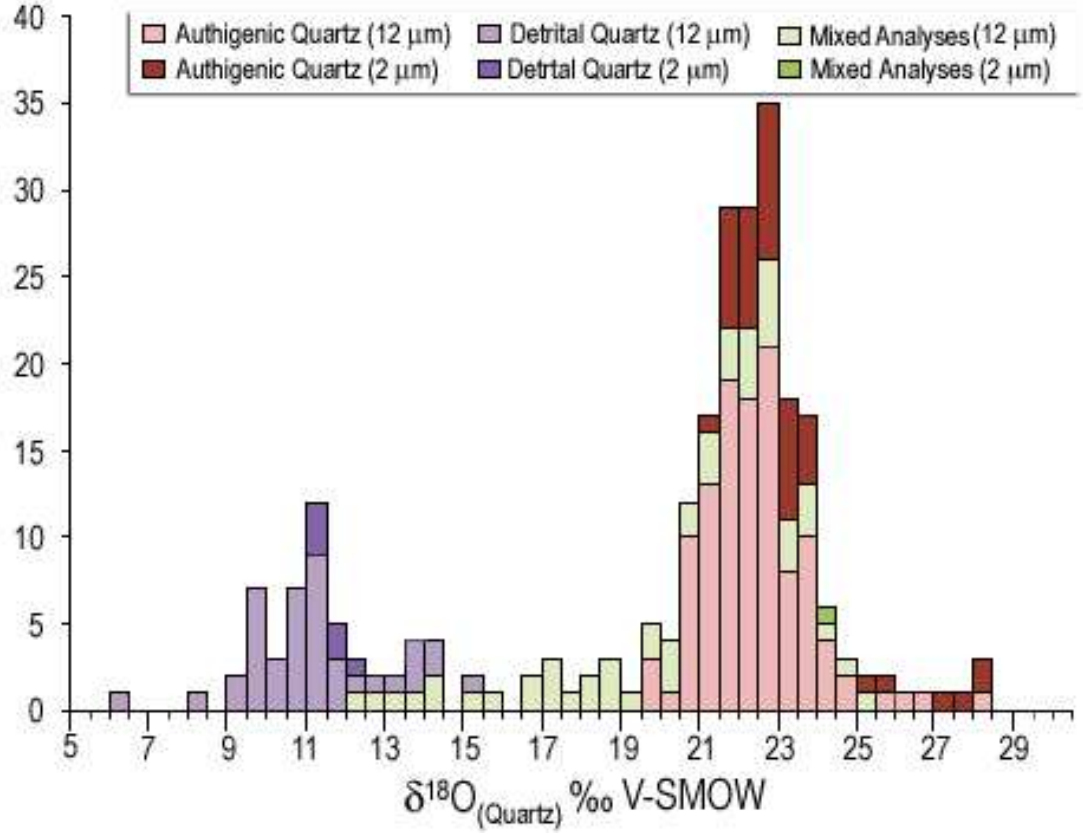

Figure 3.39 Histogram showing the frequency of $\delta^{18}O_{(quartz)}$ in the Ness formation from both 2 and 12 μm-sized spots by SIMS. Mixed analyses are on the boundary of detrital quartz and quartz overgrowth.

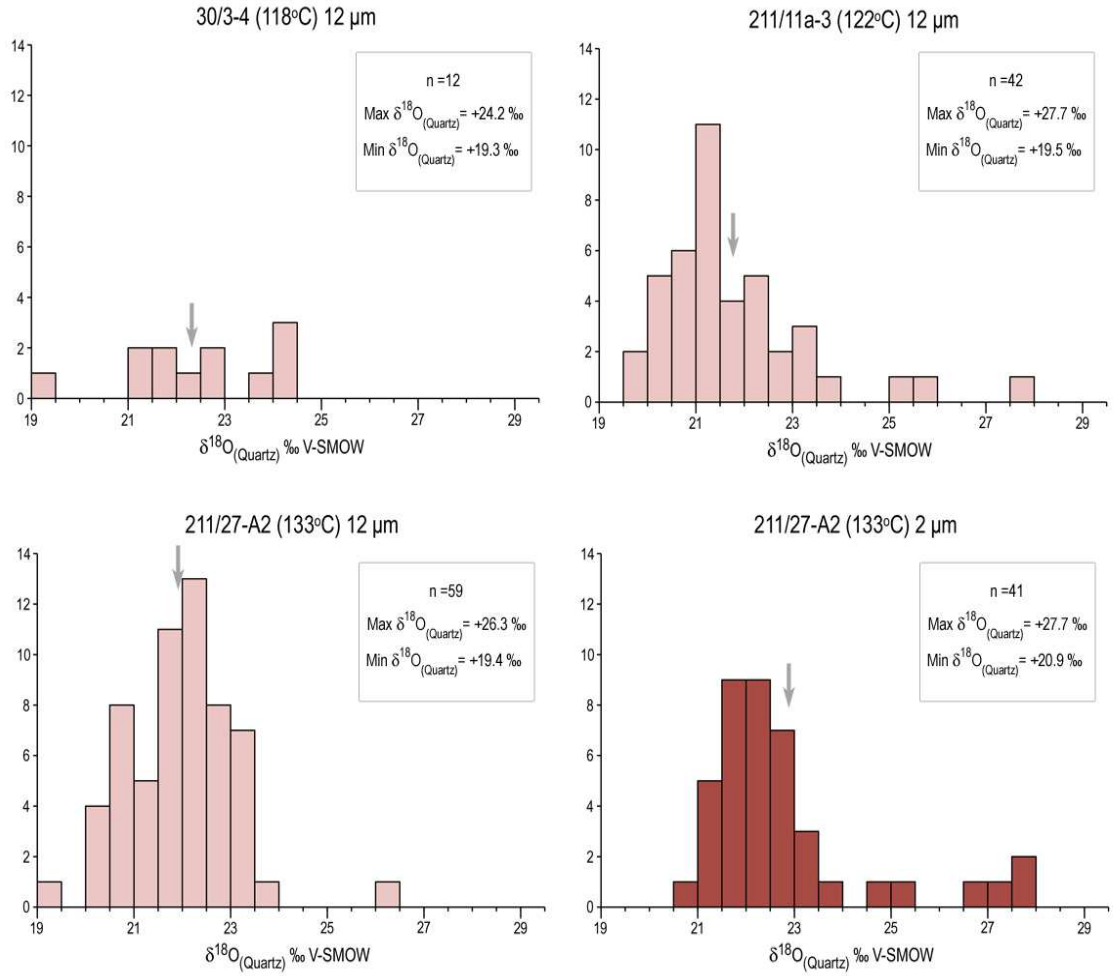

Figure 3.40 Histograms of all $\delta^{18}O_{(cement)}$ measured in Ness of each studied well. The grey arrows indicate the mean value measured in each well.

In all grains analysed, heavier $\delta^{18}O_{(cement)}$ values are recorded closer to the detrital core; a full illustration of how the SIMS data varies spatially across the cement material is shown in Figure 3.41A and B.

$\delta^{18}O_{(cement)}$ measurements were made in 5 samples from 3 wells. As each well has a unique time-temperature and quartz cementation history it is difficult to directly compare cement growth between samples. Using results from Walderhaug's (1996) cementation modelled described above (Equation 2.5) it was possible to allocate each SIMS pit a formation temperature, assuming cementation commences at 80°C (e.g.

Figure 3.33). $\delta^{18}O_{(cement)}$ can therefore be plotted as function of temperature (Figure 3.41C). Furthermore, using Clayton et al.'s (1972) quartz - water fractionation equation it is possible to calculate the $\delta^{18}O_{(Water)}$ from these modelled temperatures and $\delta^{18}O_{(cement)}$ (Figure 3.41D).

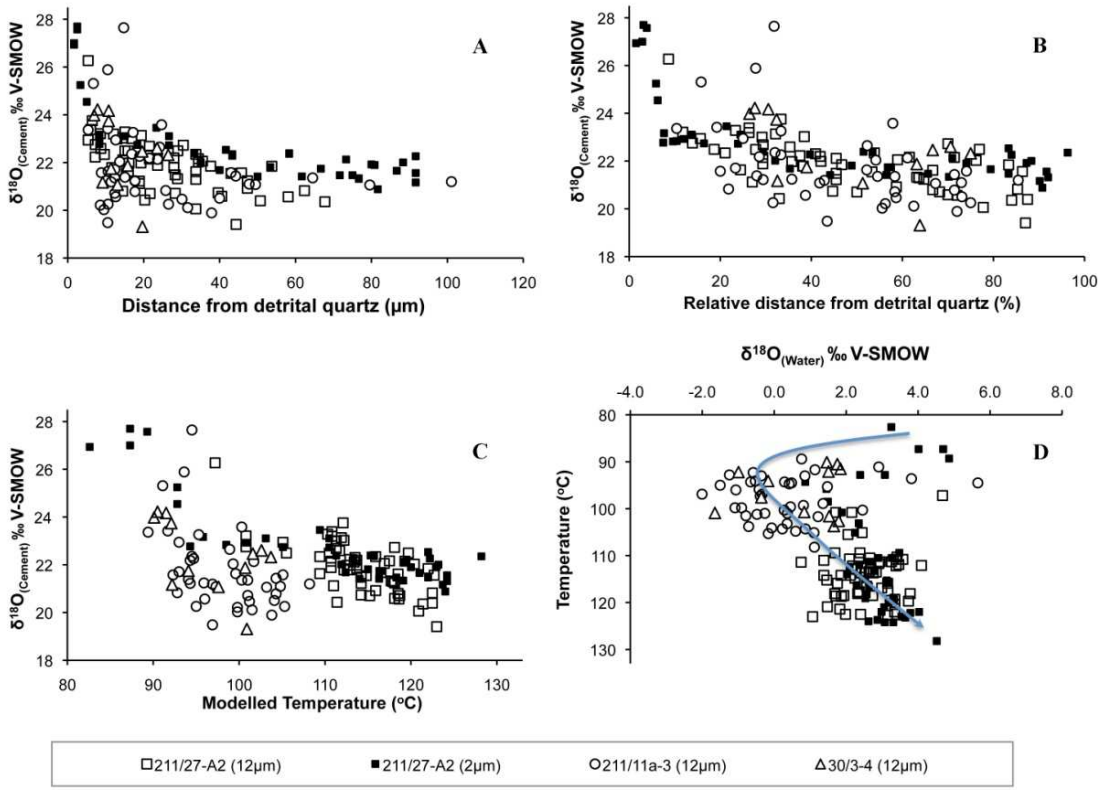

Figure 3.41 All North Sea Ness Formation 12 and 2 µm SIMS $\delta^{18}O_{(cement)}$ analyses. ***A)*** Plot of $\delta^{18}O_{(cement)}$ analyses vs. distance from detrital quartz grain (µm). **B)** Plot of $\delta^{18}O_{(cement)}$ analyses vs. relative distance from detrital quartz grain (%). **C)** Plot of $\delta^{18}O_{(cement)}$ analyses vs. modelled temperature. Modelled temperatures are estimates made using Walderhaug's (1996) cementation model (Equation 2.5). **D)** Plot showing the evolution of formation fluids should modelled temperatures be accurate. The arrow indicates modelled temperatures would require $\delta^{18}O_{(water)}$ to first become isotopically lighter then evolve towards a heavier composition above 90°C.

3.7.2.4. SIMS Analysis of Detrital Quartz

In total 53 SIMS measurements were performed in detrital quartz grains across the 5 wells. Four $\delta^{18}O_{(Detrital)}$ analyses were made using the 20 μm spot, 43 using the *12* μm spot and a further 6 in 2009 using the 2 μm spot. Across the 5 wells $\delta^{18}O_{(Detrital)}$ ranged from +5.6 to +14.9‰ (Figure 3.42, Table 3.9).

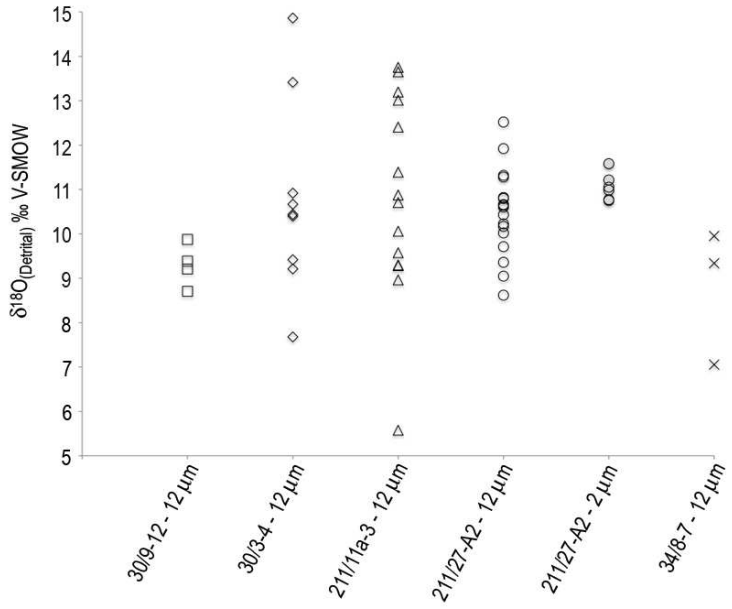

Figure 3.42 Variation in $\delta^{18}O_{(Detrital)}$ measurements across the 6 wells investigated, maximum burial temperatures range from 109 to 167°C.

Well	Samples	Temperature (°C)	Detrital Quartz Analysis		
			n	Min (‰)	Max (‰)
30/9-12	NS6	109	4	+8.71	+9.87
30/3-4	NS10	118	9	+7.7	+14.9
211/11a-3	NS23, NS1	122	14	+5.6	+13.8
211/27-A2	NS20, NS19	133	23	+8.2	+12.5
34/8-7	NS12	167	3	+7.06	+9.95

Table 3.9 Summary of all detrital quartz SIMS analyses made in the Ness Formation.

3.8.Mineralogical Analysis of the Ness Silt and Shale

In total, 20 silt and shale grade samples taken from 7 wells across the North Sea study area were examined. A petrographic analysis of the Ness formation demonstrates that neighbouring sands may contain as much as 22.5 %bv quartz cement. Previous studies have highlighted that minerals including: K-feldspar (Sorby, 1880; Hawkins, 1978); kaolinite (Lanson et al., 2002); albite (Saigal et al., 1988; Glasmann, 1992); mixed layered illite-smectite (Velde and Vasseur, 1992; Lanson et al., 2002; Sanjuan et al., 2002; van de Kamp, 2008) and chlorite-smectite (Hurst, 1985; Chang et al., 1986; Hillier, 1994) may take part in silica producing reactions within the Brent Group. Quantitative analysis of these minerals was undertaken in an attempt to assess the potential for these minerals to produce the required silica needed to precipitate around 20%bv quartz cement.

3.8.1. Bulk Quantitative X-Ray Diffraction of Ness Silt and Shale

All bulk Ness shale XRD measurements are given in Appendix 5. Figure 3.43A illustrates the actual totals quantified before mineral proportions are normalised to 100%.

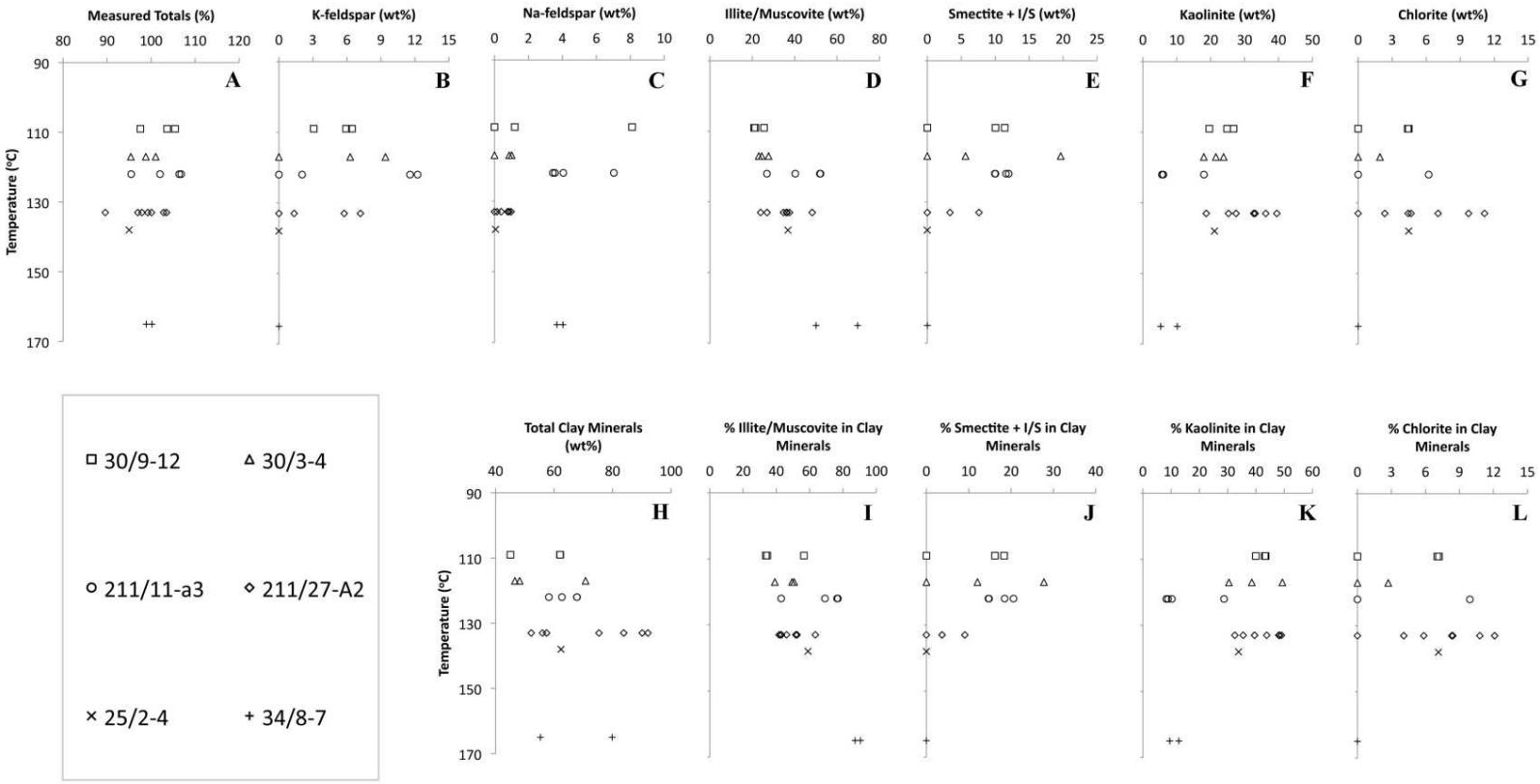

Figure 3.43 Bulk Quantitative X-Ray Diffraction of Ness silt and shale Samples. (**A**) Measured totals, showing variation from 100%. Quantitative analysis of; K-Feldspar (**B**), Na-Feldspar (**C**), Illite/Muscovite (**D**), Smectite+mixed layer I/S (**E**), Kaolinite (**F**) and Chlorite (**G**). Total clay minerals (**H**). Percentage of the total clay minerals composed of Illite/Muscovite (**I**), Smectite +I/S (**J**), Kaolinite (**K**) and Chlorite (**L**).

QXRD samples range from fine grained shales through to coarser grained silts. As a result, we see large heterogeneity between individual samples in a single well. For example in well 211/27-A2 quartz abundance alone varies from 6.1 to 42.0 wt%. This heterogeneity must be considered when assessing the effect of temperature on mineralogical processes.

K-feldspar may undergo low temperature dissolution during meteoric flushing in shallow burial (Hurst and Irwin, 1982). The lowest temperature sample analysed in the Ness suite is 109^{o}C. It is therefore difficult ascertain the extent of low temperature K-feldspar dissolution in these samples. K-feldspar is also important as it can also produce silica when reacting with kaolinite to produce illite (Bjørlykke, 1998), when it undergoes albitisation (Saigal et al., 1988), and it is may also act as a source of potassium in the illite-smectite transformation (van de Kamp, 2008). K-feldspar abundance ranges from 0 to 13 wt%, the data is largely scattered, but only minor K-feldspar remains at 167^{o}C (Figure 3.43B).

Albite or sodium rich feldspar is present in similar proportions to K-feldspar ranging from 0 to 9 wt% (Figure 3.43C). Again, data is scattered within and between individual wells, therefore it is difficult to quantify the extent of albitisation that may be occurring.

Clay minerals such as kaolinite, illite and smectite may also react directly or indirectly with K-feldspar to produce silica. In this study the volume of total clay minerals (Figure 3.43H) was determined as the combined abundance of illite/muscovite (Figure 3.43D), montmorillonite (smectite) and illite/smectite (Figure 3.43E), kaolinite (Figure 3.43F) as well as minor chlorite (Figure 3.43G). These Ness Formation samples contain between 40 and 90 wt% clay minerals, total average clay mineral content increases slightly in the hotter samples. For this reason it important to examine the abundance of each clay mineral in relation not only to the total rock but also as a fraction of the total clay (Figure 3.43 I to L). The most abundant clay minerals present are illite/muscovite and

kaolinite. Illite and Muscovite are grouped together because of the difficult resolving the differenced in d-spacings of the two minerals.

Kaolinite, which may react with K-feldspar to form illite and silica, is present in all wells. Quantities range from 39.5 wt% to 5.3 wt%. When directly examining possible trends between samples, the data appears fairly scattered (Figure 3.43F). However, when examining the total clay fraction (Figure 3.43K) there is a clear reduction in kaolinite quantities with increased burial temperatures, with the exception of well 211/11a-3.

These silt samples are rich in illite/muscovite. Abundances range from 20.8 wt% to 69.7 wt% (Figure 3.43D). Overall, illite quantities increase with increased temperature. Smectite, as a result of temperature increases, converts into illite via mixed layer illite–smectite (I/S). The maximum quantity of smectite + I/S is 19.6 wt%. At higher burial temperatures (>135^{o}C) little smectite or I/S is measured (Figure 3.43E and J).

3.8.2. Analysis of the Ness Shale 2 µm Clay Fine Fraction

The percentage illite and expandables (smectite) within in the I/S mixed layer was determined within the <2 µm clay fraction. Full results are given in Table 3.10, diffractograms are shown in Appendix 7.

Bulk QXRD analysis has shown the maximum smectite plus I/S in the total rock is 19-20 wt% (Figure 3.43E). The amount of illite measured in this mixed layer I/S increases with increased maximum burial temperature (Figure 3.44B). Furthermore, at 109^{o}C the I/S is already fairly mature and contains in excess of 60% illite, by 133^{o}C this increases to >90%. No further increases are seen between 133 and 167^{o}C. Overall, these <2 µm XRD experiments indicate that no more than 40% of the 19% total I/S is smectite (Figure 3.44B).

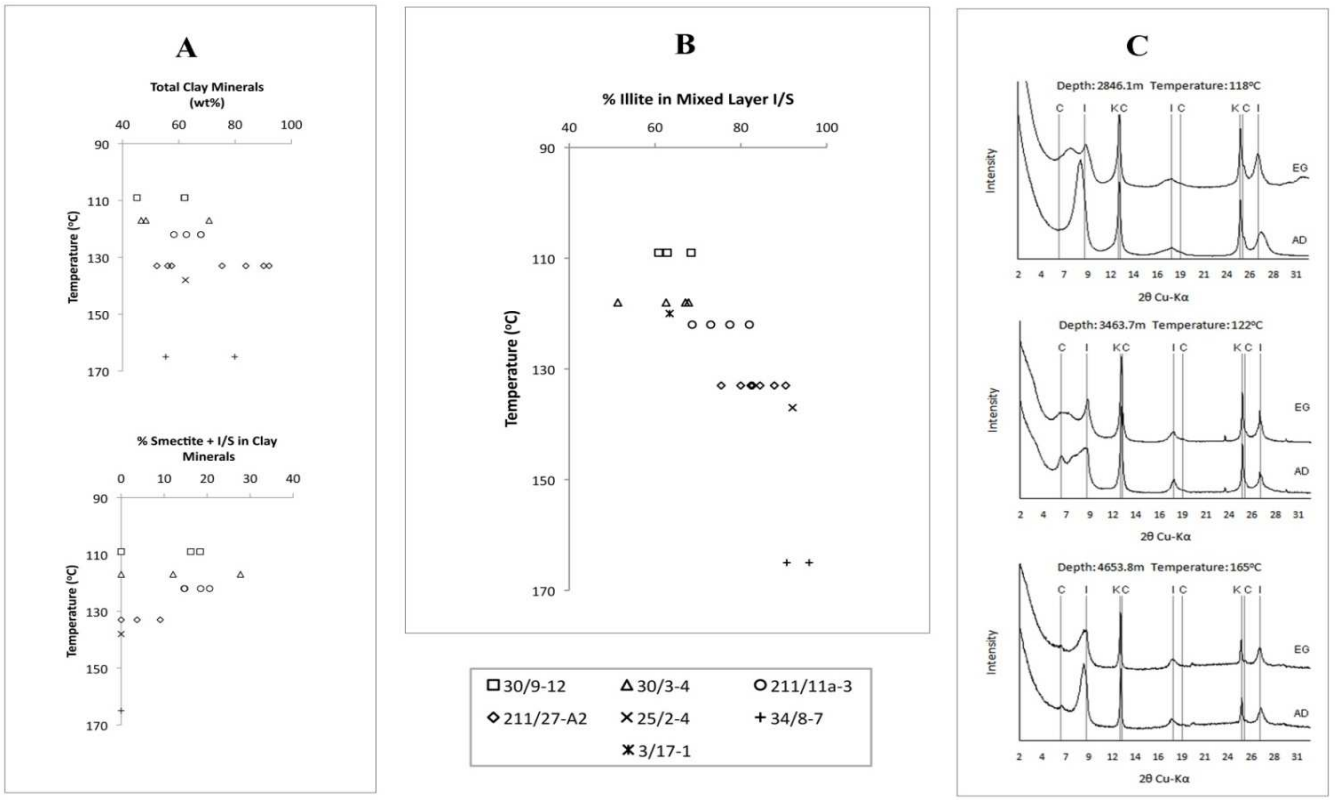

Figure 3.44 X-Ray diffraction analysis of the expandable clay fraction in the Ness Formation. **(A)** Bulk XRD analysis of Total clay and Smectite+I/S. **(B)** <2 µm clay fraction analysis of the percentage Illite within mixed layer I/S. **(C)** Diffractograms, showing Air Dried (AD) and Ethylene Glycolated (EG) treatments of the <2 µm clay fraction.

Depth (m)	Temperature (^{o}C)	001/002	002/003	%I in I/S	%EXP
2638.4	109	9.3	5.3	62.8	37.2
2638.4	109	9.3	5.3	60.9	39.1
2673.7	109	9.4	5.3	68.4	31.6
2831.8	118	9.3	5.3	67.1	32.9
2831.8	118	9.3	5.3	62.6	37.4
2845.8	118	9.4	5.3	67.8	32.2
2846.1	118	9.1	5.4	51.3	48.7
3322.0	120	9.3	5.3	63.4	36.6
3419.9	122	9.5	5.2	73.0	27.0
3463.0	122	9.6	5.2	82.0	18.0
3488.7	122	9.6	5.2	77.4	22.6
3493.0	122	9.4	5.3	68.7	31.3
3818.0	137	9.8	5.1	92.0	8.0
4311.0	133	9.7	5.2	82.3	17.7
4311.1	133	9.5	5.2	75.4	24.6
4319.0	133	10.0	5.2	82.7	17.3
4319.0	133	9.7	5.2	84.5	15.5
4319.0	133	9.6	5.2	80.0	20.0
4337.0	133	9.8	5.1	90.5	9.5
4342.5	133	9.7	5.2	87.8	12.2
4653.8	167	9.7	5.1	90.7	9.3
4655.9	167	9.8	5.1	95.9	4.1

Table 3.10 001/002 and 002/003 I/S reflection of <2 µm glycolated fine fraction in the Ness Formation. Illite (I) and expandable (EXP) percentages determined using the method described by Moore and Reynolds (1997).

3.9. Discussion

Petrographic quantification carried out in this study illustrates an increase in the volume of quartz cement in higher temperature Ness samples (Figure 3.22). These general findings are in agreement with petrographic measurements made in previous sandstone studies (Schmoker and Gautier, 1988; McBride, 1989; Giles, 1992; Walderhaug, 1994b; Primmer et al., 1997; Giles et al., 2000). However, there is a degree of scatter in the volume of quartz cement recorded at each temperature interval in these Ness samples. It is possible this scatter is the result of the mixed mineralogy and grain size of the samples analysed in this study (Table 3.3).

The sands, silts and shale samples selected in this study have all been buried above 109^{o}C. It is commonly excepted that quartz cementation commences above 80^{o}C in reservoir sandstones (Walderhaug, 1994a; Walderhaug, 1994b; Walderhaug, 1996; Wilkinson et al., 1998; Girard et al., 2001; Ajdukiewicz and Lander, 2010). Therefore, the petrographic observations made in this study were unable to further constrain either the timing of the onset or rate of quartz cementation. To constrain the timing of quartz cementation further oxygen isotopes have been used; measured $\delta^{18}O_{(cement)}$ is a dual function of precipitation temperature and the isotopic composition of the formation fluids ($\delta^{18}O_{(water)}$). However, without detailed fluid inclusion data that could arguably constrain either the early temperature or salinity conditions we are restricted to evaluating the cementation of the Brent Ness Formation using end member conditions. These conditions are:

- Jurassic Brent Marine waters, $\delta^{18}O_{(water)}$ = -1‰ (Haszeldine et al., 1992)
- Jurassic Brent Meteoric waters, $\delta^{18}O_{(water)}$ = -7‰ (Girard et al., 2001)

It is also possible to use $\delta^{18}O_{(water)}$ measurements from other Brent sandstones as a guide to the evolution of formation waters during diagenesis (Figure 3.45), this data has been taken from Egeberg and Aagaard (1989), Aplin and Warren (1994), and Warren and Smalley (1994). Furthermore, temperatures may be restricted to likely depositional conditions ~10^{o}C and by the maximum burial conditions in the three wells, 118, 122 and 133^{o}C.

Using Clayton et al.'s (1972) fractionation equation (Equation 2.8) it is possible to constrain the conditions (temperature and $\delta^{18}O_{(water)}$) under which the cement analysed from these Ness samples precipitated (Figure 3.45).

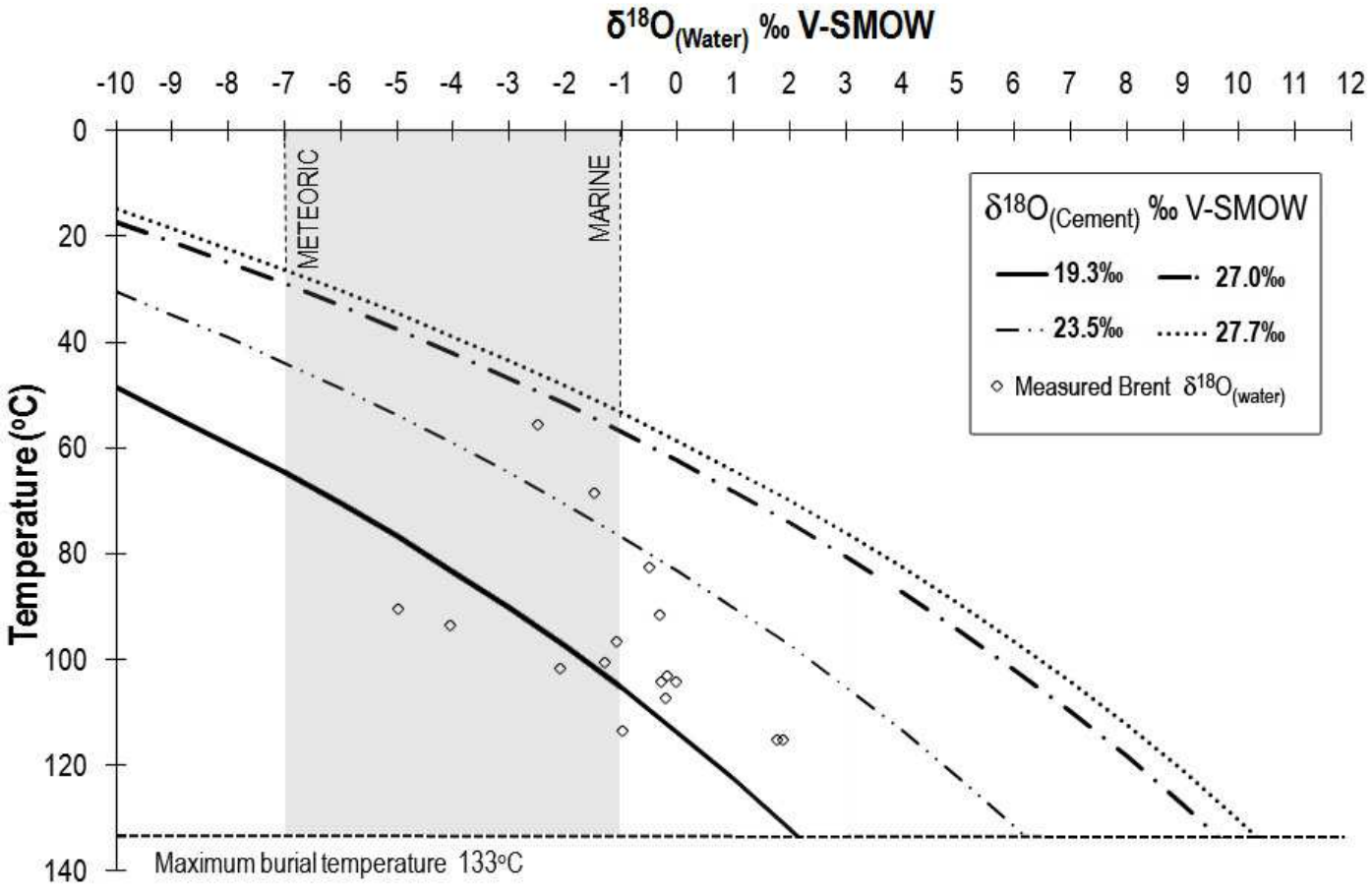

Figure 3.45 Plot of $\delta^{18}O_{(water)}$ in equilibrium with $\delta^{18}O_{(cement)}$ = +27.7‰, +27.0‰, +23.5‰ and +19.3‰ as a function of temperature (Clayton et al., 1972). $\delta^{18}O_{(cement)}$ measurements made across North Sea wells 30/3-4, 211/11a-3 and 211/27-A2.

The more positive $\delta^{18}O_{(cement)}$ values recorded in this study represent the oldest cement. In both the 2 μm and 12 μm studies the maximum $\delta^{18}O_{(cement)}$ = 27.7‰. Predictive models used in reservoir quality assessment such as Touchstone and Exemplar suggest that quartz cementation begins at 80°C (Walderhaug, 1996; Lander and Walderhaug, 1999; Ajdukiewicz and Lander, 2010). Precipitation of quartz where $\delta^{18}O_{(cement)}$ =+27.7‰ would require a water of +3.6‰ at 80°C. Although we do not have specific measurements of $\delta^{18}O_{(water)}$ in any of the wells studied here, this value is unusual positive in comparison to other North Sea water at this temperature (Egeberg and Aagaard, 1989; Aplin and Warren, 1994; Warren and Smalley, 1994). Furthermore, if quartz cementation initiates under these conditions (80°C and $\delta^{18}O_{(water)}$ = +3.6‰) and continues to maximum burial temperatures, the $\delta^{18}O_{(water)}$ must evolve towards a lighter composition during diagenesis in all wells (Figure 3.45). This scenario is geologically unlikely since the oxygen isotopic composition of formation waters generally evolve to more positive values with burial as a result of water-rock reactions (e.g. Aplin and Warren, 1994). It is therefore unlikely that cementation begins at 80°C in these studied samples.

The 80°C quartz cementation threshold is made largely based on homogenization temperature measurements taken from fluid inclusions (Walderhaug, 1994a; Walderhaug, 1994b). These inclusions form as imperfections become trapped as the crystal grows. It is reasonable to assume therefore that fluid inclusions only time the point when an inclusion becomes sealed; a temperature which must be higher than the start of cementation. Some authors report low temperature precipitation below 80°C (Vagle et al., 1994; Kraishan et al., 2000; Kelly et al., 2007), indeed Walderhaug (1994b) reports some homogenization temperature <75°C. If the Walderhaug (1996) cementation model is changed to commence quartz precipitation at around 60°C, a temperature close to that recorded in Vagle's (1994) study, then cementation would initiate in waters where $\delta^{18}O_{(water)}$ = +0.3‰ (Figure 3.45), geologically this is a more realistic proposition. However waters of +0.3‰ at 60°C are still more positive than the North Sea Brent observations (Egeberg and Aagaard, 1989; Warren and Smalley, 1994)

It is more probable that this isotopic heavier precipitate close to the detrital – overgrowth boundary relates to an early onset of quartz cementation (<80^{o}C)

Six 2 μm spots taken within the initial 8% of the cement and possibly relating to a darker luminescing rind on grain 2 (Figure 3.38b) have $\delta^{18}O_{(cement)}$ values of +24.5‰ to +27.7‰, values which were also hinted at by the 12 μm data. Whist it is clear that the two spots at +27.0‰ and +27.7‰ are taken from this darker region it is impossible to be certain if the two data points between +24.5‰ and +25.2‰ represent a mixed analysis of two isotopically distinct zones – implying two phases of cementation – or represent part of a single continuous cementation history which nevertheless generated two CL zones.

It may be possible that the initial rind has formed in Jurassic meteoric waters (-7‰) soon after deposition. In this case precipitation would have occurred at temperatures around 30^{o}C (Figure 3.45). At such low temperatures precipitation kinetics would be extremely slow (Williams and Crerar, 1985b; Bjørlykke and Egeberg, 1993). However, the thermal history generated for these samples (Figure 3.8) shows that in all the studied wells the Ness Formation has remained in a temperature window of 20-40^{o}C for up to 60 million years. Calculated precipitation rates (Equation 2.4) required to form this isotopically distinct rind at low temperature over this 60 million year period average 2.2x10^{-21}moles/cm^{2}.s across the three wells. As would be expected this rate is much slower than rates that have previously been calculated for similar sandstones in the North Sea (Walderhaug, 1994b). Similar findings have been recorded by Marchand et al. (2002) working on North Sea Brae sandstones who concluded that a zone of quartz cement had precipitated in meteoric water at temperatures below 60^{o}C.

At low temperatures (20-40^{o}C) one potential silica source is the dissolutions of K-feldspar in meteoric waters (Equation 2.6) as described by Hurst and Irwin (1982), Glasmann (1992), Bjørlykke and Egeberg (1993) and Worden and Morad (2000).

Indeed, Kraishan et al. (2000) has shown that low temperature quartz cement may be enriched with the trace metal aluminium as a consequence of being derived from early dissolution of K-feldspar. Low temperature (<50^{o}C) K- feldspar dissolution rates calculated by Helgeson (1984) are much higher than the above calculated quartz precipitation rates; the dissolution of feldspar is therefore not a rate limiting process.

The dissolution of K-feldspar in meteoric water will form kaolinite as well as silica (Equation 1.2). The isotopic composition of this kaolinite can be used to estimate the temperature of K-feldspar dissolution. Although no isotopic analysis of kaolinite was performed in this study there are a number of studies that document the characteristics of kaolinite in similar Brent sandstones (Glasmann et al., 1989a; Glasmann, 1992; Haszeldine et al., 1992; Macaulay et al., 1993; Osborne and Haszeldine, 1993; Wilkinson et al., 1998; Wilkinson et al., 2001; Girard et al., 2002; Wilkinson et al., 2006). In Haszeldine's 1992 study, followed up by Wilkinson (2006), two types of kaolinite were observed, (1) early vermicular type and (2) the higher temperature kaolin polymorph that exhibits a blocky morphology. Isotopic measurements in the early formed vermicular types demonstrate $\delta^{18}O$ = +16-18‰, whereas in the blocky type $\delta^{18}O$ = +12-15‰. Using Land and Dutton's (1978) kaolinite- water equilibrium equation it is possible to estimate the temperature of kaolinite formation (Figure 3.46). These estimates indicate that precipitation of kaolinite in the Brent takes place around 30 to 50^{o}C. This temperature range supports the theory that low temperature dissolution of feldspars is occurring (Equation 2.26).

Quantitatively, calculations (Table 1.1) indicate that for each K-feldspar grain that undergoes complete dissolution, 43.2% of its weight is released as silica. To precipitate 2.2 %bv cement, the total rock volume made up by this thin rind, around 5 %bv K-feldspar must react (Table 3.11). This would also result in the precipitation of around 3 %bv kaolinite.

As in Wilkinson's (2006) study the dissolution of feldspars is widespread throughout these North Sea sands (Figure 3.9 and Figure 3.11) and all samples are rich in kaolinite. Furthermore, the formation of kaolinite appears to predate the precipitation of quartz cement (Figure 3.16). Without carrying out a detailed isotopic study on the kaolinite observed in this study we cannot be sure of its precipitation temperature. However, owing to the analogous nature of the samples in Wilkinson's (2006) investigation to the samples here it is extremely likely the kaolinite observed in these samples precipitated under similar conditions, i.e. 30 to 50^{o}C. This temperature would sit comfortably within the early cementation window that is suggested by the 2 μm high precision isotopic analyses. However, for the Equation 1.2 to continue towards the right large quantities of water are required to supply protons and remove cations. Bjørlykke (1998) calculated that a flow of 10^3 -10^4 m^3/m^2 is required to dissolve significant quantities of K-feldspar. This flow rate is certainly attainable in a humid environment, however such a flow is also likely to remove any silica away from the sandstone and thus prevent quartz precipitation (Hurst and Irwin, 1982; Bjørlykke and Egeberg, 1993; Lanson et al., 2002).

A second low temperature possibility is that this initial cement has formed not in meteoric conditions but from Jurassic sea water ($\delta^{18}O_{(water)}$ = -1‰) at temperatures around 50^{o}C. This mechanism was realised by Mackenzie and Rees (1971) when they successfully precipitated small amounts of quartz at low temperatures from sea waters supersaturated with quartz.

A further possibility is that this heavy isotopic rind may also represent early microquartz, perhaps resulting from the recrystallisation of biogenic silica (Jahren and Ramm, 2000; Goldstein and Rossi, 2002; Haddad et al., 2006). Biogenic silica is less thermodynamically stable and more soluble than quartz. It has been shown that at low temperatures cristobalite will transform to quartz given enough time; Mizutani (1970) calculated that at 50^{o}C 90% of cristobalite will transform to quartz over a 10 million year period. The thermal histories of these samples would allow time for such

recrystallisation to occur. However, the resulting cement is likely to take the form of a chalcedonic pore filling, microcrystalline grain coatings and mesocrystalline quartz overgrowths (Vagle et al., 1994; Hendry and Trewin, 1995; Haddad et al., 2006; Weibel et al., 2010). There is no textural evidence of microquartz in these samples.

Low temperature stylolitisation may also release silica below 50^{o}C. Although normally associated with deeper burial (Walderhaug, 1996) Bjørkum's (1996) findings suggest stylolitisation can occur at pressures as low as 10 bar; equivalent to 100m overburden (<25^{o}C) with quartz dissolution enhanced at quartz - illite or quartz - mica interfaces (Bjørkum, 1996; Greene et al., 2009). However, stylolitisation may be inhibited in these kaolinite rich samples (Walderhaug et al., 2006). Quartz dissolution may also occur where extensive grain fracturing has occurred (Chuhan et al., 2001; Makowitz and Milliken, 2003; Makowitz et al., 2006). The fracturing of larger grains will also increase the quartz surface area which will increase initial quartz precipitation rates (Walderhaug, 1996). Although grain fracturing is observed in these Ness samples it is limited to the quartz rich sandstones (e.g. Figure 3.18). Fracturing in silt or clay rich samples is less common as the abundant clay materials result in a ductile psedomatrix.

Although these SIMS measurements alone cannot restrict the source of silica it is likely this cement has formed within a window normally associated with mechanical compaction (<60^{o}C). Porosity models tend to assume that during low temperatures shallow burial (<2km) increasing effective stress caused by sediment loading is the major physical force driving the reduction in porosity of sandstones. Indeed it has been shown that mechanical compaction reduces porosity from surface depositional values of 40-50% to typical values of 25-32% prior to lithification (Houseknecht, 1988; Paxton et al., 2002). At these low temperatures porosity depth trends have proven fairly good at predicting porosity (Ajdukiewicz and Lander, 2010). Porosity loss at higher temperatures is thought to be controlled by chemical processes such as cementation.

The high precision SIMS measurements indicate that cementation is occurring within this ‘compaction zone’. The effect any early cement may have on sediment compaction is difficult to quantify. Less than 8% of the total overgrowth is made up of this thin isotopically heavy rind. However, even a small amount of cement may act to restrict compaction and hold porosities open. One would therefore expect porosities to be high prior to the onset of chemical compaction (~80^{o}C), however minus cement porosities calculated for these samples do not appear to be unusually high (4-33 %bv). Early cement may also act to increase the surface area available for future cementation by holding grains apart. Sandstones in which significant meteoric flushing of K-feldspar has occurred could therefore represent good reservoir material.

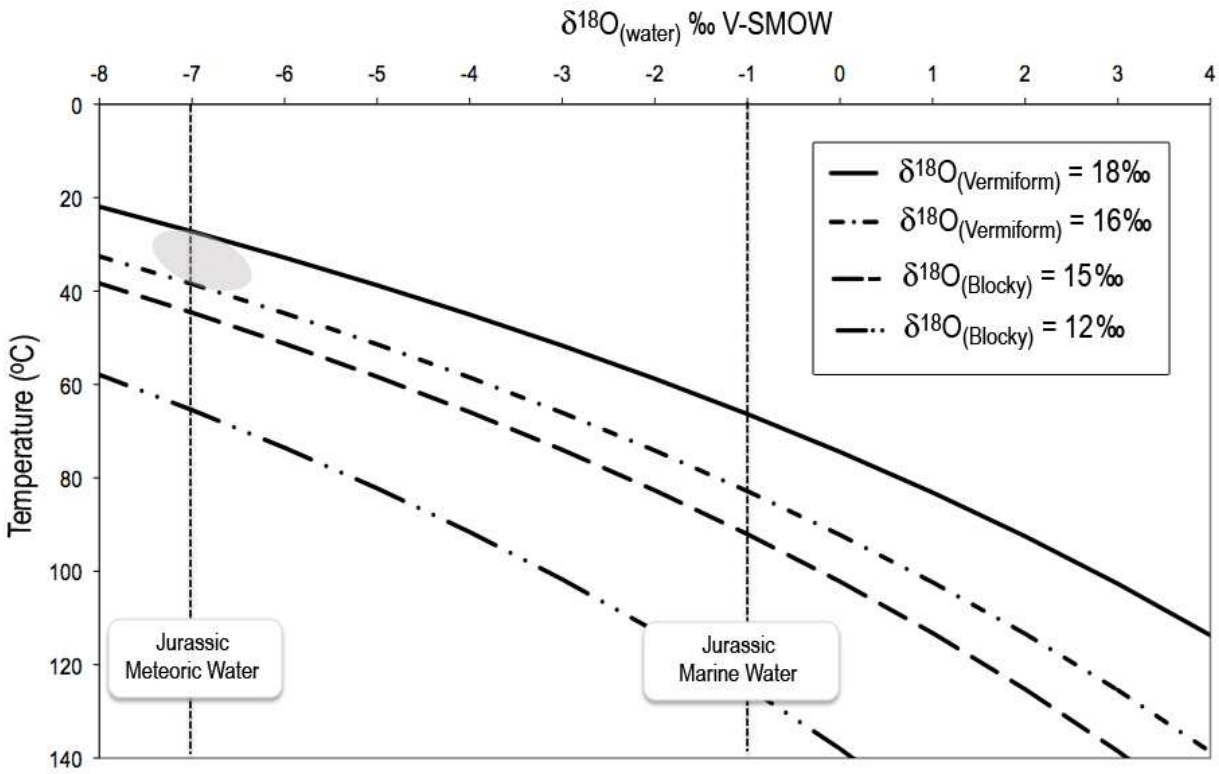

Figure 3.46 Plot of $\delta^{18}O_{(water)}$ in equilibrium with vermiform and blocky kaolinite ($\delta^{18}O_{(Vermiform)}$ = 16‰ to 18‰, $\delta^{18}O_{(Blocky)}$ =12‰ to 15‰) as a function of temperature (Land and Dutton, 1978)**.** The shaded grey area indicates the most likely formation conditions of early kaolinite, Wilkinson (2006) concluded this formed during meteoric flushing.

The distinct isotopically heavier rind observed in NS19 forms around 8% of the total overgrowth, further into the overgrowth beyond this rind the amount of variation in $\delta^{18}O_{(cement)}$ observed decreases relative to the distance across the overgrowth. The bulk of the cement from the three North Sea wells has $\delta^{18}O_{(cement)}$ between +23.5 and +19.3‰ becoming lighter away from the detrital grain.

If we take $\delta^{18}O_{(cement)}$= 23.5‰ (Figure 3.45) to represent first precipitation of the bulk cement (all cement except the thin isotopically distinct rind) then it is likely cementation started at around 65 to 70^{o}C. This value assumes that waters have evolved in a similar pattern to other Brent measurements, i.e. $\delta^{18}O_{(water)}$ at 65^{o}C = -3 to -2 (Egeberg and Aagaard, 1989; Warren and Smalley, 1994). This would indicate the formation waters were a meteoric/marine mix. This is a likely scenario in a shallow buried deltaic formation. However, without detailed fluid inclusion data this value cannot be constrained any further.

Should cementation continue to current maximum burial temperatures in all the North Sea wells studied then the average precipitation rate is calculated at 1.46x 10^{-20}mol/cm^{2}.s, a rate within the range published in Walderhaug's (1994b) study in which cementation was assumed to have begun at 80^{o}C.

It is impossible to say without doubt if this bulk cement represents a continuation of the early precipitate or if it is a separate episode. However, it is probable that silica is sourced from a separate process. If the bulk cement began to precipitate around 65-70^{o}C as the isotope data indicate it would coincide with silica producing processes such as the formation of stylolites, the illitisation of kaolinite (Lanson et al., 1996; Brosse et al., 2002; Lanson et al., 2002) and smectite (Ehrenberg and Nadeau, 1989; Lanson and Champion, 1991; Awwiller, 1993; Velde and Renac, 1996), the diagenetic formation of chlorite (Bossi, 1972; Hurst, 1985; Chang et al., 1986) as well as the albitisation of K-feldspar (Land and

Milliken, 1981; Boles, 1982b; Saigal et al., 1988; Morad et al., 1990; Glasmann, 1992). With the exception of stylolitisation each of the above process has been observed and quantified in this study within the interlayered shale units of the Ness Formation.

Although, stylolites are believed to be a major internal silica source in reservoir sandstones (Walderhaug, 1996; Taylor et al., 2010) they have not been observed in this study. However, stylolites are commonly reported within the Brent Group (Walderhaug, 1994b; Oelkers et al., 1996; Walderhaug et al., 2000; Walderhaug et al., 2001; Walderhaug and Bjørkum, 2003). It is therefore likely stylolitisation has occurred in these units, but outside the scope of the studied thin sections. Little if any localised grain to grain pressure solution has been observed in these samples. Studies of Brent sandstones in which luminescing microscopy was employed also report minimal detrital grain to grain contact (Walderhaug, 1996).

Thomas et al (1993) and Sibley and Blatt (1976) both reported that a minimum of 30% of cement observed is supplied internally via pressure solution and stylolitisation. SEM analysis of these samples has shown that by bulk volume the maximum quantity of cement observed here is 23%; measured in the clean sands of well 211/27-A2. Should 30% of this 23%bv be internally sourced a further 70% of the cement, equating to around 16% of the bulk sandstone, is sourced from other diagenetic processes occurring externally to the sandstone body.

Composite logs made in these studied wells indicate that the Ness Formation is on average made up of 48% silt or shale material. Bulk and fine fraction XRD was carried out on the shale units in an attempt to quantify their potential to act as silica sources. The following discussion use quantitative X-ray diffraction data acquired from these Ness shale units to

calculate the potential for silica to be produced externally. All calculations assume the Ness Formation is composed of 48% shale and that all mineralogical processes go to completion.

One potential external silica source is the reaction of K-feldspar with kaolinite to form illite (Equation 1.3) (Lanson et al., 1996; Bjørlykke, 1998; Lanson et al., 2002). QXRD analysis of Ness shales carried out in this study shows the presence of K-feldspar up to 133^{o}C but very little at 167^{o}C (Figure 3.43B). It also indicated the increase in illite/muscovite (Figure 3.43D) with increasing temperature. Kaolinite abundance is fairly scattered but volumetrically plenty is present to react 1:1 with K-feldspar in all wells (Figure 3.43F). Using end-member chemical formulae and molecular weights for K-feldspar, kaolinite and silica, with balanced equations; estimated silica yields were calculated (Table 1.1). In total 22% of the total weight of the reactants is released as silica.

QXRD analysis of the Ness Formation shale indicates a maximum of 12.2 wt% K-feldspar and 39.5 wt% kaolinite. At 167^{o}C K-feldspar is no longer present in the Ness shale samples. If we assume the reaction goes completion then 12.2 wt% K-feldspar reacts with 12.2 wt% kaolinite to produce a maximum of 5.5 wt% cement.

Another possible source of silica at increased burial temperatures is the albitisation of K-feldspar (Equation 1.4), a process witnessed throughout the Brent (Saigal et al., 1988; Glasmann, 1992) and these samples (Figure 3.12 and Figure 3.13). The albitisation window in the Brent is thought to close about 160^{o}C (Glasmann, 1992); within the temperature range of the cementation window highlighted by SIMS analysis. Assuming albitisation goes to completion, it is possible to use end-member chemical formulae and molecular weights for K-feldspar and silica, with balanced reactions, to estimate silica yields (Table 1.1). In total 10.0% of the total weight of the reactants is released as silica. This equates to about 5% of the weight of K-feldspar. Using the principles outlined above, 12.2 wt% K-

Feldspar reacting with 15.3 wt% kaolinite could potentially produce a maximum of 2.7 wt% cement (Table 3.11).

Both the albitisation and the formation of illite from K-feldspar have been observed in these samples. However, neither reaction can produce the quantity of cement observed here in the Ness Formation. Furthermore, as both reactions consume K-feldspar, they cannot both react to 100% completion.

Another possible silica source this study's mineralogical investigation illustrates is the transformation of illite to smectite (Equation 1.5). The smectite (montmorillonite)-to-illite transformation in shales as a source of silica for sandstone cement has been extensively studied by Towe (1962); Leder and Park (1986); Boles and Franks (1979); Lynch et al. (1997) and Van de Kamp (2008). It is well understood that smectite alter to less siliceous illite with increasing depth of burial and temperature in sedimentary basins through a number of intermediate mixed layers illite-smectite (I/S) phases (Hower et al., 1976; Nadeau and Bain, 1986; Ehrenberg and Nadeau, 1989; Lanson and Champion, 1991; Freed and Peacor, 1992; Velde and Vasseur, 1992; Lynch et al., 1997).

The I/S reaction is thought to occur over a temperature window from 80^{o}C to 140^{o}C (Hower et al., 1976; Freed and Peacor, 1989; Velde and Vasseur, 1992; Matthews et al., 1994; Velde and Renac, 1996). The majority of smectite and the mixed-layer I/S in this study was observed in the silty shale units of the sampled Ness. QXRD measurements (Figure 3.43E) show a maximum of 20% of these silts are made up of I/S. The <2 μm fine fraction XRD analysis has shown the I/S is fairly mature and contains >65% illite (Figure 3.44). However, in this study it has only been possible to observe the I/S reaction from 109^{o}C. Using the principles above it is possible to calculate the total amount of silica produce by the transformation of the remaining smectite. If we take the reaction to

completion then less that 1.5 wt% cement is produced across the total Ness Formation (Table 3.11). A further 2 wt% silica can be generated (Table 3.11) if we assume that between 80°C and 109°C a further 65% smectite is converted to illite.

A final possible silica producing reaction is the conversion of smectite to chlorite. Chlorite has been observed during bulk QXRD analysis, up to 12 wt%. However it is difficult to know the provenance of this material, diagenetic or detrital. If the chlorite is diagenetic it is likely it is present in the <2 µm fraction. Treatment of the <2 µm fraction to 550°C does show a trace chlorite component (Appendix 7). The chloritisation of smectite will occur if the smectite is Mg–Fe-rich (Chang et al., 1986). However, where K-, Ca- and Na-rich smectites are present with abundant K-feldspar smectite will tend to undergo illitisation (Bossi, 1972; Hillier, 1994; Humphreys et al., 1994; Aagaard et al., 2000). A small fraction of chloritisation has been observed in these samples but again only minimal silica can be produced.

In total, silica producing reactions that have been measured in these Ness shales can account for a maximum of 9.0%bv (Table 3.11). This value assume that all K-feldspar is consumed via the illitization of kaolinite rather than the less efficient abitisation mechanism. Furthermore, it is also assumed that all reactions go to 100% completion and that silica is mobile and can enter adjoining sandstone units. The mobility of silica is supported by the low quartz cement volumes in silt rich samples of the Ness, e.g. NS12 (167°C), where less than 2 %bv quartz cement is observed (Figure 3.22). However, as much as 20 %bv quartz cement is recorded in NS19 and NS20, these volumes of quartz cement cannot be accounted for from external mineralogical reactions alone (Table 3.11); it is therefore likely that the majority of cement is internally sourced.

Equation	Silica Released per unit mass of reactants	Reactants (wt%)				Maximum Silica Released (%bv)
		K-Feldspar	Kaolinite	Smectite	Total Reactants (wt%)	
1.2	0.43	5.0	-	-	5.0	2.2
1.3	0.22	12.2	12.2	-	24.4	5.5
1.4	0.10	12.2	15.3	-	27.5	2.7
1.5 (100%)	0.20	N/A	-	18.0*	18.0	3.5
1.5 (109-133^{o}C)	0.20	N/A	-	7.0*	7.0	1.4

Table 3.11 Calculated silica yields produced from silicate reactions occurring within the Ness Formation. Reactants highlighted in yellow represent limiting minerals. *Solid state reaction involving single reactant. N.B As K-feldspar is a reactant in both reaction 1.3 and 1.4 it is impossible for both reactions to release their maximum silica yields.

For silica formed within external shale units to precipitate in adjacent sands a suitable transport mechanism must exist. Aplin (1994) reviews 4 potential mechanisms for silica transportation; meteoric recharge; compactional driven water; convectional waters; diffusion. Many previous studies rule out the possibility of compaction driven transport due to a lack of water (Bjørlykke and Egeberg, 1993; Aplin and Warren, 1994). Isotopic measurements made in this study indicate formation waters are too isotopically heavy to be driven by any meteoric recharge. Furthermore, any large scale convection and recycling of waters would likely cause isotopic homogeneity at the reservoir scale. The range of $\delta^{18}O_{(cement)}$ measurements taken in across the Ness indicate a variable $\delta^{18}O_{(water)}$. Therefore, it is unlikely large scale convection transported silica in this system. However, it may be possible smaller convection cells are set up throughout the reservoir system during burial (Bjørlykke and Egeberg, 1993; Oelkers et al., 2000). The final possible mechanism of silica transport is diffusion. Diffusion can occur where any concentration gradient is built up. Mineralogical analysis of the Ness Formation shale indicates the occurrence of a number of silica producing reactions. The production of silica during diagenesis can potentially set up the required concentration gradient required for diffusion to occur. Furthermore, chemical examinations of shales from around the world, including the North Sea basin (van de Kamp, 2008), indicate that the Si/Al ratio in shales declines during diagenesis. This decline points towards silica migration away from shales during burial.

However, cementation within silt units, such as NS6 and NS12 (Figure 3.20), indicate that silica may be partly immobile. These observations are contrary to the common thinking in which it is believed the general absence of quartz veins or quartz lenses in clay-rich rocks signifies that silica is mobilized away from shale units (van de Kamp, 2008). Though, more recent studies including Peltonen et al. (2008) do document micro-cements in North Sea shale.

3.10. Conclusion

This investigation has illustrated that quartz cement begins to form below 50^{o}C in mixed meteoric/marine waters. However at these low diagenetic temperatures cementation rates are slow and only a small volume of cement precipitates. These findings are contrary to the standard threshold temperature of 80^{o}C often used in current quartz cementation models. It is also possible this early cement may influence the mechanical compaction of the sandstone.

Later in the diagenetic process a further 90% of the total cement forms above 60-80^{o}C and continues to precipitate to current burial temperatures. These conditions are in closer agreement with the current thinking and thus help to validate existing cementation models. However, it is unclear whether or not the two isotopically distinct regions represent separate growth episodes or if cementation is continuous.

Internally, within the sandstones of the Ness Formation, silica is sourced from reactions involving the dissolution and albitisation of feldspars. It is also likely some stylolites are present in the sampled unit however these were not observed in thin section. Externally, analysis of adjacent silt/shale material indicates that further albitisation is occurring as well as the illitisation of kaolinite and smectite. Neither the internal or external silica sources quantified in this study can account for the volume of cement observed (~20 %bv) in these Ness samples.

Calculations indicate heterogeneity in $\delta^{18}O_{(water)}$ across the region. This would rule out silica transport by large scale water movement (convection or recycling). It is therefore likely that any potential movement of silica between the shale and sandstones of the Ness occurs by diffusion.

4. Quartz Cementation and Diagenesis in the Wilcox Group

This chapter describes the diagenesis and quartz cementation in the early Eocene Texas Wilcox Group. By combining mineralogical and isotopic analysis with well defined time-temperature histories this study aimed to constrain the history of quartz cementation in the Wilcox sandstone.

4.1. Introduction to the Wilcox Group

Deposited in the late Palaeocene and early Eocene, the Wilcox Group is composed of a series of sands with interlayer silts and shales that represent the first major input of sediment into the southern Texas Gulf of Mexico area.

The Wilcox has been extensively studied by Fisher and McGowen, (1969); Boles and Franks, (1979); Fisher and Land, (1986b); Land and Fisher, (1987); Land et al., (1987); Tempel and Harrison, (2000), and Dutton and Loucks (2010). On land the Wilcox group currently lies at burial temperatures ranging from 25^{o}C to 210^{o}C, the only known uplifting event to have affected the Wilcox occurred in the North of Texas in Leon County (Fisher and Land, 1986b; Day-Stirrat et al., 2010; Dutton and Loucks, 2010). From Leon County to the current day shoreline, maximum burial temperatures increase (Dutton and Loucks, 2010). This is in response to moving from what represented a shallow fluvial tidal flat down onto a deep frontal fan complex (Fisher and Land, 1986b; Dutton and Loucks, 2010).

Throughout the depositional process all sediment is thought to be sourced from the Laramide uplands/Rocky Mountain area. This fixed sediment source restricts the mineralogy observed across the Wilcox group (Dutton and Loucks, 2010). Typical sandstones of the Wilcox Group, classified using the scheme of Folk (1965), range from quartzose lithic arkoses to feldspathic litharenites (Dutton and Loucks, 2010). Hotter samples from Harris and Brazonia counties can contain increased rock fragments as they have undergone less reworking during transportation and deposition (Dutton and Loucks, 2010).

Onshore, the Wilcox group has been producing oil and gas for a number of years. Recent studies highlight the possibilities for the Wilcox to produce from deep subsea areas in the Gulf of Mexico region (Kim and Fisher, 1999; Dutton and Loucks, 2010). However, drilling in these deep-sea regions is expensive and risky. It is therefore important to fully understand the development of reservoir quality and diagenetic

processes that may be occurring in the Wilcox prior to drilling. Onshore the Wilcox group is subject to higher geothermal gradients than offshore and so makes an ideal material to study any diagenetic processes that may be occurring in potential deep sea reservoir.

In previous diagenetic studies of the Wilcox, volumetrically significant amounts of authigenic quartz, kaolinite, calcite, ankerite and albite have been recorded (Fisher and Land, 1986b; Land and Fisher, 1987; Dutton and Loucks, 2010). Paragenesis of the Wilcox sandstones has been described in many studies (e.g. Boles, 1978; Boles and Franks, 1979; Boles, 1982b; Franks and Forester, 1984; Fisher and Land, 1986b; Land et al., 1987). To date, the established general paragenetic sequence begins with quartz cement developing early in the burial history. Kaolinite cement follows quartz cementation, but predates calcite. This is summarised in Figure 4.1, taken from Fisher and Land (1986b). However, due to the lack of high precision isotopic investigations the timing of quartz cementation in the Wilcox group is widely disputed.

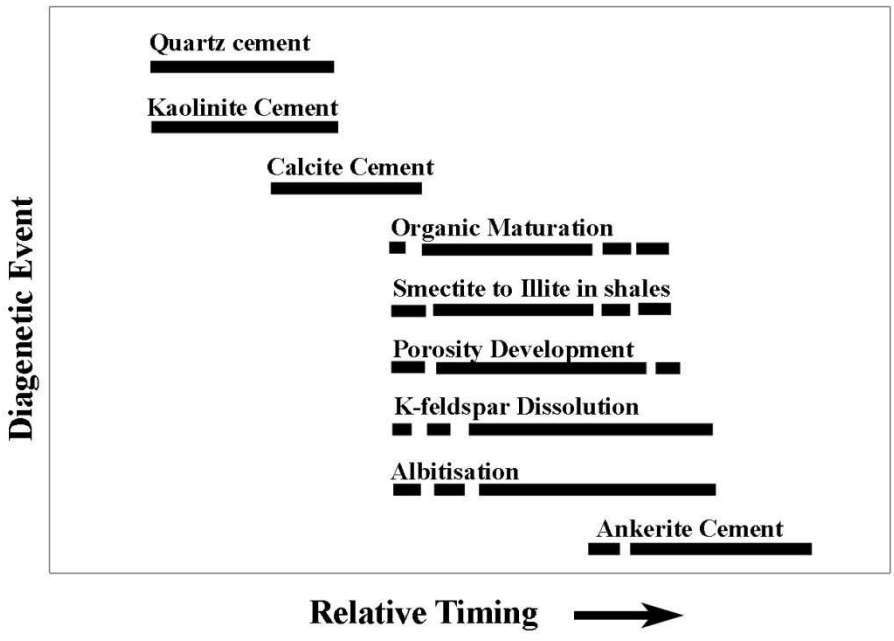

Figure 4.1 Paragenesis in the Wilcox sandstone in southern Texas (Fisher and Land, 1986b)

4.2. The Wilcox Group Study: Aims and Objectives

The specific aims of the Wilcox Study were twofold:

1. To constrain the onset of quartz cementation and resolve quartz cementation histories in the Wilcox sandstone.
2. To quantitatively evaluate potential silica sources internally within reservoir sands as well as externally in adjoining shale units.

The full objectives of this investigation were to:

- Quantify quartz cement in sandstones from a wide range of temperatures from the Wilcox Group.
- Constrain quartz cementation histories through
    - High precision isotopic analysis of quartz cements
    - Petrographic quantification of quartz cement
    - Time- temperature history modelling
- Constrain potential silica sources through
    - Quantitative petrographic examination of internal silica sources
    - Quantification of mineralogical changes in adjoining shales
- Validate current quartz cementation modelling theory

4.3. Sample Selection

Samples from the Wilcox group were selected from five wells across five counties of Texas, USA (Figure 4.2). Similar samples were selected from the same wells in studies by Dutton and Loucks (2010) and Day-Stirrat et al. (2010). From each well a series of sandstones and mudstones were selected. A description of these samples is given in Table 4.1 along with a summary of the analytical strategy. Samples were specifically selected from these wells as they represent the range of burial temperatures in which the majority of quartz cement is known to precipitate (Land and Fisher, 1987; Walderhaug, 1996; Primmer et al., 1997; Giles et al., 2000; Dutton and Loucks, 2010). This temperature range also covers a window in which many silica producing reactions are known to occur within the Wilcox sandstones (Land and Fisher, 1987; Dutton and Loucks, 2010) as well as in many other sandstones across the world (Glasmann, 1992; Bjørlykke and Egeberg, 1993; Gluyas et al., 2000; Trewin and Fallick, 2000; Kim and Lee, 2004). Furthermore, this temperature range also encompasses the period of burial in which many silica producing reactions occur within shales (Velde and Renac, 1996; Bjørlykke, 1998; Lanson et al., 2002; van de Kamp, 2008) including the Wilcox shale (Boles and Franks, 1979; Williams et al., 2001; Day-Stirrat et al., 2010).

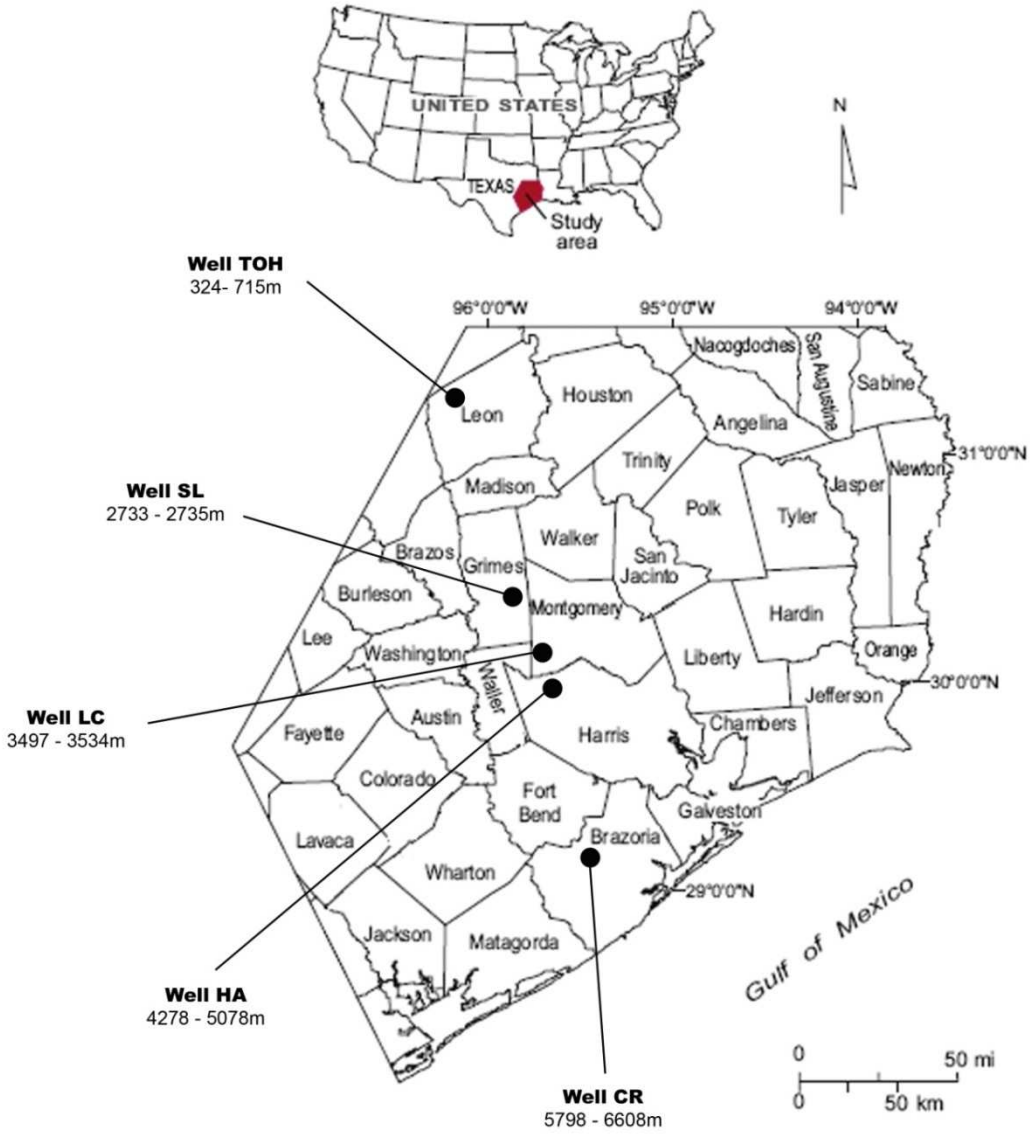

Figure 4.2 Map of Wilcox study area. Samples were selected from 5 wells across Southern Texas, USA.

Sample Overview						Analytical			
Thin Section reference	Well	Depth (m)	Max Burial Temperature (°C)	Description	Genesis 4.92	Image Analysis	QXRD	<2 μm XRD	Ion Microprobe
	TOH	324.3	27	Mst			•	•	
	TOH	411.8	36	Mst			•	•	
	TOH	482.5	45	Mst OM			•		
	TOH	482.8	45	Mst OM			•	•	
	TOH	714.5	53	Mst			•	•	
GOM 6	SL	2733.4	104	Sa	•	•	•		2+12 μm
	SL	2734.2	104	SlSh	•		•	•	
	SL	2734.4	104	SlSh	•		•	•	
	SL	2735.0	104	Sh	•		•	•	
	LC	3496.8	142	SlSh	•		•		
	LC	3500.3	142	SlSh	•		•	•	
	LC	3500.3	142	SlSa	•		•		
	LC	3504.0	143	SlSh	•		•		
	LC	3505.8	143	SlSh	•		•	•	
	LC	3510.5	143	SlSh	•		•		
	LC	3510.5	143	SlSa	•		•		
	LC	3511.6	143	SlSh	•		•		
	LC	3511.6	143	SlSa	•		•		
	LC	3513.4	143	SlSh	•		•		

Sample Overview					Analytical				
Thin Section reference	Well	Depth (m)	Max Burial Temperature (°C)	Description	Genesis 4.92	Image Analysis	QXRD	<2μm XRD	Ion Microprobe
	LC	3513.4	143	SlSa	•		•		
	LC	3518.4	143	SlSh	•		•		
GOM 8	LC	3518.4	143	Sa	•	•	•		12 μm
	LC	3527.1	144	SlSh	•		•	•	
	LC	3527.1	144	SlSa	•		•		
GOM 7	LC	3534.2	144	Sa	•	•	•		
	HA-U	4277.5	167	Sh	•		•	•	
GOM 9	HA-U	4277.6	167	Sa	•	•			
	HA-U	4287.3	168	SlSh	•			•	
	HA-U	4288.1	168	SlSh	•		•		
	HA-U	4288.1	168	SlSa	•		•		
GOM 10	HA-U	4288.5	168	Sa	•	•	•		
	HA-L	4969.8	185	SlSh	•				
	HA-L	4983.2	186	SlSh	•		•	•	
	HA-L	4983.2	186	SlSa	•		•		
	HA-L	4994.5	186	Sh	•		•		
	HA-L	4994.5	186	SlSa	•		•		
	HA-L	4998.4	186	Sh	•		•	•	
	HA-L	4998.4	186	SlSa	•		•		

Sample Overview					Analytical				
Thin Section reference	Well	Depth (m)	Max Burial Temperature (°C)	Description	Genesis 4.92	Image Analysis	QXRD	<2µm XRD	Ion Microprobe
	HA-L	5063.2	187	Sh	•		•	•	
GOM 11	HA-L	5063.3	188	Sa	•	•	•		12 µm
	HA-L	5076.7	188	Sh	•		•	•	
	HA-L	5076.7	188	SlSa	•		•		
	CR-U	5797.9	189	SlSa	•		•		
	CR-U	5813.1	189	ShSl	•		•	•	
	CR-U	5818.3	189	Sh	•		•	•	
	CR-L	6374.9	204	Sh	•		•	•	
	CR-L	6605.9	209	Sh	•		•	•	
	CR-L	6607.1	210	Sh	•		•	•	
	CR-L	6608.4	210	ShSl	•		•	•	
	CR-L	6608.4	210	SlSa	•		•		

Table 4.1 Overview of Wilcox samples and analytical study. Hand specimen abbreviations are: Mst (mudstone, unlithified mud), Sh (shale), Sa (sand), Sl (silt), ShSa (shaley sand), SlSh (silty shale), SlSa (silty sand) Lm (limestone), Ca… (carbonate rich ...), OM (organic rich, coal etc), Lam (laminations). A number of samples are taken direct from sand shale boundaries; these are noted by the suffix A (shale) and B (sand) after the depth measurements. In wells Ha and CR samples were selected from the Upper (U) and Lower (L) Wilcox.

4.4. Time - Temperature Histories

This project deals with samples from five separate wells from onshore Texas (Figure 4.2). Each individual well has a separate burial and thermal history. Temperature plays a key role in on the rate of quartz cementation (Walderhaug, 1994b; Bjørkum, 1996); clay mineral reactions (Hower et al., 1976; Wilkinson et al., 2006) as well as many other diagenetic reactions known to occur in the Wilcox sands (Fisher and Land, 1986b; Dutton and Loucks, 2010). It is therefore important to consider a sample's maximum burial temperature rather than its current burial depth.

In this project Genesis 4.92, a 1-D basin-modelling (maturity model) package was employed to formulate burial history curves for each well. Burial histories provide us with an enhanced understanding of the intricate relationship that has occurred over time between stratigraphy, lithology and erosion. From the formulated burial history curves the maximum maturity of each individual sample was assessed and time vs. temperature relationships produced, allowing us to ascertain the role temperature has on any potential diagenetic processes.

Time – temperature models were supplied by R. Day-Stirrat from the Bureau of Economic Geology, Austin, Texas. The models are constructed using stratigraphic data from well logs and calibrated using down hole temperature measurements (Chapter 2).

Full stratigraphic logs as well as the temperature calibration made during modelling are given in Figure 4.3 to Figure 4.6. Time vs. temperature histories of all wells are compared given in Figure 4.7. In the Harris county well (Figure 4.5) two time temperature curves were constructed, one to represent the Lower Wilcox (HA-L) and one for the Upper Wilcox (HA-U). No thermal modelling was performed on the Leon county well (TOH). However, it is believed the deepest TOH sample was never buried above 53^{o}C (Dutton and Loucks, 2010).

For later cementation modelling each time temperature history has been broken up into a number of linear segments above 80^{o}C. Details of these time-temperature segments are given in Table 4.2.

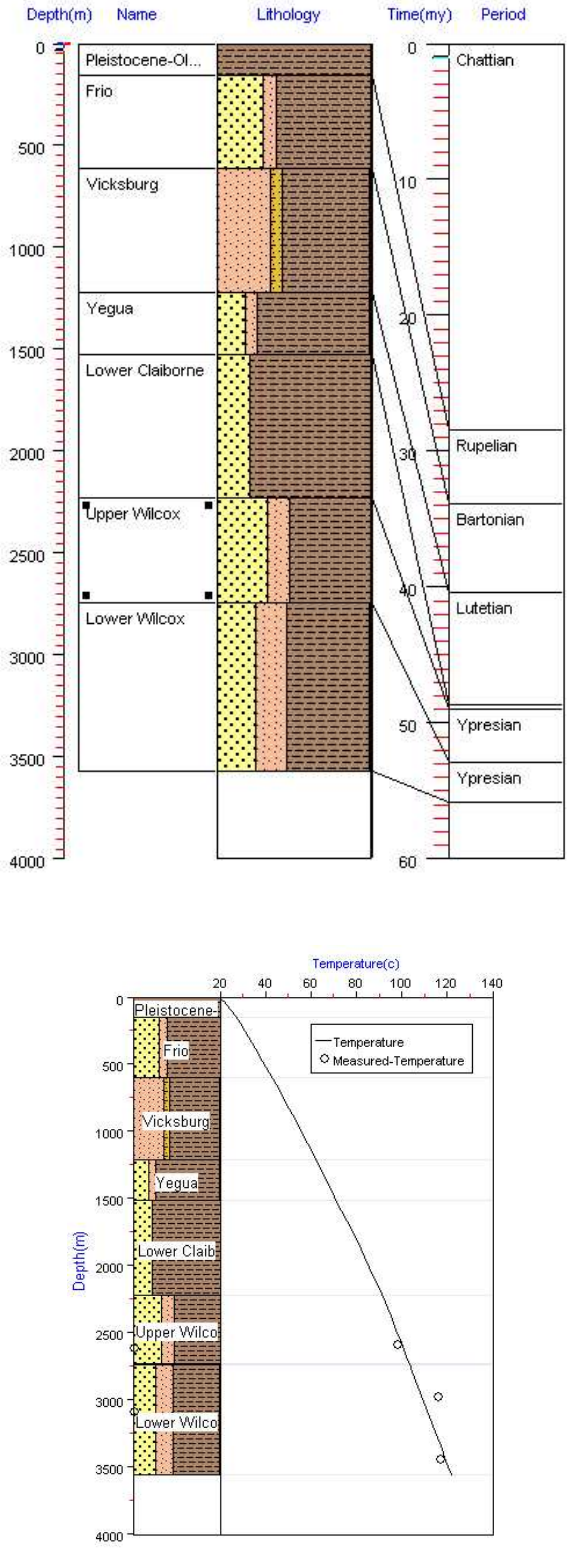

Figure 4.3 Stratigraphic log and temperature calibration constructed for Grimes County Selected Lands (SL). Modelled and measured temperatures show a good fit throughout the Wilcox.

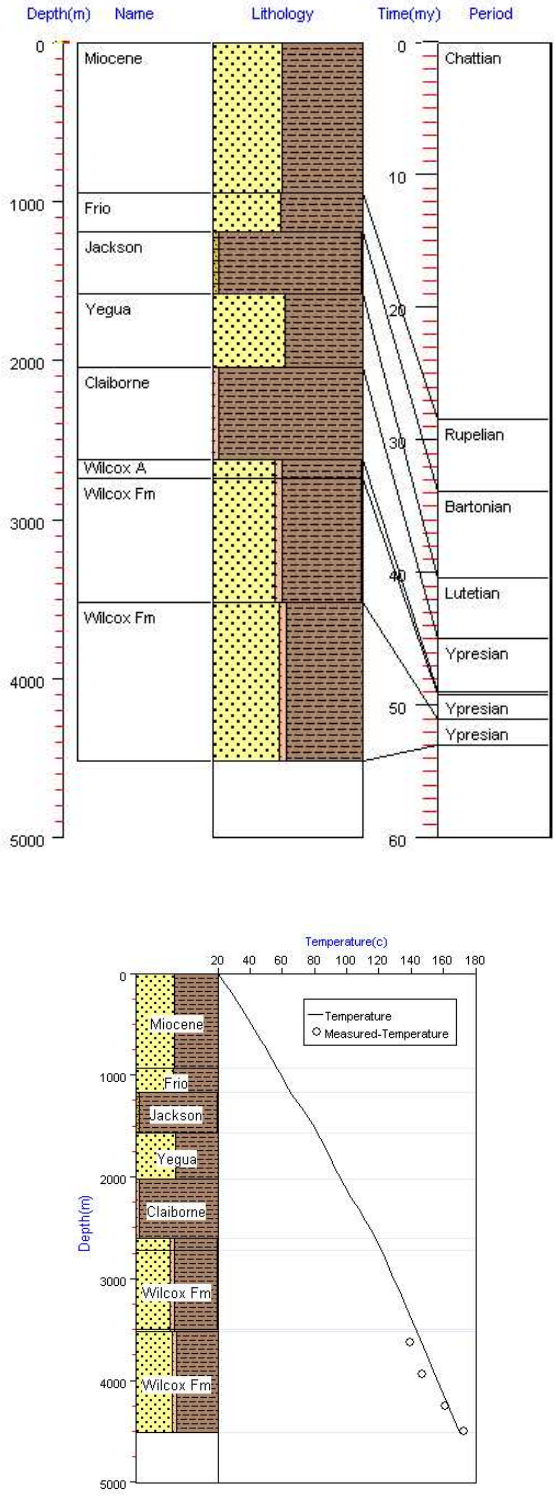

Figure 4.4 Stratigraphic log and temperature calibration constructed for the Montgomery County – Lake Creek well (LC). Modelled and measured temperatures show a good fit throughout the Wilcox.

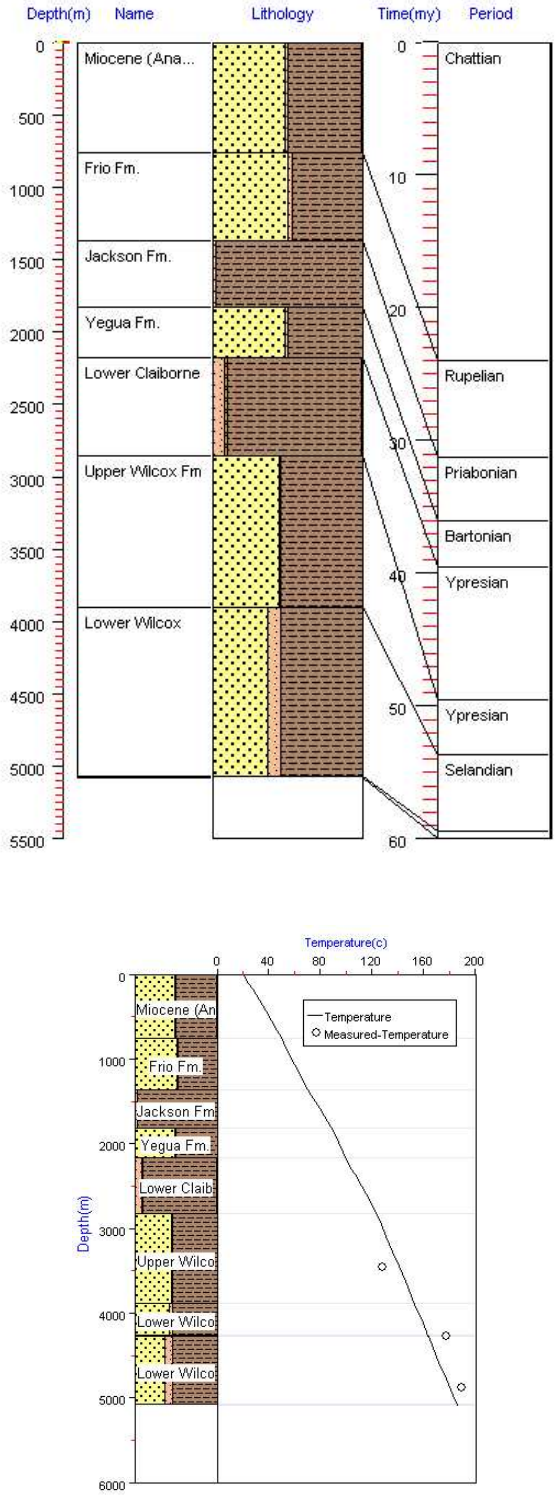

Figure 4.5 Stratigraphic log and temperature calibration constructed for the Harris County Hallison well (HA), modelled and measured temperatures show a good fit throughout the Wilcox.

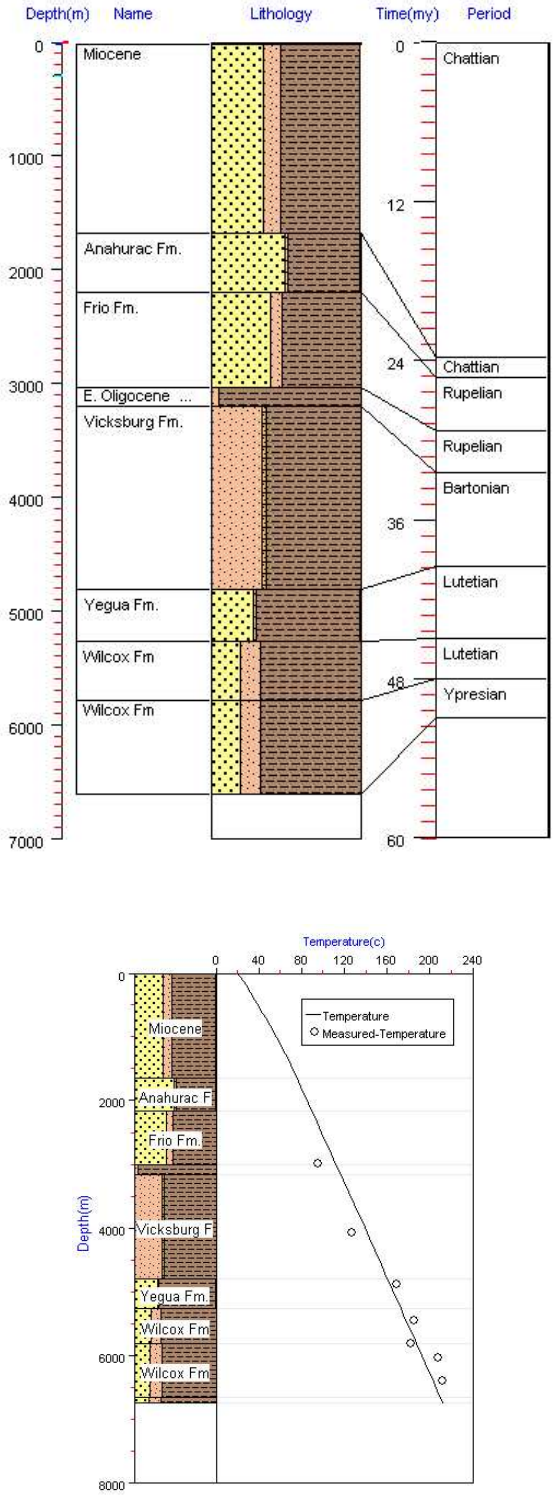

Figure 4.6 Stratigraphic log and temperature calibration constructed for the Brazonia county - Arco Crews well (CR). Modelled and measured temperatures show a good fit throughout the Wilcox.

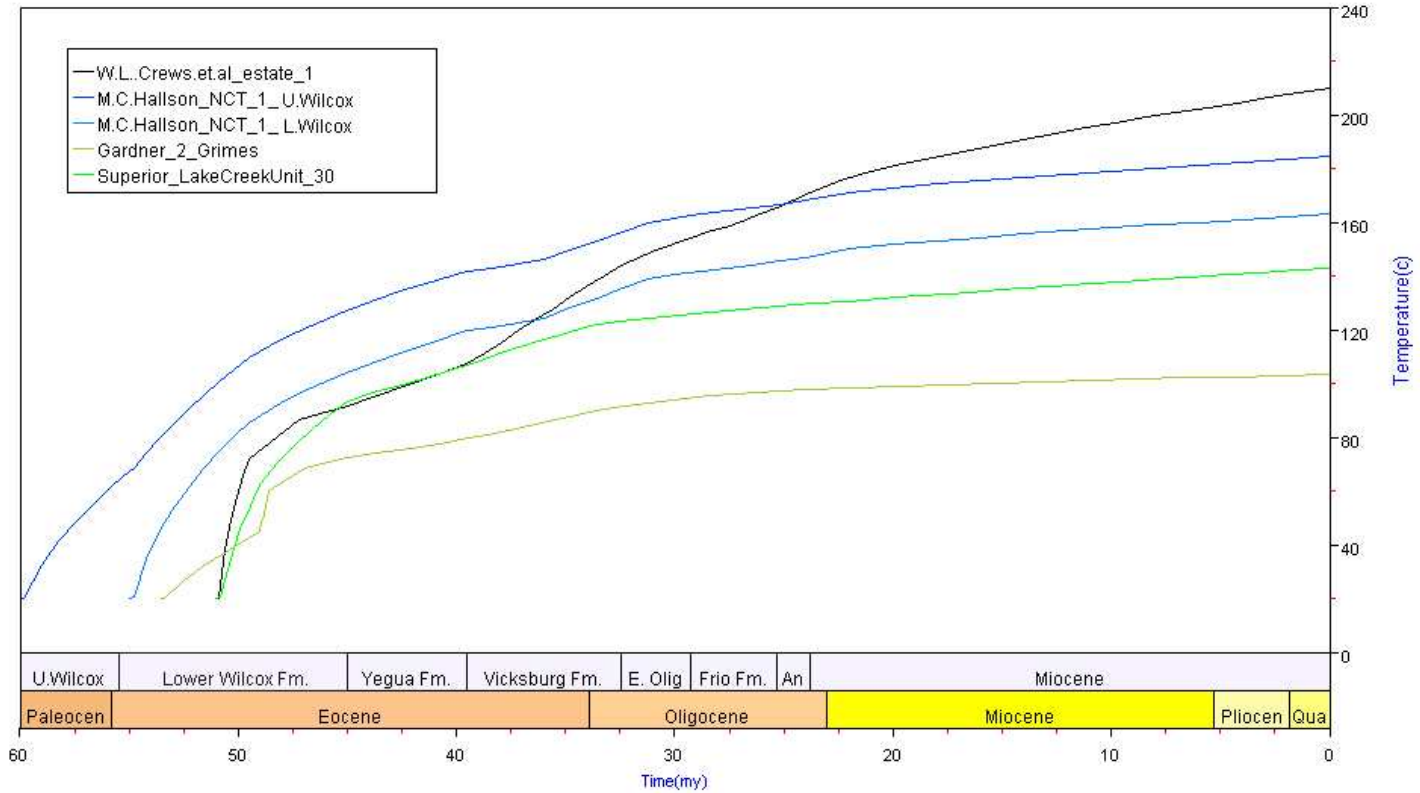

Figure 4.7 Time vs. temperature histories generated in Genesis 4.92 for the Wilcox Group in the five wells studied

	S1		S2		S3		S4		S5		S6		S7	
Samples	**t (my)**	**^{o}C/my**	**t (my)**	**^{o}C/my**	**t (my)**	**^{o}C/my**	**t (my)**	**^{o}C/my**	**t (my)**	**^{o}C/my**	**t (my)**	**^{o}C/my**	**t (my)**	**^{o}C/my**
GOM6	-	-	-	-	-	-	-	-	5.8	1.8	5.5	1.1	27.9	0.3
GOM8	-	-	-	-	-	-	-	-	2.0	6.5	11.3	2.6	33.7	0.6
GOM7	-	-	-	-	-	-	-	-	2.0	6.5	11.3	2.6	33.7	0.6
GOM9	0.9	7.2	9.8	3.4	3.3	1.0	5.1	3.1	7.3	1.0	2.0	2.1	21.8	0.6
GOM10	0.9	7.2	9.8	3.4	3.3	1.0	5.1	3.1	7.3	1.0	2.0	2.1	21.8	0.6
GOM11	4.7	6.7	9.3	3.3	3.9	0.9	5.1	2.9	6.8	1.0	1.9	1.7	22.0	0.7

Table 4.2 Calculated heating rates in the sampled Wilcox wells (^{o}C/my). S1, S2 and S3… refer to linear time-temperature segments of each well above 80^{o}C.

4.5. Wilcox Sandstone: Mineralogical History

To examine the mineralogy and diagenetic processes occurring in the Wilcox sandstone quantitative X-Ray Diffraction and petrography was carried out on a series of 20 samples. These samples were selected across four wells (SL, LC, Ha and CR) representing a temperature range of 104 to 210^{o}C.

The sandstones have compositions ranging from clean quartz rich arkoses through to feldspathic litharenites (Figure 4.8). Quantitative X-Ray Diffraction indicates large mineralogical heterogeneities between the Wilcox sandstones (Figure 4.9). Furthermore, petrographic analysis of six Wilcox sandstones highlights further mineralogical and physical heterogeneity (Figure 4.10).

Minerals including illite, kaolinite, smectite and feldspar may take part in silica producing reactions (Equation 1.2 to Equation 1.5). However, as a consequence of such large scale heterogeneity no discernable mineralogical-temperatures trends are observed (Figure 4.9). However, petrographic evidence of K-feldspar dissolution and subsequent illite formation (Figure 4.11) as well as the albitisation of feldspar (Figure 4.13 and Figure 4.14) were recorded. Furthermore, evidence of other pore filling cements including calcite forming below 104^{o}C (Figure 4.16**)**, platey illite at 188^{o}C (Figure 4.17) as well as ankerite at 188^{o}C (Figure 4.17) were observed.

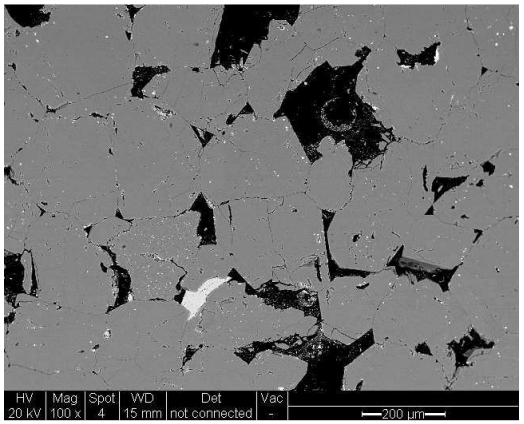

A) GOM6 (104°C) Clean quartz rich arkose containing minor siderite

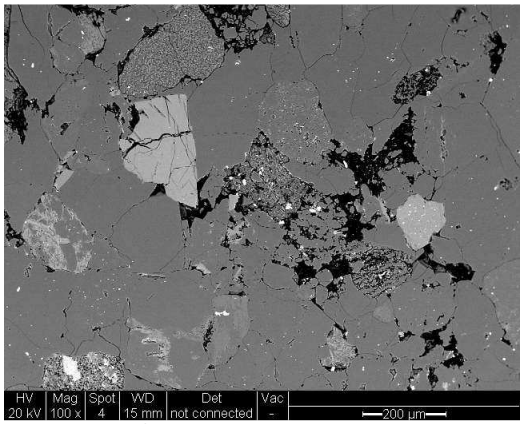

B) GOM8 (144°C) major dissolution and albitisation and of feldspar, pore filling illite also visible.

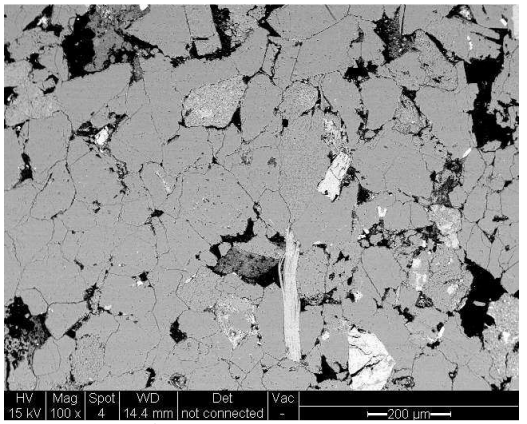

C) GOM7 (144°C) Feldspar rich sandstone, major dissolution and albitisation visible

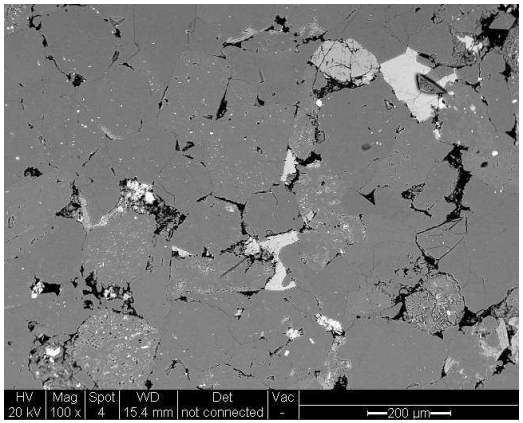

D) GOM9 (164°C) Feldspar rich sandstone, containing siderite. Major dissolution and albitisation visible

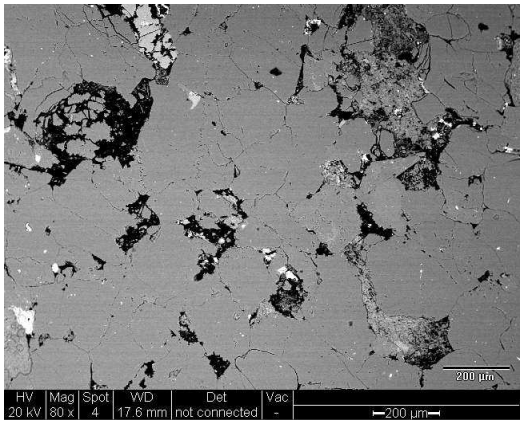

E) GOM10 (164°C) Feldspar rich sandstone. Major dissolution and albitisation visible. Illite present.

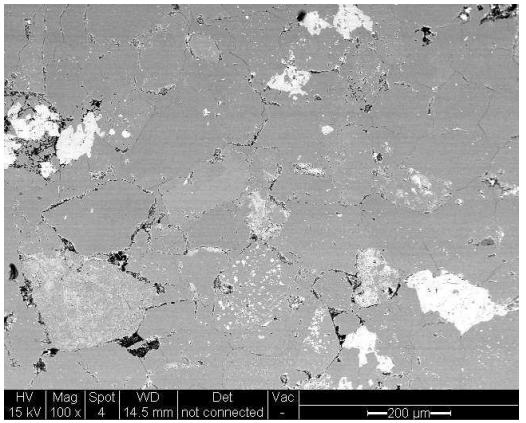

F) GOM11 (187°C) Tightly cemented feldspar rich sandstone. Major albitisation visible. Illite present along with ankerite and dolomite.

Figure 4.8 Overview of the Wilcox sandstones

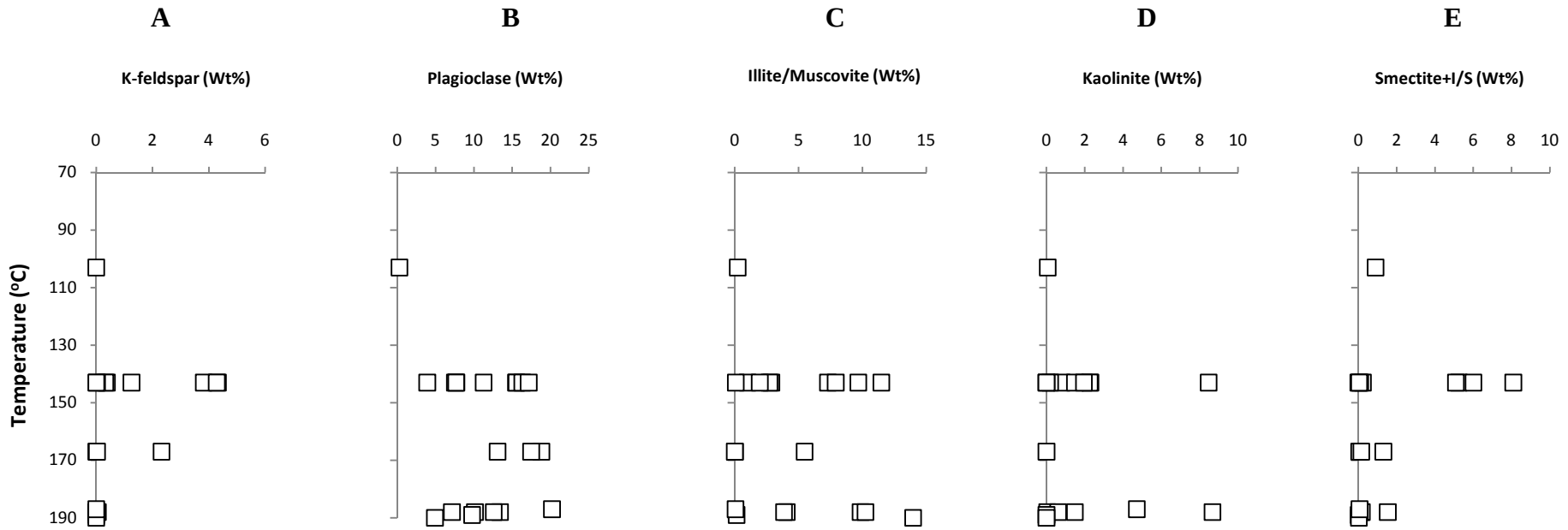

Figure 4.9 Quantitative X-ray diffraction analysis of a series of Wilcox sandstones. **A)** K-feldspar, **B)** plagioclase, **C)** illite/muscovite, **D)** kaolinite and **E)** Smectite + I/S.

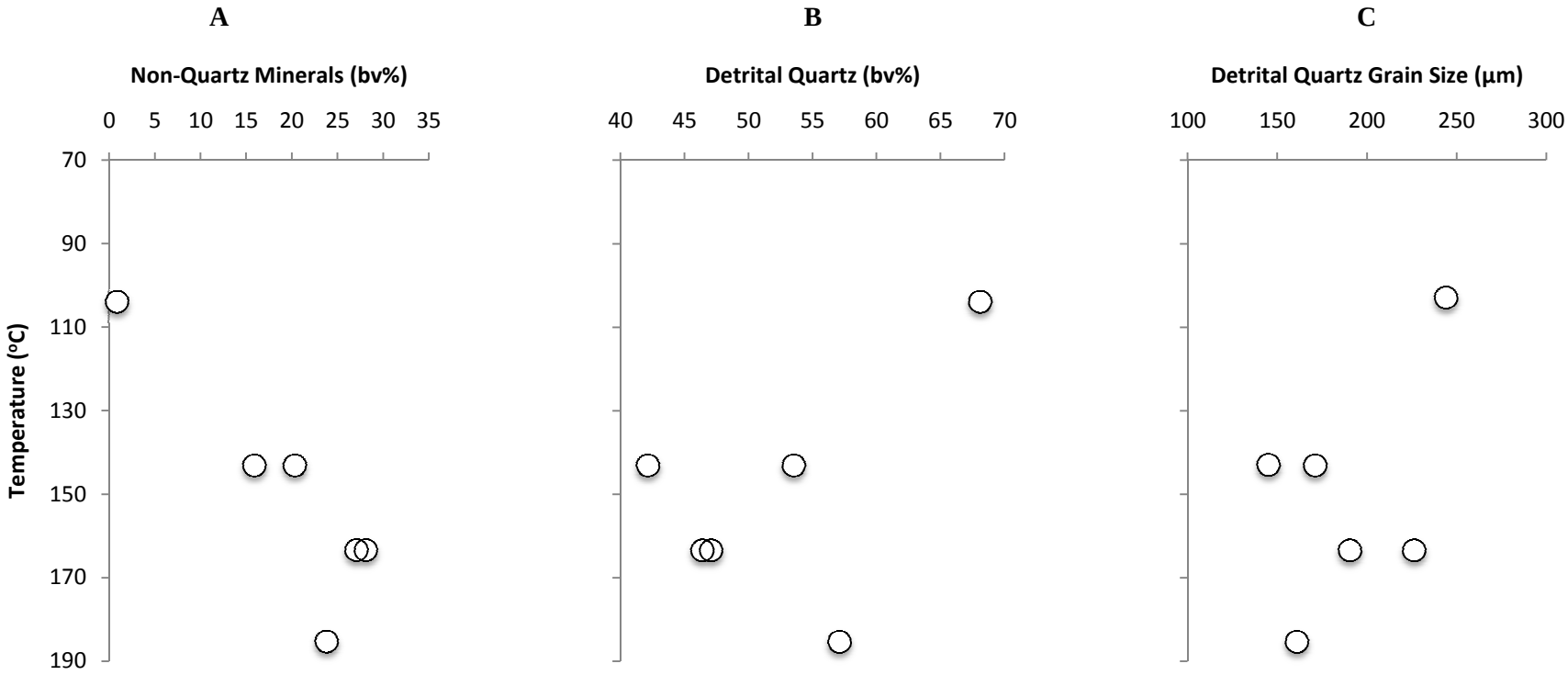

Figure 4.10 Variation in Wilcox sandstones. A) Volume of non-quartz minerals observed petrographically, B) volume of detrital quartz, determine using SEM-CL, C) Average detrital quartz grain size (µm) determined from measurements using SEM-CL.

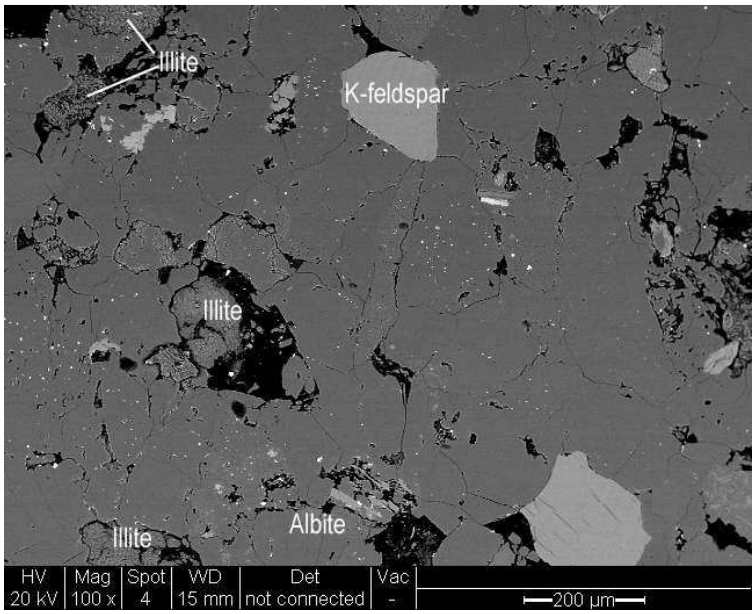

Figure 4.11 BSE image of Wilcox sandstone GOM8 (143^{o}C) containing K-feldspar and albite grains. Relic feldspar grains and illite deposits are also visible.

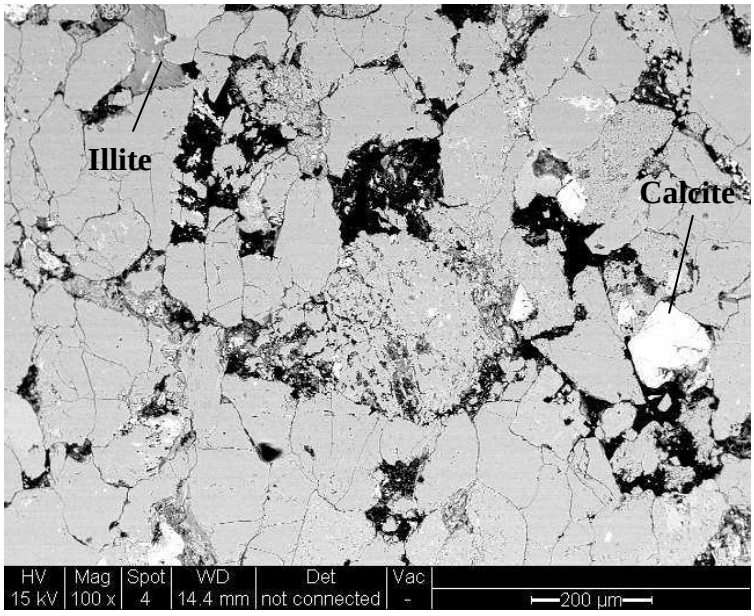

Figure 4.12 BSE image of sample GOM7 (143^{o}C). Large scale feldspar dissolution and quartz replacement (central grain). Illite and calcite also observed.

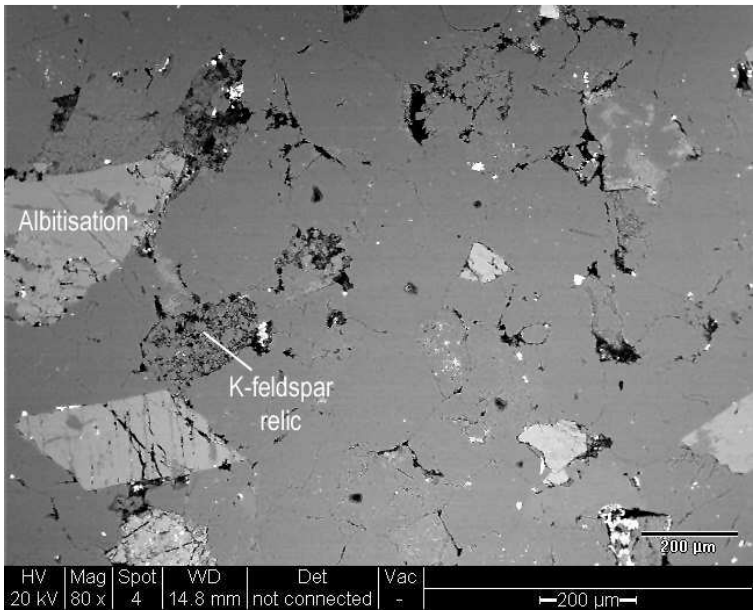

Figure 4.13 BSE image of Wilcox sandstone GOM9 (164^{o}C). Albitisation and dissolution of K-feldspar is visible. K-feldspar has been replaced by illite

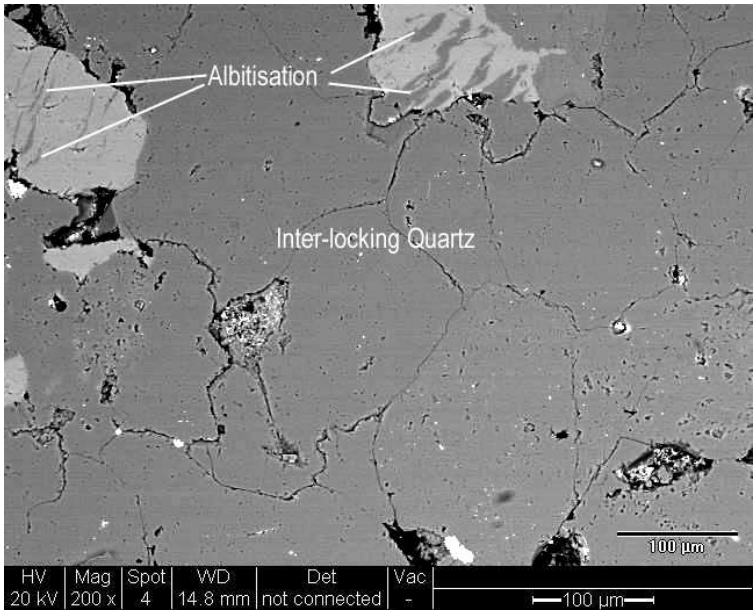

Figure 4.14 BSE Image of GOM9 (164^{o}C). Wilcox sandstone showing albitisation of K-feldspar as well as interlocking quartz grains.

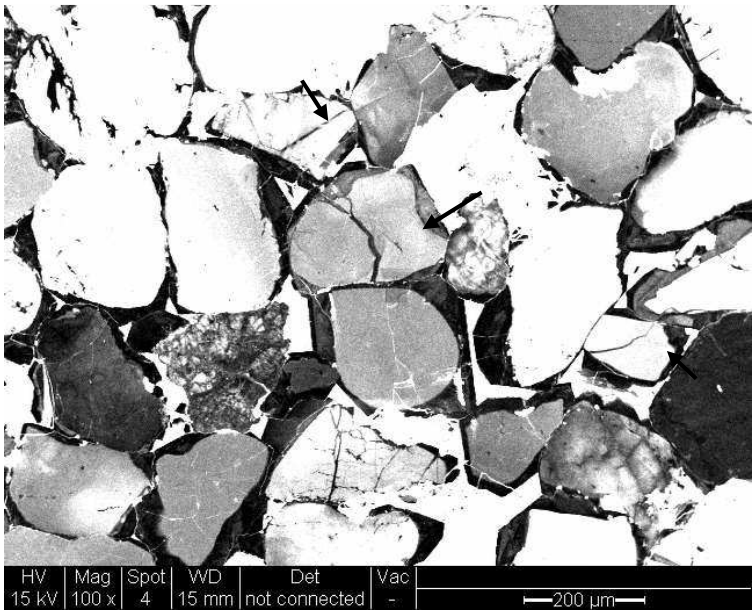

Figure 4.15 SEM-CL Image of GOM6 (104^{o}C). Grain fracturing can be seen (arrows) preceding later quartz cementation (darker material).

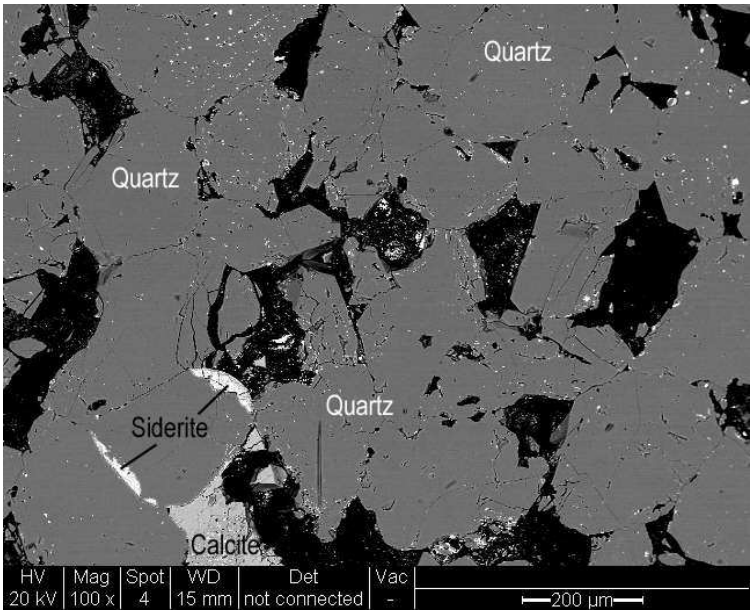

Figure 4.16 BSE Image of GOM6 (104^{o}C). Quartz rich sandstone containing siderite and calcite cements.

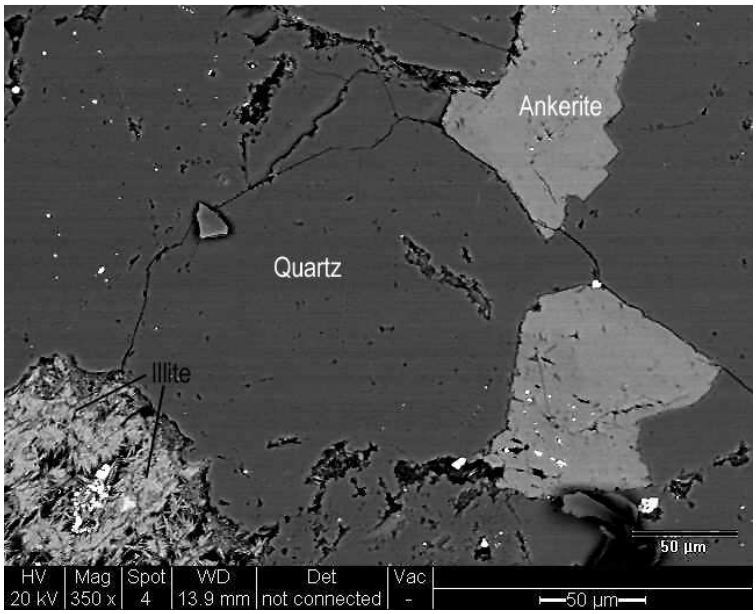

Figure 4.17 BSE image of GOM11 (188^{o}C). Quartz grain surrounded by ankerite grains and platey illite deposits. Both late stage precipitates act to reduce free quartz surface area.

Quartz cement was quantified by image analysis; total volumes range from 12.3 to 18.8 %bv (Table 4.3). The volume of cement observed increases with burial temperature up to ~140^{o}C; above 140^{o}C the volume of cement decreases (Figure 4.18A). These data are consistent with Dutton and Loucks' (2010) extensive study of the Wilcox Formation (Figure 4.18B). One sample, GOM6, taken from the SL well at 104^{o}C shows two distinct SEM-CL zones within the cement. Closest to the detrital grain an inner, lighter grey cement zone has precipitated that is superseded by later, darker cement. However, the inner grey zone is not apparent on all grains (Figure 4.19). In a second image analysis study these two zones were quantified (Table 4.4). The earlier grey cement is less abundant than the darker cement (Figure 4.20).

Porosity in the Wilcox sandstones examined ranges from 6.8 to 21.1 %bv (Table 4.5). With the exception of GOM7 (LC,143^{o}C), measured porosity decreases with increased burial temperature (Figure 4.21A). Petrographic observations indicate there may be large scale feldspar dissolution in sample GOM7 (Figure 4.12) which may account for the high porosities recorded. Data from Dutton and Loucks' (2010) supports these trends, however all results from this study lie at the top end of Dutton and Loucks' (2010) observations (Figure 4.21B).

	GOM6	GOM8	GOM7	GOM9	GOM10	GOM11
Depth (m)	2733.4	3518.4	3534.2	4277.6	4288.5	5063.3
Temperature (oC)	103.5	143.2	143.2	163.5	163.5	185.4
Ave. Quartz Cement (%bv)	13.6	18.8	16.5	15.0	17.8	12.3
95% Confidence (±)	1.6	3.6	2.3	1.4	2.0	2.5
Minimum (%bv)	10.5	14.2	11.8	12.9	13.6	6.8
Maximum (%bv)	16.0	26.4	20.3	17.0	20.3	15.4

Table 4.3 Quantification of quartz cement in the Wilcox sandstones by image analysis

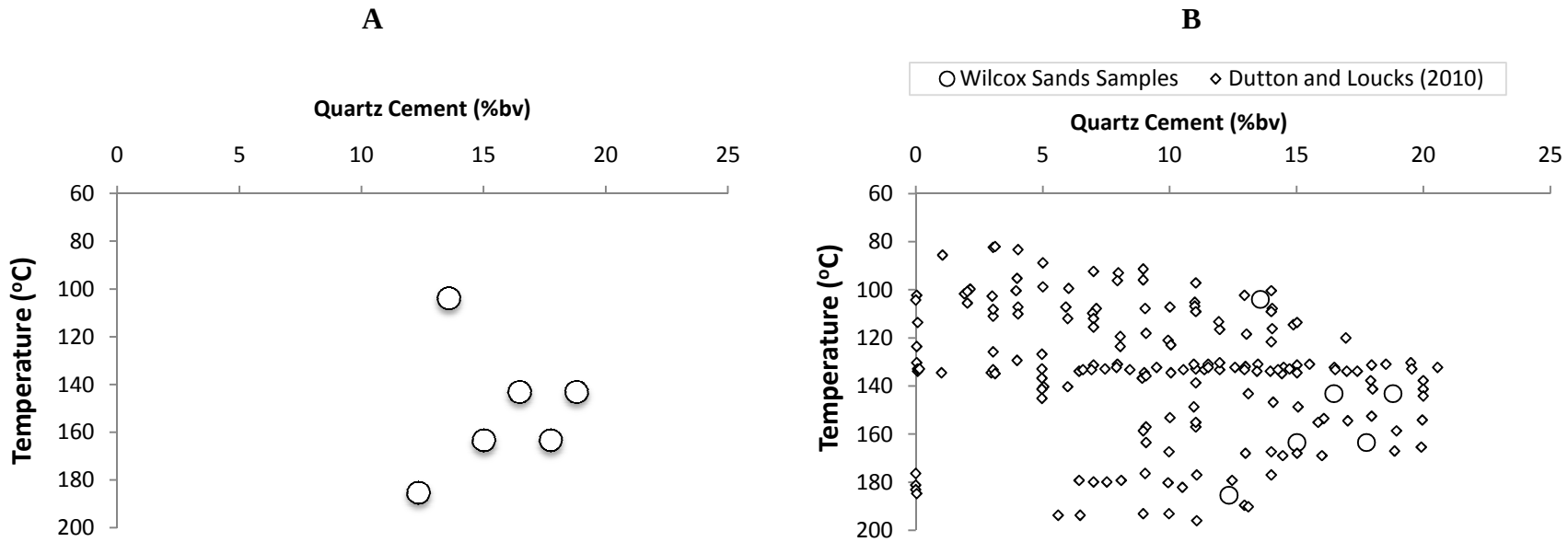

Figure 4.18 Quantification of the quartz cement present in Wilcox sandstone. **A)** Quantification carried out by image analysis in this study. **B)** Quantification reported in this study (Wilcox sands sample) and literature data taken from Dutton and Loucks' (2010).

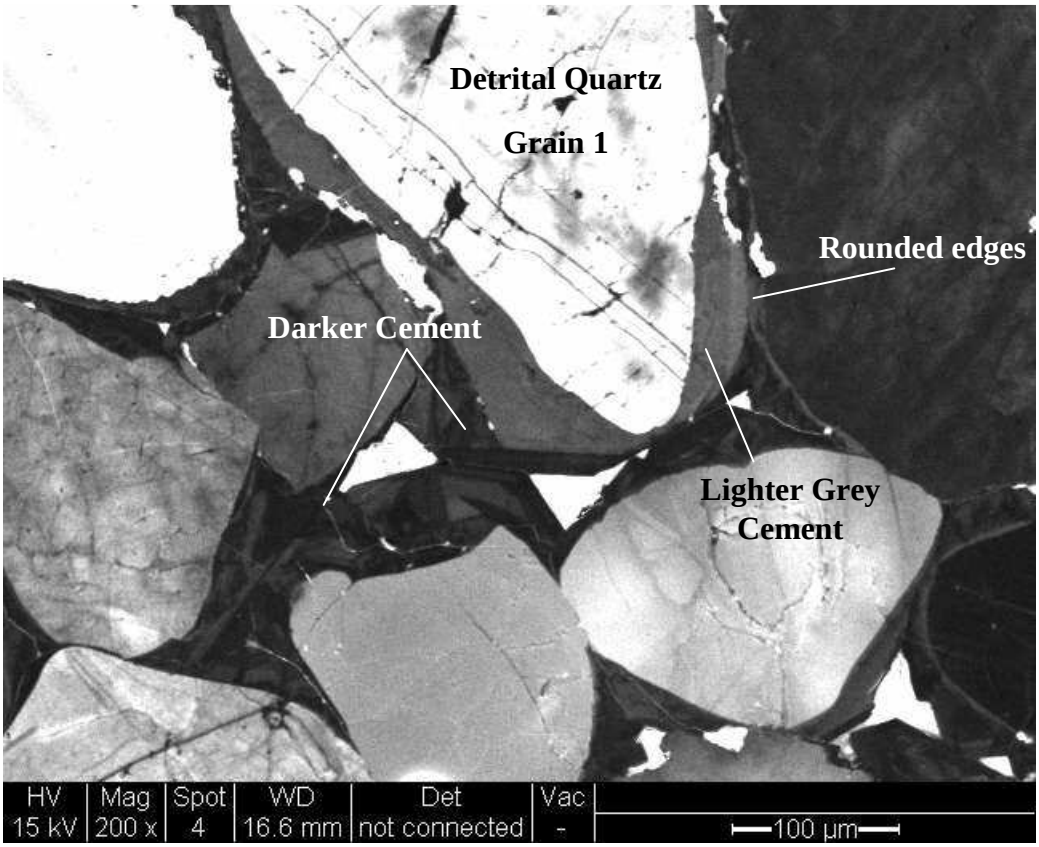

Figure 4.19 SEM-CL image of GOM6 (SL, 104^{o}C) showing detrital quartz grains with two cement types. Grain 1 has a band of lighter grey cement closest to the detrital grain that is then superseded by a darker cement. The lighter grey cement has a more rounded edge compared to the sharper exterior of the darker cement.

	Total	Light Grey Cement	Darker Cement
GOM6 Cement	13.6	2.8	10.7
95% Confidence	1.6	1.1	2.3
Standard Deviation	2.0	1.4	2.8
Minimum (%bv)	10.5	1.1	7.4
Maximum (%bv)	16.0	4.7	14.6

Table 4.4 Quantification of the two distinct CL zones observed in the quartz cement of GOM6 by image analysis

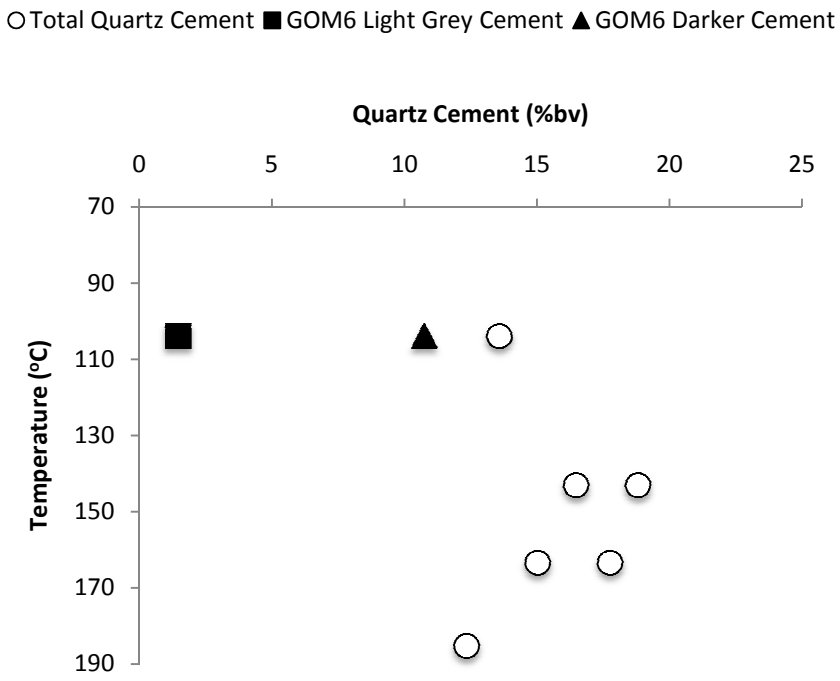

Figure 4.20 Quartz cement abundance in the Wilcox sandstone. Plus quantitative image analysis of the distinct CL zones in GOM6. The darker cement form 10.7 %bv of the total rock.

	GOM6	GOM8	GOM7	GOM9	GOM10	GOM11
Depth (m)	2733.4	3518.4	3534.2	4277.6	4288.5	5063.3
Temperature (^{o}C)	103.5	143.2	143.2	163.5	163.5	185.4
Ave. Porosity (%bv)	17.5	11.8	21.1	9.8	8.8	6.8
95% Confidence (±)	2.3	2.0	3.1	2.1	2.2	1.4
Standard Deviation	2.9	2.5	3.8	2.7	2.8	1.7
Minimum(%bv)	12.6	10.4	16.8	7.1	5.1	4.9
Maximum(%bv)	20.4	16.7	26.8	13.8	12.3	9.7

Table 4.5 Quantification of porosity in the Wilcox sandstones by image analysis

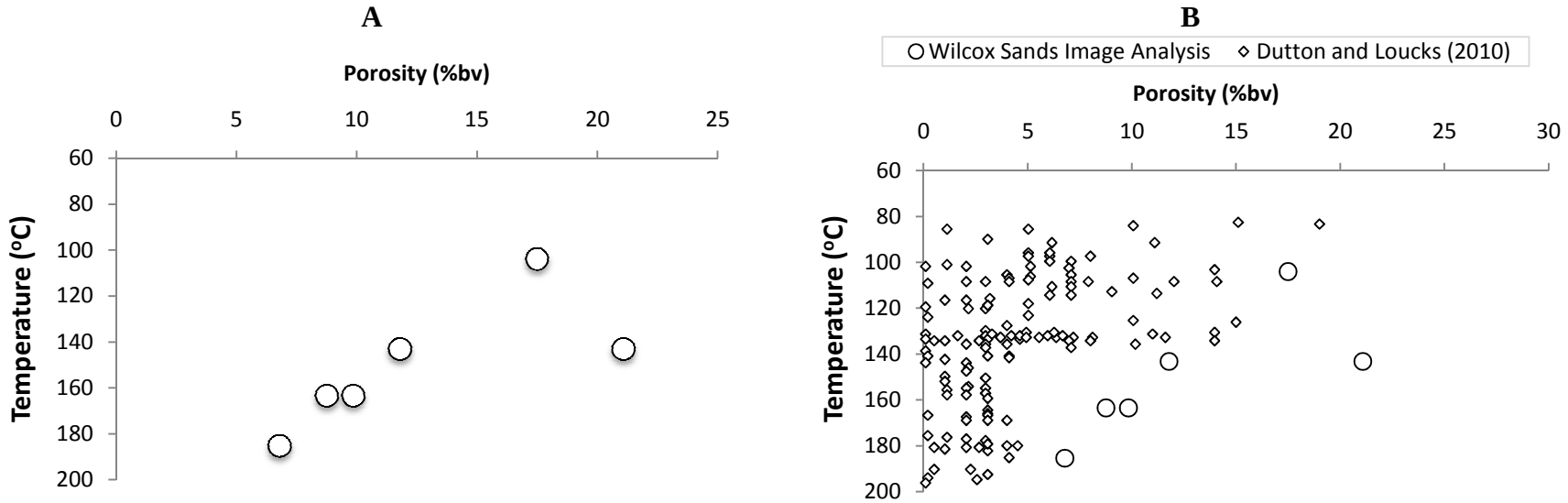

Figure 4.21 Quantification of the porosity present in Wilcox sandstone. **A)** Quantification carried out by image analysis in this study. **B)** Quantification reported in this study (image analysis) and literature data taken from Dutton and Loucks' (2010).

In summary, the sandstone samples selected in this study display physical and mineralogical heterogeneity. K-feldspar, plagioclase, illite, kaolinite and mixed I/S are all recorded in these Wilcox samples. Petrographic observations indicate these minerals are involved in silica-producing processes such as the dissolution and albitisation of feldspars. Quartz cement volumes range from 10.7 and 18.8 %bv, increasing with burial temperature until ~143^{o}C. In addition 2.8 %bv lighter grey cement is observed in the lowest temperature sample (GOM6, 104^{o}C).

At higher temperatures (>143^{o}C) the volume of quartz cement falls, although porosity continues to fall throughout the sampled Wilcox sandstones. Above 143^{o}C the precipitation of other diagenetic minerals, such as illite and ankerite, was observed. The formation of these late stage diagenetic minerals will contribute to additional porosity loss.

4.6. Quartz Cementation Modelling

Quartz cementation was modelled according to the mathematical formulation of Walderhaug (1996) shown in Equation 2.5. The model assumes that quartz is sourced from stylolites, diffuses into the inter-stylolite regions, and then precipitates as overgrowths on quartz grains. It is further assumed that the precipitation step is the slowest and therefore rate-controlling step in the overall process. The main input for modelling of quartz cementation is detrital mineralogy (Figure 4.10), grain size (Figure 4.10) and temperature history (Figure 4.7 and Table 4.2).

In total six sandstone samples were modelled from four different Texas wells (Table 4.1). Table 4.6 gives details of the modelled cement totals and Table 4.7 shows modelled porosity. The best measured/modelled fit occurs at 143^{o}C (Figure 4.23 and Figure 4.24). Below 143^{o}C cement is underestimated and porosity overestimated. Samples from above 143^{o}C show the opposite trend with cement overestimated and porosity underestimated; the magnitude of these discrepancies increases with increasing temperatures.

	GOM 6	GOM 8	GOM7	GOM 9	GOM 10	GOM 11
Depth (m)	2733.4	3518.4	3518.4	4277.6	4288.5	5063.3
Temperature (^{o}C)	103.5	143.2	143.2	163.5	163.5	185.4
Modelled Quartz Cement (%bv)	5.5	19.2	19.6	22.0	22.9	27.9
Measured Quartz Cement (%bv)	13.6	18.8	16.5	15.0	17.8	12.3

Table 4.6 Details of measured and modelled quartz cement totals in the Wilcox sandstone

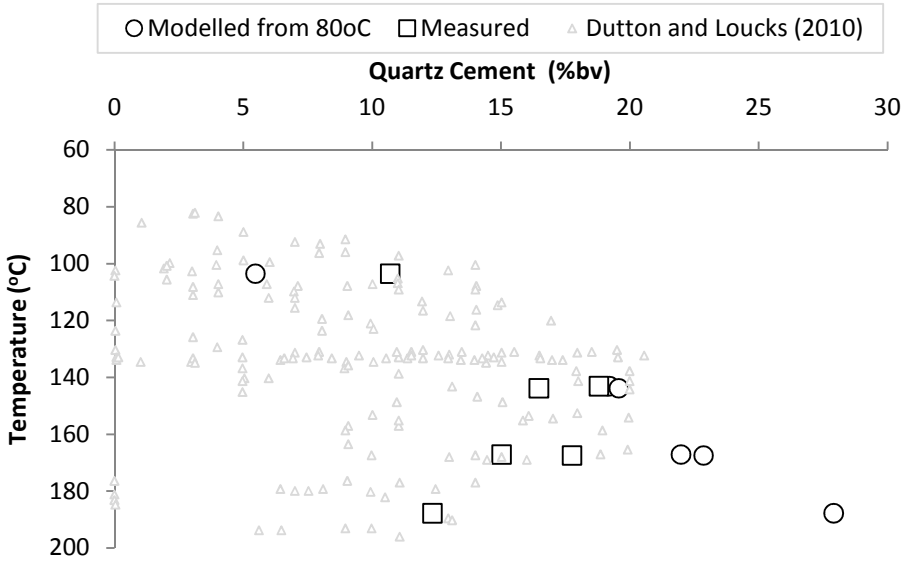

Figure 4.22 Measured and modelled quartz cement totals recorded in the Wilcox sandstone of this study. Literature data taken from Dutton and Loucks' (2010) is also shown.

	GOM 6	GOM 8	GOM 7	GOM 9	GOM 10	GOM 11
Depth (m)	2733.4	3518.4	3518.4	4277.6	4288.5	5063.3
Temperature (°C)	103.5	143.2	143.2	163.5	163.5	185.4
Modelled Porosity (%bv)	24.2	11.8	18.5	3.0	3.6	0.1
Measured Porosity(%bv)	17.5	11.8	21.1	9.8	8.8	6.8

Table 4.7 Measured and modelled porosity totals in the Wilcox sandstone

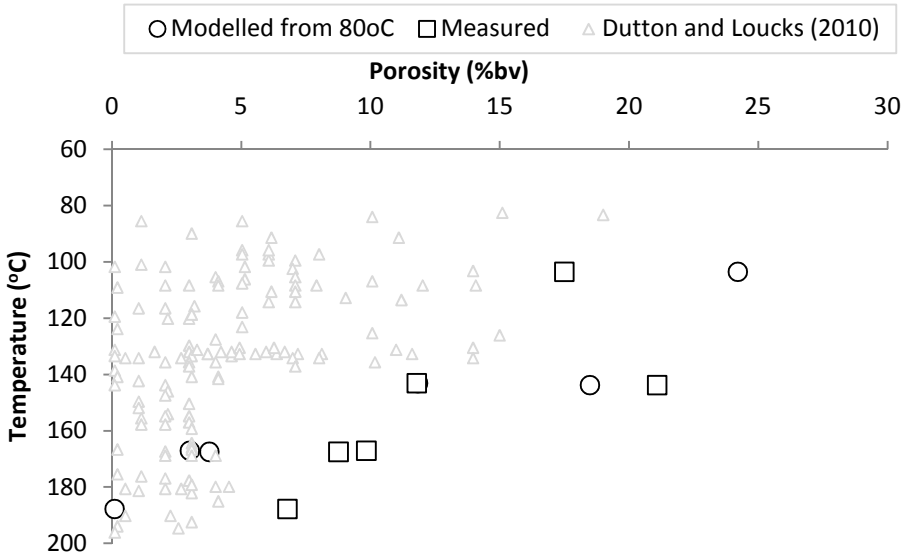

Figure 4.23 Measured and modelled porosities recorded in the Wilcox sandstone of this study. Literature data taken from Dutton and Loucks' (2010) is also shown.

It is likely that the discrepancies between the modelled cement volumes and measured data recorded (Figure 4.22) relate to the limitations of the model used. This model (Walderhaug, 1996) is a kinetic equation that predicts the volume of quartz cement that will precipitate in any quartz rich sandstone of known mineralogy and grain size.

Problems arise when the initial mineralogy is altered during diagenesis. In these Wilcox sandstones illite and ankerite have been observed precipitating in and around quartz grains (Figure 4.17). As a consequence the overall surface area of quartz available for further quartz precipitation will be affected. Walderhaug's (1996) model (Equation 2.5) does not account for such scenarios; the model believes quartz precipitation remains uninhibited during burial. Furthermore, Walderhaug's (1996) model does not account for the formation of secondary porosity. Secondary porosity is observed throughout the Wilcox sample set as a result of feldspar dissolution (Figure 4.11 and 4.12) and may further effect quartz surface area.

It should be noted that commercial cement modelling software packages, including EXEMPLAR© and TOUCHSTONE©, which were developed from Walderhaug's early work (Walderhaug, 1994a; Walderhaug, 1994b; Walderhaug, 1996) do have the capacity to factor in other mineralogical processes which may affect the rate of quartz cementation (Walderhaug et al., 2000). As a result these cementation models are successfully and routinely used in the Gulf of Mexico region (Walderhaug et al., 2000; Ajdukiewicz and Lander, 2010).

The model is also reliant on accurate thermal modelling. If modelled temperature histories are too low, then the value of b ($0.0185/^{o}C$), equivalent to the activation energy, will be too. If the modelled temperature is too hot, then the value of b will be too high (Walderhaug, 2000). More precise modelling results can be obtained if the value of b is varied in each Texas well (Table 4.8). However, if this quartz cementation model adequately reflects the actual processes taking place, then the optimal value of

the exponential factor *b* in Equation 2.5 should be the same for all quartz-cemented sandstones where silica is supplied from stylolites (Walderhaug, 2000).

	GOM 6	GOM 8	GOM 7	GOM 9	GOM 10	GOM 11
Well	**SL**	**LC**	**LC**	**HA-U**	**HA-U**	**HA-L**
Temperature (^{o}C)	103.5	143.2	143.2	167.1	167.5	187.8
Modelled (%bv)	10.7	18.5	16.8	15.3	17.6	12.7
Measured (%bv)	10.7	18.8	16.5	15.0	17.8	12.3
Optimal kinetics (/^{o}C)	0.0220	0.0183	0.0178	0.0162	0.0168	0.0128

Table 4.8 The optimum kinetics for Wilcox samples using Walderhaug's (1996) cementation model. The average fit for the GOM are is 0.0173/^{o}C.

The large discrepancies in the modelling and measured data makes it difficult to accurately predict the temperature evolution across each individual quartz overgrowth. These quartz cementation modelling results were therefore not used to predict the temperature represented by each SIMS analyses.

4.7. Isotope Analysis

4.7.1. Wilcox sandstone SIMS samples

A full description of the Wilcox samples selected for isotope analysis can be found in Table 4.1. These samples were selected as they represent a temperature range of 104 to 188^{o}C; which should encompass all diagenetic reactions previously observed in the Wilcox (Fisher and Land, 1986b; Land and Fisher, 1987). The three SIMS samples also contained quartz overgrowths >50 µm thick. Quantitative petrography, QXRD and Genesis 1-D modelling analyses are summarised in Table 4.9.

4.7.2. SIMS Analysis

During a 48-hour period between the 2nd and 3rd of June, 2009, 238 oxygen isotope analyses were made on the three selected Wilcox Formation sandstones. Initially 151 measurements were made across the three sandstone samples and 42 on an internal quartz standard (UWQ-1) using a 12 µm SIMS beam. During a second session the spot size was reduced to 2 µm; during this session a further 29 $\delta^{18}O$ measurements were made, plus an additional 16 on UWQ-1.

4.7.2.1. UWQ-1 Analysis

In both sessions the UWQ-1 standard was used to calibrate oxygen isotope ratios to the V-SMOW scale and to provide an internal measurement of precision as described in Kelly et al. (2007). During the first session the average precision across the 3 samples was measured at ±0.27 ‰ (2SD) using the 12 µm beam, n=151 (Figure 4.24). In the second session precision was measured at ±0.67 ‰ (2SD) using the 2 µm beam, n=29 (Figure 4.25).

Sample	Well	Depth (m)	Max Burial Temperature (^{o}C)	Non quartz minerals (%bv)	Porosity (%bv)	Quartz Cement (%bv)	Ave. Grain Size (µm)
GOM6	**SL**	2733.4	104	Bt, Pl (<1%)	17.5	13.6	244
GOM8	**LC**	3518.4	143	M/I, Bt, K-F (16%)	11.8	18.8	171
GOM11	**HA-L**	5063.3	188	Ch, M/I, Bt, Na-F, An (24%)	6.8	12.3	161

Table 4.9 Overview of the Wilcox samples selected for SIMS analysis. Bt = Berthierine, M/I = Mica/Illite, K-F = K-Feldspar, Na-F = Na-Feldspar, Pl = Plagioclase, Ch = Chlorite, An = Ankerite.

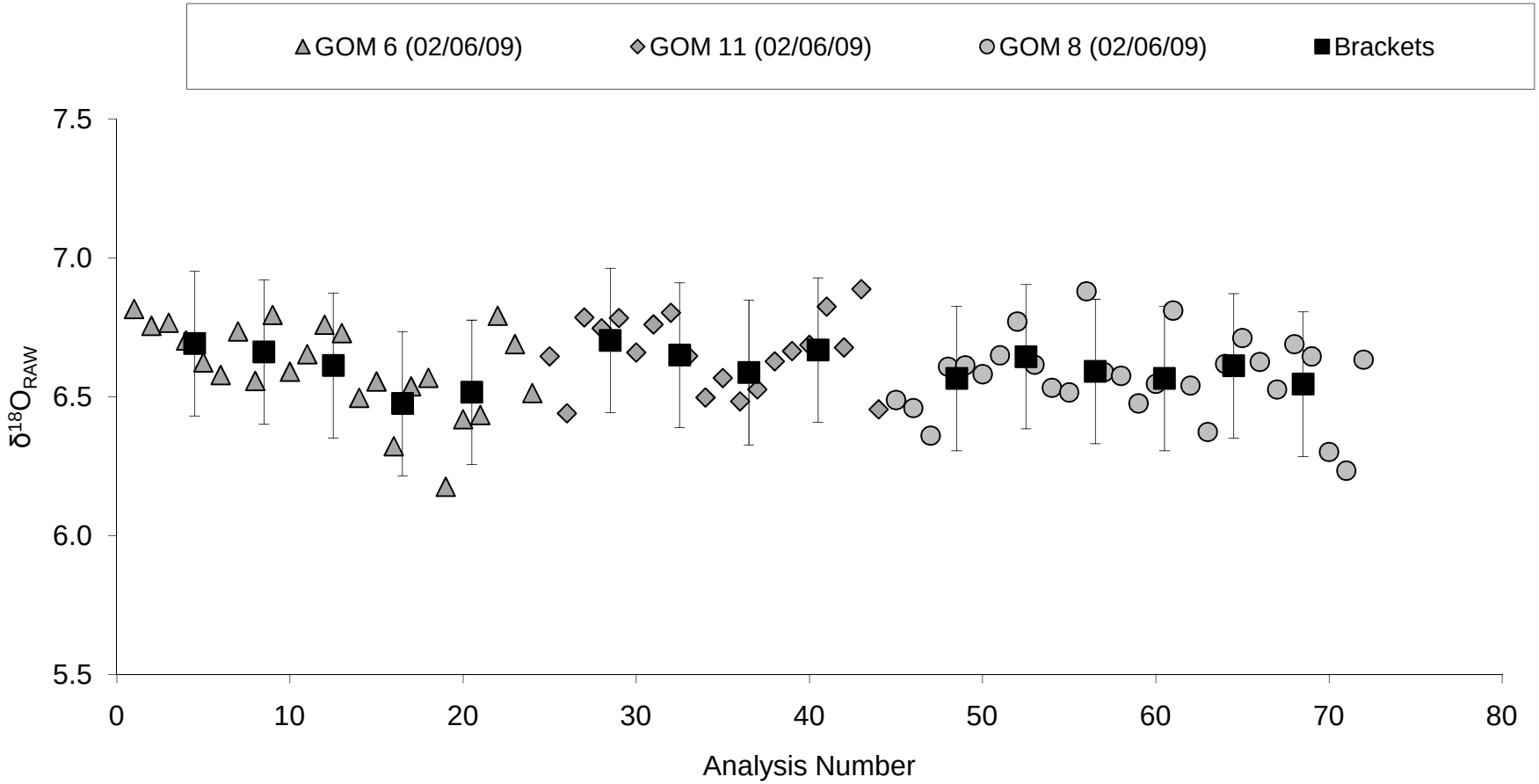

Figure 4.24 UWQ-1 Standard analysis. Brackets are averages of 8 or 9 individual measurements made before and after each set of sample measurements. All analyses were carried out with a 12 µm spot size.

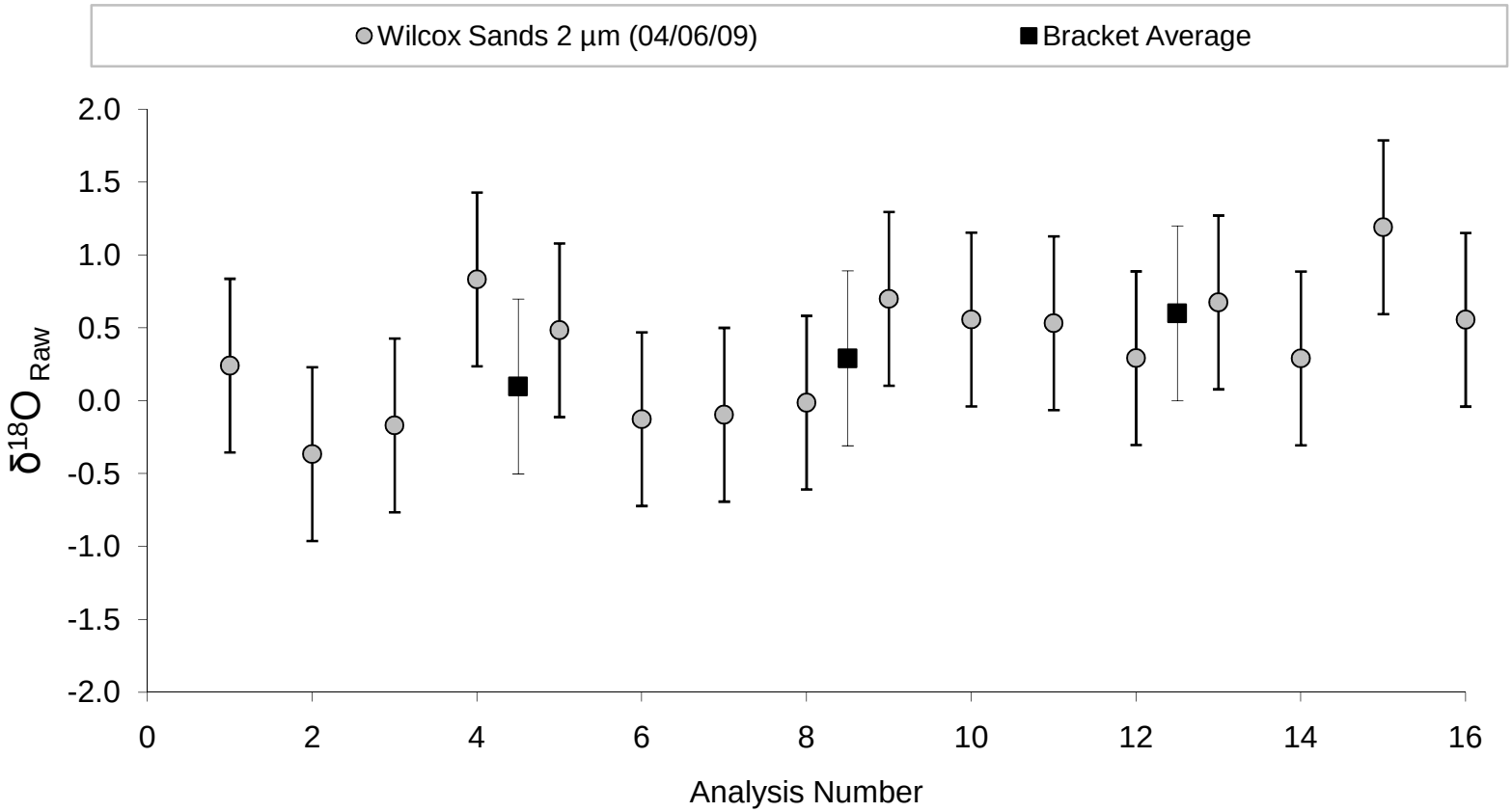

Figure 4.25 UWQ-1 standard analyses performed during the 2 µm high precision SIMS investigation. Error bars show the average bracket error that consists of 8 standard measurements.

4.7.2.2. SIMS Pit Characterisation

After the completion of the SIMS investigation a combination of Secondary Electron (SE), Back Scattered (BSE) and Cathodoluminescence (SEM-CL) microscopy was used to relocate and characterise each individual pit. A full account of how each pit was interpreted with reasoning for each pit's inclusion or exclusion from this study is given in Appendix 4, an example is given in Figure 4.26.

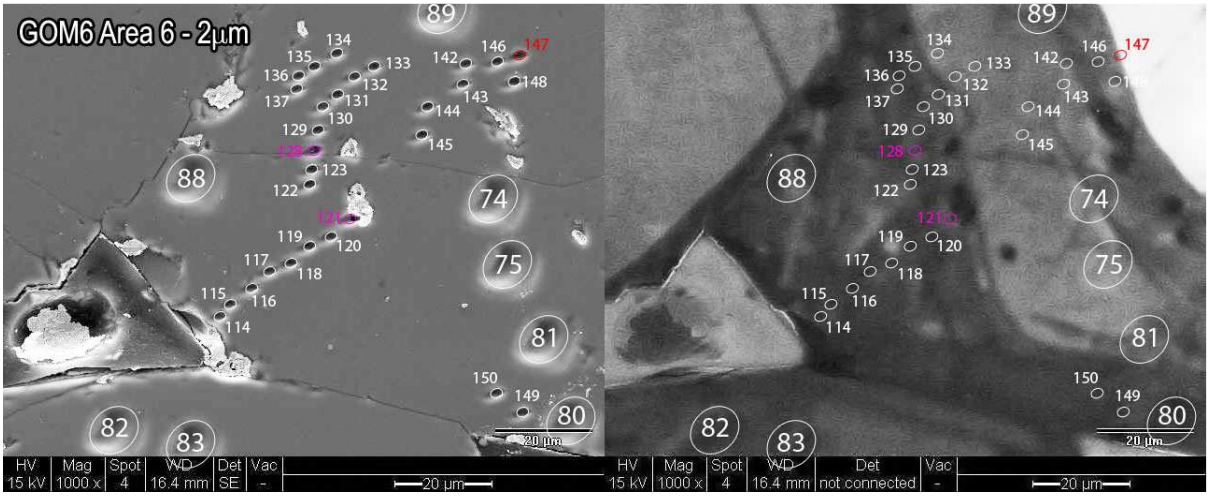

Figure 4.26 SE (left) and SEM-CL (right) image of sample GOM6 (104^{o}C) the smaller circles represent the 2 µm analyses, the larger circles the 12 µm pits. White = authigenic quartz, red = mixed analyses (authigenic and detrital) and pink = crack.

4.7.2.3. SIMS Analysis of Authigenic Quartz

79 analyses were carried out on four areas across GOM6. Initially 50 SIMS pits were made using a 12 µm spot; 33 of these pits were made in authigenic quartz cement. Later a second session was performed in which a 2 µm spot size was utilised to examine GOM6 Area 6 (Figure 4.26). Of the 29 analyses made using the smaller 2 µm spot, 26 spots were performed on quartz cement.

SEM-CL examination of sample GOM6 showed the presence of two clear zones within the quartz cement. The inner grey luminescing layer is distinct from the detrital quartz, but is not present on all detrital grains (Figure 4.26). Throughout the sample a common darker band of cement is seen (Figure 4.19). Where both the grey and darker cement occur on a single grain, the grey cement is always closer to the detrital material. The darker material therefore represents a younger precipitate. The two layers also have distinctively different isotopic signatures (Figure 4.27A and B). In the grey zone, $\delta^{18}O_{(cement)}$ ranges from +25.1‰ to +27.5‰. In contrast, the darker zone reveals lower $\delta^{18}O_{(cement)}$ values between +23.5‰ and +24.9‰. These initial 12 µm SIMS investigations indicate little isotopic variation within each zone.

Petrographically and isotopically the two regions of the GOM6 cement are different. These differences hint towards the two regions being two separate phases. If this is the case then SIMS spots in the darker cement should be measured from the initiation of cementation i.e. the darker cement/ light grey cement boundary or where no grey cement is present the detrital quartz grain/darker cement boundary. At the 12 µm scale this only affected measurements for 4 pits (Figure 4.27C and D).

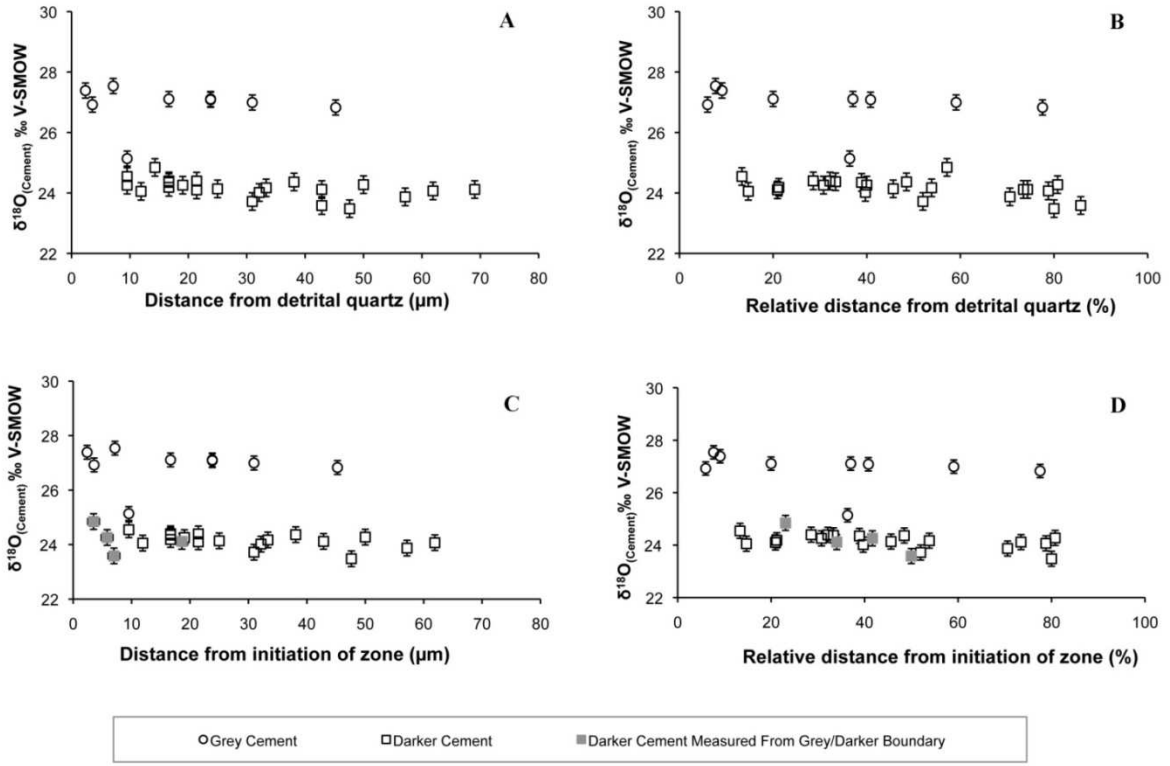

Figure 4.27 12 µm SIMS analysis of GOM6 (104°C). **A)** $\delta^{18}O_{(cement)}$ vs. distance from detrital quartz. **B)** $\delta^{18}O_{(cement)}$ vs. relative distance from detrital quartz. **C)** $\delta^{18}O_{(cement)}$ vs. distance from the start of cement. **D)** $\delta^{18}O_{(cement)}$ vs. relative distance from the start of cement. Isotopically the grey cement and darker cement are distinct.

During the 12 µm SIMS analysis of GOM6 eight separate pits were made into the detrital quartz grains. Four were made in detrital grains hosting both grey and darker cement and four into detrital grains only hosting the more abundant darker cement. Detrital grains hosting the grey cement have a lower $\delta^{18}O$ (+6.5 to +11.0‰), whereas the grains only hosting the darker cement have higher $\delta^{18}O$ (+11.5 to +15.0‰).

At the 2 µm scale, as with the 12 µm investigation, data from the grey region exhibits very little spatial variation. $\delta^{18}O_{(cement)}$ ranges from 28.3 ‰ to 26.3‰. Overall, in the grey cement, the 2 µm data supports the 12 µm investigation (Figure 4.28A and B).

In contrast the range of $\delta^{18}O_{(cement)}$ observed in the darker zone increases to ~ 4.5‰ (+28.5‰ to +23.9‰) using the 2 µm analysis beam. The 2 µm SIMS study also highlights a clear spatial variation, with $\delta^{18}O_{(cement)}$ become less positive away from the detrital quartz (Figure 4.28C and D). However it must be noted that the isotope stratigraphy recorded only covers 80% of the darker cement; no measurements were successfully performed in the youngest 20% of the darker cement (Figure 4.28D). It is likely that the outer most $\delta^{18}O_{(cement)}$ measurement made in this sample (+23.9‰) correspond to a lower temperature than the maximum burial temperature of the GOM6 well (104^{o}C).

Importantly analysis with a 2 µm pit in this GOM6 samples indicates the existence of a thin isotopically heavier rind close to the detrital grain (Figure 4.28C and D). This rind forms around 8% of the total cement observed in the GOM6 sample.

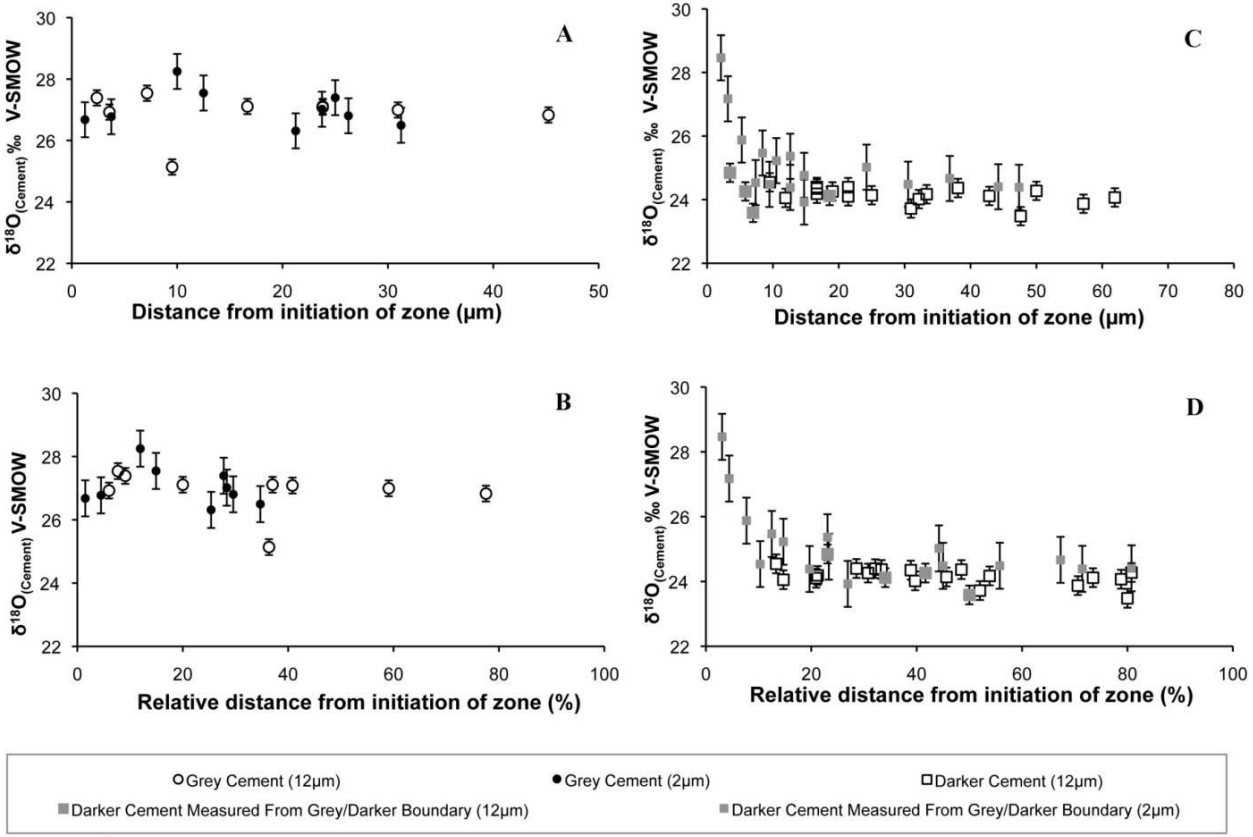

Figure 4.28 2 µm and 12 µm SIMS analysis of GOM6 (104°C). **A)** $\delta^{18}O_{(cement)}$of the grey zone vs. distance from the start of cement. **B)** $\delta^{18}O_{(cement)}$ of the grey zone vs. relative distance from detrital quartz. **C)** $\delta^{18}O_{(cement)}$ of the darker cement vs. distance from the start of cement. **D)** $\delta^{18}O_{(cement)}$of the darker cement vs. relative distance from the start of cement. Isotopically the grey cement and darker cement distinct.

SIMS sample GOM8 was analysed using only the 12 µm beam. $\delta^{18}O_{(cement)}$ measured over 6 separate areas ranges from +18.6‰ to +24.69‰ (n=45). Values of $\delta^{18}O$ for detrital grains range from +8‰ to +14‰ (n=12).

The average width of overgrowth material in GOM8 was between 20 and 40 µm similar to that observed in GOM6 in which no spatial variation was measured at the 12 µm scale. However, in GOM8 a clear change in $\delta^{18}O_{(cement)}$ away from the detrital grain was observed with values becoming less positive towards the edge of each grain (Figure 4.29A and B). It is important to note that in many instances across GOM8 this termination at the grain's edge represents a grain-to-grain contact. It is therefore possible that the modelled maximum burial temperature may not correspond to a maximum cementation temperature.

Petrographically the quartz cement material of GOM11 is very similar to GOM8. In total 60 analyses were made across GOM11 with a 12 µm beam. 36 pits were performed in quartz cement material from four areas. $\delta^{18}O_{(cement)}$ ranged from +18.3 ‰ to +23.8‰. Again $\delta^{18}O_{(cement)}$ becomes less positive towards the grain edge (Figure 4.29C and D). The $\delta^{18}O$ of detrital quartz measured in GOM11 ranges from +3.7‰ to +13.6‰ (n=9).

In the two higher temperature Wilcox sandstones, GOM8 and GOM11, the isotopic stratigraphy measured across overgrowths is nearly identical, ranging from ~24‰ close to the detrital quartz grains to ~18‰ at the outer edge of the overgrowth (Figure 4.29E and F).

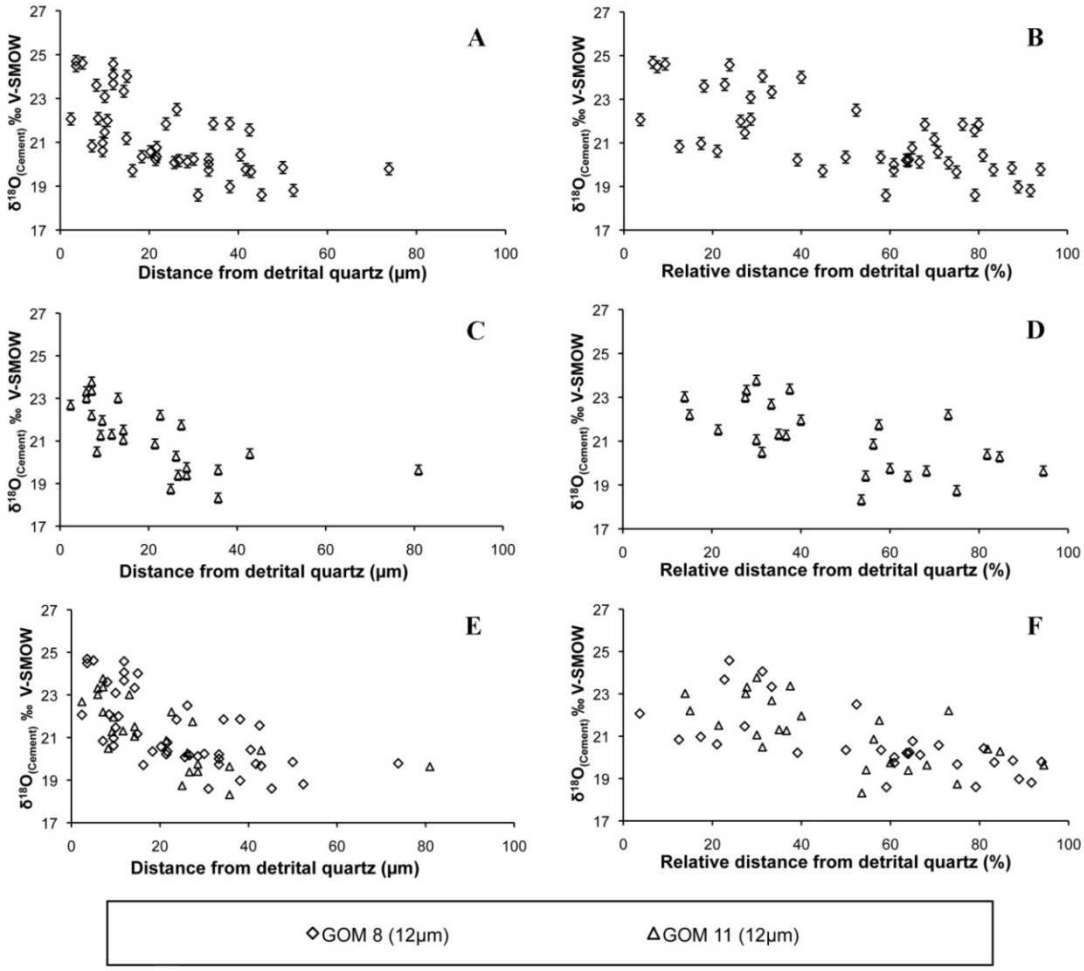

Figure 4.29 12 µm SIMS analysis of GOM8 (143°C) and GOM11 (188°C). $\delta^{18}O_{(cement)}$ vs. distance from detrital quartz: **A)** GOM8; **C)** GOM11 and **E)** both GOM8 and GOM11. $\delta^{18}O_{(cement)}$ vs. relative distance from detrital quartz: **B)** GOM8; **D)** GOM11 and **F)** GOM8 and GOM11.

Across the three samples the total range of $\delta^{18}O_{(cement)}$ recorded spanned from +28.5‰ to +18.3 ‰. In all the Wilcox samples the heavier $\delta^{18}O_{(cement)}$ measured are closest to the detrital quartz and thus represent the earliest precipitation of quartz cement, the lightest values represent the outer cement and thus the youngest cement. Although the samples represent ~40°C intervals (104, 143 and 188°C) the majority of the variation in $\delta^{18}O_{(cement)}$ is recorded between 104 and 143°C; little variation is observed between 143 and 188°C (Figure 4.30).

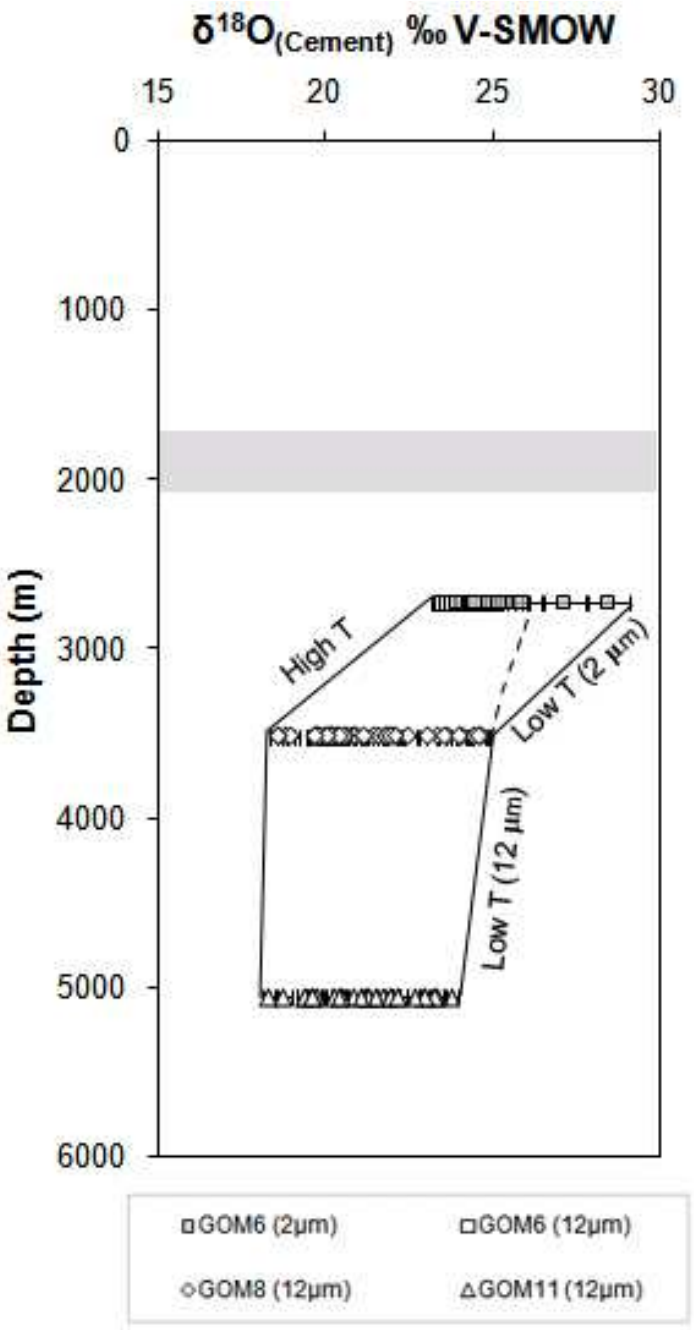

Figure 4.30 $\delta^{18}O_{(cement)}$ variation across the samples Wilcox sandstones. The high temperature line represents measurements made in the outer regions of overgrowths. The low temperature line represents analyses made closest to the detrital grain. The dotted line represents a continuation of the "Low T" 12 µm line. The shaded area corresponds to the 80°C threshold temperature for quartz cementation suggested by Walderhaug (1996; 2000) and Ajdukiewicz and Lander (2010)

4.8.Mineralogical Analysis: X-Ray Diffraction

In total 32 shale samples taken from 5 wells across the Texas study area were examined. All sample details are given in Table 4.1; samples have been selected from a depth of 324m to 6804m representing maximum burial temperatures of 27^{o}C to 210^{o}C.

Previous studies have highlighted that minerals including: K-feldspar (Sorby, 1880; Hawkins, 1978); kaolinite (Boles and Franks, 1979; Lanson et al., 2002; Day-Stirrat et al., 2010); albite (Boles, 1982b; Saigal et al., 1988; Glasmann, 1992); mixed layered illite-smectite (Velde and Vasseur, 1992; Lanson et al., 2002; Sanjuan et al., 2002; van de Kamp, 2008) and chlorite-smectite (Hurst, 1985; Chang et al., 1986; Hillier, 1994) may take part in diagenetic, silica producing reactions. Quantitative analysis of these minerals was undertaken in an attempt to assess the potential for these minerals to produce the required silica need to produce the ~18%bv cement observed in adjoining sandstone units.

4.8.1. Bulk Quantitative X-Ray Diffraction of Wilcox Shale

All bulk QXRD measurements for the Wilcox shake are given in Appendix 6. Figure 4.31A illustrates the actual totals quantified before mineral proportions are normalised to 100%.

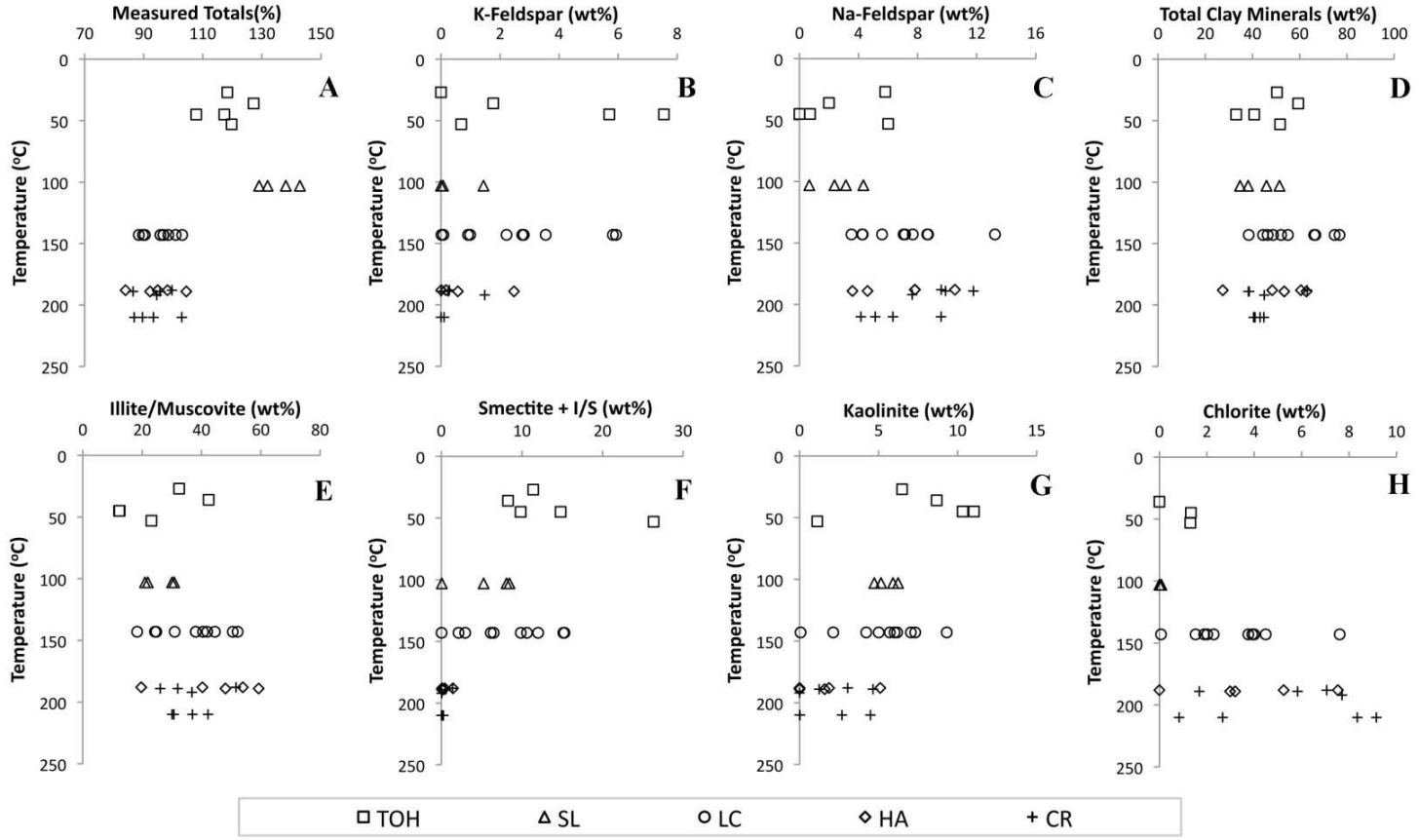

Figure 4.31 Bulk Quantitative X-Ray Diffraction of Wilcox Shale Samples. (**A**) Measured totals, showing variation from 100%. Quantitative analysis normalised to 100% of; (**B**) K-Feldspar, (**C**) Na-Feldspar, (**D**) Total clay minerals, (**E**) Illite/Muscovite, (**F**) Smectite + mixed layer I/S, (**G**) Kaolinite and (**H**) Chlorite.

K-feldspar abundance varies from a maximum of 8 wt% down to 0 wt%. At temperatures >180^{o}C 3 wt% K-feldspar still remains (Figure 4.31B). Na-Feldspar (Figure 4.31C) levels averaged across individual wells range from 3 to 10 wt% in the shale rich Wilcox units, becoming more abundant above 104^{o}C.

Significant clay mineral quantities are recorded in these shale units. Total volumes range between 27 and 70 wt%. The volume of total clay mineral (Figure 4.31D) was determined as the combined abundance of illite/muscovite (Figure 4.31E), smectite + mixed layer I/S (Figure 4.31F), kaolinite (Figure 4.31G) and chlorite (Figure 4.31H).

As the total volume of clay minerals recorded in each sample is varied, it is important to examine the volume of the individual mineral not only as a percentage of the total rock but as a fraction of the total clay mineral assemblage (Figure 4.32). This will reduce the impact of any trends related to the depositional heterogeneity.

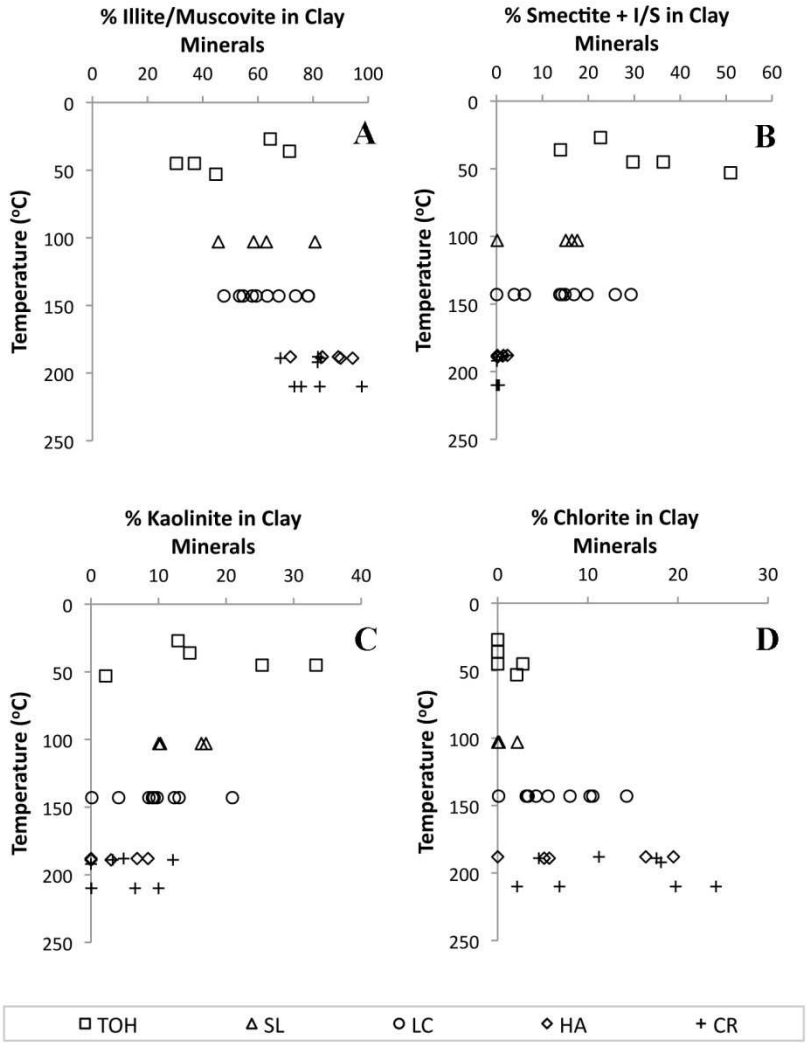

Figure 4.32 Analysis of the clay mineral fraction measured in the bulk sample by QXRD. Percent **A**) Illite, **B**) Smectite + I/S, **C**) Kaolinite and **D**) Chlorite within the clay fraction.

QXRD analysis of the bulk rock illustrates that samples from the lower temperature TOH well (27-50^{o}C) are composed of around 30wt% smectite or I/S. (Figure 4.31F); around 50% of the total clay minerals measured in these TOH is smectite or I/S (Figure 4.32B). The abundance of smectite + I/S falls throughout the Wilcox shale as temperatures increase. At 188^{o}C <1wt% smectite + I/S is recorded.

As with smectite, kaolinite is most abundant in the lower temperature TOH well (27-50^{o}C), averaging 8 wt%. The amount of kaolinite falls to 2 wt% at 188^{o}C, similar levels were also measured in the hotter CR-L samples (Figure 4.31G).

In the bulk clay fraction illite/muscovite is the dominant clay mineral. Total weight percentage in the whole rock averages 25 wt% in the lower temperature TOH wells and increases to ~40 wt% in the hotter CR and HA wells, 188-210^{o}C (Figure 4.31E). As a percentage of the total clay the same trend is observed (Figure 4.32A). The average in the TOH well is 51.5%. This increases to >80% in the hotter HA and CR wells.

Chlorite is also recorded in the shale suite sampled in the Wilcox group. Chlorite abundance increases with increased temperature. Below 104^{o}C less than 1 wt% chlorite is present in the Wilcox shale, abundance increases to between 5 and 6 wt% in the hotter wells above 180^{o}C (Figure 4.31H). The same trend is observed when considering the percentage chlorite in the total clay component (Figure 4.32D).

4.8.2. Analysis of the Wilcox Shale <2 µm Clay Fine Fraction

The percentage illite and expandables (smectite) within in the I/S mixed layer was determined within the <2 µm clay fraction. Full results are given in Table 4.10. Diffractograms are shown in Appendix 8.

Bulk analysis indicates that there was up to 25% I/S and discrete smectite in the lower temperature TOH well (Figure 4.31F). Analysis of the <2µm clay fraction indicates that the I/S in the low temperature TOH well is dominated by the smectite fraction with less than 20% illite (Figure 4.33A). With increased burial temperatures there is a trend towards more illite in the I/S fraction. In the SL well at 104^{o}C ~60% is illite this increases to ~70% by 143^{o}C in the LC well. Measurements in the hotter HA and CR wells are more scattered and illite percentage ranges from 60 to 90%.

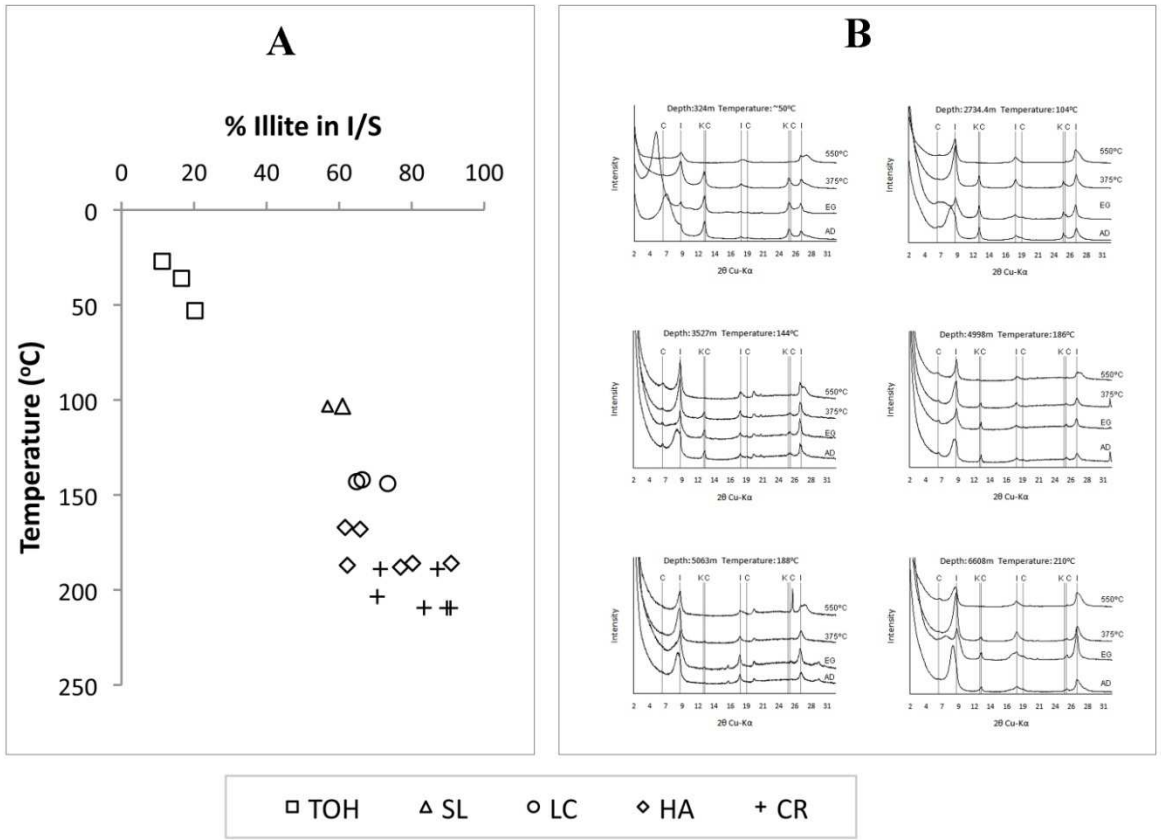

Figure 4.33 X-Ray diffraction analysis of the <2 µm clay fraction. (**A**) <2 µm clay fraction analysis of the percentage illite within mixed layer I/S. (**B**) Diffractograms, showing Air Dried (AD) and Ethylene Glycolated (EG) and heat (375^{o}C and 550^{o}C) treatments of the <2 µm clay fraction.

Well	Depth (m)	Temperature (^{o}C)	001/002	002/003	%I in I/S	%EXP
TOH	324.3	27	8.5	5.7	11.2	88.8
TOH	411.8	36	8.6	5.6	16.5	83.5
TOH	714.5	53	8.7	5.6	20.2	79.8
SL	2734.2	104	9.3	5.3	60.9	39.1
SL	2735.0	104	9.2	5.3	56.8	43.2
LC	3500.3	142	9.3	5.3	66.3	33.7
LC	3505.8	143	9.4	5.3	64.8	35.2
LC	3527.1	144	9.5	5.2	73.4	26.6
HA	4277.3	167	9.3	5.3	61.7	38.3
HA	4287.3	168	9.4	5.3	65.8	34.2
HA	4983.2	186	9.7	5.1	90.9	9.1
HA	4998.4	186	9.5	5.2	80.2	19.8
HA	5063.0	187	9.3	5.3	62.3	37.7
HA	5076.7	188	9.5	5.2	76.9	23.1
CR	5813.1	189	9.5	5.3	71.3	28.7
CR	5818.3	189	9.7	5.2	87.1	12.9
CR	6374.9	204	9.4	5.3	70.5	29.5
CR	6605.9	209	9.7	5.2	83.4	16.6
CR	6607.1	210	9.8	5.2	89.7	10.3
CR	6608.4	210	9.7	5.1	90.7	9.3

Table 4.10 001/002 and 002/003 I/S reflection of <2 µm glycolated fine fraction. Illite (I) and expandable (EXP) percentages determined using the method described by Moore and Reynolds (1997).

4.9. Discussion

Petrographic analysis of Wilcox sandstones in this study indicates that the amount of quartz cement increases as a function of temperature up to ~150^{o}C. Above 150^{o}C the overall volume of quartz cement falls. Similar results were recorded by Land and Fisher (1987) and Dutton and Loucks (2010). One possibility for the reduction of quartz cement in these hotter Wilcox samples is the increase in rock fragments observed in samples >150^{o}C (Dutton and Loucks, 2010). The overall effect is to reduce the available quartz surface area which in turn will result in limited quartz cementation (Walderhaug, 1996; Walderhaug et al., 2000; Taylor et al., 2010).

In addition to the increase in rock fragments in the deeper Wilcox sandstone samples the early and late precipitations of carbonates and illite have been observed in this study. Indeed these minerals have been observed precipitated up against quartz faces (Figure 4.17). Studies show that the precipitation of both clay minerals (Heald and Larese, 1974; Pittman et al., 1992; Aagaard et al., 2000; Walderhaug et al., 2006; Franks and Zwingmann, 2010) and carbonates (Boles, 1978; Hendry et al., 2000; Gier et al., 2008) will act to further reduce quartz surface area and pore space, thus having a negative impact on quartz cementation.

The impact that clay mineral and carbonate precipitates have on quartz cementation is illustrated by the discrepancies that occur when attempting to model the volume of quartz cement that precipitates in high temperature (>150^{o}C) Wilcox sandstones (Figure 4.22). In sample GOM11 (188^{o}C) quartz cement was overestimated by 14.4 %bv a result of modelling quartz cementation alone and not accounting for other precipitates. These findings strongly indicate that available quartz surface area is a major control on quartz cementation, indicating that quartz cementation is controlled by the rate of quartz precipitation.

To understand the full quartz cementation history of these Wilcox sandstones measurements of $\delta^{18}O_{(cement)}$ were made. However, $\delta^{18}O_{(cement)}$ is a dual function of the temperature at which the cement formed and the isotopic composition of the formation

fluids $\delta^{18}O_{(water)}$. It is therefore difficult to determine full cement histories from $\delta^{18}O_{(cement)}$ measurements alone.

It is argued that detailed fluid inclusion analysis could constrain the temperature, salinity and $\delta^{18}O_{(water)}$ in which cement formed (Haszeldine et al., 1984; Burley et al., 1989; Osborne and Haszeldine, 1993; Walderhaug, 1994a; Wilkinson et al., 1998; Girard et al., 2001). However, these inclusions are often only located close to the detrital quartz (Walderhaug, 1994a; Rossi et al., 2002) and may be subject to resetting (Osborne and Haszeldine, 1993; Osborne and Haszeldine, 1995; Worden et al., 1995; Goldstein and Rossi, 2002). No such measurements have been made in this study. Therefore, the timing of quartz cementation in this study is constrained using a range of known end member thermal and isotopic conditions. These conditions are, the $\delta^{18}O_{(water)}$ composition of likely depositional water:

Eocene Texas marine (-1‰) and meteoric (-3‰) waters (Fisher and Land, 1986b).

Furthermore formation temperatures can be restricted to anywhere between likely depositional conditions and known maximum burial temperatures of each well:

~10^{o}C, 104^{o}C, 143^{o}C and 188^{o}C

In addition the 80^{o}C cementation threshold suggested in current quartz cementation modelling can be examined. Measurements of $\delta^{18}O_{(water)}$ made in the Gulf of Mexico region over a wide range of temperatures (Morad et al., 2002) can also be used as a guide.

Initial petrographic analysis highlighted the existence of 2 different luminescing zones in the low temperature (104^{o}C) GOM6 sample. The lighter grey zone predates the darker zone as it has been observed sandwiched between the detrital grain and the later darker precipitate. However, it should be noted this grey cement is not observed on every grain of sample GOM6, indicating that it may not have formed in-situ. Isotopic analysis of GOM6 detrital quartz grains shows that grains containing the grey cement ($\delta^{18}O$ = +6.5 to +11.0‰) have a lighter average $\delta^{18}O$ compared to grains hosting only the darker cement ($\delta^{18}O$ = +11.5 to +15.0‰), indicating that grains may have a separate provenance.

Furthermore, isotopic evaluation of the lighter grey cement illustrated $\delta^{18}O_{(cement)}$ is 2‰ heavier than the more common darker cement. High resolution isotopic profiling using a 2 μm SIMS beam indicates little isotopic variation in the grey zone. To assess when this grey cement may have precipitated Clayton et al.'s (1972) fractionation equation was used to calculate the formation conditions that must be satisfied to precipitate the $\delta^{18}O_{(cement)}$ recorded in the initial lighter grey zone (+27.5 to +26.8‰) (Figure 4.34). Also plotted are measured $\delta^{18}O_{(water)}$ of formation waters in the Gulf of Mexico region (Morad et al., 2002) as well as estimated Gulf of Mexico Eocene meteoric and marine conditions (Fisher and Land, 1986b).

One possible scenario is that this region of quartz cement has formed on the Texas delta at temperatures ~40^{o}C in a mixture of Eocene meteoric and marine water ($\delta^{18}O_{(water)}$ = -3 to -1‰). However, this lighter grey cement represents ~3 %bv and at such low temperatures the kinetics of quartz precipitation are slow (Williams and Crerar, 1985b; Walderhaug, 1996). Although it has been shown that over a long period of time (+10 million years) it may be possible to precipitate quartz at these temperatures (Matsuhisa et al., 1979), thermal modelling of the Wilcox sandstone indicates that the Wilcox is only at this temperature for around 1-2 million years (Figure 4.7). It is therefore unlikely this substantial volume of cement represents an early diagenetic precipitate.

A more likely scenario is that the grey cement is pre-depositional. The majority of the detrital quartz that forms the Wilcox can be traced back to the southern Rockies, forming during the Laramide orogeny, a period of intense metamorphic activity (Galloway et al., 2000; McDonnell et al., 2008). Taylor (1974) suggests $\delta^{18}O$ values of metamorphic waters range from +5 and +25‰. This would equate to a precipitation temperature of between 80 and 200°C (Figure 4.34), lower than expected for metamorphic activity.

It is therefore more probable that the grey area represents a pre-depositional diagenetic cement formed in waters of unknown $\delta^{18}O$. Precipitation prior to deposition on the Texas delta is a scenario supported by weathering characteristics such as the rounding of the grey cement on grain 1 (Figure 4.19).

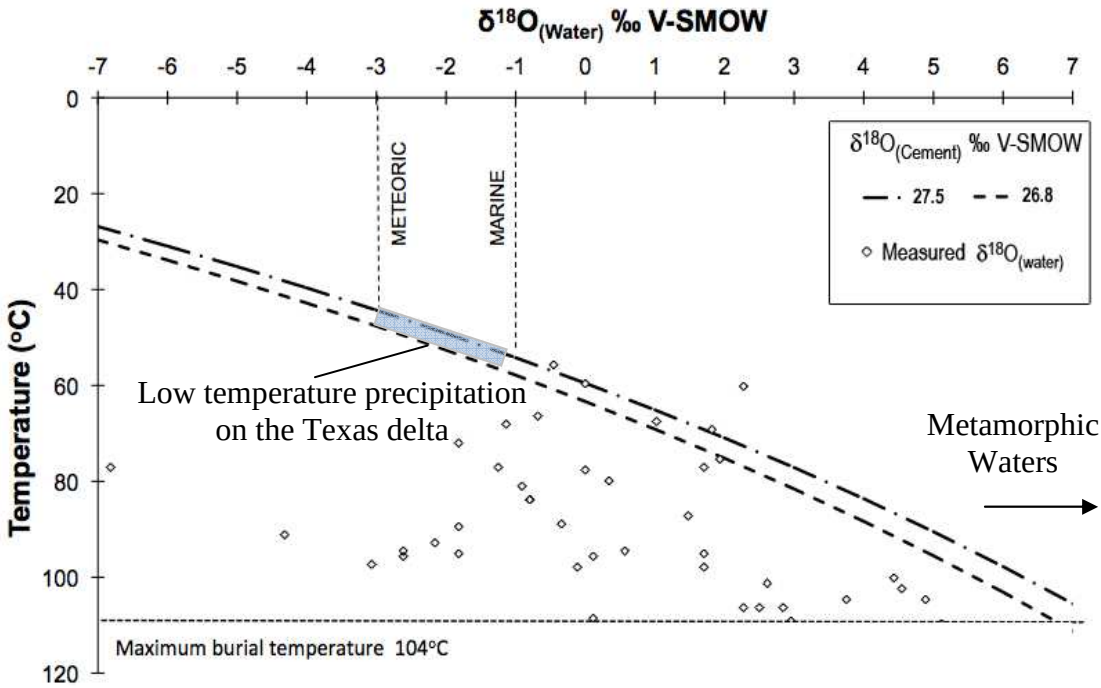

Figure 4.34 Plot of $\delta^{18}O_{(water)}$ in equilibrium with $\delta^{18}O_{(cement)}$ = +27.5‰ and 26.8‰ as a function of temperature (Clayton et al., 1972). $\delta^{18}O_{(cement)}$ measurements made across the cement that appears lighter grey under SEM-CL of sample GOM6.

In the Wilcox, as in the North Sea Ness study, the darker cement consists of two distinct isotopic regions. Initially a thin rind of isotopically heavier cement is observed ($\delta^{18}O_{(cement)}$ = +28.5 to +25.5‰) closest to the detrital grain. The $\delta^{18}O_{(cement)}$ of the remaining 90% of the cement, referred to here after as the 'bulk cement', continues to decrease towards the edge of the overgrowth but at a less dramatic rate ($\delta^{18}O_{(cement)}$ = +25 to +18.3‰). The variable $\delta^{18}O_{(water)}$ and temperature conditions at which the cement could form are illustrated in Figure 4.35.

According to current quartz cementation modelling theory the excepted threshold at which precipitation initiates is around 70-80^{o}C (Bloch and Helmold, 1995; Canals and Meunier, 1995; Walderhaug, 1996; Lander and Walderhaug, 1999; Wangen, 1999; Walderhaug, 2000; Walderhaug et al., 2000; Ajdukiewicz and Lander, 2010; Taylor et al., 2010). For this rind to have precipitated at these temperatures a water where $\delta^{18}O_{(water)}$ = +4.4‰ is required (Point W, Figure 4.35). This value is much heavier than direct $\delta^{18}O_{(water)}$ measurements made in the Gulf of Mexico region at this temperature (Morad et al., 2002).

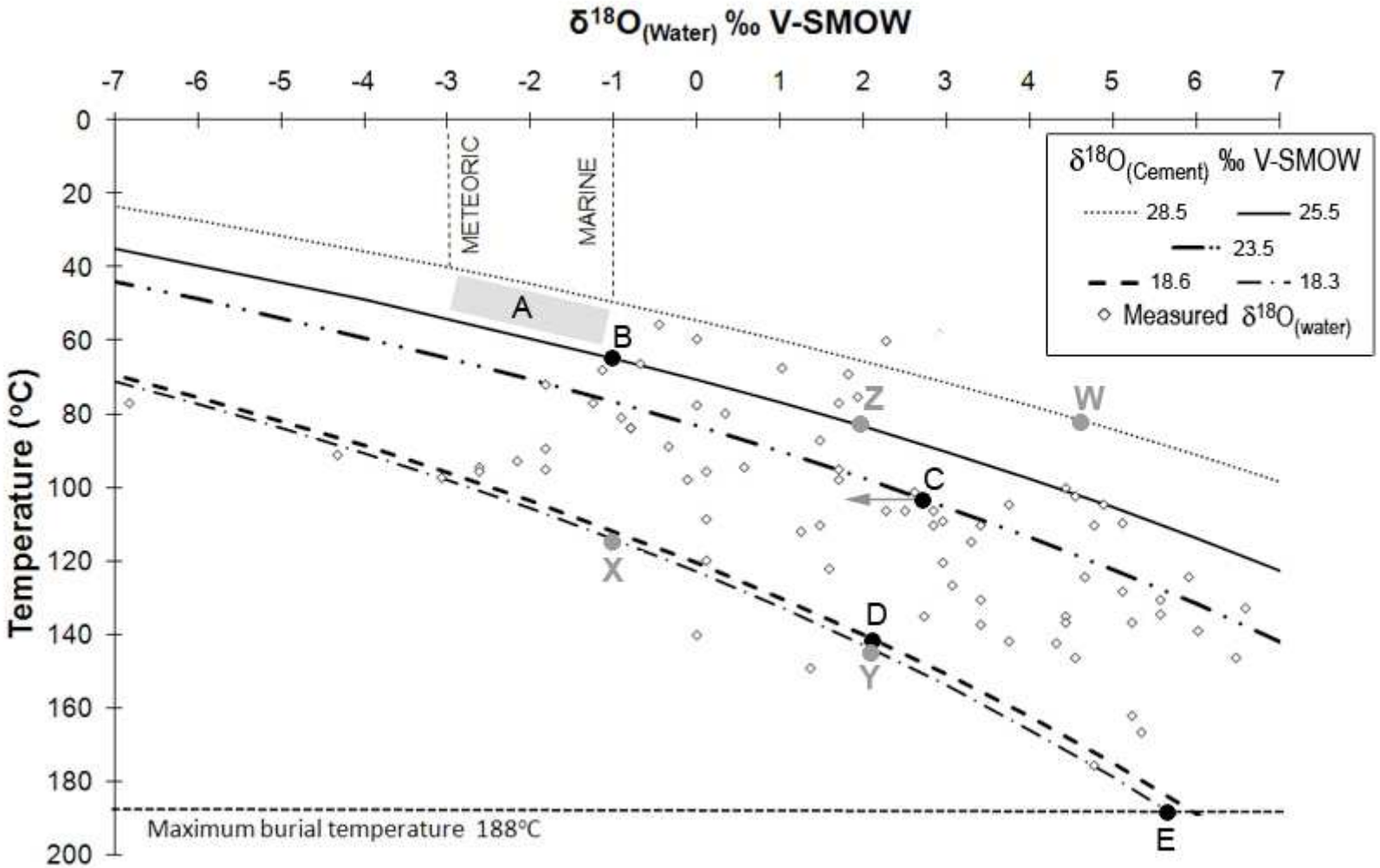
δ18O(Water) ‰ V-SMOW
-7 -6 -5 -4 -3 -2 -1 0 1 2 3 4 5 6 7
0 20 40 60 80 100 120 140 160 180 200
Temperature (°C)
METEORIC
MARINE
A
B
C
D
E
W
X
Y
Z
δ18O(Cement) ‰ V-SMOW
28.5
25.5
23.5
18.6
18.3
Measured δ18O(water)
Maximum burial temperature 188°C

Figure 4.35 Plot of $\delta^{18}O_{(water)}$ in equilibrium with $\delta^{18}O_{(cement)}$ = +28.5‰, +25.5‰, +23.5‰, +18.6‰ and +18.3‰ as a function of temperature (Clayton et al., 1972). $\delta^{18}O_{(cement)}$ of initial cement "rind" indicates precipitation within the grey box A. The bulk cement forms from point B or at hotter temperatures along the 25.5‰ line. Minimum $\delta^{18}O_{(cement)}$ (youngest cement) and maximum temperatures are represented at points C (GOM6, 104^{o}C), D (GOM8, 143^{o}C) and E (GOM11, 188^{o}C). As no measurements were made in the outer 20% of the overgrowths in GOM6 it is likely the 23.5‰ represent a lower temperature compared to the maximum burial temperature. The grey line from point C indicates the possible conditions of the outer 20% of cement in GOM6. Measured $\delta^{18}O_{(water)}$ data is taken from Morad et al. (2002).

It is more probable that quartz cementation begins below 80^{o}C. One possibility is that this isotopic rind formed in a mixture of meteoric and marine waters ($\delta^{18}O_{(water)}$ = -3‰ to -1‰) at temperatures around 50^{o}C (shaded area A, Figure 4.35). Unlike the North Sea Ness the Wilcox has been buried in a relatively short period of time (60 million years). Time temperature modelling indicates that the Wilcox only remained below 50^{o}C for as little as 5 million years (Figure 4.7). For precipitation to have occurred during this window a growth rate of 1.16x10^{-20}mol/cm^{2}.s is required. This rate is much higher than those predicted by Walderhaug's (1994b) rate equation at these temperatures; extrapolation of Walderhaug's kinetics to 45^{o}C yields a rate of 1.93x10^{-21} mol/cm^{2}.s.

In the North Sea Ness study it is proposed that silica may be sourced from the early low temperature dissolution of K-feldspar. Similar processes have been recorded in the Wilcox (Boles and Franks, 1979; Fisher and Land, 1986b; Dutton and Loucks, 2010). Helgeson (1984) calculated that at low temperatures, K-feldspar dissolution rates are higher than the above cement growth rates and therefore is not a rate limiting process. However, the dissolution of feldspar as shown in Equation 1.2 will result in the formation of kaolinite. Sample GOM6 in which these measurements were performed contains <1 %bv of non quartz minerals. Furthermore, the majority of this fraction is composed of carbonate minerals (Figure 4.16). The lack of substantial kaolinite in this sample makes it unlikely silica is sourced from K-feldspar.

At these temperatures other possible silica sources could include low temperature biogenic recrystallisation (Siever, 1957; Carver, 1980; Hurst and Irwin, 1982; Vagle et al., 1994; Hesse and Schacht, 2011) and the precipitation of quartz direct from sea waters supersaturated with respect quartz (Mackenzie and Gees, 1971; McBride, 1989). However, quartz sourced from the aforementioned processes produces characteristic textures (Vagle et al., 1994; Goldstein and Rossi, 2002; Weibel et al., 2010) that are not visible in these samples. Furthermore, limited biogenic material is reported in the Wilcox (Dutton and Loucks, 2010).

A further possible silica source is pressure solution. Bjørkum (1996) concludes that quartz dissolution is enhanced at quartz - illite or quartz - mica interfaces (clay induced dissolution or CID). Furthermore Bjørkum (1996) indicates that this process can occur at pressures as small as 10 bar, equivalent to 100 m overburden (<25^{o}C). However, internally within this sandstone sample little illite or mica is observed. It may be possible silica is sourced externally in local shale units which, even at low temperatures (TOH well), are rich in illite and mica (Figure 4.31E); quartz grains found in shale are likely to be more susceptible to dissolution because of their smaller grain size (Evans, 1990; Peltonen et al., 2008).

Below 50^{o}C mechanical processes dominate; chemical processes such as quartz cementation have always been considered a later (>80^{o}C) stage process (McBride et al., 1991; Pittman and Larese, 1991; Lander and Walderhaug, 1999). However recent evidence suggests that silica may be released from grain fracturing a product of this early compaction (Chuhan et al., 2002; Makowitz et al., 2006). Grain fracturing is common in rapidly subsiding basins such as the Gulf of Mexico (Makowitz and Milliken, 2003) and is a process that was observed in sample GOM6 (Figure 4.15). Grain fracturing will reduce grain size, which can increase the amount of quartz dissolution as well as increase quartz surface area; both outcomes will enhance the possibility of low temperature quartz precipitation (Walderhaug, 1996).

Overall within GOM6 no clear low temperature silica source was observed. However, it may be possible that either K-feldspar dissolution or illite/mica induce pressure solution has occurred locally internally or externally outside the scope of these observations. It is also possible that grain fracturing resulting from mechanical compaction enhances quartz dissolution at low temperatures facilitating the precipitation of the observed cement rind.

This early rind equates to only around 1%bv of the total rock; the precipitation of a small amount of quartz cement at temperatures lower than 50^{o}C may impact on degree mechanical compactional that can be achieved. However, it is usually considered that compaction is only inhibited by the precipitation of around 2 to 3% quartz cement (Bjørlykke and Egeberg, 1993; Bjørlykke and Høeg, 1997). Indeed, McBride et al (1991) only observed localised effects on compaction with the precipitation of >5% cement in the Wilcox. However, this rind is likely to impact on velocity measurement; similar volumes of cement have been recorded to effect velocity readings around 70^{o}C by Marcussen (2010).

Out into the overgrowth away from this isotopic rind the remaining 'bulk cement' (~90% of the total cement) has precipitated with an isotopic composition where $\delta^{18}O_{(cement)}$ ranges from +25.5‰ to +18.3‰. It is unclear if this bulk material represents a separate cementation episode or simply a continuation of the rind. Should precipitation initiate ($\delta^{18}O_{(cement)}$ = +25.5‰) directly or soon after the initial rind formation waters are likely to be close to $\delta^{18}O_{(water)}$ = -1‰ at temperatures around 60^{o}C (Point B, Figure 4.35).

$\delta^{18}O_{(cement)}$ is a function of the formation temperature and isotopic composition of the formation waters. The isotopic stratigraphy observed across overgrowth in the three Wilcox samples (+25‰ to +18.3‰) therefore reflects either a change in formation waters, temperature, or both.

This $\delta^{18}O_{(cement)}$ stratigraphy is unlikely to be created by a change in $\delta^{18}O_{(water)}$ alone; such a scenario would require formation waters to evolve in a negative direction, this is unusual as the oxygen isotopic composition of formation waters generally evolve to more positive values with burial as a result of water-rock reactions (Aplin and Warren, 1994; Morad et al., 2002). Furthermore, this scenario would require temperature to remain constant for a substantial period of time; over 1000 million years in the case of

GOM6 at 104^{o}C (Walderhaug 1994b). Obviously time-temperatures histories of the Wilcox (Figure 4.7) illustrate that there is no such period.

A second possibility is that this cement precipitates in constant $\delta^{18}O_{(water),}$ in this scenario the $\delta^{18}O_{(cement)}$ stratigraphy represents change in temperature alone. If cementation is continuous between the rind and bulk cement then precipitation would occur in formation waters where $\delta^{18}O_{(water)}$ was around -1‰ (Point B to point X, Figure 4.35). This would indicate quartz cementation ends around 110^{o}C in the Wilcox sandstone. This is contrary to all known petrographic quartz quantification studies of the Wilcox (Dutton and Loucks, 2010), including this study (Figure 4.18); quartz cement quantities continue to increase up to temperatures around 150^{o}C.

It is possible that bulk cement is a separate phase from the rind and begins to precipitate at a higher temperature, for example at 80^{o}C (Point Z, Figure 4.35). In such a scenario quartz cementation would continue to 150^{o}C (Point Y, Figure 4.35). However, there is no petrographic evidence that may suggest more than one episode of cementation (e.g. Girard et al., 2001; Girard et al., 2002).

It is more likely that the isotopic stratigraphy measured in these Wilcox samples is a result of the dual influence of changing temperature and formation waters. Using the maximum burial temperatures for each well (Figure 4.7) it is possible to constrain the evolution of the formation waters (Table 4.11).

Sample	Maximum burial temperature (^{o}C)	Youngest $\delta^{18}O_{(cement)}$ (‰)	$\delta^{18}O_{(water)}$ (‰)	Relative distance of youngest cement measured from DQ	Point on Figure 4.35
GOM6	104	23.5	2.8	~80%	C
GOM8	143	18.6	2.4	~95%	D
GOM11	188	18.3	5.6	~95%	E

Table 4.11 Calculation of the evolution of $\delta^{18}O_{(water)}$ in the Wilcox sandstone using Clayton et al. (1972) fractionation equation. In the GOM6 sample the youngest was not successfully analysed, the captured isotopic stratigraphy in this sample only represent 80% of the growth of the cement.

The $\delta^{18}O_{(water)}$ values calculated in Table 4.11 fall within the limits of measured data for the Gulf of Mexico region shown in Figure 4.35. These calculations indicate that at 104^{o}C $\delta^{18}O_{(water)}$ is slightly heavier than at 143^{o}C. However, the youngest cement measured in the GOM6 sample is only represents the growth of 80% of the overgrowth. It is likely therefore that where $\delta^{18}O_{(cement)}$ = 23.5‰ is not a true representation of the maximum temperature of that sample. It is probable the true $\delta^{18}O_{(water)}$ is much lower at 104^{o}C (as indicated by the grey arrow from point C, Figure 4.35).

If the bulk cement begins to precipitate in formation waters around -1‰ at 60^{o}C and continues through to 188^{o}C (point B to E, Figure 4.35) then $\delta^{18}O_{(water)}$ must evolve by around 6.6‰ (Table 4.11); significantly the majority of this change (3.6‰) would occur above 143^{o}C (point D to E, Figure 4.35).

Using Taylor's (1974) mass balance equation it is also possible to estimate the evolution of $\delta^{18}O_{(water)}$ that occurs as a response to mineralogical changes in a closed system. As outlined in Aplin and Warren (1994) this is achieved by estimating the initial isotopic composition of the formation waters, the minerals reacting and the temperature these minerals react. The most likely minerals to react are low temperature clay minerals such as smectite and kaolinite which have been observed undergoing illitisation in these

samples and across the Wilcox (Boles and Franks, 1979). Assuming the initial $\delta^{18}O$ composition of the smectite and kaolinite are +22‰, illite = +19‰ (Aplin and Warren, 1994) with a volume of water equal to the rock porosity it is possible to estimate changes in the $\delta^{18}O_{(water)}$ (Table 4.12)

Maximum burial Temperature (^{o}C)	**Smectite (Ave.wt%) record in Wilcox Shale**	**Kaolinite (Ave.wt%) record in Wilcox Shale**	**$\delta^{18}O_{(water)}$ (‰)**
0-50	12.0	10.0	-1
104	6.0	5.0	+2.2
143	4.5	4.0	+2.9
188	3.8	3.0	+3.5

Table 4.12 Calculated evolution of $\delta^{18}O_{(water)}$ in the Wilcox Shale using Taylor's (1974) mass balance equation

The calculations made in Table 4.12 illustrate that the biggest change in $\delta^{18}O_{(water)}$ occurs below 143^{o}C. Importantly these calculations demonstrate that very little variation in $\delta^{18}O_{(water)}$ as a response to diagenetic reactions is likely to occur between 143 to 188^{o}C. These calculations are contrary to the calculation made in Table 4.11; there are two possible scenarios that may account for this:

1. The Wilcox system is open and has been invaded by a late (>143^{o}C) influx of isotopically heavy basinal brines.
2. $\delta^{18}O_{(cement)}$ values recorded for the youngest cement in GOM11 (188^{o}C) represent a lower precipitation temperature, i.e. cementation terminated before maximum burial.

An influx of $\delta^{18}O$ enriched basin brines into the Wilcox would require the large scale movement of large quantities of waters. The movement of large masses of water is unlikely as was proven by Bjørlykke and Egeberg (1993) and Aplin and Warren (1994).

The lack of available water indicates that it is more probable that quartz cementation has terminated around 150^{o}C. There are three factors are needed for quartz cementation to occur:

1. A silica source
2. A suitable transport mechanism
3. A quartz surface on which to precipitate

If cementation has terminated at around 150^{o}C as the $\delta^{18}O_{(cement)}$ measurements indicate then one or more of these three processes must be impeded.

Mineralogical analysis of the Wilcox Group indicates that the majority of silica is produced internally within the Wilcox sandstone (Table 4.13); the most likely silica source is stylolitisation and pressure solution (Heald, 1955; Heald, 1959; Park and Schot, 1968; Robin, 1978; Houseknecht, 1988; Tada and Siever, 1989; Dewers and Ortoleva, 1990; Walderhaug, 1996; Bjørkum et al., 1998; Walderhaug, 2000; Walderhaug et al., 2000; Walderhaug and Bjørkum, 2003; Kim and Lee, 2004; Baron and Parnell, 2007). As there is no evidence to suggest that stylolites are finite or 'dry up' within the temperature range of these Wilcox sandstones (Heald, 1955; Park and Schot, 1968; Robin, 1978; Walderhaug et al., 2006) it must be assumed that the internal silica source is still active above 140^{o}C. Although it is possible an increase in the volume of kaolinite may reduce the effect of stylolites (Walderhaug et al., 2006) there is no evidence of authigenic kaolin growth at high temperatures in these rocks (Figure 4.8F).

Reaction	Change in limiting mineral (%bv)	Silica produced (per mass of reactant)	Total silica released (%bv of Wilcox sandstone)
Illitisation of kaolinite	Kaolinite ~10	0.22	4.5
Illitisation of smectite	Smectite ~ 15	0.20	2.9
Albitisation of feldspar	Feldspar ~6	0.10	1.3
		Max[†]	7.4

Table 4.13 Calculation of the maximum silica production in the Wilcox shale. Calculations are based on Equation 1.3 to Equation 1.5. Mineral volumes are maximum recorded values (Figure 4.31). [†]As K-feldspar is a reactant in both Equation 1.3 and 1.4 it is impossible for both reactions to release the maximum silica yields calculated. Therefore if all silica were to be transported into the adjacent sandstones and precipitate as quartz cement it would fill a maximum of 7.4 %bv of the Wilcox sandstone.

As was discussed in the North Sea study the heterogeneity of the formation waters inferred by the $\delta^{18}O_{(cement)}$ measurements (Table 4.11) indicates that silica is most likely transported by diffusion. For diffusive processes to be repressed the initial concentration gradient that acts to drive transportation must be lost. This could occur either by the silica source 'drying up' or by precipitation being retarded. In the first instance a lack of a silica source will prevent the diffusive gradient being maintained. However, as mentioned before there is no evidence stylolites stop producing silica; this would imply that diffusion and thus cementation is hindered by precipitation sites being limited or blocked.

In these samples ankerite is seen replacing plagioclase (Figure 4.17) above 150^{o}C, furthermore illite is observed coating quartz grains (Figure 4.17). These findings are in agreement with Dutton and Loucks (2010) who also recorded ankerite replacing quartz. Ankerite and illite precipitation will reduce porosity, block intergranular pore space and overall quartz surface area (Boles, 1978; Boles and Franks, 1979; Hendry et al., 2000). The precipitation of late stage diagenetic ankerite and illite will therefore act not only to

hinder potential silica transport mechanisms but also to reduce the available space for quartz cementation to occur. It is therefore likely that the $\delta^{18}O_{(cement)}$ recorded in GOM11 represents precipitation of quartz across a similar window as GOM8 and that this window closes around 150^{o}C.

4.10. Conclusion

The conditions and timing of quartz cementation in the Wilcox sandstone from 5 onshore Texas wells has been constrained by use of SIMS oxygen isotope microanalysis, quantitative petrography and quantitative X-Ray Diffraction. The results indicate that quartz cementation begins around 50^{o}C.

At these low temperatures quartz would have formed in waters close to meteoric composition. Petrographic analysis reveals little remnants of K-feldspar or kaolinite deposits; it is therefore unlikely that silica is sourced K-feldspar dissolution. This would indicate that silica is sourced from low temperature quartz pressure solution or possibly as a result of grain fracturing.

The majority of the cement observed (+90%) in the Wilcox Formation has precipitated above 60-80^{o}C. Although silica producing reactions are recorded in the adjoining Wilcox shale units, calculations (Table 4.13) highlight that the majority of the silica is internally produced. Internal sources are likely to include stylolite and local pressure solution.

Quantification of mineralogical processes occurring in the Wilcox shale indicate that it is likely $\delta^{18}O$ of the formation waters evolves in a positive direction as a response to clay mineral reactions. These estimates of $\delta^{18}O_{(water)}$ indicate that if the Wilcox is a closed system then quartz cementation is inhibited around 150^{o}C. This coincides with the reduction in mineralogical activity recorded in the Wilcox shales, but also with the precipitation of pore reducing ankerite and illite in the Wilcox sandstone. These minerals appear to reduce the overall rate of quartz precipitation by reducing the surface area of quartz on which quartz cementation may nucleate.

5. Quartz Cementation Mechanisms in Reservoir Sandstones

Quartz cement is the most volumetrically significant diagenetic mineral observed in reservoir sandstones (Bjørlykke, 1979; McBride, 1989; Bjørlykke and Egeberg, 1993; Primmer et al., 1997; Giles et al., 2000; Worden and Morad, 2000). Precipitation of quartz during burial reduces porosity and is detrimental to reservoir quality. It is therefore important to accurately predict the extent and timing of cementation when considering the economical potential of a reservoir system and during the management of that reservoir. However, although broadly based predictive quartz cementation models exist they have never been validated on the microscopic scale at which cement forms.

In the two case studies presented in this investigation the conditions of quartz cementation have been constrained through the use of petrographic, mineralogical and high precision oxygen isotope analysis. The aim of this chapter is to compare and contrast the major findings of the North Sea Ness and Texas Wilcox studies to evaluate the overall controls on:

1. The timing of quartz cementation in reservoir sandstones
2. The sources of quartz cementation in reservoir sandstones

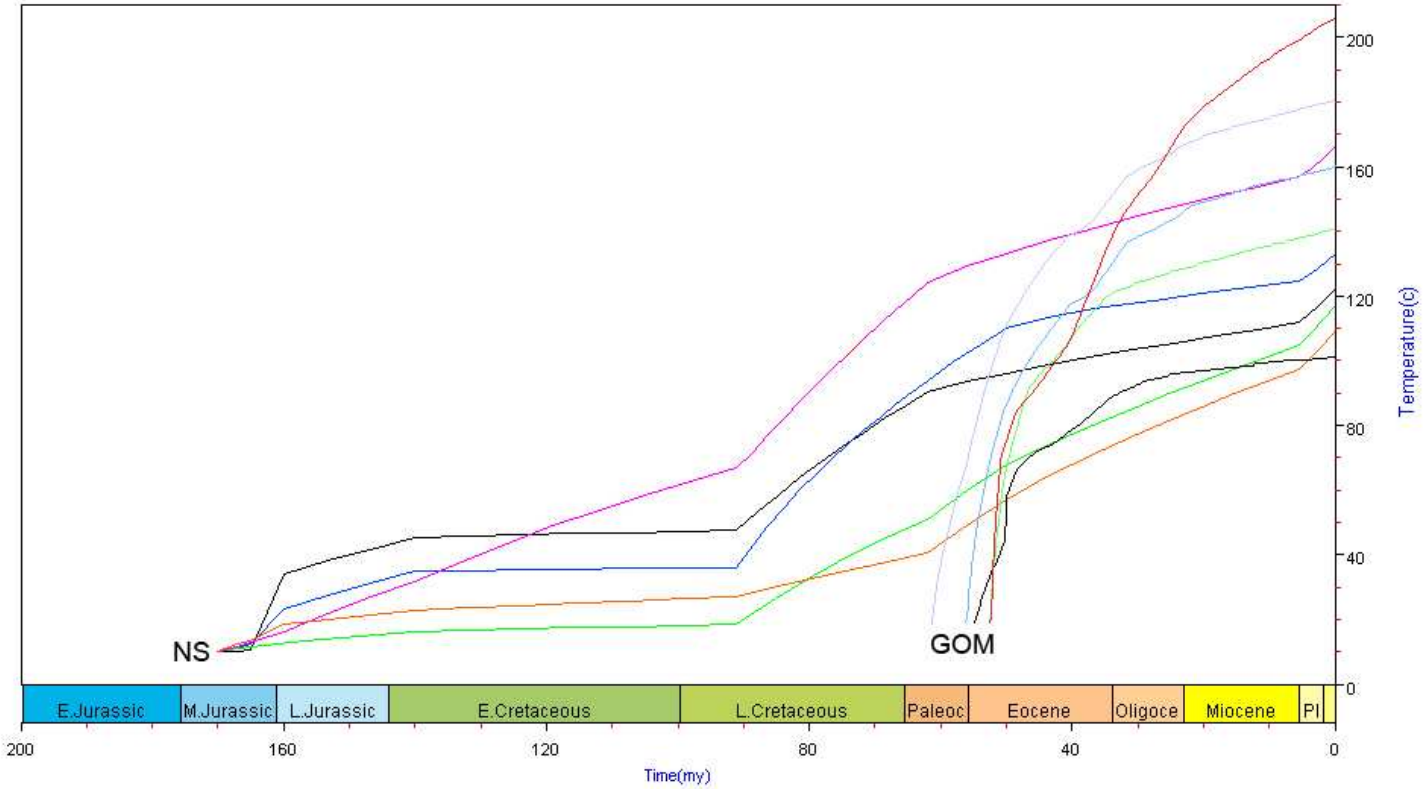

Figure 5.1 Time-Temperature histories of the Ness (NS) and Wilcox (GOM) wells.

5.1. The Timing of Quartz Cementation

$\delta^{18}O$ measurements of authigenic quartz cement are a function of the $\delta^{18}O$ of formation waters and the formation temperature. By combining time – temperature histories (Figure 5.1) with high precision SIMS analyses (Figure 5.2) the timing and conditions of quartz cementation in the North Sea Ness Formation (Chapter 3) and the Texas Wilcox (Chapter 4) sandstones were constrained.

Quartz cementation is believed to have a threshold temperature of 80°C (Ajdukiewicz and Lander, 2010). If this threshold is correct the oxygen isotopic composition of the quartz cement closest to the detrital grain should reflect the probable $\delta^{18}O_{(water)}$ at 80°C. In both studies the oldest cement analysed formed a rind of cement with a distinctly heavier $\delta^{18}O$ compared to that measured further out into the overgrowth (Figure 5.2). The heaviest and oldest $\delta^{18}O_{(cement)}$ recorded in this rind in the Ness Formation was +27.7‰ and +28.5‰ in the Wilcox sandstone.

Using Clayton et al.'s (1972) fractionation equation it is possible to calculate the $\delta^{18}O_{(water)}$ from which this rind would precipitate at 80°C (Table 5.1).

Temperature (°C)	**Ness** $\delta^{18}O_{(cement)}$ **= +27.7‰**	**Wilcox** $\delta^{18}O_{(cement)}$ **= +28.5‰**
80	+3.6	+4.4
50	-1.7	-0.9

Table 5.1 Calculation of $\delta^{18}O_{(water)}$ at 80°C and 50°C

In the North Sea Ness this rind would precipitate out at 80°C in a water where $\delta^{18}O_{(water)}$ is +3.6‰ , similarly in the Wilcox formation waters with a $\delta^{18}O$ of +4.4‰ would be required at 80°C. In both basins the $\delta^{18}O_{(water)}$ are more positive than would be expected at 80°C (see Figure 3.45 and Figure 4.35). Furthermore, in both basins precipitation from 80°C would require the $\delta^{18}O_{(water)}$ to become lighter during burial; this is unlikely

as waters usually become enriched with $\delta^{18}O$ as a response to recrystallisation of minerals during diagenesis (Aplin and Warren, 1994). It is therefore likely that quartz cementation begins below this 80^{o}C threshold.

It is more likely that the isotopic rind measured in the Ness and the Wilcox precipitates below 50^{o}C (Table 5.1,Figure 3.45 and Figure 4.35) in marine waters. At these lower temperatures the rate of precipitation is slow and only a small amount of cement precipitates; around 8% of the total cement in both basins. Although only a few microns in thickness the precipitation of low temperature quartz cement is likely to increase sandstone velocities and densities (Marcussen et al., 2010), fundamental parameters for reservoir quality modelling.

The remaining cement forms around 92% of the quartz cement observed in both studies. It is unclear if this bulk cement represents a continuation of this rind or if it is a separate episode of precipitation. Petrographically there is no clear evidence of more than one zone of cement (e.g. Girard et al., 2001) in either the Ness or Wilcox sandstone.

In the Ness the $\delta^{18}O_{(cement)}$ recorded in the 'bulk cement' ranges from +23.5‰ to +19.3‰, whereas in the Wilcox the range is +25.5‰ to +18.3‰ . Values of $\delta^{18}O_{(cement)}$ recorded for the 'bulk cement' in both basins are consistent with precipitation from 60-80^{o}C with $\delta^{18}O_{(water)}$ close to marine composition (Figure 3.45 and Figure 4.35). Furthermore, the smooth isotopic stratigraphies recorded across samples in both basins are consistent with precipitation in continuously evolving $\delta^{18}O_{(water)}$ and increasing temperatures.

These findings are in agreement with existing models proposed by Walderhaug (1996; 2000). Furthermore, the overall kinetics of quartz precipitation in both the North Sea Ness and Wilcox sandstone are consistent with those established in Walderhaug (1996;

2000) when calculated from 50^{o}C (Figure 5.3), with the exception of sample GOM11, where quartz cementation is inhibited around 150^{o}C.

Overall the high precision isotopic analyses carried out in this investigation illustrate that quartz cementation begins at a temperature as much as 30^{o}C lower than any previous isotopic or petrographic studies have documented (Walderhaug, 1994a; Walderhaug, 1994b; Primmer et al., 1997; Girard et al., 2001; Ajdukiewicz and Lander, 2010). The isotopic stratigraphies recorded in both studies indicate that, where free quartz surfaces remain available for precipitation, the bulk of quartz cementation occurs as a continuous process from around 50^{o}C through to maximum burial temperatures.

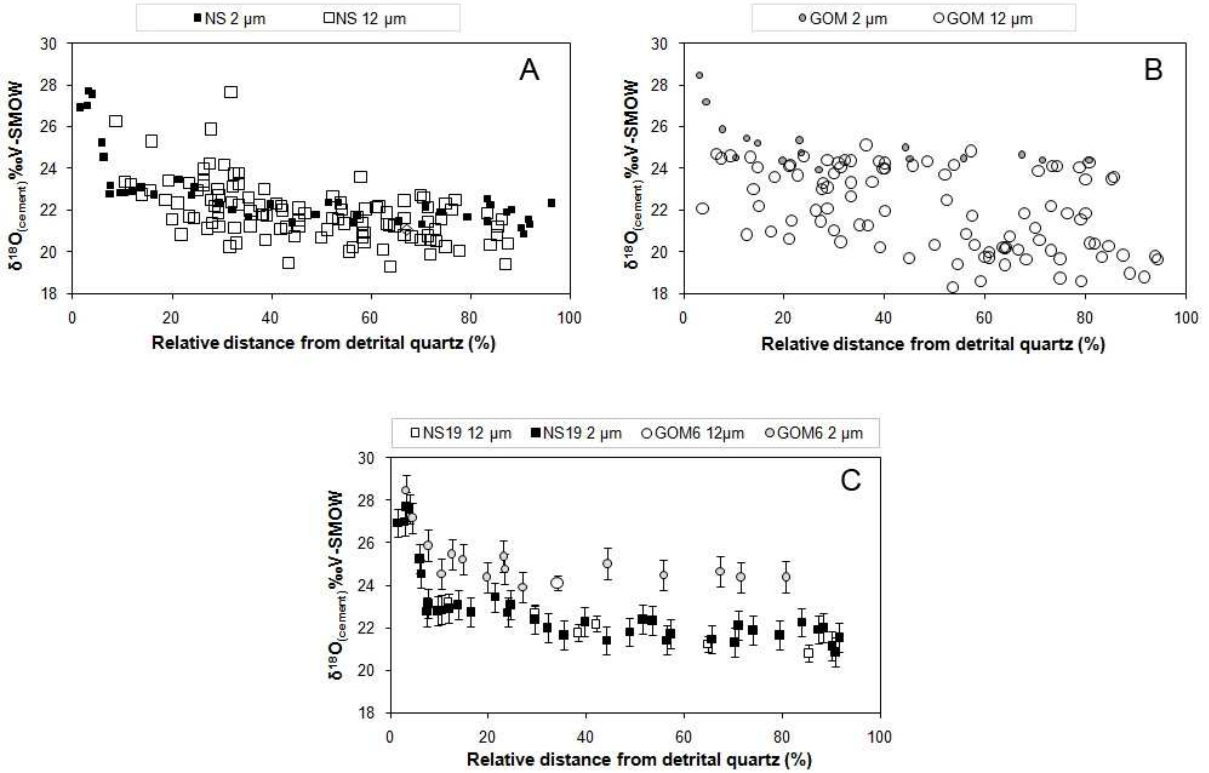

Figure 5.2 2 µm and 12 µm SIMS analysis of the North Sea Ness and Texas Wilcox sandstones. **A)** $\delta^{18}O_{(cement)}$ of the Ness sandstone vs. relative distance from the detrital quartz grain (%). **B)** $\delta^{18}O_{(cement)}$ of Wilcox sandstone vs. relative distance from initiation of cementation (%). **C)** 2 µm $\delta^{18}O_{(cement)}$ of Ness and Wilcox sandstone vs. relative distance from initiation of cementation (%).

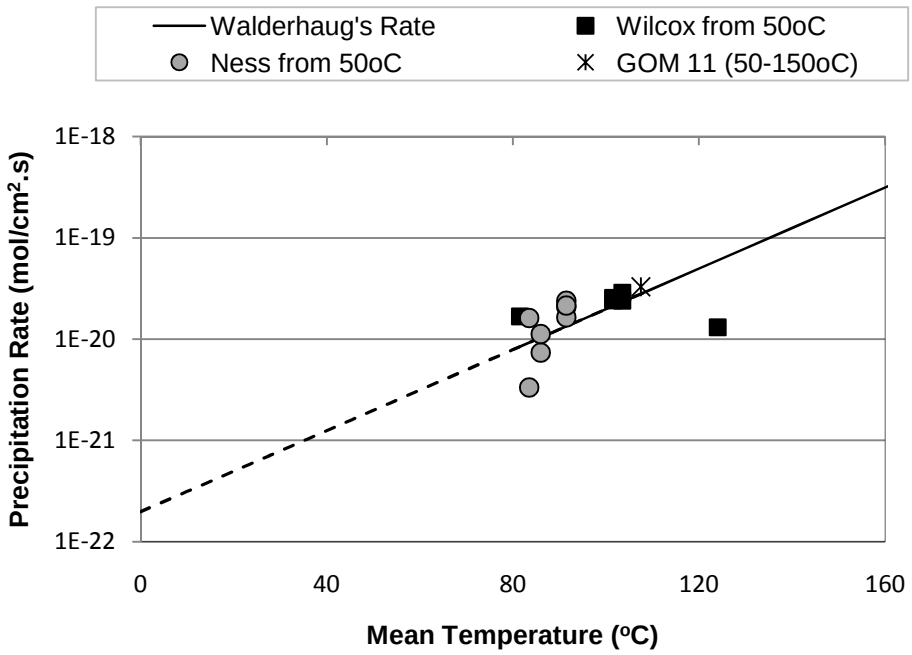

Figure 5.3 Average quartz cement growth rates expressed as a function of temperature. Growth rates are plotted against mean temperature; 50°C to maximum burial. The solid line represents the kinetics described by Walderhaug (1994b; 1996; 2000) Growth rates for GOM11 are recalculated assuming precipitation is terminated at 150°C.

5.2. The Source of Quartz Cement

In both the Ness and Wilcox studies many silica producing processes were observed; petrographic analysis revealed K-feldspar dissolution and albitisation, while the illitisation of smectite was recorded by XRD. These mineralogical studies were combined with time-temperature histories and high precision SIMS micro-analyses to constrain the source/s of the observed quartz cement.

The dissolution of K-Feldspar and subsequent precipitation of kaolinite has been discussed as a possible source of silica in many basins around the world (Land and Milliken, 1981; Glasmann, 1992; Wilkinson et al., 2001). Isotopic investigations (e.g. Haszeldine et al., 1992; Wilkinson et al., 2006) indicate this process can occur at temperatures as low as 30^{o}C in meteoric waters. It is therefore feasible that low temperature quartz cements are sourced from the dissolution of K-feldspar. However, in this investigation a low temperature (~50^{o}C) quartz cement rind was recorded in sample GOM6 (Figure 5.2) yet no clear evidence of K-feldspar dissolution is observed in this thin section (Figure 4.16). Furthermore, K-feldspar dissolution is also dependant on a constant influx of meteoric water; although this is possible in these deltaic sandstones it would remove silica from the system, preventing quartz cementation (Hurst and Irwin, 1982; Bjørlykke and Egeberg, 1993). It is therefore unlikely that silica is sourced from the dissolution of K-feldspar.

A further possibility is that the initial isotopically heavy rind is an early microquartz precipitate, perhaps resulting from the recrystallisation of biogenic silica (Jahren and Ramm, 2000; Goldstein and Rossi, 2002; Haddad et al., 2006). Biogenic silica is less thermodynamically stable and more soluble than quartz. It has been shown that at low temperatures cristobalite will transform to quartz given enough time; Mizutani (1970) calculated that at 50^{o}C 90% of cristobalite will transform to quartz over a 10 million year period. However, the thermal histories of the Wilcox samples indicate that there is insufficient time for such recrystallisation to occur (Figure 5.1). The resulting cement is

also likely to take the form of a chalcedonic pore filling, microcrystalline grain coating or mesocrystalline quartz overgrowths (Vagle et al., 1994; Hendry and Trewin, 1995; Haddad et al., 2006; Weibel et al., 2010). These textures are not evident in any samples analysed in this investigation, it is therefore unlikely that the quartz cement observed in this study is biogenic in origin.

Recent evidence also suggests that silica may be released by grain fracturing occurring during early compaction (Chuhan et al., 2001; Makowitz et al., 2006). Grain fracturing is more common in rapidly subsiding basins such as the Gulf of Mexico and is a process that was observed in sample GOM6 (Figure 4.15). The fracturing of quartz grains will cause quartz dissolution as well as increase quartz surface area; both outcomes will enhance the possibility of low temperature quartz precipitation. However, it is unlikely that the cement rinds observed in the Ness and Wilcox sandstones are generated from grain fracturing as the silica released from this process is more likely to precipitate around the active fracture as healing veins (Makowitz and Milliken, 2003; Makowitz et al., 2006).

Silica may be sourced from pressure solution or stylolitisation (Heald, 1955; Weyl, 1959; Park and Schot, 1968; de Boer, 1977; Robin, 1978; Baron and Parnell, 2007; Greene et al., 2009). Bjørkum (1996) indicates that this process can occur at pressures as small as 10 bar; equivalent to 100 m overburden (<25^{o}C). It is therefore feasible that silica for the rind and the bulk cement is derived from stylolitisation. However, within the scope of the thin sections analysed in this study limited pressure solution is observed, although stylolites and pressure solution are reported throughout the Brent and Wilcox Groups as well as sandstones across the world (Trurnit, 1968; Sibley and Blatt, 1976; Houseknecht, 1984; Houseknecht, 1988; Tada and Siever, 1989; Walderhaug, 1996; Spötl et al., 2000; Walderhaug, 2000; Baron and Parnell, 2007). Further pressure solution may also occur in local shale units (Evans, 1990).

At higher temperatures the transition of illite to smectite is often reported as a potential silica source (Towe, 1962; Hower et al., 1976; van de Kamp, 2008). The illitisation window is reported to open from around 80^{o}C (Velde and Vasseur, 1992; Velde and Renac, 1996; Williams et al., 2001). In both basins < 2 µm clay mineral analysis indicates that the illitisation of smectite is near completion around 120^{o}C (Figure 3.44 and Figure 4.33). However, SIMS measurements in the outer edges of overgrowths in the Ness and Wilcox indicate quartz cementation continues to temperature greater than 130^{o}C, it is therefore unlikely silica is sourced solely from this clay mineral reaction. Furthermore, mass balance calculations made in the clay rich deposits of both basins indicate that insufficient silica can be sourced externally. These findings are in agreement with a closed shale system (e.g. Chuhan et al., 2001; Thyberg et al., 2010). Indeed both the Ness and Wilcox studies presented in this investigation have highlighted that insufficient silica is produced from the albitisation of feldspar and the illitisation of kaolinite.

Overall the petrographic, mineralogical and $\delta^{18}O_{(cement)}$ measurements made in this investigation indicate silica is most likely sourced internally within the sandstone units of both formation from pressure solution and stylolitisation.

5.3. Conclusion

The rationale for this study was to evaluate the timing and sources of quartz cementation; on average responsible for 20% of the porosity loss recorded in reservoir sandstones. The results of this investigation show that quartz cementation initiates below or around 50^{o}C with the formation of an isotopically distinct thin rind. Above 60^{o}C a marked increase in the volume of cement precipitated is observed. The quartz cementation window then continues through to maximum burial temperatures if quartz surface areas remain available.

Mineralogical analysis of both the Ness and Wilcox Formations indicates that external sources, i.e. shale, may only contribute a fraction of the silica needed for quartz cementation. Of specific interest to this study was the potential for the transformation of smectite → mixed layer I/S → illite to act as a silica source; the results of this study indicate that the quartz cementation window spans a greater temperature range than this transformation and therefore must have alternative sources. These findings indicate that the majority of silica is source internally within the sandstone body, most likely from stylolites and local pressure solution.

These findings are in general agreement with the kinetic models proposed by Walderhaug (1996; 2000), although these results indicate that quartz cementation begins below the commonly accepted 80^{o}C threshold. Precipitation of quartz cement at these low temperatures will have implications on sandstone velocities and densities; measurements fundamental for accurate reservoir quality modelling.

5.4.Future work

This investigation has illustrated how high precision SIMS can be employed as a tool for constraining the conditions of quartz cementation in reservoir sandstones. The SIMS technology used in this investigation could be used further to examine the wider diagenetic history. For example analysis of other authigenic minerals observed in these samples e.g. clay or carbonate cements may help to constrain the paragenetic sequence and provide a dual thermometer.

The use of a 2 µm SIMS beam to analysis quartz overgrowths in sandstones also highlights the potential to analyse cements observed in finer grained shale. Peltonen et al. (2008) highlight the existence of authigenic quartz in North Sea shales. As in this study end member models could be used to explore potential formation conditions. This has the potential to answer many questions about the chemical and physical evolution of shales; an important factor to considering when evaluating caprock potential. Likewise the diagenesis of carbonate reservoirs could also be explored.

The mechanism of silica recrystallisation could also be examined (e.g. Williams and Crerar, 1985b). High precision <2 µm SIMS could be utilised to constrain the kinetics of the opal A → opal CT→ quartz sequence.

Within the field of sandstone diagenesis other uncertainties remain; for example, it is still unclear to what extent stylolitisation and oil emplacement may effect quartz cementation. Although fluid inclusion investigations have analysed stylolite formation in North Sea sandstones (Baron and Parnell, 2007), the conditions and timing of stylolitisation are yet to be constrained isotopically. Furthermore, the effect relative distance from a stylolite has on overall quartz cementation at low temperatures is unclear.

How oil emplacement may affect the rate of quartz cementation is also unclear. The theory that oil emplacement inhibits cementation is based on the apparent preservation of porosity in some oil-bearing sandstone reservoirs (Dixon et al., 1989; Worden et al., 1998; Marchand et al., 2000; Marchand et al., 2001). However, primary oil inclusions are often recorded in quartz cements (Walderhaug, 1994a; Walderhaug, 1994b) indicating that cementation in sandstones is not affected by oil emplacement, a theory supported by Aase and Walderhaug (2005). High precision SIMS analysis of overgrowths from the water and oil wet regions of a single reservoir in combination with detailed reservoir modelling could theoretically determine if cementation is indeed retarded in oil wet systems.

6. References

Aagaard, P., Jahren, J. S., Harstad, A. O., Nilsen, O. and Ramm, M. (2000) 'Formation of grain-coating chlorite in sandstones. Laboratory synthesized vs. natural occurrences', *Clay Minerals*, 35, (1), pp. 261-269.

Aase, N. E., Bjørkum, P. A. and Nadeau, P. H. (1996) 'The effect of grain-coating microquartz on preservation of reservoir porosity', *AAPG Bulletin*, 80, (10), pp. 1654-1673.

Aase, N. E. and Walderhaug, O. (2005) 'The effect of hydrocarbons on quartz cementation: Diagenesis in the Upper Jurassic sandstones of the Miller Field, North Sea, revisited', *Petroleum Geoscience*, 11, (3), pp. 215-223.

Abercrombie, H. J., Hutcheon, I. E., Bloch, J. D. and De Caritat, P. (1994) 'Silica activity and the smectite-illite reaction', *Geology*, 22, (6), pp. 539-542.

Ahn, J. H. and Peacor, D. R. (1986) 'Transmission and analytical electron microscopy of the smectite- to-illite transition', *Clays & Clay Minerals*, 34, (2), pp. 165-179.

Ajdukiewicz, J. M. and Lander, R. H. (2010) 'Sandstone reservoir quality prediction: The state of the art', *AAPG Bulletin*, 94, (8), pp. 1083-1091.

Ajdukiewicz, J. M., Nicholson, P. H. and Esch, W. L. (2010) 'Prediction of deep reservoir quality using early diagenetic process models in the Jurassic Norphlet Formation, Gulf of Mexico', *AAPG Bulletin*, 94, (8), pp. 1189-1227.

Alexandre, A., Basile-Doelsch, I., Sonzogni, C., Sylvestre, F., Parron, C., Meunier, J. D. and Colin, F. (2006) 'Oxygen isotope analyses of fine silica grains using laser-extraction technique: Comparison with oxygen isotope data obtained from ion microprobe analyses and application to quartzite and silcrete cement investigation', *Geochimica et Cosmochimica Acta*, 70, (11), pp. 2827-2835.

Alexandre, A., Meunier, J. D., Llorens, E., Hill, S. M. and Savin, S. M. (2004) 'Methodological improvements for investigating silcrete formation: Petrography, FT-IR and oxygen isotope ratio of silcrete quartz cement, Lake Eyre Basin (Australia)', *Chemical Geology*, 211, (3-4), pp. 261-274.

Aplin, A. C. and Warren, E. A. (1994) 'Oxygen isotopic indications of the mechanisms of silica transport and quartz cementation in deeply buried sandstones', *Geology*, 22, (9), pp. 847-850.

Awwiller, D. N. (1993) 'Illite/smectite formation and potassium mass transfer during burial diagenesis of mudrocks: a study from the Texas Gulf Coast Paleocene-Eocene', *Journal of Sedimentary Petrology*, 63, (3), pp. 501-512.

Baron, M. and Parnell, J. (2007) 'Relationships between stylolites and cementation in sandstone reservoirs: Examples from the North Sea, U.K. and East Greenland', *Sedimentary Geology,* 194, (1-2), pp. 17-35.

Berger, G., Lacharpagne, J. C., Velde, B., Beaufort, D. and Lanson, B. (1997) 'Kinetic constraints on illitization reactions and the effects of organic diagenesis in sandstone/shale sequences', *Applied Geochemistry,* 12, (1), pp. 23-35.

Berner, R. A. and Holdren Jr, G. R. (1979) 'Mechanism of feldspar weathering-II. Observations of feldspars from soils', *Geochimica et Cosmochimica Acta,* 43, (8), pp. 1173-1186.

Bjørkum, P. A. (1996) 'How important is pressure in causing dissolution of quartz in sandstones?', *Journal of Sedimentary Research,* 66, (1), pp. 147-154.

Bjørkum, P. A., Oelkers, E. H., Nadeau, P. H., Walderhaug, O. and Murphy, W. M. (1998) 'Porosity prediction in quartzose sandstones as a function of time, temperature, depth, stylolite frequency, and hydrocarbon saturation', *AAPG Bulletin,* 82, (4), pp. 637-647.

Bjørlykke, K. (1979) 'Discussion. Cementation of sandstones', *Journal of Sedimentary Petrology,* 49, (4), pp. 1358-1359.

Bjørlykke, K. (1983) 'Diagenetic reactions in sandstones', in Parker, A. and Sellwood, B. W.(eds) *Sediment Diagenesis.*Reading, UK: Reidel Publication Company, pp. 169-213.

Bjørlykke, K. (1998) 'Clay mineral diagenesis in sedimentary basins - A key to the prediction of rock properties. Examples from the North Sea Basin', *Clay Minerals,* 33, (1), pp. 14-34.

Bjørlykke, K. and Egeberg, P. K. (1993) 'Quartz cementation in sedimentary basins', *American Association of Petroleum Geologists Bulletin,* 77, (9), pp. 1538-1548.

Bjørlykke, K. and Høeg, K. (1997) 'Effects of burial diagenesis on stresses, compaction and fluid flow in sedimentary basins', *Marine and Petroleum Geology,* 14, (3), pp. 267-276.

Bjørlykke, K., Nedkvitne, T., Ramm, M. and Saigal, G. C. (1992) 'Diagenetic processes in the Brent Group (Middle Jurassic) reservoirs of the North Sea: an overview', *Geology of the Brent Group,* pp. 263-287.

Blackbourn, G. A. (1984) 'Diagenetic history and reservoir quality of a Brent sand sequence', *Clay Minerals,* 19, (3), pp. 377-389.

Blanche, J. B. and Whitaker, J. H. M. D. (1978) 'Diagenesis of part of the Brent Sand Formation (Middle Jurassic) of the northern North Sea Basin', *Journal of the Geological Society,* 135, (1), pp. 73-82.

Blatt, H. (1987) 'Oxygen isotopes and the origin of quartz', *Journal of Sedimentary Petrology,* 57, (2), pp. 373-377.

Bloch, S. and Helmold, K. P. (1995) 'Approaches to predicting reservoir quality in sandstones', *American Association of Petroleum Geologists Bulletin,* 79, (1), pp. 97-115.

Boggs Jr, S., Kwon, Y. I., Goles, G. G., Rusk, B. G., Krinsley, D. and Seyedolali, A. (2002) 'Is quartz cathodoluminescence color a reliable provenance tool? A quantitative examination', *Journal of Sedimentary Research,* 72, (3), pp. 408-415.

Boles, J. R. (1978) 'Active ankerite cementation in the subsurface Eocene of southwest Texas', *Contributions to Mineralogy and Petrology,* 68, (1), pp. 13-22.

Boles, J. R. (1982a) 'Active albitisation of plagioclase, Gulf Coast Tertiary', *American Journal of Science,* 282, (2), pp. 165-180.

Boles, J. R. (1982b) 'Active albitization of plagioclase, Gulf Coast Tertiary', *American Journal of Science,* 282, (2), pp. 165-180.

Boles, J. R. and Franks, S. G. (1979) 'Clay diagenesis in Wilcox sandstones of southwest Texas: Implications of smectite diagenesis on sandstone cementation', *Journal of Sedimentary Petrology,* 49, (1), pp. 55-70.

Bossi, G. E. (1972) 'A chloritized montmorillonite from The Rio Chiflon formation (TR) of Argentina', *Clays and Clay Minerals,* 20, (5), pp. 251-258.

Brindley, G. W. and Brown, G. (1980) *Crystal structures of clay minerals and their X-ray identification* London: Mineralogical Society.

Brint, J. F., Hamilton, P. J., Haszeldine, R. S., Fallick, A. E. and Brown, S. (1991) 'Oxgyen isotopic analysis of diagenetic quartz overgrowths from the Brent Sands: a comparison of two preparation methods', *Journal of Sedimentary Petrology,* 61, (4), pp. 527-533.

Brosse, É., Margueron, T., Cassou, C., Sanjuan, B., Canham, A., Girard, J. P., Lacharpagne, J. C. and Sommer, F. (2002) 'The formation and stability of kaolinite in Brent sandstone reservoirs: A modelling approach', *International Association of Sedimentologists Special Publications,* (34), pp. 383-408.

Burley, S. D., Mullis, J. and Matter, A. (1989) 'Timing diagenesis in the Tartan Reservoir (UK North Sea): constraints from combined cathodoluminescence microscopy and fluid inclusion studies', *Marine and Petroleum Geology,* 6, (2).

Calvert, S. E. (1968) 'Silica balance in the ocean and diagenesis', *Nature,* 219, (5157), pp. 919-920.

Canals, M. and Meunier, J. D. (1995) 'A model for porosity reduction in quartzite reservoirs by quartz cementation', *Geochimica et Cosmochimica Acta,* 59, (4), pp. 699-709.

Carver, R. E. (1980) 'Petrology of Paleocene- Eocene and Miocene opaline sediments, southeastern Atlantic coastal plain', *Journal of Sedimentary Petrology,* 50, (2), pp. 569-582.

Chadwick, R. A. and Pharaoh, T. C. (1998) 'The seismic reflection Moho beneath the United Kingdom and adjacent areas', *Tectonophysics,* 299, (4), pp. 255-279.

Chang, H. K., Mackenzie, F. T. and Schoonmaker, J. (1986) 'Comparisons between the diagenesis of dioctahedral and trioctahedral smectite, Brazilian offshore basins', *Clays & Clay Minerals,* 34, (4), pp. 407-423.

Chayes, F. (1949) 'A simple point counter for thin-section analysis.', *American Mineralogist,* 34, (1), pp. 1-11.

Chayes, F. and Fairbairn, H. W. (1951) 'A test of the precision of thin section analysis by point counter.', *American Mineralogist,* 36, (9), pp. 704–712.

Chipera, S. J. and Bish, D. L. (2002) 'FULLPAT: A full-pattern quantitative analysis program for X-ray powder diffraction using measured and calculated patterns', *Journal of Applied Crystallography,* 35, (6), pp. 744-749.

Chuhan, F. A., Bjørlykke, K. and Lowrey, C. J. (2001) 'Closed-system burial diagenesis in reservoir sandstones: Examples from the garn formation at haltenbanken area, offshore mid-norway', *Journal of Sedimentary Research,* 71, (1), pp. 15-26.

Chuhan, F. A., Kjeldstad, A., Bjørlykke, K. and Høeg, K. (2002) 'Porosity loss in sand by grain crushing - Experimental evidence and relevance to reservoir quality', *Marine and Petroleum Geology,* 19, (1), pp. 39-53.

Clark, G. L. and Reynolds, D. H. (1936) 'Quantitative analysis of mine dusts: An x-ray diffraction method', *Industrial and Engineering Chemistry,* 8, pp. 36-40.

Clayton, R. N., O'Neil, J. R. and Mayeda, T. K. (1972) 'Oxygen Isotope Exchange between Quartz and Water', *J. Geophys. Res.,* 77, (17), pp. 3057-3067.

Cooper, M. R., Evans, J., Flint, S. S., Hogg, A. J. C. and Hunter, R. H. (2000) 'Quantification of detrital, authigenic and porosity components of the Fontainebleau Sandstone: A comparison of conventional optical and combined scanning electron microscope-based methods of modal analyses', in Worden, R. H. and Morad, S.(eds) *Quartz Cementation in Sandstones.* Vol. 29 Oxford: Wiley-Blackwell pp. 89-101.

Day-Stirrat, R. J., Milliken, K. L., Dutton, S. P., Loucks, R. G., Hillier, S., Aplin, A. C. and Schleicher, A. M. (2010) 'Open-system chemical behavior in deep Wilcox

Group mudstones, Texas Gulf Coast, USA', *Marine and Petroleum Geology,* 27, (9), pp. 1804-1818.

de Boer, R. B. (1977) 'Pressure solution: Theory and experiments', *Tectonophysics,* 39, (1-3), pp. 287-301.

Demars, C., Pagel, M., Deloule, E. and Blanc, P. (1996) 'Cathodoluminescence of quartz from sandstones: Interpretation of the UV range by determination of trace element distributions and fluid-inclusion P-T-X properties in anthigenic quartz', *American Mineralogist,* 81, (7-8), pp. 891-901.

Dewers, T. and Ortoleva, P. (1990) 'A coupled reaction/transport/mechanical model for intergranular pressure solution, stylolites, and differential compaction and cementation in clean sandstones', *Geochimica et Cosmochimica Acta,* 54, (6), pp. 1609-1625.

Dixon, S. A., Summers, D. M. and Surdam, R. C. (1989) 'Diagenesis and preservation of porosity in Norphlet Formation (Upper Jurassic), southern Alabama', *American Association of Petroleum Geologists Bulletin,* 73, (6), pp. 707-728.

Dutton, S. P. and Loucks, R. G. (2010) 'Diagenetic controls on evolution of porosity and permeability in lower Tertiary Wilcox sandstones from shallow to ultradeep (200-6700 m) burial, Gulf of Mexico Basin, U.S.A', *Marine and Petroleum Geology,* 27, (1), pp. 69-81.

Egeberg, P. K. and Aagaard, P. (1989) 'Origin and evolution of formation waters from oil fields on the Norwegian shelf', *Applied Geochemistry,* 4, (2), pp. 131-142.

Ehrenberg, S. N. and Jakobsen, K. G. (2001) 'Plagioclase dissolution related to biodegradation of oil in Brent Group sandstones (Middle Jurassic) of Gullfaks Field, Northern North Sea', *Sedimentology,* 48, (4), pp. 703-721.

Ehrenberg, S. N. and Nadeau, P. H. (1989) 'Formation of diagenetic illite in sandstones of the Garn Formation, Haltenbanken area, mid-Norwegian continental shelf', *Clay Minerals,* 24, (2), pp. 233-253.

Evans, J. (1990) 'Quartz dissolution during shale diagenesis implications for quartz cementation in sandstones', *Chemical Geology,* 84, (1-4), pp. 239-240.

Evans, J., Hogg, A. J. C., Hopkins, M. S. and Howarth, R. J. (1994) 'Quantification of quartz cements using combined SEM, CL, and image analysis', *Journal of Sedimentary Research A: Sedimentary Petrology & Processes,* 64 A, (2), pp. 334-338.

Fisher, Q. J., Knipe, R. J. and Worden, R. H. (2000) 'Microstructures of deformed and non-deformed sandstones from the North Sea: Implications for the origins of quartz cement in sandstones', in Worden, R. H. and Morad, S.(eds) *Quartz Cementation in Sandstones.* Vol. 29 Oxford: Wiley-Blackwell pp. 129-146.

Fisher, R. S. and Land, L. S. (1986a) 'Diagenetic history of Eocene Wilcox sandstones, South-Central Texas', *Geochimica et Cosmochimica Acta,* 50, (4), pp. 551-561.

Fisher, R. S. and Land, L. S. (1986b) 'Diagenetic history of Eocene Wilcox sandstones, South-Central Texas', *Geochimica et Cosmochimica Acta,* 51, (11), pp. 3073-3074.

Fisher, W. L. and McGowen, J. H. (1969) 'Depositional systems in Wilcox Group (Eocene) of Texas and their relation to occurrence of oil and gas', *American Association of Petroleum Geologists Bulletin,* 53, (1), pp. 30-54.

Folk, R. L. (1965) *Petrology of Sedimentary Rocks.* Austin, Texas: Hemphill Publishing Company.

Franks, S. G. and Forester, R. W. (1984) 'Relationships among secondary porosity, pore-fluid chemistry and carbon dioxide, Texas gulf coast', *Clastic Diagenesis*, pp. 63-79.

Franks, S. G. and Zwingmann, H. (2010) 'Origin and timing of late diagenetic illite in the permian-carboniferous unayzah sandstone reservoirs of Saudi Arabia', *AAPG Bulletin,* 94, (8), pp. 1133-1159.

Freed, R. L. and Peacor, D. R. (1989) 'Variability in temperature of the smectite/illite reaction in Gulf Coast sediments', *Clay Minerals,* 24, (2), pp. 171-180.

Freed, R. L. and Peacor, D. R. (1992) 'Diagenesis and the formation of authigenic illite-rich I/S crystals in Gulf Coast shales: TEM study of clay separates', *Journal of Sedimentary Petrology,* 62, (2), pp. 220-234.

Galloway, W. E., Ganey-Curry, P. E., Li, X. and Buffler, R. T. (2000) 'Cenozoic depositional history of the Gulf of Mexico basin', *AAPG Bulletin,* 84, (11), pp. 1743-1774.

Gier, S., Worden, R. H., Johns, W. D. and Kurzweil, H. (2008) 'Diagenesis and reservoir quality of Miocene sandstones in the Vienna Basin, Austria', *Marine and Petroleum Geology,* 25, (8), pp. 681-695.

Giles, M. R. (1992) 'The reservoir properties and diagenesis of the Brent Group: a regional perspective', *Geology of the Brent Group*, pp. 289-327.

Giles, M. R., Indrelid, S. L., Beynon, G. V. and Amthor, J. (2000) 'The origin of large-scale quartz cementation: Evidence from large data sets and coupled heat-fluid mass transport modelling', in Worden, R. H. and Morad, S.(eds) *Quartz Cementation in Sandstones.* Vol. 29 Oxford: Wiley-Blackwell pp. 21-38.

Girard, J. P., Munz, I. A., Johansen, H., Hill, S. and Canham, A. (2001) 'Conditions and timing of quartz cementation in Brent reservoirs, Hild Field, North Sea: Constraints from fluid inclusions and SIMS oxygen isotope microanalysis', *Chemical Geology,* 176, (1-4), pp. 73-92.

Girard, J. P., Munz, I. A., Johansen, H., Lacharpagne, J. C. and Sommer, F. (2002) 'Diagenesis of the hild Brent sandstones, Northern North Sea: Isotopic evidence for the prevailing influence of deep basinal water', *Journal of Sedimentary Research*, 72, (6), pp. 746-759.

Glasmann, J. R. (1992) 'The fate of feldspar in Brent Group reservoirs, North Sea: a regional synthesis of diagenesis in shallow, intermediate, and deep burial environments', *Geology of the Brent Group*, pp. 329-350.

Glasmann, J. R., Clark, R. A., Larter, S., Briedis, N. A. and Lundegard, P. D. (1989a) 'Diagenesis and hydrocarbon accumulation, Brent Sandstone (Jurassic), Bergen High area, North Sea', *American Association of Petroleum Geologists Bulletin*, 73, (11), pp. 1341-1360.

Glasmann, J. R., Lundegard, P. D., Clark, R. A., Penny, B. K. and Collins, I. D. (1989b) 'Geochemical evidence for the history of diagenesis and fluid migration: Brent Sandstone, Heather Field, North Sea', *Clay Minerals*, 24, (2), pp. 255-284.

Gluyas, J., Garland, C., Oxtoby, N. H. and Hogg, A. J. C. (2000) 'Quartz cement: the Miller's Tale', in Worden, R. H. and Morad, S.(eds) *Quartz Cementation in Sandstones.* Vol. 29 Oxford: Wiley-Blackwell pp. 199–218.

Goldstein, R. H. and Rossi, C. (2002) 'Recrystallization in quartz overgrowths', *Journal of Sedimentary Research*, 72, (3), pp. 432-440.

Götze, J., Plötze, M. and Habermann, D. (2001) 'Origin, spectral characteristics and practical applications of the cathodoluminescence (CL) of quartz - A review', *Mineralogy and Petrology*, 71, (3-4), pp. 225-250.

Graham, C. M., Valley, J. W. and Winter, B. L. (1996) 'Ion microprobe analysis of 18O/16O in authigenic and detrital quartz in the St. Peter Sandstone, Michigan Basin and Wisconsin Arch, USA: Contrasting diagenetic histories', *Geochimica et Cosmochimica Acta*, 60, (24), pp. 5101-5116.

Gran, K. (1989) *A correlation of mineralogy, compaction and seismic velocities in shales of the Tertiary and Cretaceous age in the Viking graben and Horda Platform area*. thesis. University of Oslo.

Gratier, J. P. and Guiguet Irigm, R. (1986) 'Experimental pressure solution-deposition on quartz grains: the crucial effect of the nature of the fluid', *Journal of Structural Geology*, 8, (8), pp. 845-856.

Greene, G. W., Kristiansen, K., Meyer, E. E., Boles, J. R. and Israelachvili, J. N. (2009) 'Role of electrochemical reactions in pressure solution', *Geochimica et Cosmochimica Acta*, 73, (10), pp. 2862-2874.

Haddad, S. C., Worden, R. H., Prior, D. J. and Smalley, P. C. (2006) 'Quartz cement in the fontainebleau sandstone, Paris Basin, France: Crystallography and

implications for mechanisms of cement growth', *Journal of Sedimentary Research,* 76, (1-2), pp. 244-256.

Harris, N. B. (1992) 'Burial diagenesis of Brent sandstones: a study of Statfjord, Hutton and Lyell fields', *Geology of the Brent Group*, pp. 351-375.

Hassouta, L., Buatier, M. D., Potdevin, J. L. and Liewig, N. (1999) 'Clay diagenesis in the sandstone reservoir of the Ellon Field (Alwyn, North Sea)', *Clays and Clay Minerals,* 47, (3), pp. 269-285.

Haszeldine, R. S., Brint, J. F., Fallick, A. E., Hamilton, P. J. and Brown, S. (1992) 'Open and restricted hydrologies', *Geology of the Brent Group,* 61, pp. 401-419.

Haszeldine, R. S., Samson, I. M. and Cornford, C. (1984) 'Dating diagenesis in a petroleum basin, a new fluid inclusion method', *Nature,* 307, (5949), pp. 354-357.

Hawkins, P. J. (1978) 'Relationship between diagenesis, porosity reduction, and oil emplacement in late Carboniferous sandstone reservoirs, Bothamsall Oilfield, E Midlands', *Journal of the Geological Society,* 135, (1), pp. 7-24.

Heald, M. T. (1955) 'Stylolites in sandstones', *Journal of Geology,* 63, (2), pp. 101-114.

Heald, M. T. (1959) 'Significance of stylolites in permeable sandstones', *Journal of Sedimentary Petrology,* 29, pp. 251-253.

Heald, M. T. and Larese, R. E. (1974) 'Influence of coatings on quartz cementation', *Journal of Sedimentary Research,* 44, (4), pp. 1269-1274.

Helgeson, H. C., Murphy, W.M., Aagaard, P. . (1984) 'Thermodynamic and kinetic constraints on reaction rates among minerals and aqueous solutions. II. Rate constants, effective surface area, and the hydrolysis of feldspar', *Geochimica et Cosmochimica Acta,* 48, (12), pp. 2405-2432

Hendry, J. P. and Trewin, N. H. (1995) 'Authigenic quartz microfabrics in Cretaceous turbidites: Evidence for silica transformation processes in sandstones', *Journal of Sedimentary Research,* A65, (2), pp. 380-392.

Hendry, J. P., Wilkinson, M., Fallick, A. E. and Haszeldine, R. S. (2000) 'Ankerite Cementation in Deeply Buried Jurassic Sandstone Reservoirs of the Central North Sea', *Journal of Sedimentary Research,* 70, (1), pp. 227-239.

Hesse, R. and Schacht, U. (2011) 'Early diagenesis of deep-sea sediments', in HüNeke, H. and Mulder, T.(eds) *Developments in Sedimentology.* Vol. 63 Oxford, UK: Elsevier, pp. 557-713.

Hillier, S. (1994) 'Pore-lining chlorites in siliciclastic reservoir sandstones: electron microprobe, SEM and XRD data, and implications for their origin', *Clay Minerals,* 29, (4), pp. 665-679.

Hillier, S. (2003) 'Quantitative analysis of clay and other minerals in sandstones by X-ray powder diffraction (XRPD)', *Clay Mineral Cements in Sandstones,* 34, pp. 213-251.

Hogg, A. J. C., Pearson, M. J., Fallick, A. E. and Hamilton, P. J. (1995) 'An integrated thermal and isotopic study of the diagenesis of the Brent group, Alwyn South, U.K. North Sea', *Applied Geochemistry,* 10, (5), pp. 531-546.

Hogg, A. J. C., Sellier, E. and Jourdan, A. J. (1992) 'Cathodoluminescence of quartz cements in Brent Group sandstones, Alwyn South, UK North Sea', *Geology of the Brent Group,* pp. 421-440.

Holdren Jr, G. R. and Berner, R. A. (1979) 'Mechanism of feldspar weathering-I. Experimental studies', *Geochimica et Cosmochimica Acta,* 43, (8), pp. 1161-1171.

Houseknecht, D. W. (1984) 'Influence of grain size and temperature on intergranular pressure solution, quartz cementation, and porosity in a quartzose sandstone', *Journal of Sedimentary Petrology,* 54, (2), pp. 348-361.

Houseknecht, D. W. (1988) 'Intergranular pressure solution in four quartzose sandstones', *Journal of Sedimentary Petrology,* 58, (2), pp. 228-246.

Hower, J., Eslinger, E. V., Hower, M. E. and Perry, E. A. (1976) 'Mechanism of burial metamorphism of argillaceous sediment: 1. Mineralogical and chemical evidence', *Geological Society of America Bulletin,* 87, pp. 725-737.

Hu, G. and Clayton, R. N. (2003) 'Oxygen isotope salt effects at high pressure and high temperature and the calibration of oxygen isotope geothermometers', *Geochimica et Cosmochimica Acta,* 67, (17), pp. 3227-3246.

Humphreys, B., Kemp, S. J., Lott, G. K., Bermanto, Dharmayanti, D. A. and Samsori, I. (1994) 'Origin of grain-coating chlorite by smectite transformation: an example from Miocene sandstones, North Sumatra back-arc basin, Indonesia', *Clay Minerals,* 29, (4), pp. 681-692.

Hurst, A. (1985) 'Diagenetic chlorite formation in some Mesozoic shales from the Sleipner area of the North Sea', *Clay Minerals,* 20, (1), pp. 69-79.

Hurst, A. and Irwin, H. (1982) 'Geological modelling of clay diagenesis in sandstones', *Clay Minerals,* 17, (1), pp. 5-22.

Jahren, J. and Ramm, M. (2000) 'The porosity-preserving effects of microcrystalline quartz coatings in arenitic sandstones: Examples from the Norwegian continental shelf', in Worden, R. H. and Morad, S.(eds) *Quartz Cementation in Sandstones.* Vol. 29 Oxford: Wiley-Blackwell pp. 271-280.

Javoy, M. (1977) 'Stable isotopes and geothermometry', *Journal of the Geological Society,* 133, (6), pp. 609-636.

Kelly, J. L., Fu, B., Kita, N. T. and Valley, J. W. (2007) 'Optically continuous silcrete quartz cements of the St. Peter Sandstone: High precision oxygen isotope analysis by ion microprobe', *Geochimica et Cosmochimica Acta,* 71, (15), pp. 3812-3832.

Kim, E. M. and Fisher, W. L. (1999) 'Further growth lies ahead for South Texas Wilcox plays', *Oil and Gas Journal,* 97, (9), pp. 79-83.

Kim, Y. and Lee, Y. I. (2004) 'Origin of quartz cement in the Lower Ordovician Dongjeom formation, Korea', *Journal of Asian Earth Sciences,* 24, (3), pp. 327-335.

Kita, N. T., Ushikubo, T., Fu, B. and Valley, J. W. (2009) 'High precision SIMS oxygen isotope analysis and the effect of sample topography', *Chemical Geology,* 264, (1-4), pp. 43-57.

Kozdon, R., Ushikubo, T., Kita, N. T., Spicuzza, M. and Valley, J. W. (2009) 'Intratest oxygen isotope variability in the planktonic foraminifer N. pachyderma: Real vs. apparent vital effects by ion microprobe', *Chemical Geology,* 258, (3-4), pp. 327-337.

Kraishan, G. M., Rezaee, M. R. and Worden, R. H. (2000) 'Significance of trace element composition of quartz cement as a key to reveal the origin of silica in sandstones: An example from the Cretaceous of the Barrow sub-basin, Western Australia', in Worden, R. H. and Morad, S.(eds) *Quartz Cementation in Sandstones.* Vol. 29 Oxford: Wiley-Blackwell pp. 317-331.

Labeyrie Jr, L. (1974) 'New approach to surface seawater palaeotemperatures using $^{18}O/^{16}O$ ratios in silica of diatom frustules', *Nature,* 248, (5443), pp. 40-42.

Land, L. S. and Dutton, S. P. (1978) 'Cementation of a Pennsylvanian deltaic sandstone; isotopic data', *Journal of Sedimentary Research,* 48, (4), pp. 1167-1176.

Land, L. S. and Dutton, S. P. (1979) 'Reply. Cementation of sandstones', *Journal of Sedimentary Petrology,* 49, (4), pp. 1359-1361.

Land, L. S. and Fisher, R. S. (1987) 'Wilcox sandstone diagenesis, Texas Gulf Coast: a regional isotopic comparison with the Frio Formation', *Geological Society, London, Special Publications,* 36, (1), pp. 219-235.

Land, L. S. and Milliken, K. L. (1981) 'Feldspar diagenesis in the Frio Formation, Brazoria County, Texas Gulf Coast', *Geology,* 9, (7), pp. 314-318.

Land, L. S., Milliken, K. L. and McBride, E. F. (1987) 'Diagenetic evolution of Cenozoic sandstones, Gulf of Mexico sedimentary basin', *Sedimentary Geology,* 50, (1-3), pp. 195-225.

Lander, R. H. and Walderhaug, O. (1999) 'Predicting porosity through simulating sandstone compaction and quartz cementation', *AAPG Bulletin (American Association of Petroleum Geologists),* 83, (2-3), pp. 433-449.

Lanson, B., Beaufort, D., Berger, G., Baradat, J. and Lacharpagne, J. C. (1996) 'Illitization of diagenetic kaolinite-to-dickite conversion series: Late-stage diagenesis of the lower permian Rotliegend sandstone reservoir, offshore of the Netherlands', *Journal of Sedimentary Research,* 66, (3), pp. 501-518.

Lanson, B., Beaufort, D., Berger, G., Bauer, A., Cassagnabère, A. and Meunier, A. (2002) 'Authigenic kaolin and illitic minerals during burial diagenesis of sandstones: A review', *Clay Minerals,* 37, (1), pp. 1-22.

Lanson, B. and Champion, D. (1991) 'The I/S-to-illite reaction in the late stage diagenesis', *American Journal of Science,* 291, (5), pp. 473-506.

Lasaga, A. C. (1984) 'Chemical Kinetics of Water-Rock Interactions', *Journal of Geophysical Research,* 89, pp. 4009-4025.

Leder, F. and Park, W. C. (1986) 'Porosity Reduction in Sandstone by Quartz Overgrowth', *American Association of Petroleum Geologists Bulletin,* 70, (11), pp. 1713-1728.

Lee, M. and Savin, S. M. (1985) 'Isolation of diagenetic overgrowths on quartz sand grains for oxygen isotopic analysis', *Geochimica et Cosmochimica Acta,* 49, (2), pp. 497-501.

Lynch, F. L. (1997) 'Frio shale mineralogy and the stoichiometry of the smectite-to-illite reaction: The most important reaction in clastic sedimentary diagenesis', *Clays and Clay Minerals,* 45, (5), pp. 618-631.

Lynch, F. L., Mack, L. E. and Land, L. S. (1997) 'Burial diagenesis of illite/smectite in shales and the origins of authigenic quartz and secondary porosity in sandstones', *Geochimica et Cosmochimica Acta,* 61, (10), pp. 1995-2006.

Macaulay, C. I., Fallick, A. E. and Haszeldine, R. S. (1993) 'Textural and isotopic variations in diagenetic kaolinite from the Magnus Oilfield sandstones', *Clay Minerals,* 28, (4), pp. 625-639.

Mackenzie, F. T. and Gees, R. (1971) 'Quartz: Synthesis at Earth-surface conditions', *Science,* 173, (3996), pp. 533-535.

MacQuaker, J. H. S. and Adams, A. E. (2003) 'Maximizing information from fine-grained sedimentary rocks: An inclusive nomenclature for mudstones', *Journal of Sedimentary Research,* 73, (5), pp. 735-744.

Makowitz, A., Lander, R. H. and Milliken, K. L. (2006) 'Diagenetic modeling to assess the relative timing of quartz cementation and brittle grain processes during compaction', *AAPG Bulletin*, 90, (6), pp. 873-885.

Makowitz, A., Lander, R. H. and Milliken, K. L. (2010) 'Chemical diagenetic constraints on the timing of cataclasis in deformed sandstone along the Pine Mountain overthrust, eastern Kentucky', *Journal of Structural Geology*, 32, (12), pp. 1923-1932.

Makowitz, A. and Milliken, K. L. (2003) 'Quantification of brittle deformation in burial compaction, Frio and Mount Simon Formation sandstones', *Journal of Sedimentary Research*, 73, (6), pp. 1007-1021.

Marchand, A. M. E., Haszeldine, R. S., Macaulay, C. I., Swennen, R. and Fallick, A. E. (2000) 'Quartz cementation inhibited by crestal oil charge: Miller deep water sandstone, UK North Sea', *Clay Minerals*, 35, (1), pp. 201-210.

Marchand, A. M. E., Haszeldine, R. S., Smalley, P. C., Macaulay, C. I. and Fallick, A. E. (2001) 'Evidence for reduced quartz-cementation rates in oil-filled sandstones', *Geology*, 29, (10), pp. 915-918.

Marchand, A. M. E., Macaulay, C. I., Haszeldine, R. S. and Fallick, A. E. (2002) 'Pore water evolution in oilfield sandstones: Constraints from oxygen isotope microanalyses of quartz cement', *Chemical Geology*, 191, (4), pp. 285-304.

Marcussen, O., Maast, T. E., Mondol, N. H., Jahren, J. and Bjørlykke, K. (2010) 'Changes in physical properties of a reservoir sandstone as a function of burial depth - The Etive Formation, northern North Sea', *Marine and Petroleum Geology*.

Matsuhisa, Y., Goldsmith, J. R. and Clayton, R. N. (1979) 'Oxygen isotopic fractionation in the system quartz-albite-anorthite-water', *Geochimica et Cosmochimica Acta*, 43, (7), pp. 1131-1140.

Matthews, A. and Beckinsale, R. D. (1979) 'Oxygen isotope equilibration systematics between quartz and water', *American Mineralogist*, 64, pp. 232-24.

Matthews, J. C., Velde, B. and Johansen, H. (1994) 'Significance of K-Ar ages of authigenic illitic clay minerals in sandstones and shales from the North Sea', *Clay Minerals*, 29, (3), pp. 379-389.

McBride, E. F. (1987) 'Diagenesis of the Maxon sandstone (Early Cretaceous), Marathon region, Texas: a diagenetic quartzarenite', *Journal of Sedimentary Petrology*, 57, (1), pp. 98-107.

McBride, E. F. (1989) 'Quartz cement in sandstones: a review', *Earth Science Reviews*, 26, (C), pp. 69-112.

McBride, E. F., Diggs, T. N. and Wilson, J. C. (1991) 'Compaction of Wilcox and Carrizo sandstones (Paleocene-Eocene) to 4420 m, Texas Gulf Coast', *Journal of Sedimentary Petrology*, 61, (1), pp. 73-85.

McDonnell, A., Loucks, R. G. and Galloway, W. E. (2008) 'Paleocene to Eocene deep-water slope canyons, western Gulf of Mexico: Further insights for the provenance of deep-water offshore Wilcox Group plays', *AAPG Bulletin*, 92, (9), pp. 1169-1189.

Milliken, K. L. (1992) 'Chemical behavior of detrital feldspars in mudrocks versus sandstones, Frio Formation (Oligocene), south Texas', *Journal of Sedimentary Petrology*, 62, (5), pp. 790-801.

Mizutani, S. (1970) 'Silica minerals in the early stage of diagenesis', *Sedimentology*, 15, pp. 419 - 436.

Moore, D. M. and Reynolds, R. C. (1997) *X-Ray Diffraction and the Identification and Analysis of Clay Minerals* New York: Oxford Univ Press.

Morad, S., Bergan, M., Knarud, R. and Nystuen, J. P. (1990) 'Albitization of detrital plagioclase in Triassic reservoir sandstones from the Snorre Field, Norwegian North Sea', *Journal of Sedimentary Petrology*, 60, (3), pp. 411-425.

Morad, S., Worden, R. H. and Ketzer, J. M. (2002) 'Oxygen and hydrogen isotopic composition of diagenetic clay minerals in sandstones: A review of the data and controls', *International Association of Sedimentologists Special Publications*, (34), pp. 63-91.

Morton, A. C., Haszeldine, R. S., Giles, M. R. and Brown, S. (1992) 'Geology of the Brent Group', *Geology of the Brent Group*.

Morton, R. A. and Land, L. S. (1987) 'Regional variations in formation water chemistry, Frio Formation (Oligocene), Texas Gulf Coast (USA)', *American Association of Petroleum Geologists Bulletin*, 71, (2), pp. 191-206.

Murata, K. J. and Larson, R. R. (1975) 'Diagenesis of Miocene siliceous shales, Temblor range, California', *J Res US Geol Surv*, 3, (5), pp. 553-566.

Nadeau, P. H. and Bain, D. C. (1986) 'Composition of some smectites and diagenetic illitic clays and implications for their origin', *Clays & Clay Minerals*, 34, (4), pp. 455-464.

NPD (2011) *Norwegian Petroleum Directorate Fact Pages*. Available at: (Accessed: 04/01/2011).

Oelkers, E. H., Bjorkum, P. A. and Murphy, W. M. (1996) 'A petrographic and computational investigation of quartz cementation and porosity reduction in North Sea sandstones', *American Journal of Science*, 296, (4), pp. 420-452.

Oelkers, E. H., Bjørkum, P. A., Walderhaug, O., Nadeau, P. H. and Murphy, W. M. (2000) 'Making diagenesis obey thermodynamics and kinetics: The case of quartz cementation in sandstones from offshore mid-Norway', *Applied Geochemistry,* 15, (3), pp. 295-309.

Osborne, M. and Haszeldine, R. S. (1995) 'Reply to a discussion of 'Evidence for resetting of fluid inclusion temperatures from quartz cements in oilfields' by Osborne and Haszeldine (1993)', *Marine and Petroleum Geology,* 12, (5), pp. 561-565.

Osborne, M. and Haszeldine, S. (1993) 'Evidence for resetting of fluid inclusion temperatures from quartz cements in oilfields', *Marine and Petroleum Geology,* 10, (3), pp. 271-278.

Page, F. Z., Ushikubo, T., Kita, N. T., Riciputi, L. R. and Valley, J. W. (2007) 'High-precision oxygen isotope analysis of picogram samples reveals 2 µm gradients and slow diffusion in zircon', *American Mineralogist,* 92, (10), pp. 1772-1775.

Park, W. C. and Schot, E. H. (1968) 'Stylolites: Their nature and origin', *Journal of Sedimentary Petrology,* 38, (1), pp. 175-191.

Paxton, S. T., Szabo, J. O., Ajdukiewicz, J. M. and Klimentidis, R. E. (2002) 'Construction of an intergranular volume compaction curve for evaluating and predicting compaction and porosity loss in rigid-grain sandstone reservoirs', *AAPG Bulletin,* 86, (12), pp. 2047-2067.

Peltonen, C., Marcussen, Ø., Bjørlykke, K. and Jahren, J. (2008) 'Mineralogical control on mudstone compaction: A study of late Cretaceous to early Tertiary mudstones of the Vøring and Møre basins, Norwegian Sea', *Petroleum Geoscience,* 14, (2), pp. 127-138.

Perez, R. J. and Boles, J. R. (2005) 'An empirically derived kinetic model for albitization of detrital plagioclase', *American Journal of Science,* 305, (4), pp. 312-343.

Pisciotto, K. A. (1981) 'Diagenetic trends in the siliceous facies of the Monterey Shale in the Santa Maria region, California', *Sedimentology,* 28, (4), pp. 547-571.

Pittman, E. D. and Larese, R. E. (1991) 'Compaction of lithic sands: experimental results and applications', *American Association of Petroleum Geologists Bulletin,* 75, (8), pp. 1279-1299.

Pittman, E. D., Larse, R. E. and Heald, M. T. (1992) 'Clay coats: occurrence and relevance to preservation of porosity in sandstones.', in Houseknecht, D. W. and Pittman, E. D.(eds) *Origin, Diagenesis and Petrophysics of Clay Minerals in Sandstone.* Vol. 47 Tulsa: SEPM (Society for Sedimentary Geology), pp. 241–255.

Prentice, M. L. and Matthews, R. K. (1988) 'Cenozoic ice-volume history: development of a composite oxygen isotope record', *Geology*, 16, (11), pp. 963-966.

Primmer, T. J., Cade, C. A., Evans, J., Gluyas, J. G., Hopkins, M. S., Oxtoby, N. H., Craig Smalley, P., Warren, E. A. and Worden, R. H. (1997) 'Global patterns in sandstone diagenesis: Their application to reservoir quality prediction for petroleum exploration', *AAPG Memoir*, (69), pp. 61-77.

Ramm, M. (1992) 'Porosity-depth trends in reservoir sandstones: theoretical models related to Jurassic sandstones offshore Norway', *Marine and Petroleum Geology*, 9, (5), pp. 553-567.

Renton, J. J., Heald, M. T. and Cecil, C. B. (1969) 'Experimental investigation of pressure solution of quartz', *J. Sediment. Petrol.*, 39, (3), pp. 1107-1117.

Robin, P. Y. F. (1978) 'Pressure solution at grain-to-grain contacts', *Geochimica et Cosmochimica Acta*, 42, (9), pp. 1383-1389.

Robinson, A. and Gluyas, J. (1992) 'Model calculations of loss of porosity in sandstones as a result of compaction and quartz cementation', *Marine and Petroleum Geology*, 9, (3), pp. 319-323.

Rossi, C., Goldstein, R. H., Ceriani, A. and Marfil, R. (2002) 'Fluid inclusions record thermal and fluid evolution in reservoir sandstones, Khatatba Formation, Western Desert, Egypt: A case for fluid injection', *AAPG Bulletin*, 86, (10), pp. 1773-1799.

Saigal, G. C., Morad, S., Bjørlykke, K., Egeberg, P. K. and Aagaard, P. (1988) 'Diagenetic albitization of detrital K-feldspar in Jurassic, Lower Cretaceous, and Tertiary clastic reservoir rocks from offshore Norway, I. Textures and origin', *Journal of Sedimentary Petrology*, 58, (6), pp. 1003-1013.

Sanjuan, B., Girard, J. P., Lanini, S., Bourguignon, A. and Brosse, É. (2002) 'Geochemical modelling of diagenetic illite and quartz cement formation in Brent sandstone reservoirs: Example of the Hild Field, Norwegian North Sea', *International Association of Sedimentologists Special Publications*, (34), pp. 425-452.

Schmoker, J. W. and Gautier, D. L. (1988) 'Sandstone porosity as a function of thermal maturity', *Geology*, 16, (11), pp. 1007-1010.

Scotchman, I. C., Johnes, L. H. and Miller, R. S. (1989) 'Clay diagenesis and oil migration in Brent Group sandstones of NW Hutton Field, UK North Sea', *Clay Minerals*, 24, (2), pp. 339-374.

Sibley, D. F. and Blatt, H. (1976) 'Intergranular pressure solution and cementation of the Tuscarora orthoquartzite', *Journal of Sedimentary Petrology*, 46, (4), pp. 881-896.

Siever, R. (1957) 'Pennsylvanian sandstones of the Eastern Interior Coal Basin', *Journal of Sedimentary Research,* 27, (3), pp. 227-250.

Siever, R. (1962) 'Silica solubility, 0- 200 ^{o}C and the diagenesis of siliceous sediments', *Journal of Geology,* 70, pp. 127-151.

Smale, D. (1978) 'Silcretes and associated silica diagenesis in Southern Africa and Australia', *Silcrete in Australia*, pp. 261-279.

Sorby, H. C. (1880) 'On the structure and origin of non-calcareous stratified rocks.', *Quarterly Journal of the Geological Society London,* 37, pp. 49–92.

Spötl, C., Houseknecht, D. W. and Riciputi, L. R. (2000) 'High-temperature quartz cement and the role of stylolites in a deep gas reservoir, Spiro sandstone, Arkoma basin, USA.', in Worden, R. H. and Morad, S.(eds) *Quartz Cementation in Sandstones.* Vol. 29 Oxford: Wiley-Blackwell pp. 281–297.

Tada, R. and Siever, R. (1989) 'Pressure solution during diagenesis', *Annual review of earth and planetary sciences. Vol. 17,* pp. 89-118.

Tanner, C. B. and Jackson, M. L. (1947) 'Nomographs of sedimentation times for soil particles under gravity or centrifugal acceleration', *Soil Science Society Preceedings,* pp. 60-65.

Taylor, H. P. (1974) 'The Application of Oxygen and Hydrogen Isotope Studies to Problems of Hydrothermal Alteration and Ore Deposition', *Economic Geology,* 69, (6), pp. 843-883.

Taylor, H. P. (1977) 'Water/rock interactions and the origin of H_2O in granitic batholiths', *J. Geol. Soc. London,* 133, pp. 509-558.

Taylor, T. R., Giles, M. R., Hathon, L. A., Diggs, T. N., Braunsdorf, N. R., Birbiglia, G. V., Kittridge, M. G., MacAulay, C. I. and Espejo, I. S. (2010) 'Sandstone diagenesis and reservoir quality prediction: Models, myths, and reality', *AAPG Bulletin,* 94, (8), pp. 1093-1132.

Tempel, R. N. and Harrison, W. J. (2000) 'Simulation of burial diagenesis in the Eocene Wilcox group of the Gulf of Mexico basin', *Applied Geochemistry,* 15, (8), pp. 1071-1083.

Thiry, M. and Millot, G. (1987) 'Mineralogical forms of silica and their sequence of formation in silcretes', *Journal of Sedimentary Petrology,* 57, (2), pp. 343-352.

Thomas, A. R., Dahl, W. M., Hall, C. M. and York, D. (1993) '40Ar/39Ar analyses of authigenic muscovite, timing of stylolitization, and implications for pressure solution mechanisms: Jurassic Norphlet Formation, offshore Alabama', *Clays & Clay Minerals,* 41, (3), pp. 269-279.

Thyberg, B., Jahren, J., Winje, T., Bjørlykke, K., Faleide, J. I. and Marcussen, Ø. (2010) 'Quartz cementation in Late Cretaceous mudstones, northern North Sea: Changes in rock properties due to dissolution of smectite and precipitation of micro-quartz crystals', *Marine and Petroleum Geology,* 27, (8), pp. 1752-1764.

Thyne, G., Boudreau, B. P., Ramm, M. and Midtbø, R. E. (2001) 'Simulation of potassium feldspar dissolution and illitization in the Statfjord Formation, North Sea', *AAPG Bulletin,* 85, (4), pp. 621-635.

Todd, T. W. (1963) 'Post-depositional history of Tensleep Sandstone (Pennsylvanian), Big Horn Basin, Wyoming', *AAPG Bulletin,* 47, (4), pp. 599-616.

Towe, K. M. (1962) 'Clay mineral diagenesis as a possible source of silica cement in sedimentary rocks', *Journal of Sedimentary Petrology,* 32, (1), pp. 26-28.

Trewin, N. H. and Fallick, A. E. (2000) 'Quartz cement origins and budget in the Tumblagooda sandstone, Western Australia', in Worden, R. H. and Morad, S.(eds) *Quartz Cementation in Sandstones.* Vol. 29 Oxford: Wiley-Blackwell pp. 219-230.

Trurnit, P. (1968) 'Pressure solution phenomena in detrital rocks', *Sedimentary Geology,* 2, (2), pp. 89-114.

Urey, H. (1947) 'The thermodynamic properties of isotopic substances.', *Journal of Chemical Society,* pp. 562-581.

Vagle, G. B., Hurst, A. and Dypvik, H. (1994) 'Origin of quartz cements in some sandstones from the Jurassic of the inner Moray Firth (UK)', *Sedimentology,* 41, (2), pp. 363-377.

Valley, J. W. and Kita, N. T. (2009) 'In situ oxygen isotope geochemistry by ion microprobe', *Mineralogical Association Canada Short Course,* 41, pp. 19-63.

van de Kamp, P. C. (2008) 'Smectite-illite-muscovite transformations, quartz dissolution, and silica release in shales', *Clays and Clay Minerals,* 56, (1), pp. 66-81.

Velde, B. and Renac, C. (1996) 'Smectite to illite conversion and K-AR ages', *Clay Minerals,* 31, (1), pp. 25-32.

Velde, B. and Vasseur, G. (1992) 'Estimation of the diagenetic smectite to illite transformation in time-temperature space', *American Mineralogist,* 77, (9-10), pp. 967-976.

Walderhaug, O. (1994a) 'Temperatures of quartz cementation in Jurassic sandstones from the Norwegian continental shelf - evidence from fluid inclusions', *Journal of Sedimentary Research A: Sedimentary Petrology & Processes,* 64 A, (2), pp. 311-323.

Walderhaug, O. (1994b) 'Precipitation rates for quartz cement in sandstones determined by fluid-inclusion microthermometry and temperature-history modeling', *Journal of Sedimentary Research A: Sedimentary Petrology & Processes,* 64 A, (2), pp. 324-333.

Walderhaug, O. (1996) 'Kinetic modeling of quartz cementation and porosity loss in deeply buried sandstone reservoirs', *American Association of Petroleum Geologists Bulletin,* 80, (5), pp. 731-745.

Walderhaug, O. (2000) 'Modeling quartz cementation and porosity in Middle Jurassic Brent Group sandstones of the Kvitebjorn field, Northern North Sea', *American Association of Petroleum Geologists Bulletin,* 84, (9), pp. 1325-1339.

Walderhaug, O. and Bjørkum, P. A. (2003) 'The effect of stylolite spacing on quartz cementation in the Lower Jurassic Stø Formation, Southern Barents Sea', *Journal of Sedimentary Research,* 73, (2), pp. 146-156.

Walderhaug, O., Bjørkum, P. A. and Aase, N. E. (2006) 'Kaolin-coating of stylolites, effect on quartz cementation and general implications for dissolution at mineral interfaces', *Journal of Sedimentary Research,* 76, (1-2), pp. 234-243.

Walderhaug, O., Bjørkum, P. A., Nadeau, P. H. and Langnes, O. (2001) 'Quantitative modelling of basin subsidence caused by temperature-driven silica dissolution and reprecipitation', *Petroleum Geoscience,* 7, (2), pp. 107-113.

Walderhaug, O., Lander, R. H., Bjørkum, P. A., Oelkers, E. H., Bjørlykke, K. and Nadeau, P. H. (2000) 'Modelling quartz cementation and porosity in reservoir sandstones: Examples from the Norwegian continental shelf', in Worden, R. H. and Morad, S.(eds) *Quartz Cementation in Sandstones.* Vol. 29 Oxford: Wiley-Blackwell pp. 39-49.

Wangen, M. (1999) 'Modelling quartz cementation of quartzose sandstones', *Basin Research,* 11, (2), pp. 113-126.

Warren, E. A. and Smalley, P. C. (1994) *North Sea Formation Waters Atlas.* London: The Geological Society.

Weibel, R., Friis, H., Kazerouni, A. M., Svendsen, J. B., Stokkendal, J. and Poulsen, M. L. K. (2010) 'Development of early diagenetic silica and quartz morphologies - Examples from the Siri Canyon, Danish North Sea', *Sedimentary Geology,* 228, (3-4), pp. 151-170.

Weltje, G. J. (2002) 'Quantitative analysis of detrital modes: Statistically rigorous confidence regions in ternary diagrams and their use in sedimentary petrology', *Earth-Science Reviews,* 57, (3-4), pp. 211-253.

Weyl, P. K. (1959) 'Pressure solution and the force of crystallization - A phenomenological theory', *Journal of Geophysical Research,* 64, (11), pp. 2001-2025.

Wilkinson, J. J., Lonergan, L., Fairs, T. and Herrington, R. J. (1998) 'Fluid inclusion constraints on conditions and timing of hydrocarbon migration and quartz cementation in Brent Group reservoir sandstones, Columba Terrace, northern North Sea', in *Geological Society Special Publication* pp 69-89.

Wilkinson, M., Haszeldine, R. S. and Fallick, A. E. (2006) 'Jurassic and Cretaceous clays of the northern and central North Sea hydrocarbon reservoirs reviewed', *Clay Minerals,* 41, (1), pp. 151-186.

Wilkinson, M., Milliken, K. L. and Haszeldine, R. S. (2001) 'Systematic destruction of K-feldspar in deeply buried rift and passive margin sandstones', *Journal of the Geological Society,* 158, (4), pp. 675-683.

Williams, L. A. and Crerar, D. A. (1985b) 'Silica diagenesis: II. General mechanisms', *Journal of Sedimentary Petrology,* 55, (3), pp. 312-321.

Williams, L. A., Parks, G. A. and Crerar, D. A. (1985a) 'Silica diagenesis: I. Solubility controls', *Journal of Sedimentary Petrology,* 55, (3), pp. 301-311.

Williams, L. B., Hervig, R. L. and Bjørlykke, K. (1997) 'New evidence for the origin of quartz cements in hydrocarbon reservoirs revealed by oxygen isotope microanalyses', *Geochimica et Cosmochimica Acta,* 61, (12), pp. 2529-2538.

Williams, L. B., Hervig, R. L. and Hutcheon, I. (2001) 'Boron isotope geochemistry during diagenesis. Part II. Applications to organic-rich sediments', *Geochimica et Cosmochimica Acta,* 65, (11), pp. 1783-1794.

Wood, J. R. and Hewett, T. A. (1982) 'Fluid convection and mass transfer in porous sandstones-a theoretical model', *Geochimica et Cosmochimica Acta,* 46, (10), pp. 1707-1713.

Worden, R. H. and Morad, S. (2000) 'Quartz Cementation in Oil Field Sandstones: A Review of the Key Controversies', in Worden, R. H. and Morad, S.(eds) *Quartz Cementation in Sandstones.* Vol. 29 Oxford: Wiley-Blackwell pp. 1-20.

Worden, R. H. and Morad, S. (2002) 'Clay minerals in sandstones: Controls on formation, distribution and evolution', *International Association of Sedimentologists Special Publications,* (34), pp. 3-41.

Worden, R. H., Oxtoby, N. H. and Smalley, P. C. (1998) 'Can oil emplacement prevent quartz cementation in sandstones?', *Petroleum Geoscience,* 4, (2), pp. 129-137.

Worden, R. H., Warren, E. A., Smalley, P. C., Primmer, T. J. and Oxtoby, N. H. (1995) 'Discussion of 'Evidence for resetting of fluid inclusion temperatures from quartz cements in oilfields' by Osborne and Haszeldine (1993)', *Marine and Petroleum Geology,* 12, (5), pp. 566-570.

Yang, Y. and Aplin, A. C. (1997) 'A method for the disaggregation of mudstones', *Sedimentology*, 44, (3), pp. 559-562.

Zhang, L., Liu, J., Zhou, H. and Chen, Z. (1989) 'Oxygen isotope fractionation in the quartz-water-salt system', *Economic Geology*, 84, (6), pp. 1643-1650.

7. Appendices

Appendix 1: **North Sea Ness Formation Quantitative Petrography**

Sample	NS4	NS1	NS1	NS2	NS1	NS2	NS1	NS2	NS1	NS1	NS1
Depth (m)	2678	2845	2846	3420	3462	4313	4332	4343	4344	3831	465
Temperature (^{o}C)	109	118	118	122	122	133	133	133	133	137	165
Ave. Grain Size	125.	94.3	193	173.	398	366.	163.	243.	322.	141	103.
Ave. Quartz	**1.3**	**6.3**	**3.3**	**6.7**	**7.0**	**13.3**	**15.3**	**18.7**	**16.0**	**7.3**	**2.3**
95% Confidence	0.8	3.4	1.9	2.4	1.7	5.8	4.4	4.7	2.9	2.2	1.9
Standard Deviation	1.0	4.3	2.4	3.0	2.1	7.2	5.5	5.9	3.6	2.7	2.3
Minimum Quartz	0.0	0.0	2.0	4.0	4.0	6.0	8.0	10.0	10.0	4.0	0.0
Maximum Quartz	2.0	12.0	8.0	10.0	10.0	24.0	24.0	26.0	20.0	12.0	6.0
Ave. Porosity	**18.3**	**0.3**	**1.3**	**2.3**	**1.0**	**13.7**	**4.0**	**10.3**	**17.0**	**5.3**	**0.7**
95% Confidence	9.4	0.7	1.3	2.6	2.0	4.6	4.7	4.9	9.4	4.3	0.8
Standard Deviation	11.7	0.8	1.6	3.2	2.4	5.7	5.9	6.1	11.8	5.3	1.0
Minimum Porosity	6.0	0.0	0.0	0.0	0.0	8.0	0.0	4.0	8.0	0.0	0.0
Maximum Porosity	40.0	2.0	4.0	8.0	6.0	20.0	16.0	22.0	40.0	12.0	2.0
Ave. Detrital	**47.3**	**49.3**	**64.3**	**64.0**	**58.3**	**68.0**	**54.0**	**68.7**	**66.0**	**67.3**	**45.7**
95% Confidence	9.4	7.9	4.2	5.7	8.8	5.0	5.8	6.8	7.1	7.4	13.9
Standard Deviation	11.8	9.9	5.3	7.2	11.0	6.2	7.3	8.5	8.9	9.3	17.3
Minimum Detrital	26.0	38.0	58.0	54.0	46.0	58.0	44.0	58.0	50.0	56.0	20.0
Maximum Detrital	60.0	66.0	72.0	74.0	74.0	74.0	62.0	80.0	76.0	80.0	68.0
Ave. Non Quartz	**33.0**	**44.0**	**31.0**	**27.0**	**33.7**	**5.0**	**26.7**	**2.3**	**1.0**	**20.0**	**51.3**
95% Confidence	7.4	7.5	3.6	7.8	9.7	3.0	9.9	2.6	1.3	5.6	14.7
Standard Deviation	9.2	9.4	4.5	9.8	12.1	3.7	12.4	3.2	1.7	7.0	18.4
Minimum Non	24.0	28.0	24.0	14.0	16.0	2.0	12.0	0.0	0.0	10.0	26.0
Maximum Non	48.0	56.0	38.0	42.0	50.0	12.0	48.0	8.0	4.0	28.0	78.0

Quantitative petrography using the point counting method. Non quartz relates to all minerals other than quartz.

Sample	NS11	NS10	NS23	NS25	NS17	NS20	NS19	NS14
Depth (m)	2845.8	2846.0	3420.8	4313.5	4332.7	4343.4	4344.3	3831.4
Temperature (^{o}C)	118	118	122	133	133	133	133	137
Ave. Grain Size	94.3	193.0	173.1	366.7	163.3	243.9	322.6	141.0
Ave. Quartz Cement	**3.9**	**11.8**	**9.1**	**16.2**	**20.7**	**22.5**	**13.4**	**18.9**
95% Confidence (±)	2.0	2.9	2.4	3.8	3.5	1.9	1.6	2.8
Standard Deviation	2.5	3.6	3.0	4.7	4.7	3.2	2.8	3.4
Minimum Quartz	1.3	6.8	4.9	12.0	14.2	19.6	6.8	15.3
Maximum Quartz	7.0	16.3	13.1	24.8	27.3	30.1	16.7	23.6
Ave. Porosity (%bv)	**0.7**	**2.0**	**6.9**	**11.1**	**2.1**	**5.6**	**15.1**	**3.3**
95% Confidence (±)	0.6	0.7	6.4	2.1	2.7	3.7	4.5	2.5
Standard Deviation	0.8	0.8	8.0	2.6	3.6	6.2	7.6	3.2
Minimum Porosity	0.1	1.3	1.1	6.7	0.1	0.8	6.2	0.4
Maximum Porosity	1.9	3.7	18.5	14.2	9.8	18.5	28.8	7.2
Ave. Detrital Quartz	**36.3**	**47.1**	**50.1**	**68.2**	**49.7**	**62.2**	**64.7**	**59.6**
95% Confidence (±)	10.4	3.2	6.2	5.1	5.1	3.6	5.0	5.1
Standard Deviation	13.1	4.0	7.7	6.4	6.8	6.0	8.5	6.4
Minimum Detrital	21.5	42.4	38.0	57.0	40.1	52.5	46.0	50.4
Maximum Detrital	54.8	52.7	56.6	75.8	58.8	69.3	73.6	67.9
Ave. Non Quartz	**59.2**	**39.1**	**33.8**	**4.6**	**27.5**	**9.7**	**6.7**	**18.2**
95% Confidence (±)	12.6	1.0	7.3	1.3	5.5	1.4	1.3	5.6
Standard Deviation	15.8	1.2	9.2	1.6	7.5	2.4	2.2	7.0
Minimum Non	36.3	37.4	17.5	2.5	14.0	6.1	3.3	11.6
Maximum Non	76.9	41.0	42.5	7.2	34.7	15.2	11.0	28.7

Quantitative petrography using the image analysis method**.** Non quartz relates to all minerals other than quartz.

Sample	NS4	NS11	NS1	NS23	NS1	NS25	NS17	NS20	NS19	NS14	NS12
Depth (m)	2678.	2845.	284	3420.	3462.	4313.	4332.	4343.	4344.	3831.	4653.
Temperatu	100	118	118	122	122	133	133	133	133	137	165
Ave. Grain	**125.3**	**94.3**	**193.**	**173.1**	**398.0**	**366.7**	**162.3**	**243.9**	**322.6**	**141.0**	**103.5**
95%	12.2	16.3	16.8	15.4	53.1	56.2	15.4	32.8	23.1	16.2	12.5
Standard	43.9	60.0	63.7	56.5	155.7	202.6	59.3	158.0	104.8	58.5	42.6
Minimum	55.6	26.7	73.3	40.0	166.7	66.7	60.0	58.3	100.0	58.3	55.6
Maximum	277.8	276.7	340.	320.0	777.8	1250.	293.3	1083.	616.7	291.7	277.8

Appendix 2: Texas Wilcox Sandstone Quantitative Petrography

Sample	GOM6	GOM8	GOM7	GOM9	GOM10	GOM11
Depth (m)	2733.4	3518.4	3534.2	4277.6	4288.5	5063.3
Temperature (^{o}C)	103.5	143.2	143.2	163.5	163.5	185.4
Ave. Grain Size (µm)	**244**	**171**	**145**	**190**	**226**	**161**
95% Confidence (±)	17.0	19.5	11.7	16.9	21.7	13.6
Standard Deviation	77.1	79.7	45.6	65.2	82.9	51.0
Minimum Grain Size	120.0	66.7	53.3	73.3	80.0	60.0
Maximum Grain Size	480.0	486.7	220.0	413.3	420.0	293.3
Ave. Detrital Quartz	**68.1**	**53.5**	**54.3**	**47.1**	**46.4**	**57.1**
95% Confidence (±)	3.1	6.7	3.6	5.4	7.6	4.0
Standard Deviation	3.9	8.4	4.6	6.7	9.5	5.0
Minimum Detrital	64.7	41.1	48.7	40.6	31.6	50.1
Maximum Detrital	73.6	63.9	62.5	58.0	58.9	64.5
Ave. Non Quartz	**0.8**	**15.9**	**20.3**	**28.1**	**27.1**	**23.8**
95% Confidence (±)	0.6	3.9	3.7	4.2	7.6	5.3
Standard Deviation	0.8	4.8	4.6	5.2	9.5	6.7
Minimum Non Quartz	0.2	10.4	11.5	20.1	13.7	15.6
Maximum Non Quartz	1.9	22.1	24.4	34.3	39.1	32.5

Quantification of the Wilcox sandstone by image analysis

Appendix 3: North Sea Ness Formation SIMS Data

Material Type	Pit Colour
Detrital	Black
Overgrowth	White
Mixed (authigenic and detrital quartz)	Red
Low secondary ion yield	Yellow
Pit overlap	Green
Sample cracked	Pink
Unknown detrital host (NS20 Area 2)	Gold
Unknown	Grey

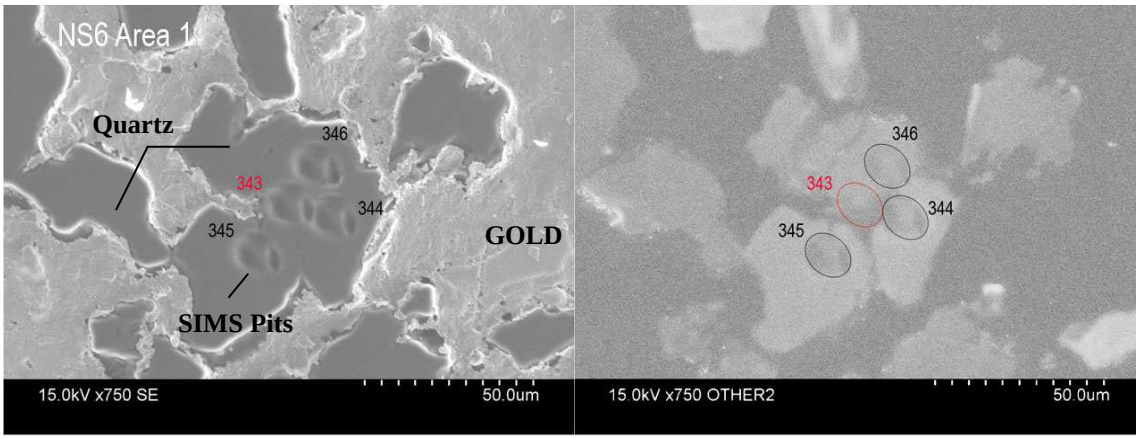
NS6 Area 1
Quartz
346
343
344
345
GOLD
SIMS Pits
15.0kV x750 SE
50.0um
346
343
344
345
15.0kV x750 OTHER2
50.0um

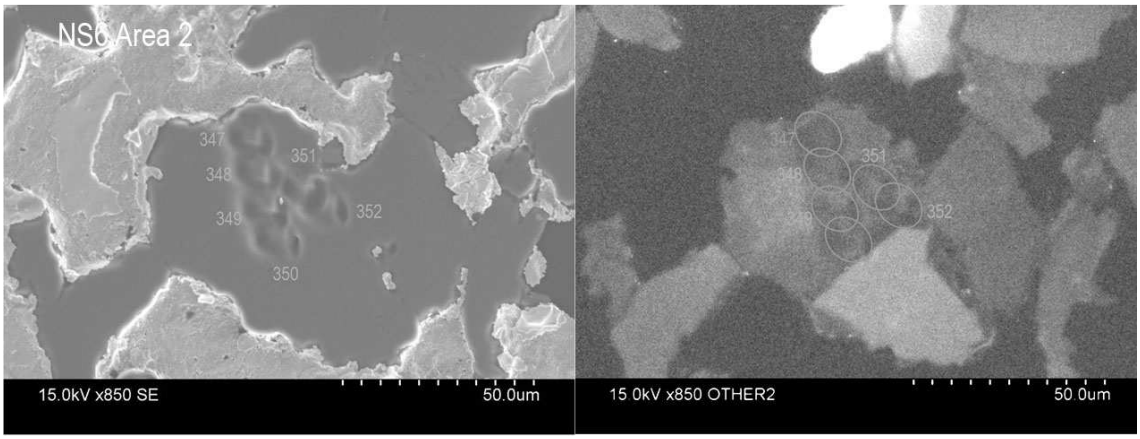
NS6 Area 2
347
348
349
350
351
352
15.0kV x850 SE
50.0um
15 0kV x850 OTHER2
50.0um

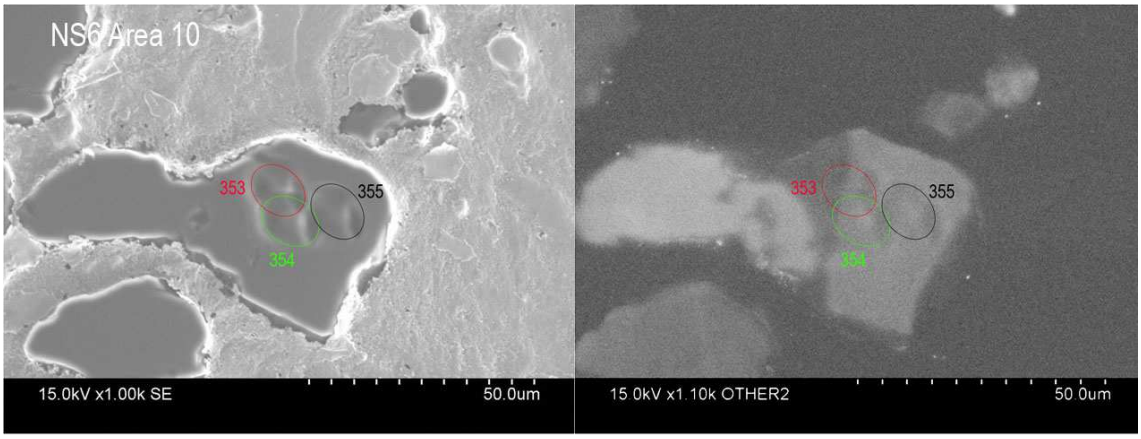
NS6 Area 10
353
354
355
15.0kV x1.00k SE
50.0um
353
354
355
15 0kV x1.10k OTHER2
50.0um

Well 30/9-12 NS6 (109°C) 12 µm beam, 2.3nA intensity. May 8 , 2008.

Analyses #	Sample	^{16}O cps x10^9	$\delta^{18}O$ RAW	2 SE	$\delta^{18}O$ V-SMOW	2 SD	Comments	µm from DQ	% from DQ
339	UWQ-1	1.70	7.63	0.22					
340	UWQ-1	172	7.33	0.39					
341	UWQ-1	1.63	7.44	0.35					
342	UWQ-1	1.66	7.58	0.30					
343	06_A1_01	1.60	13.27	0.40	**18.03**	**0.36**	Mixed		
344	06_A1_02	1.60	4.67	0.31	**9.39**	**0.36**	Detrital		
345	06_A1_03	1.58	5.15	0.34	**9.87**	**0.36**	Detrital		
346	06_A1_04	1.60	3.99	0.37	**8.71**	**0.36**	Detrital		
347	06_A2_01	1.60	10.30	0.27	**15.05**	**0.36**	?		
348	06_A2_02	1.67	8.68	0.29	**13.42**	**0.36**	?		
349	06_A2_03	1.70	8.33	0.27	**13.07**	**0.36**	?		
350	06_A2_04	1.73	11.23	0.29	**15.98**	**0.36**	?		
351	06_A2_05	1.74	9.13	0.27	**13.87**	**0.36**	?		
352	06_A2_06	1.75	11.44	0.30	**16.20**	**0.36**	?		
353	06_A10_01	1.68	15.91	0.31	**20.68**	**0.36**	Mixed		
354	06_A10_02	16.5	7.78	0.36	**12.52**	**0.36**	Overlaps 1		
355	06_A10_03	1.57	4.49	0.36	**9.21**	**0.36**	Detrital		
356	UWQ-1	1.57	7.45	0.33					
357	UWQ-1	1.57	7.77	0.34					
358	UWQ-1	1.60	7.73	0.28					
359	UWQ-1	1.61	7.83	0.27					
Bracket (339-342 356-359)		**average**	**7.59**			**2 SD = 0.36**			

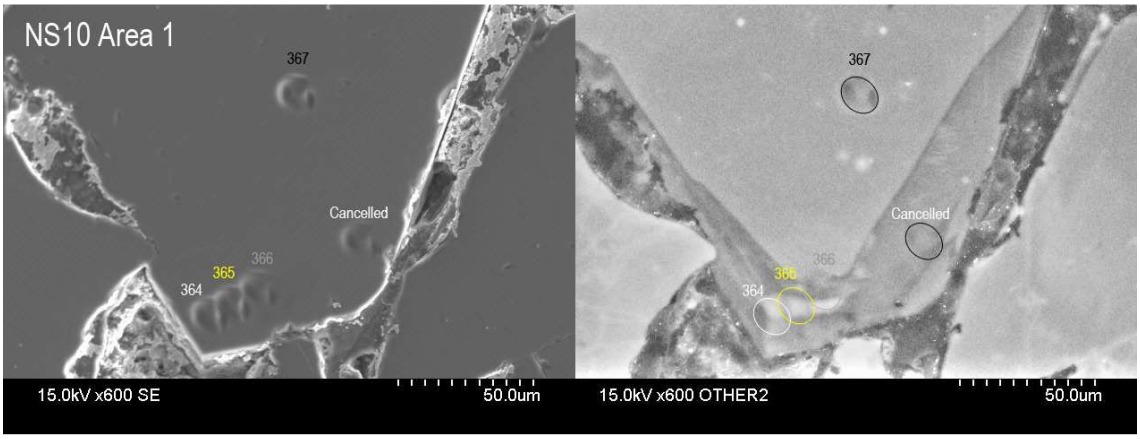
NS10 Area 1
367
Cancelled
366
365
364
15.0kV x600 SE
50.0um
367
Cancelled
366
365
364
15.0kV x600 OTHER2
50.0um

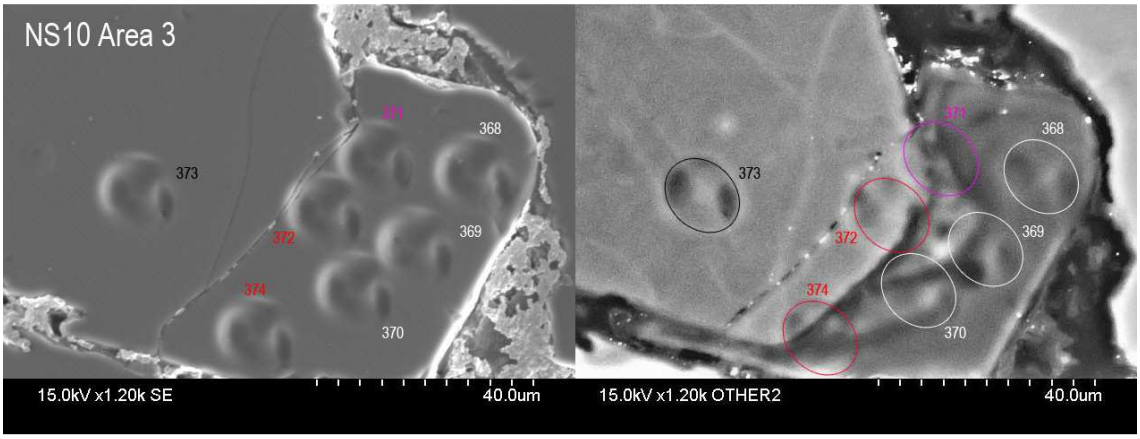
NS10 Area 3
371
368
373
372
369
374
370
15.0kV x1.20k SE
40.0um
371
368
373
372
369
374
370
15.0kV x1.20k OTHER2
40.0um

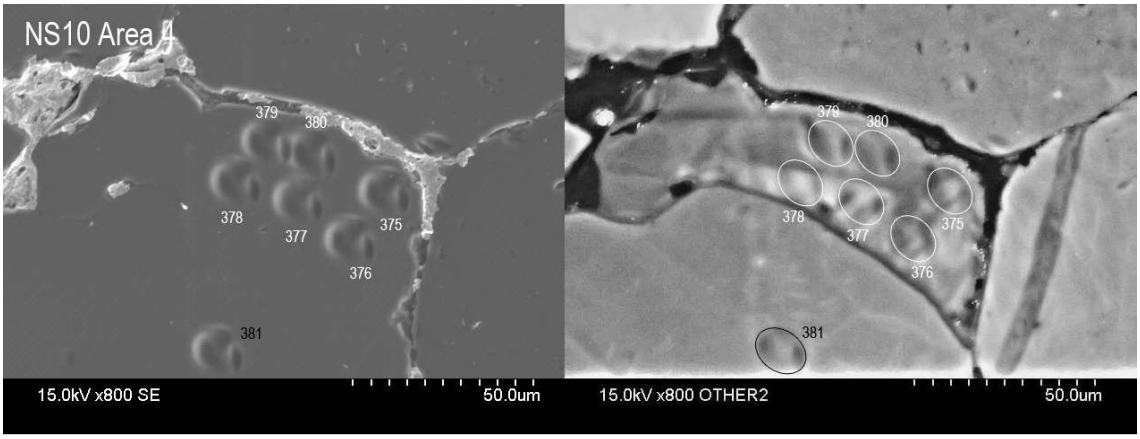
NS10 Area 4
379
380
378
377
375
376
381
15.0kV x800 SE
50.0um
379
380
378
377
375
376
381
15.0kV x800 OTHER2
50.0um

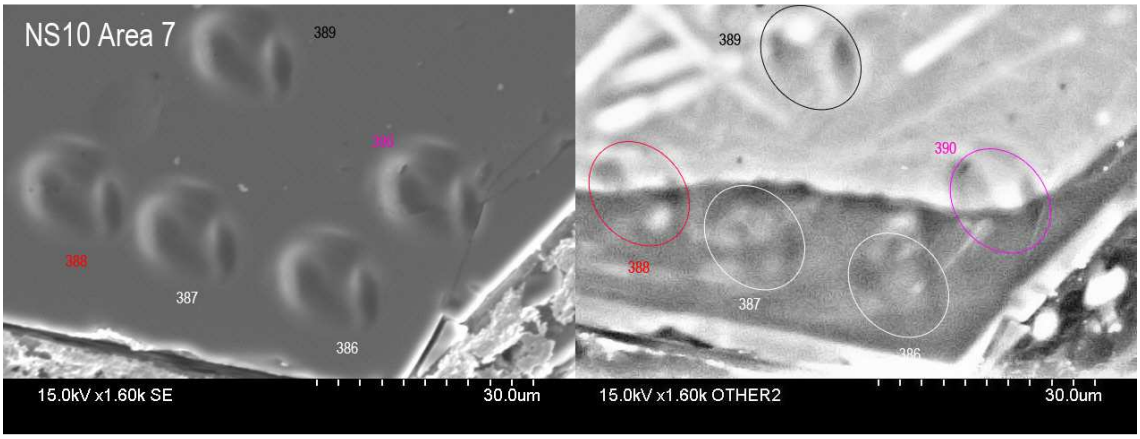
NS10 Area 7
389
390
388
387
386
15.0kV x1.60k SE
30.0um
389
390
388
387
386
15.0kV x1.60k OTHER2
30.0um

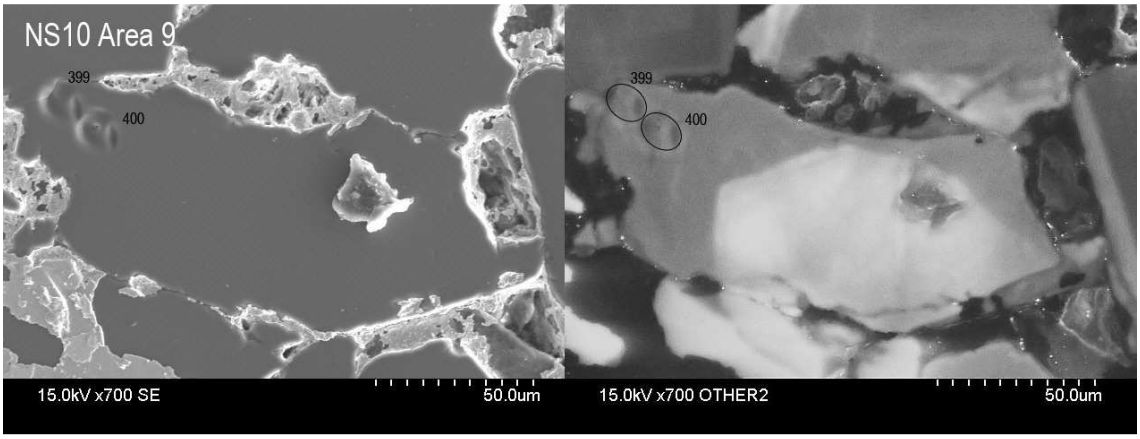
NS10 Area 9
399
400
15.0kV x700 SE
50.0um
399
400
15.0kV x700 OTHER2
50.0um

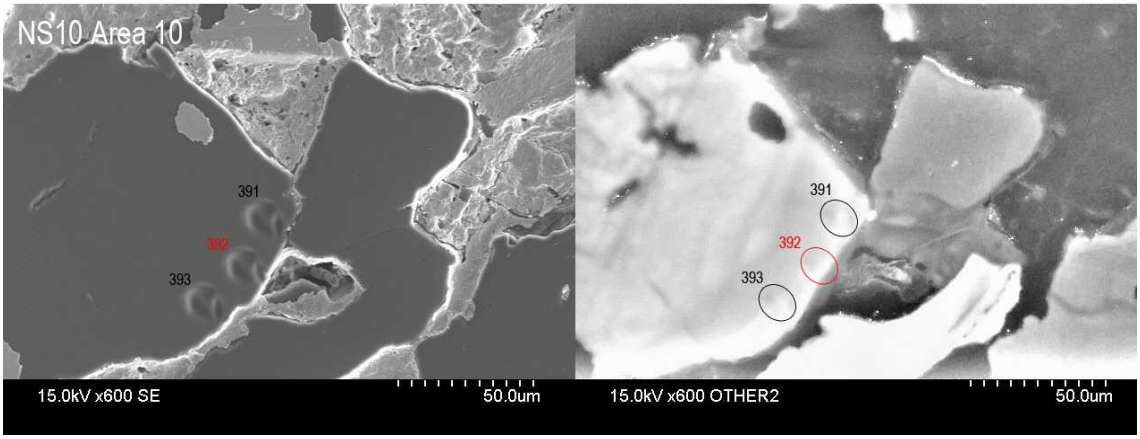
NS10 Area 10
391
392
393
15.0kV x600 SE
50.0um
391
392
393
15.0kV x600 OTHER2
50.0um

Well 30/3-4 NS 10 (118°C) 12 µm beam, 2.3nA intensity. May 7, 2008.

Analyses #	Sample	^{16}O cps x10^9	$\delta^{18}O$ RAW	2 SE	$\delta^{18}O$ VSMOW	2 SD	Comments	µm from DQ	% from DQ
360	UWQ-1	1.63	7.65	0.37					
361	UWQ-1	1.64	7.61	0.27					
362	UWQ-1	1.62	7.43	0.33					
363	UWQ-1	1.61	7.49	0.39					
364	10_A1_01	1.55	17.06	0.36	**21.87**	**0.27**	Cement	15.8	63.2
365	10_A1_02	1.54	18.44	0.38	**23.26**	**0.27**	High Yield		
366	10_A1_03	1.59	15.66	0.29	**20.47**	**0.27**	Coating		
367	10_A1_04	1.73	2.93	0.28	**7.68**	**0.27**	Detrital		
368	10_A3_01	1.66	14.51	0.29	**19.31**	**0.27**	Cement	19.7	63.8
369	10_A3_02	1.65	16.26	0.26	**21.07**	**0.27**	Cement	13.1	51.3
370	10_A3_03	1.65	16.36	0.33	**21.17**	**0.27**	Cement	9.2	32.6
371	10_A3_04	1.65	7.82	0.30	**12.59**	**0.27**	Cracked		
372	10_A3_05	1.65	13.47	0.25	**18.27**	**0.27**	Mixed		
373	10_A3_06	1.62	5.68	0.42	**10.44**	**0.27**	Detrital		
374	10_A3_07	1.59	15.50	0.20	**20.31**	**0.27**	Mixed		
375	10_A4_01	1.63	17.50	0.31	**22.32**	**0.27**	Cement	26.5	75.0
376	10_A4_02	1.62	19.35	0.27	**24.17**	**0.27**	Cement	10.8	30.6
377	10_A4_03	1.62	18.92	0.35	**23.74**	**0.27**	Cement	10.8	32.4
378	10_A4_04	1.63	19.40	0.25	**24.22**	**0.27**	Cement	7.8	27.6
379	10_A4_05	1.63	17.65	0.38	**22.46**	**0.27**	Cement	19.6	66.7
380	10_A4_06	1.64	17.78	0.21	**22.60**	**0.27**	Cement	23.5	70.6
381	10_A4_07	1.63	4.66	0.32	**9.42**	**0.27**	Detrital		
382	UWQ-1	1.62	7.35	0.43					
383	UWQ-1	1.64	7.70	0.26					
384	UWQ-1	1.69	7.74	0.27					
385	UWQ-1	1.71	7.53	0.28					
Bracket (360-363, 382-385)		**average**	**7.56**			**2 SD = 0.27**			

Analyses #	Sample	^{16}O cps x10^9	$\delta^{18}O$ RAW	2 SE	$\delta^{18}O$ VSMOW	2 SD	Comments	µm from DQ	% from DQ
386	10_A7_01	1.69	16.83	0.19	**21.75**	**0.40**	Cement	11.4	39.0
387	10_A7_02	1.68	19.06	0.39	**23.98**	**0.40**	Cement	6.9	26.4
388	10_A7_03	1.74	15.63	0.23	**20.54**	**0.40**	Mixed		
389	10_A7_04	1.74	9.98	0.29	**14.86**	**0.40**	Detrital		
390	10_A7_05	1.75	11.20	0.29	**16.09**	**0.40**	Cracked		
391	10_A10_01	1.63	6.06	0.37	**10.92**	**0.40**	Detrital		
392	10_A10_02	1.63	7.34	0.29	**12.21**	**0.40**	Mixed		
393	10_A10_03	1.62	5.81	0.27	**10.67**	**0.40**	Detrital		
394	10_A11_01	1.67	17.48	0.37	**22.39**	**0.40**	Mixed		
395	10_A11_02	1.65	16.87	0.42	**21.78**	**0.40**	Mixed		
396	10_A11_03	1.65	16.59	0.28	**21.50**	**0.40**	Cracked		
397	10_A11_04	1.65	4.36	0.28	**9.21**	**0.40**	Detrital		
398	10_A11_05	1.66	2.84	0.37	**7.69**	**0.40**	Cracked		
399	10_A09_01	1.63	8.54	0.35	**13.41**	**0.40**	Detrital		
400	10_A09_02	1.63	5.54	0.38	**10.40**	**0.40**	Detrital		
401	UWQ-1	1.61	7.57	0.36					
402	UWQ-1	1.61	7.21	0.38					
403	UWQ-1	1.62	7.36	0.37					
404	UWQ-1	1.60	7.25	0.44					
Bracket (360-363, 382-385)		**average**	**7.46**			**2 SD = 0.40**			

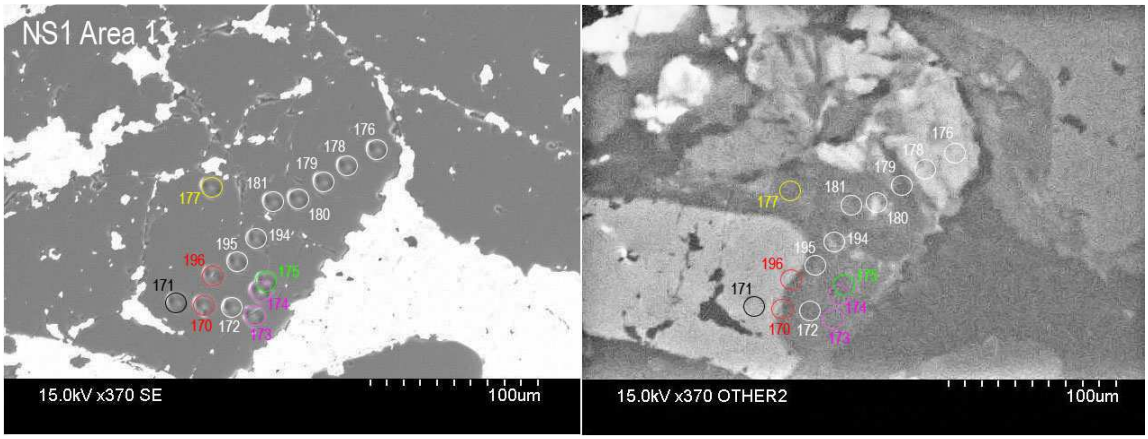
NS1 Area 1
15.0kV x370 SE
100um
15.0kV x370 OTHER2
100um

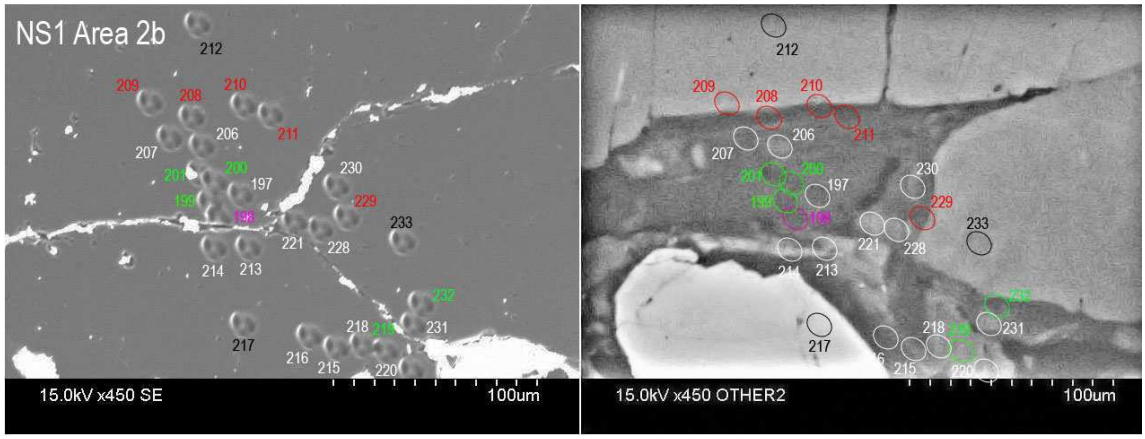
NS1 Area 2b
15.0kV x450 SE
100um
15.0kV x450 OTHER2
100um

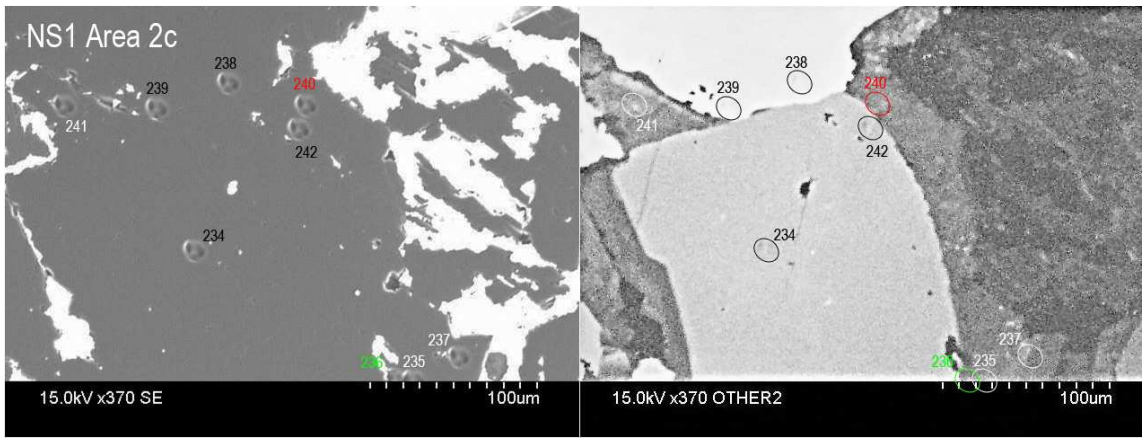
NS1 Area 2c
15.0kV x370 SE
100um
15.0kV x370 OTHER2
100um

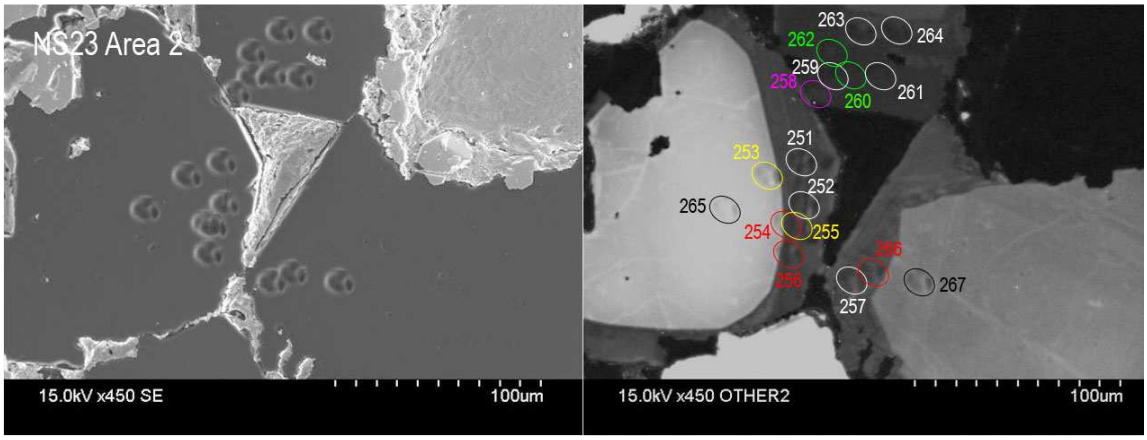
NS23 Area 2
15.0kV x450 SE
100um
263
264
262
259
258
260
261
251
253
252
265
254
255
256
257
267
15.0kV x450 OTHER2
100um

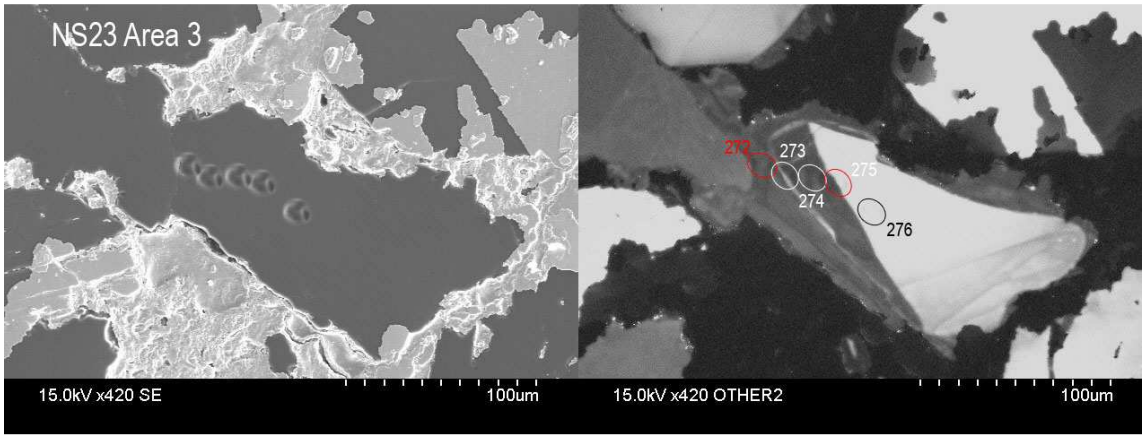
NS23 Area 3
15.0kV x420 SE
100um
272
273
275
274
276
15.0kV x420 OTHER2
100um

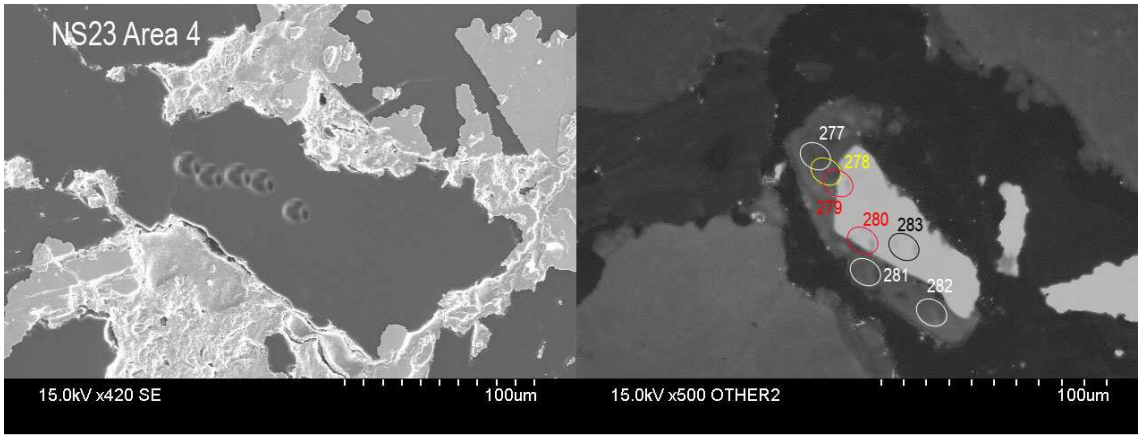
NS23 Area 4
15.0kV x420 SE
100um
277
278
279
280
283
281
282
15.0kV x500 OTHER2
100um

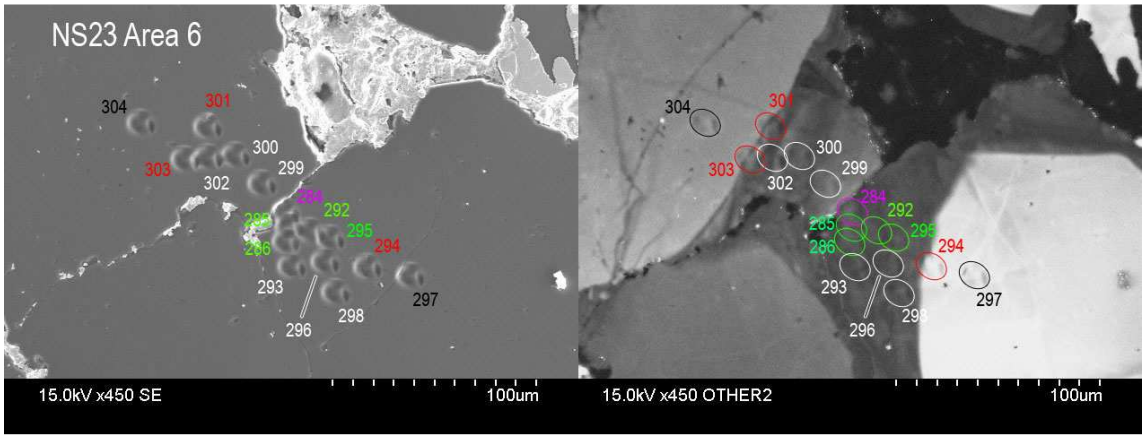
NS23 Area 6
304
301
300
299
303
302
284
292
285
295
286
294
293
297
298
296
15.0kV x450 SE
100um
304
301
300
299
303
302
284
292
285
295
286
294
293
297
298
296
15.0kV x450 OTHER2
100um

Well 211/11a-3 NS 1 and NS23 (122°C) 12 µm beam, 2.3nA intensity. May 7, 2008.

Analyses #	Sample	^{16}O cps x10^9	$\delta^{18}O$ RAW	2 SE	$\delta^{18}O$ VSMOW	2 SD	Comments	µm from DQ	% from DQ
166	UWQ-1	1.59	6.90	0.33					
167	UWQ-1	1.61	6.54	0.31					
168	UWQ-1	1.60	6.91	0.28					
169	UWQ-1	1.59	6.76	0.33					
170	1_A01_01	1.59	12.28	0.50	**17.94**	**0.48**	Mixed		
171	1_A01_02	1.59	-0.02	0.34	**5.58**	**0.48**	Detrital		
172	1_A01_03	1.60	17.57	0.25	**23.26**	**0.48**	Cement	17.2	33.3
173	1_A01_04	1.64	15.68	0.40	**21.36**	**0.48**	Cracked		
174	1_A01_05	1.61	17.13	0.23	**22.82**	**0.48**	Cracked		
175	1_A01_06	1.66	16.27	0.37	**22.95**	**0.48**	Overlaps 5		
176	1_A01_07	1.58	15.52	0.35	**21.20**	**0.48**	Cement	101.1	85.5
177	1_A01_08	1.56	15.83	0.38	**21.52**	**0.48**	Low Yield		
178	1_A01_09	1.60	15.38	0.19	**21.06**	**0.48**	Cement	79.6	67.3
179	1_A01_10	1.60	15.67	0.21	**21.36**	**0.48**	Cement	64.5	54.5
180	1_A01_11	1.60	15.40	0.32	**21.08**	**0.48**	Cement	49.5	41.8
181	1_A01_12	1.61	15.15	0.40	**20.83**	**0.48**	Cement	25.8	21.8
182	UWQ-1	1.61	6.66	0.37					
183	UWQ-1	1.65	6.20	0.24					
184	UWQ-1	1.63	6.89	0.36					
185	UWQ-1	1.63	6.71	0.30					
Bracket (166-169, 182-185)		**average**	**6.70**			**2 SD = 0.48**			
May 8, 2008									
Continue the same mount (NS1), Mass Calib NMR=0.1005923, FC OFFSET done									
190	UWQ-1	1.44	7.34	0.44					
191	UWQ-1	1.44	7.53	0.29					
192	UWQ-1	1.43	7.39	0.38					
193	UWQ-1	1.44	7.38	0.39					

Analyses #	Sample	^{16}O cps x10^9	$\delta^{18}O$ RAW	2 SE	$\delta^{18}O$ VSMOW	2 SD	Comments	µm from DQ	% from DQ
194	1_A01_13	1.44	17.13	0.37	**22.18**	**0.23**	Cement	21.5	28.6
195	1_A01_14	1.44	18.31	0.32	**23.37**	**0.23**	Cement	5.4	10.4
196	1_A01_15	1.46	8.88	0.43	**13.89**	**0.23**	Mixed		
197	1_A02b_01	1.44	16.39	0.32	**21.43**	**0.23**	Cement	44.2	71.4
198	1_A02b_02	1.39	14.16	0.38	**19.19**	**0.23**	Cracked		
199	1_A02b_03	1.48	15.82	0.32	**20.86**	**0.23**	Overlaps 2		
200	1_A02b_04	1.46	15.76	0.41	**20.81**	**0.23**	Overlaps 3		
201	1_A02b_05	1.50	16.23	0.33	**21.27**	**0.23**	Overlaps 4		
202	UWQ-1	1.45	7.28	0.37					
203	UWQ-1	1.45	7.16	0.38					
204	UWQ-1	1.45	7.31	0.44					
205	UWQ-1	1.44	7.24	0.31					
Bracket (190-193, 202-205)		**average**	**7.33**			**2 SD = 0.23**			
206	1_A02b_06	1.45	16.14	0.35	**21.22**	**0.15**	Cement	17.7	29.4
207	1_A02b_07	1.44	16.62	0.32	**21.71**	**0.15**	Cement	12.4	23.3
208	1_A02b_08	1.45	18.33	0.23	**23.43**	**0.15**	Mixed		
209	1_A02b_08	1.44	8.77	0.43	**13.82**	**0.15**	Mixed		
210	1_A02b_09	1.45	14.85	0.42	**19.93**	**0.15**	Mixed		
211	1_A02b_10	1.44	17.48	0.31	**22.57**	**0.15**	Mixed		
212	1_A02b_11	1.45	8.15	0.38	**13.20**	**0.15**	Detrital		
213	1_A02b_12	1.44	15.70	0.26	**20.78**	**0.15**	Cement	17.7	71.4
214	1_A02b_13	1.44	16.27	0.32	**21.36**	**0.15**	Cement	12.4	58.3
215	1_A02b_14	1.46	16.16	0.38	**21.24**	**0.15**	Cement	17.7	35.7
216	1_A02b_15	1.46	16.49	0.35	**21.57**	**0.15**	Cement	8.8	20.0
217	1_A02b_16	1.45	5.03	0.35	**10.06**	**0.15**	Detrital		
218	1_A02b_17	1.47	15.39	0.49	**20.47**	**0.15**	Cement	30.1	58.6
219	1_A02b_18	1.47	14.62	0.32	**19.70**	**0.15**	Overlaps 18		
220	1_A02b_19	1.46	16.01	0.50	**21.10**	**0.15**	Cement	47.8	73.0
221	1_A02b_20	1.44	15.18	0.41	**20.26**	**0.15**	Cement	26.5	75.0
222	UWQ-1	1.47	7.31	0.32					

Analyses #	Sample	^{16}O cps x10^9	$\delta^{18}O$ RAW	2 SE	$\delta^{18}O$ VSMOW	2 SD	Comments	µm from DQ	% from DQ
223	UWQ-1	1.48	7.39	0.35					
226	UWQ-1	1.45	7.38	0.30					
227	UWQ-1	1.45	7.26	0.40					
Bracket (202-205, 222-227)		**average**	**7.29**			**2 SD = 0.15**			
228	1_A02b_21	1.47	15.21	0.37	**20.26**	**0.40**	Cement	10.6	31.6
229	1_A02b_22	1.47	14.46	0.42	**19.50**	**0.40**	Mixed		
230	1_A02b_23	1.47	16.58	0.38	**21.63**	**0.40**	Cement	10.6	52.2
231	1_A02b_24	1.48	15.67	0.29	**20.72**	**0.40**	Cement	12.4	58.3
232	1_A02b_25	1.48	16.10	0.30	**21.15**	**0.40**	Overlaps 25		
233	1_A02b_26	1.47	6.39	0.43	**11.39**	**0.40**	Detrital		
234	1_A02c_01	1.46	4.31	0.34	**9.30**	**0.40**	Detrital		
235	1_A02c_02	1.48	16.33	0.34	**21.38**	**0.40**	Cement	15.1	28.0
236	1_A02c_03	1.49	16.70	0.37	**21.75**	**0.40**	Mixed		
237	1_A02c_04	1.46	16.53	0.41	**21.58**	**0.40**	Cement	43.0	74.1
238	1_A02c_05	1.46	5.71	0.39	**10.71**	**0.40**	Detrital		
239	1_A02c_06	1.45	5.88	0.32	**10.88**	**0.40**	Detrital		
240	1_A02c_07	1.44	19.46	0.46	**24.53**	**0.40**	Mixed		
241	1_A02c_08	1.45	17.08	0.40	**22.13**	**0.40**	Cement	23.7	61.1
242	1_A02c_09	1.45	4.59	0.39	**9.58**	**0.40**	Detrital		
243	UWQ-1	1.46	7.19	0.39					
244	UWQ-1	1.44	7.01	0.35					
245	UWQ-1	1.46	7.35	0.35					
246	UWQ-1	1.47	7.72	0.24					
Bracket (222-227, 243-246)		**average**	**7.32**			**2 SD = 0.40**			
Sample change: NS1 out, NS23 in									
247	UWQ-1	1.43	7.83	0.43					
248	UWQ-1	1.42	7.32	0.32					
249	UWQ-1	1.43	7.34	0.28					
250	UWQ-1	1.43	7.25	0.31					
251	23_A02_01	1.44	15.59	0.36	**20.57**	**0.51**	Cement	12.6	38.7

Analyses #	Sample	^{16}O cps x10^9	$\delta^{18}O$ RAW	2 SE	$\delta^{18}O$ VSMOW	2 SD	Comments	µm from DQ	% from DQ
252	23_A02_02	1.45	14.52	0.30	**19.48**	**0.51**	Cement	10.5	43.5
253	23_A02_03	1.47	8.42	0.35	**13.36**	**0.51**	High Yield		
254	23_A02_04	1.46	13.35	0.30	**18.31**	**0.51**	Mixed		
255	23_A02_05	1.57	15.19	0.29	**20.16**	**0.51**	High Yield		
256	23_A02_06	1.47	14.69	0.38	**19.66**	**0.51**	Mixed		
257	23_A02_07	1.46	17.06	0.26	**22.04**	**0.51**	Cement	13.7	54.2
258	23_A02_08	1.43	14.40	0.37	**19.37**	**0.51**	Cracked		
259	23_A02_09	1.47	15.53	0.26	**20.50**	**0.51**	Cement	40.0	73.1
260	23_A02_010	1.47	16.09	0.33	**21.07**	**0.51**	Overlaps 9		
261	23_A02_011	1.47	15.14	0.30	**20.11**	**0.51**	Cement	31.6	62.5
262	23_A02_12	1.46	15.35	0.37	**20.32**	**0.51**	Overlaps 10		
263	23_A02_13	1.48	17.38	0.26	**22.36**	**0.51**	Cement	16.8	32.0
264	23_A02_14	1.47	17.96	0.29	**22.95**	**0.51**	Cement	12.6	25.0
265	23_A02_15	1.48	8.08	0.43	**13.01**	**0.51**	Detrital		
266	23_A02_16	1.46	19.02	0.24	**24.00**	**0.51**	Mixed		
267	23_A02_17	1.45	4.05	0.32	**8.96**	**0.51**	Detrital		
268	UWQ-1	1.46	7.17	0.41					
269	UWQ-1	1.45	7.08	0.29					
270	UWQ-1	1.44	7.66	0.37					
271	UWQ-1	1.44	7.53	0.43					
Bracket (247-250, 268-271)		**average**	**7.40**			**2 SD = 0.51**			
272	23_A03_01	1.47	16.06	0.32	**20.94**	**0.47**	Mixed		
273	23_A03_02	1.47	18.69	0.29	**23.58**	**0.47**	Cement	24.7	57.9
274	23_A03_03	1.46	20.41	0.38	**25.31**	**0.47**	Cement	6.7	15.8
275	23_A03_04	1.48	14.79	0.45	**19.66**	**0.47**	Mixed		
276	23_A03_05	1.47	8.91	0.32	**13.75**	**0.47**	Detrital		
277	23_A04_01	1.49	16.31	0.35	**21.19**	**0.47**	Cement	11.4	42.9
278	23_A04_02	1.59	16.70	0.34	**21.58**	**0.47**	High Yield		
279	23_A04_03	1.57	13.80	0.28	**18.67**	**0.47**	Mixed		
280	23_A04_04	1.49	11.54	0.44	**16.40**	**0.47**	Mixed		

Analyses #	Sample	^{16}O cps x10^9	$\delta^{18}O$ RAW	2 SE	$\delta^{18}O$ VSMOW	2 SD	Comments	µm from DQ	% from DQ
281	23_A04_05	1.50	15.34	0.26	**20.22**	**0.47**	Cement	8.6	56.3
282	23_A04_06	1.50	15.15	0.34	**20.03**	**0.47**	Cement	9.5	55.6
283	23_A04_07	1.50	8.81	0.33	**13.65**	**0.47**	Detrital		
284	23_A06_01	1.48	17.74	0.35	**22.63**	**0.47**	Grain boundary		
285	23_A06_02	1.54	18.33	0.23	**23.22**	**0.47**	Overlaps 1		
286	23_A06_03	1.52	17.76	0.22	**22.65**	**0.47**	Overlaps 2		
287	UWQ-1	1.46	7.64	0.41					
288	UWQ-1	1.47	7.53	0.32					
289	UWQ-1	1.46	7.43	0.27					
290	UWQ-1	1.44	7.84	0.41		Cs reservoir 163-165			
291	UWQ-1	1.43	7.52	0.32					
Bracket (268-271, 287-291)		**average**	**7.49**			**2 SD = 0.47**			
292	23_A06_04	1.46	20.69	0.31	**25.55**	**0.39**	Overlaps 2		
293	23_A06_05	1.45	17.80	0.33	**22.65**	**0.39**	Cement	24.2	52.3
294	23_A06_06	1.45	11.88	0.36	**16.70**	**0.39**	Mixed		
295	23_A06_07	1.47	22.44	0.34	**27.30**	**0.39**	Overlaps 4		
296	23_A06_08	1.46	22.78	0.35	**27.65**	**0.39**	Cement	14.7	31.8
297	23_A06_09	1.43	7.61	0.42	**12.41**	**0.39**	Detrital		
298	23_A06_10	1.44	21.03	0.38	**25.89**	**0.39**	Cement	10.5	27.8
299	23_A06_11	1.43	15.06	0.45	**19.89**	**0.39**	Cement	37.9	72.0
300	23_A06_12	1.43	17.42	0.31	**22.26**	**0.39**	Cement	18.9	33.3
301	23_A06_13	1.45	16.36	0.28	**21.20**	**0.39**	Mixed		
302	23_A06_14	1.41	18.57	0.40	**23.42**	**0.39**	Cement	10.5	19.2
303	23_A06_15	1.44	13.54	0.39	**18.37**	**0.39**	Mixed		
304	23_A06_16	1.44	4.50	0.39	**9.29**	**0.39**	Detrital		
305	UWQ-1	1.44	7.62	0.38					
306	UWQ-1	1.43	7.11	0.41					
307	UWQ-1	1.44	7.55	0.28					
308	UWQ-1	1.43	7.55	0.37					
Bracket (287-291,305-308)		**average**	**7.53**			**2 SD = 0.39**			

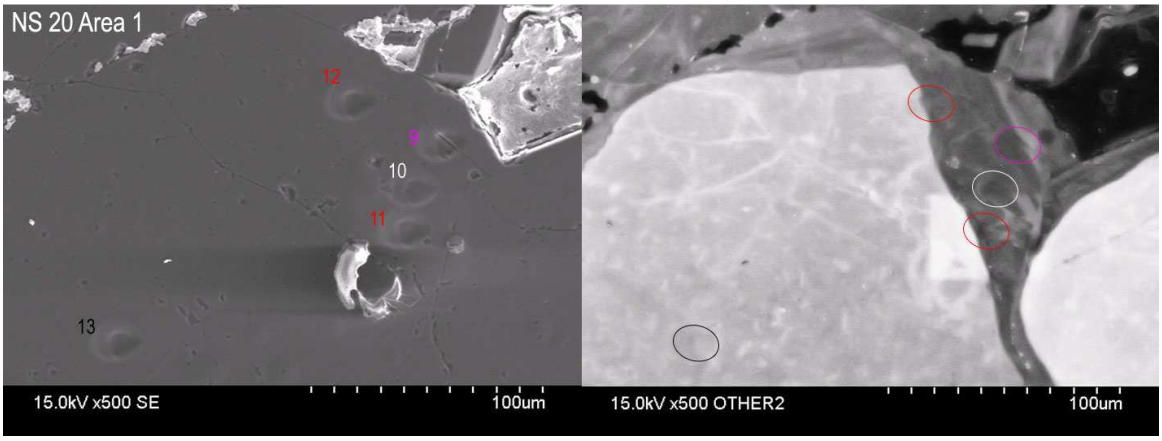
NS 20 Area 1
12
9
10
11
13
15.0kV x500 SE
100um
15.0kV x500 OTHER2
100um

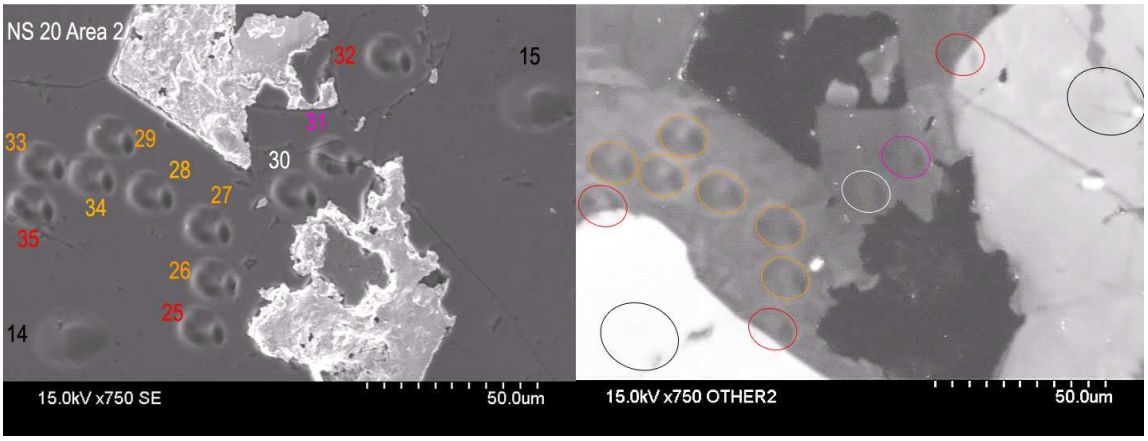
NS 20 Area 2
32
15
31
33
29
28
30
27
34
35
26
25
14
15.0kV x750 SE
50.0um
15.0kV x750 OTHER2
50.0um

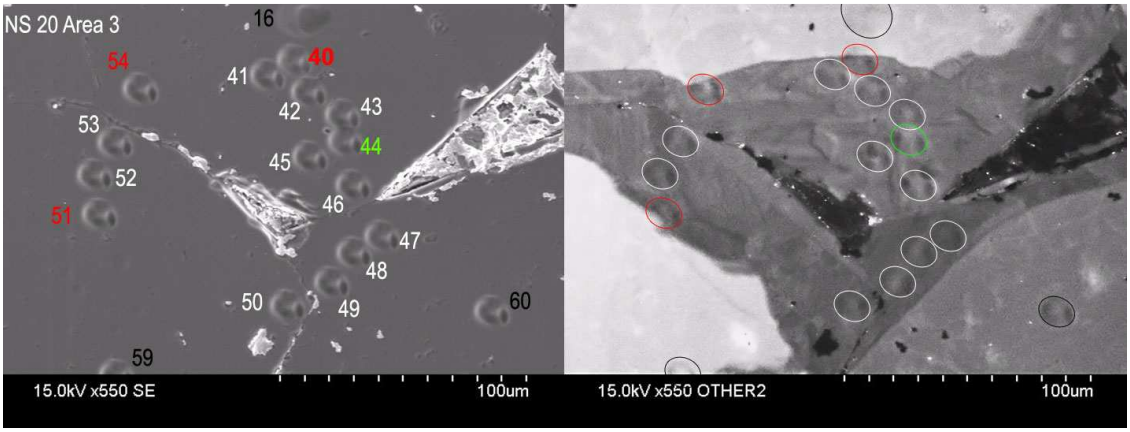
NS 20 Area 3
16
54
40
41
42
43
53
44
45
52
46
51
47
48
50
49
60
59
15.0kV x550 SE
100um
15.0kV x550 OTHER2
100um

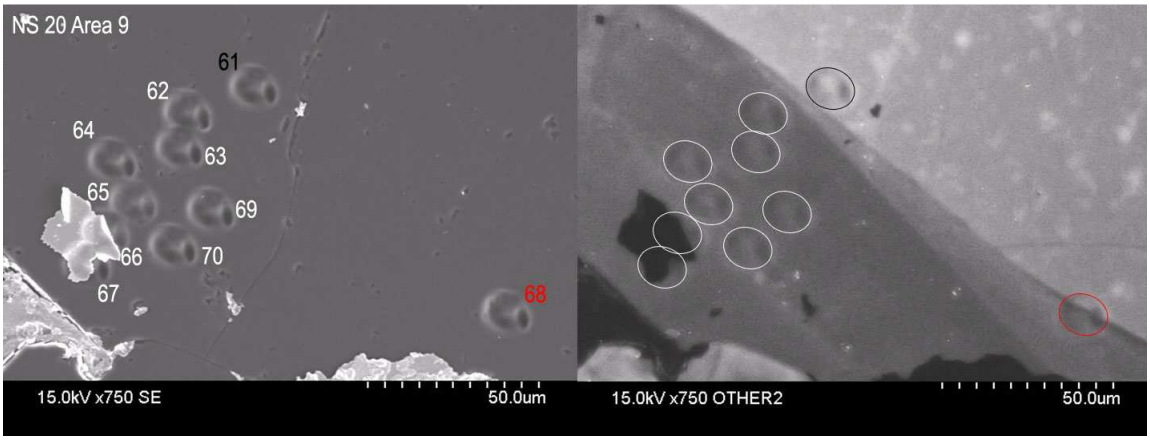
NS 20 Area 9
61
62
64
63
65
69
66
70
67
68
15.0kV x750 SE
50.0um
15.0kV x750 OTHER2
50.0um

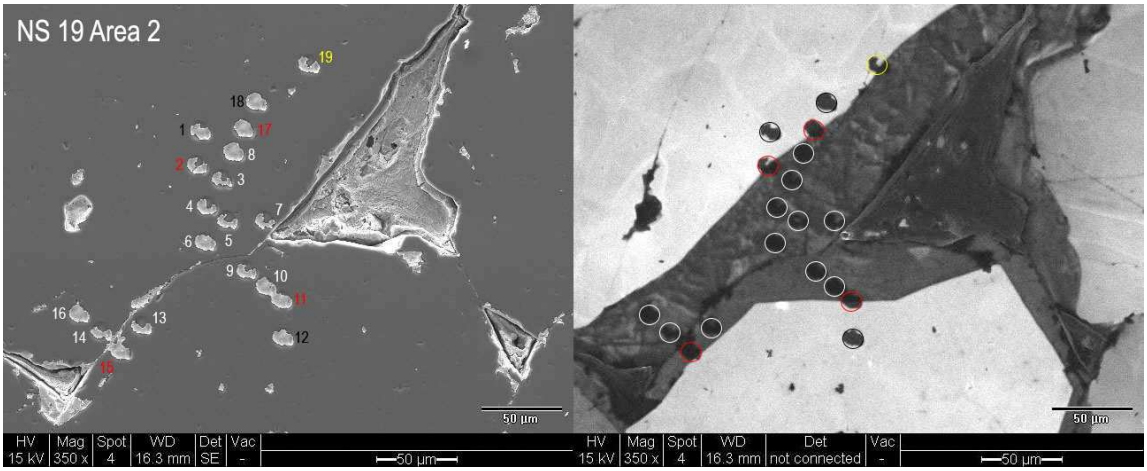
NS 19 Area 2
19
18
1
17
8
2
3
4
7
6
5
9
10
11
16
13
14
12
15
50 µm
HV 15 kV | Mag 350 x | Spot 4 | WD 16.3 mm | Det SE | Vac -
50 µm
HV 15 kV | Mag 350 x | Spot 4 | WD 16.3 mm | Det not connected | Vac -
50 µm

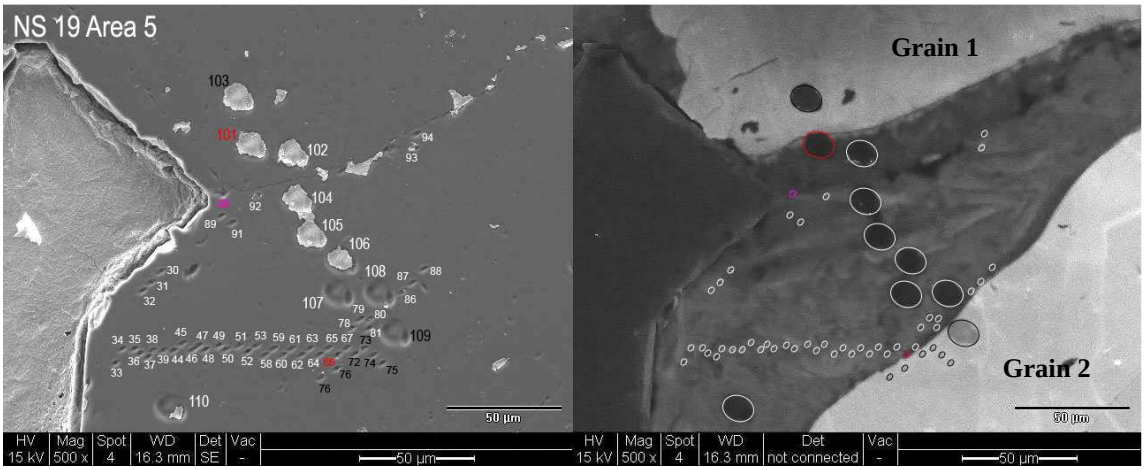
NS 19 Area 5
103
101
102
94
93
104
92
89
91
105
106
108
87
88
30
31
32
107
79
80
86
78
81
109
34 35 38 45 47 49 51 53 59 61 63 65 67 73
36 37 39 44 46 48 50 52 58 60 62 64 72 74 75
33
76
110
50 µm
HV 15 kV | Mag 500 x | Spot 4 | WD 16.3 mm | Det SE | Vac -
50 µm
Grain 1
Grain 2
50 µm
HV 15 kV | Mag 500 x | Spot 4 | WD 16.3 mm | Det not connected | Vac -
50 µm

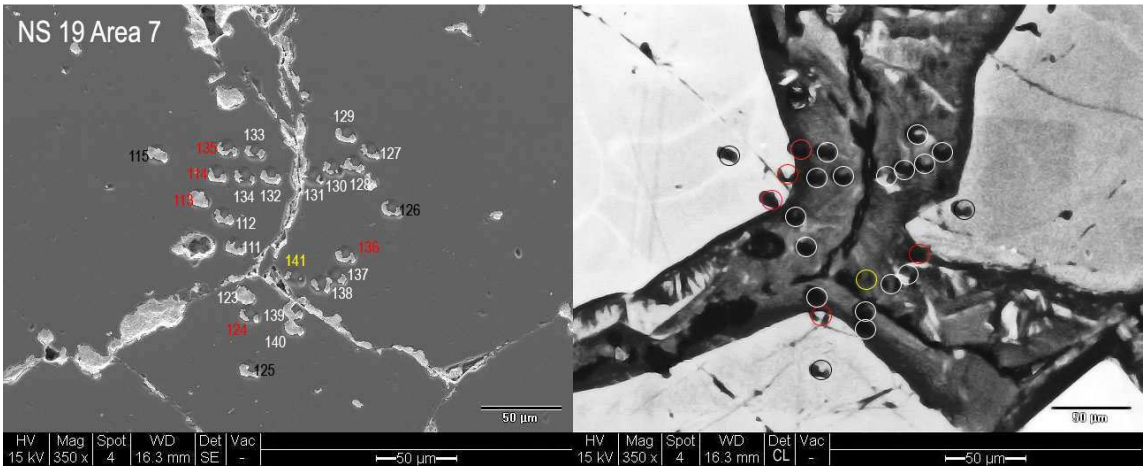
NS 19 Area 7
129
133
135
115
127
118
131
130
128
134
132
126
119
112
111
136
141
137
123
138
139
124
140
125
50 µm
HV
15 kV
Mag
350 x
Spot
4
WD
16.3 mm
Det
SE
Vac
-
50 µm
HV
15 kV
Mag
350 x
Spot
4
WD
16.3 mm
Det
CL
Vac
-
50 µm

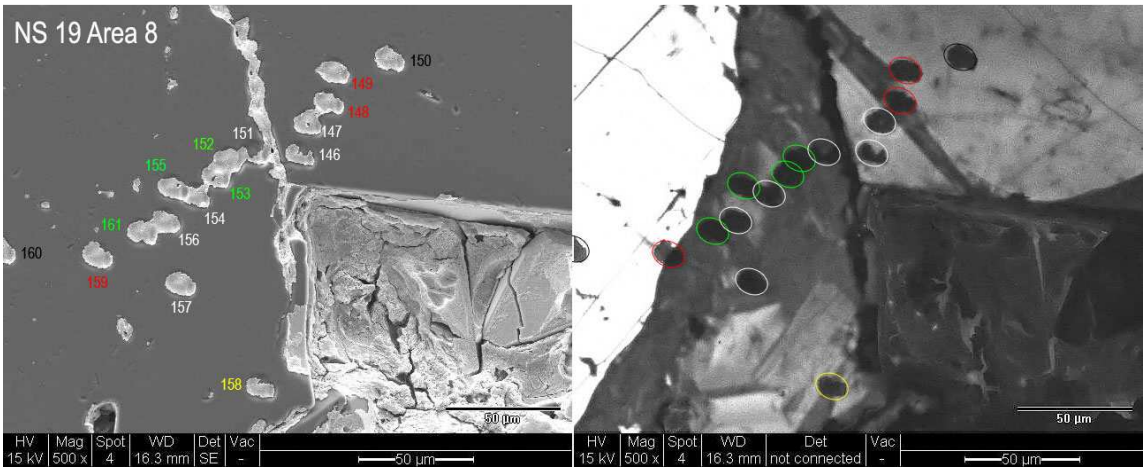
NS 19 Area 8
150
149
148
151
147
152
146
155
153
154
161
156
160
159
157
158
50 µm
HV
15 kV
Mag
500 x
Spot
4
WD
16.3 mm
Det
SE
Vac
-
50 µm
HV
15 kV
Mag
500 x
Spot
4
WD
16.3 mm
Det
not connected
Vac
-
50 µm

Well 211/27-A2 NS 20 and NS19 (133°C). Initially a 20 µm and 12 µm beam with a 2.3nA intensity, May 7, 2008.

Analyses #	Sample	^{16}O cps x10^9	$\delta^{18}O$ RAW	2 SE	$\delta^{18}O$ VSMOW	2 SD	Comments	µm from DQ	% from DQ
					***20 µm**				
5	UWQ-1	2.95	6.93	0.22					
6	UWQ-1	2.84	6.90	0.35					
7	UWQ-1	2.95	7.03	0.13					
8	UWQ-1	2.88	6.91	0.14					
9	20_A01_01	2.88	13.90	0.19	**19.24**	**0.40**	Cement*	38.1	68.6
10	20_A01_02	2.86	17.13	0.18	**22.49**	**0.40**	Cement*	15.9	27.8
11	20_A01_03	2.90	18.23	0.21	**23.59**	**0.40**	Mixed*		
12	20_A01_04	2.90	16.14	0.17	**21.49**	**0.40**	Mixed*		
13	20_A01_05	2.87	3.34	0.16	**8.62**	**0.40**	Detrital*		
14	20_A02_01	2.86	5.14	0.22	**10.43**	**0.40**	Detrital*		
15	20_A02_02	2.89	6.02	0.16	**11.32**	**0.40**	Detrital*		
16	20_A03_01a	2.87	3.76	0.17	**9.05**	**0.40**	Detrital*		
17	UWQ-1	2.78	7.07	0.25		0.32			
18	UWQ-1	2.72	7.48	0.24					
19	UWQ-1	2.75	7.06	0.28					
20	UWQ-1	2.87	6.85	0.17					
Bracket (5-8, 17-20)		**average**	**7.03**			**2 SD = 0.40**			
					12 µm				
21	UWQ-1	1.49	6.73	0.33					
22	UWQ-1	1.47	7.06	0.37					
23	UWQ-1	1.48	6.92	0.40					
24	UWQ-1	1.51	6.78	0.33					
25	20_A02_03	1.50	16.88	0.40	**22.25**	**0.45**	Mixed		
26	20_A02_04	1.54	14.08	0.25	**19.45**	**0.45**	Cement	16.1	37.5
27	20_A02_05	1.51	14.57	0.23	**19.94**	**0.45**	Cement	28.0	59.1
28	20_A02_06	1.48	14.69	0.32	**20.05**	**0.45**	Cement	18.3	42.5

Analyses #	Sample	^{16}O cps x10^9	$\delta^{18}O$ RAW	2 SE	$\delta^{18}O$ VSMOW	2 SD	Comments	µm from DQ	% from DQ
29	20_A02_07	1.41	15.28	0.41	**20.65**	**0.45**	Cement	26.9	67.6
30	20_A02_08	1.42	15.31	0.43	**20.68**	**0.45**	Cement	32.3	88.2
31	20_A02_09	1.49	14.14	0.29	**19.50**	**0.45**	Cracked		
32	20_A02_10	1.49	14.67	0.35	**20.04**	**0.45**	Mixed		
33	20_A02_11	1.49	14.82	0.38	**20.18**	**0.45**	Cement	12.9	32.4
34	20_A02_12	1.45	15.55	0.46	**20.92**	**0.45**	Cement	14.0	36.1
35	20_A02_13	1.49	15.62	0.32	**20.99**	**0.45**	Mixed		
36	UWQ-1	1.48	7.16	0.35					
37	UWQ-1	1.47	6.94	0.28					
38	UWQ-1	1.47	7.44	0.33					
39	UWQ-1	1.45	7.00	0.35					
Bracket (21-24, 36-39)		**average**	**7.00**			**2 SD = 0.45**			
40	20_A03_01	1.43	16.92	0.45	**22.24**	**0.34**	Mixed		
41	20_A03_02	1.44	17.44	0.56	**22.75**	**0.34**	Cement	7.2	13.9
42	20_A03_03	1.52	16.32	0.29	**21.63**	**0.34**	Cement	15.9	24.4
43	20_A03_04	1.50	15.12	0.27	**20.43**	**0.34**	Cement	20.3	32.9
44	20_A03_05	1.54	15.25	0.25	**20.56**	**0.34**	Overlaps 4		
45	20_A03_06	1.51	15.28	0.37	**20.59**	**0.34**	Cement	40.6	70.0
46	20_A03_07	1.50	15.09	0.29	**20.40**	**0.34**	Cement	50.7	87.5
47	20_A03_08	1.50	17.27	0.38	**22.59**	**0.34**	Cement	8.7	35.3
48	20_A03_09	1.51	16.80	0.33	**22.11**	**0.34**	Cement	14.5	45.5
49	20_A03_10	1.49	16.47	0.39	**21.79**	**0.34**	Cement	11.6	38.1
50	20_A03_11	1.49	17.41	0.32	**22.73**	**0.34**	Cement	30.4	70.0
51	20_A03_12	1.48	15.88	0.31	**21.19**	**0.34**	Mixed		
52	20_A03_13	1.49	17.71	0.41	**23.02**	**0.34**	Cement	14.5	38.5
53	20_A03_14	1.50	17.18	0.35	**22.49**	**0.34**	Cement	29.0	76.9
54	20_A03_15	1.50	17.16	0.45	**22.48**	**0.34**	Mixed		
55	UWQ-1	1.50	7.05	0.36					
56	UWQ-1	1.51	7.07	0.33					
57	UWQ-1	1.51	6.89	0.32					

Analyses #	Sample	^{16}O cps x10^9	$\delta^{18}O$ RAW	2 SE	$\delta^{18}O$ VSMOW	2 SD	Comments	µm from DQ	% from DQ
58	UWQ-1	1.51	6.99	0.28					
Bracket (36-39, 55-58)		**average**	**7.07**			**2 SD = 0.34**			
59	20_A03_16	1.48	5.49	0.39	**10.82**	**0.28**	Detrital		
60	20_A03_17	1.50	5.94	0.48	**11.28**	**0.28**	Detrital		
61	20_A09_01	1.53	4.03	0.28	**9.36**	**0.28**	Detrital		
62	20_A09_02	1.52	17.09	0.30	**22.49**	**0.28**	Cement	15.1	18.7
63	20_A09_03	1.55	16.76	0.29	**22.15**	**0.28**	Cement	23.7	29.3
64	20_A09_04	1.52	16.45	0.36	**21.85**	**0.28**	Cement	37.6	46.7
65	20_A09_05	1.55	16.15	0.33	**21.55**	**0.28**	Cement	43.0	53.3
66	20_A09_06	1.54	15.18	0.34	**20.56**	**0.28**	Cement	58.1	72.0
67	20_A09_07	1.55	14.97	0.20	**20.36**	**0.28**	Cement	67.7	84.0
68	20_A09_08	1.54	16.36	0.34	**21.75**	**0.28**	Mixed		
69	20_A09_09	1.55	16.49	0.43	**21.88**	**0.28**	Cement	23.7	29.3
70	20_A09_10	1.54	15.53	0.34	**20.92**	**0.28**	Cement	47.3	58.7
71	UWQ-1	1.53	7.02	0.42					
72	UWQ-1	1.53	6.76	0.37					
73	UWQ-1	1.53	6.90	0.26					
74	UWQ-1	1.54	7.22	0.35					
Bracket (55-58,71-74)		**average**	**6.99**			**2 SD = 0.28**			
Sample change: NS20 out NS19 in									
75	UWQ-1	1.53	7.04	0.34					
76	UWQ-1	1.53	7.00	0.28					
77	UWQ-1	1.55	6.64	0.32					
78	UWQ-1	1.55	6.55	0.28					
79	19_A02_01	1.55	4.54	0.28	**10.17**	**0.44**	Detrital		
80	19_A02_02	1.55	11.83	0.29	**17.50**	**0.44**	Mixed		
81	19_A02_03	1.54	17.58	0.33	**23.28**	**0.44**	Cement	15.1	23.3
82	19_A02_04	1.55	17.44	0.29	**23.14**	**0.44**	Cement	19.4	32.1
83	19_A02_05	1.55	16.36	0.44	**22.06**	**0.44**	Cement	35.5	58.9

Analyses #	Sample	^{16}O cps x10^9	$\delta^{18}O$ RAW	2 SE	$\delta^{18}O$ VSMOW	2 SD	Comments	µm from DQ	% from DQ
84	19_A02_06	1.52	16.47	0.24	**22.16**	**0.44**	Cement	34.4	61.5
85	19_A02_07	1.51	16.15	0.38	**21.84**	**0.44**	Cement	53.8	83.3
86	19_A02_08	1.51	20.55	0.39	**26.27**	**0.44**	Cement	5.4	8.6
87	19_A02_09	1.54	16.46	1.12	**22.15**	**0.44**	Cement	21.5	71.4
88	19_A02_10	1.55	17.24	0.34	**22.94**	**0.44**	Cement	5.4	15.6
89	19_A02_11	1.60	11.33	0.31	**17.00**	**0.44**	Mixed		
90	19_A02_12	1.55	4.09	0.41	**9.71**	**0.44**	Detrital		
91	19_A02_13	1.54	18.05	0.32	**23.75**	**0.44**	Cement	6.5	33.3
92	19_A02_14	1.53	16.33	0.27	**22.03**	**0.44**	Cement	34.4	76.2
93	19_A02_15	1.55	17.79	0.36	**23.49**	**0.44**	Mixed		
94	19_A02_16	1.54	16.28	0.29	**21.98**	**0.44**	Cement	16.1	35.7
95	UWQ-1	1.55	6.57	0.30					
96	UWQ-1	1.56	6.58	0.33					
97	UWQ-1	1.54	6.71	0.43					
98	UWQ-1	1.55	6.44	0.46					
Bracket (75-78, 95-98)		**average**	**6.69**			**2 SD = 0.44**			
99	19_A03_01	1.55	5.16	0.43	**10.92**	**0.32**	Miss fire		
100	19_A03_02	1.27	14.38	5.34	**20.19**	**0.32**	Miss fire		
101	19_A05_01	1.52	16.90	0.32	**22.73**	**0.32**	Mixed		
102	19_A05_02	1.53	15.86	0.26	**21.68**	**0.32**	Cement	12.9	57.1
103	19_A05_03	1.53	4.27	0.31	**10.02**	**0.32**	Detrital		
104	19_A05_04	1.56	15.01	0.32	**20.82**	**0.32**	Cement	62.4	85.3
105	19_A05_05	1.55	15.42	0.32	**21.24**	**0.32**	Cement	47.3	64.7
106	19_A05_06	1.55	15.97	0.30	**21.79**	**0.32**	Cement	28.0	38.2
107	19_A05_07	1.55	16.86	0.31	**22.68**	**0.32**	Cement	21.5	29.4
108	19_A05_08	1.55	17.38	0.29	**23.21**	**0.32**	Cement	8.6	11.8
109	19_A05_09	1.55	4.90	0.34	**10.66**	**0.32**	Detrital		
110	19_A05_10	1.54	16.37	0.41	**22.20**	**0.32**	Cement	28.0	41.9
111	19_A07_01	1.55	15.80	0.33	**21.62**	**0.32**	Cement	33.7	66.7
112	19_A07_02	1.52	16.52	0.29	**22.34**	**0.32**	Cement	9.6	21.1

Analyses #	Sample	^{16}O cps x10^9	$\delta^{18}O$ RAW	2 SE	$\delta^{18}O$ VSMOW	2 SD	Comments	µm from DQ	% from DQ
113	19_A07_03	1.54	6.66	0.26	**12.42**	**0.32**	Mixed		
114	19_A07_04	1.55	9.20	0.24	**14.98**	**0.32**	Mixed		
115	19_A07_05	1.55	6.16	0.44	**11.92**	**0.32**	Detrital		
116	UWQ-1	1.56	6.32	0.37					
117	UWQ-1	1.55	6.47	0.32					
118	UWQ-1	1.57	6.61	0.22					
119	UWQ-1	1.55	6.82	0.25					
Bracket (95-98, 116-119)		**average**	**6.56**			**2 SD = 0.32**			
120	19_A02_017	1.55	10.78	0.38	**16.45**	**0.39**	Mixed		
121	19_A02_018	1.55	4.85	0.34	**10.61**	**0.39**	Detrital		
122	19_A02_019	1.52	11.04	0.42	**16.83**	**0.39**	Low Yield		
123	19_A07_06	1.56	16.52	0.37	**22.23**	**0.39**	Cement	7.2	37.5
124	19_A07_07	1.58	11.26	0.37	**16.93**	**0.39**	Mixed		
125	19_A07_08	1.55	6.87	0.32	**12.52**	**0.39**	Detrital		
126	19_A07_09	1.55	4.59	0.32	**10.23**	**0.39**	Detrital		
127	19_A07_10	1.55	17.29	0.38	**23.00**	**0.39**	Cement	16.9	29.2
128	19_A07_11	1.57	16.60	0.29	**22.31**	**0.39**	Cement	21.7	40.9
129	19_A07_12	1.56	16.64	0.33	**22.34**	**0.39**	Cement	33.7	53.8
130	19_A07_13	1.57	15.60	0.29	**21.29**	**0.39**	Cement	33.7	63.6
131	19_A07_14	1.57	15.86	0.36	**21.56**	**0.39**	Cement	45.8	86.4
132	19_A07_15	1.56	15.63	0.27	**21.32**	**0.39**	Cement	28.9	63.2
133	19_A07_16	1.55	16.29	0.30	**21.99**	**0.39**	Cement	19.3	42.1
134	19_A07_17	1.57	17.49	0.33	**23.19**	**0.39**	Cement	12.0	26.3
135	19_A07_18	1.57	16.93	0.32	**22.64**	**0.39**	Mixed		
136	19_A07_19	1.58	16.17	0.36	**21.87**	**0.39**	Mixed		
137	19_A07_20	1.58	15.01	0.23	**20.70**	**0.39**	Cement	21.7	50.0
138	19_A07_21	1.59	14.37	0.19	**20.06**	**0.39**	Cement	33.7	77.8
139	19_A07_22	1.52	15.11	0.40	**20.80**	**0.39**	Cement	14.5	66.7
140	19_A07_23	1.63	17.68	0.27	**23.39**	**0.39**	Cement	6.0	26.3
141	19_A07_24	1.51	15.03	0.48	**20.72**	**0.39**	Low Yield		

Analyses #	Sample	^{16}O cps x10^9	$\delta^{18}O$ RAW	2 SE	$\delta^{18}O$ VSMOW	2 SD	Comments	µm from DQ	% from DQ
142	UWQ-1	1.60	6.82	0.39					
143	UWQ-1	1.59	6.78	0.28					
144	UWQ-1	1.62	6.79	0.35					
145	UWQ-1	1.59	6.85	0.30					
Bracket (116-119, 142-145)		**average**	**6.68**			**2 SD = 0.39**			
146	19_A08_01	1.57	14.95	0.39	**20.71**	**0.44**	Cement	28.3	68.2
147	19_A08_02	1.58	15.46	0.25	**21.22**	**0.44**	Cement	18.9	45.5
148	19_A08_03	1.59	17.46	0.42	**23.23**	**0.44**	Mixed		
149	19_A08_04	1.59	7.36	0.39	**13.08**	**0.44**	Mixed		
150	19_A08_05	1.58	5.10	0.29	**10.80**	**0.44**	Detrital		
151	19_A08_06	1.59	13.66	0.31	**19.41**	**0.44**	Cement	44.3	87.0
152	19_A08_07	1.56	15.24	0.31	**21.00**	**0.44**	Overlaps 6		
153	19_A08_08	1.60	15.38	0.36	**21.14**	**0.44**	Overlaps 7		
154	19_A08_09	1.59	15.72	0.28	**21.49**	**0.44**	Cement	28.3	45.5
155	19_A08_10	1.60	14.83	0.23	**20.59**	**0.44**	Overlaps 9		
156	19_A08_11	1.58	15.36	0.40	**21.12**	**0.44**	Cement	18.9	27.0
157	19_A08_12	1.59	14.98	0.17	**20.74**	**0.44**	Cement	39.6	44.7
158	19_A08_13	1.53	14.05	0.27	**19.80**	**0.44**	Low Yield		
159	19_A08_14	1.58	11.93	0.34	**17.68**	**0.44**	Mixed		
160	19_A08_15	1.58	4.94	0.23	**10.65**	**0.44**	Detrital		
161	19_A08_16	1.60	15.81	0.27	**21.58**	**0.44**	Overlaps 11		
162	UWQ-1	1.58	6.34	0.27					
163	UWQ-1	1.58	6.37	0.40					
164	UWQ-1	1.59	6.60	0.42					
165	UWQ-1	1.58	6.41	0.39					
Bracket (142-145, 162-164)		**average**	**6.62**			**2 SD = 0.44**			

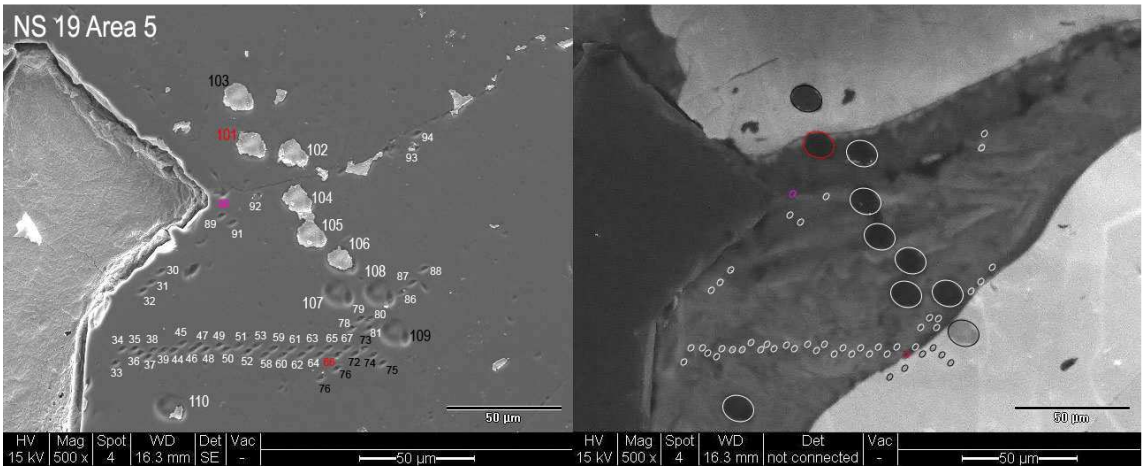
NS 19 Area 5
103
101
102
94
93
104
92
89
91
105
106
108
87
88
30
31
32
107
79
80
86
78
81
109
34 35 38 45 47 49 51 53 59 61 63 65 67 73
36 37 39 44 46 48 50 52 58 60 62 64 72 74 75
33
76
76
110
50 µm
HV 15 kV | Mag 500 x | Spot 4 | WD 16.3 mm | Det SE | Vac -
50 µm
50 µm
HV 15 kV | Mag 500 x | Spot 4 | WD 16.3 mm | Det not connected | Vac -
50 µm

Well 211/27-A2 NS 19 (133°C) 2 µm beam, 2.3nA intensity. June 3, 2009

Analyses #	Sample	^{16}O cps x10^9	$\delta^{18}O$ RAW	2 SE	$\delta^{18}O$ VSMOW	2 SD	Comments	µm from DQ	% from DQ
26	UWQ-1	34.39	-0.74	0.57					
27	UWQ-1	32.14	0.02	0.55					
28	UWQ-1	32.08	-0.27	0.51					
29	UWQ-1	31.67	-0.01	0.48					
30	NS19 .2_ A5_1	31.15	8.69	0.63	**21.17**	**0.83**	Cement	91.7	90.2
31	NS19 .2_ A5_2	30.84	9.08	0.51	**21.56**	**0.83**	Cement	91.7	91.7
32	NS19 .2_ A5_3	30.46	9.52	0.47	**22.01**	**0.83**	Cement	88.3	88.3
33	NS19 .2_ A5_4	29.69	9.43	0.62	**21.92**	**0.83**	Cement	80.0	87.3
34	NS19 .2_ A5_5	30.21	9.77	0.59	**22.26**	**0.83**	Cement	91.7	84.0
35	NS19 .2_ A5_6	30.19	9.17	0.54	**21.66**	**0.83**	Cement	86.7	79.4
36	NS19 .2_ A5_7	29.69	9.41	0.76	**21.90**	**0.83**	Cement	80.8	74.0
37	NS19 .2_ A5_8	30.04	9.64	0.69	**22.13**	**0.83**	Cement	73.3	71.0
38	NS19 .2_ A5_9	29.33	8.86	0.67	**21.34**	**0.83**	Cement	76.7	70.2
39	NS19 .2_ A5_10	30.46	8.99	0.70	**21.47**	**0.83**	Cement	71.7	65.6
40	UWQ-1	31.71	0.26	0.73					
41	UWQ-1	31.66	-0.41	0.62					
42	UWQ-1	31.66	0.43	0.55			EM HV 3068		
43	UWQ-1	31.62	0.41	0.46					
Bracket (26-29, 40-43)		**average**	**-0.04**			**2 SD = 0.83**			
44	NS19 .2_A5_11	31.82	9.27	0.67	**21.42**	**0.65**	Cement	61.7	56.5
45	NS19 .2_A5_12	31.64	9.59	0.65	**21.74**	**0.65**	Cement	66.7	57.1
46	NS19 .2_A5_13	31.39	10.20	0.56	**22.37**	**0.65**	Cement	58.3	53.4
47	NS19 .2_A5_14	31.59	10.23	0.45	**22.39**	**0.65**	Cement	58.3	51.5
48	NS19 .2_A5_15	31.22	9.65	0.45	**21.81**	**0.65**	Cement	53.3	48.9
49	NS19 .2_A5_16	31.01	9.26	0.60	**21.41**	**0.65**	Cement	50.0	44.1
50	NS19 .2_A5_17	30.98	10.12	0.45	**22.28**	**0.65**	Cement	43.3	39.7
51	NS19 .2_A5_18	30.88	9.53	0.62	**21.68**	**0.65**	Cement	40.0	35.3
52	NS19 .2_A5_19	30.95	9.86	0.54	**22.02**	**0.65**	Cement	35.0	32.1

Analyses #	Sample	^{16}O cps x10^9	$\delta^{18}O$ RAW	2 SE	$\delta^{18}O$ VSMOW	2 SD	Comments	µm from DQ	% from DQ
53	NS19 .2_A5_20	31.31	10.23	0.55	**22.39**	**0.65**	Cement	33.3	29.4
54	UWQ-1	30.24	0.31	0.62					
55	UWQ-1	30.21	0.70	0.51					
56	UWQ-1	29.72	0.15	0.48			EM HV 3071		
57	UWQ-1	29.81	0.44	0.51					
Bracket (40-43, 54-57)		**average**	**0.29**		**2 SD = 0.65**				
58	NS19 .2_A5_21	29.59	10.95	0.57	**23.11**	**0.38**	Cement	26.7	24.4
59	NS19 .2_A5_22	29.98	10.57	0.82	**22.73**	**0.38**	Cement	26.7	23.9
60	NS19 .2_A5_23	29.57	11.30	0.41	**23.46**	**0.38**	Cement	23.3	21.4
61	NS19 .2_A5_24	29.85	10.59	0.65	**22.74**	**0.38**	Cement	18.3	16.4
62	NS19 .2_A5_25	29.02	10.95	0.47	**23.11**	**0.38**	Cement	15.0	13.7
63	NS19 .2_A5_26	29.28	10.77	0.58	**22.93**	**0.38**	Cement	13.3	11.9
64	NS19 .2_A5_27	28.80	11.01	0.64	**23.16**	**0.38**	Cement	8.3	7.6
65	NS19 .2_A5_28	28.94	10.62	0.44	**22.77**	**0.38**	Cement	8.3	7.5
66	NS19 .2_A5_29	28.04	12.22	0.76	**24.39**	**0.38**	Mixed		
67	NS19 .2_A5_30	28.70	14.73	0.58	**26.94**	**0.38**	Cement	1.7	1.5
68	UWQ-1	30.21	0.13	0.65					
69	UWQ-1	30.59	0.15	0.80					
70	UWQ-1	30.50	0.30	0.44			EM HV 3075		
71	UWQ-1	30.51	0.24	0.63					
Bracket (54-57, 68-71)		**average**	**0.30**		**2 SD = 0.38**				
72	NS19 .2_A5_31	30.23	-0.42	0.65	**11.58**	**0.55**	Detrital		
73	NS19 .2_A5_32	30.53	-0.78	0.69	**11.22**	**0.55**	Detrital		
74	NS19 .2_A5_33	30.20	-1.22	0.68	**10.77**	**0.55**	Detrital		
75	NS19 .2_A5_34	30.21	-0.95	0.53	**11.05**	**0.55**	Detrital		
76	NS19 .2_A5_35	29.00	-1.24	0.66	**10.75**	**0.55**	Detrital		
77	NS19 .2_A5_36	29.33	-1.01	0.72	**10.99**	**0.55**	Detrital		
78	NS19 .2_A5_37	29.64	10.68	0.52	**22.82**	**0.55**	Cement	8.3	9.6
79	NS19 .2_A5_38	29.68	10.70	0.71	**22.84**	**0.55**	Cement	8.3	10.4
80	NS19 .2_A5_39	29.65	12.39	0.51	**24.54**	**0.55**	Cement	5.0	6.3

Analyses #	Sample	^{16}O cps x10^9	$\delta^{18}O$ RAW	2 SE	$\delta^{18}O$ VSMOW	2 SD	Comments	µm from DQ	% from DQ
81	NS19 .2_A5_40	28.07	15.50	0.72	**27.70**	**0.55**	Cement	2.5	3.1
82	UWQ-1	30.12	0.71	0.48					
83	UWQ-1	29.94	-0.06	0.62					
84	UWQ-1	29.52	0.71	0.58			EM HV unchanged		
85	UWQ-1	29.26	0.36	0.61					
Bracket (68-71, 82-85)		**average**	**0.32**		**2 SD = 0.55**				
86	NS19 .2_A5_41	29.12	15.24	0.55	**27.57**	**0.96**	Cement	2.5	3.8
87	NS19 .2_A5_42	29.16	14.67	0.50	**27.00**	**0.96**	Cement	1.7	2.9
88	NS19 .2_A5_43	29.44	12.94	0.61	**25.25**	**0.96**	Cement	3.3	5.9
89	NS19 .2_A5_44	28.35	8.63	0.64	**20.88**	**0.96**	Cement	81.7	90.7
90	NS19 .2_A5_45	26.54	6.76	0.69	**18.98**	**0.96**	Cracked		
91	NS19 .2_A5_46	28.04	9.21	0.58	**21.47**	**0.96**	Cement	75.0	83.3
92	NS19 .2_A5_47	28.44	9.06	0.59	**21.32**	**0.96**	Cement	76.7	92.0
93	NS19 .2_A5_48	28.51	10.26	0.54	**22.53**	**0.96**	Cement	41.7	83.3
94	NS19 .2_A5_49	28.54	10.08	0.62	**22.35**	**0.96**	Cement	43.3	96.3
95	UWQ-1	30.17	0.15	0.53			Cs res=129		
96	UWQ-1	30.12	0.33	0.55					
97	UWQ-1	30.22	-0.78	0.48			EM HV 3075-3078		
98	UWQ-1	30.41	0.03	0.75					
Bracket (82-85, 95-98)		**average**	**0.18**		**2 SD = 0.96**				

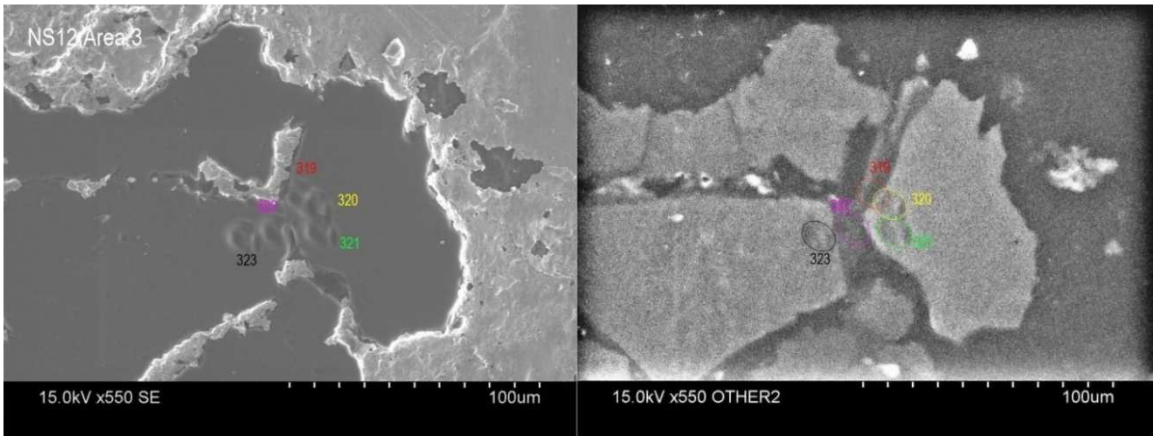
NS12 Area 3
319
320
321
323
15.0kV x550 SE
100um
15.0kV x550 OTHER2
100um

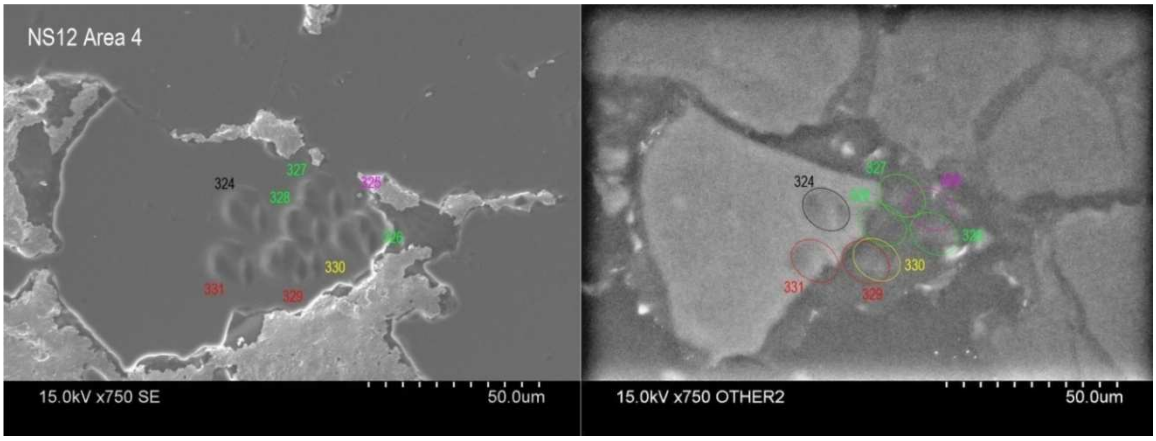
NS12 Area 4
324
327
328
330
331
329
15.0kV x750 SE
50.0um
15.0kV x750 OTHER2
50.0um

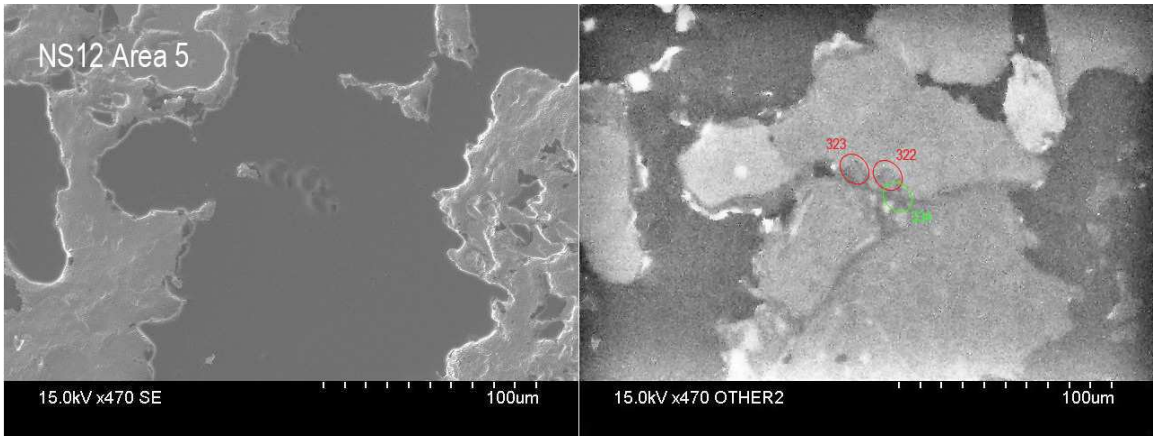
NS12 Area 5
323
322
15.0kV x470 SE
100um
15.0kV x470 OTHER2
100um

Well 34/8-7 NS 12 (165°C) 12 µm beam, 2.3nA intensity. May 8 , 2008.

Analyses #	Sample	^{16}O cps x10^9	$\delta^{18}O$ RAW	2 SE	$\delta^{18}O$ VSMOW	2 SD	Comments	µm from DQ	% from DQ
309	UWQ-1	1.52	8.01	0.30					
310	UWQ-1	1.52	7.97	0.37					
311	UWQ-1	1.55	7.43	0.28					
312	UWQ-1	1.57	7.58	0.22					
313	UWQ-1	1.55	7.29	0.27					
314	12_A015_01	1.68	17.58	0.29	**22.36**	**0.48**	?		
315	12_A015_02	1.76	12.57	0.30	**17.32**	**0.48**	?		
316	12_A015_03	1.80	11.96	0.39	**16.71**	**0.48**	?		
317	12_A015_04	1.84	10.01	0.24	**14.74**	**0.48**	?		
318	12_A015_05	1.88	8.32	0.44	**13.05**	**0.48**	?		
319	12_A03_01	1.72	14.67	0.21	**19.43**	**0.48**	Mixed		
320	12_A03_02	1.86	3.24	0.33	**7.95**	**0.48**	High Yield		
321	12_A03_03	1,76	2.35	0.28	**7.06**	**0.48**	Detrital		
322	12_A03_04	1.70	16.82	0.33	**21.59**	**0.48**	Mixed		
323	12_A03_05	1.67	4.63	0.28	**9.34**	**0.48**	Detrital		
324	12_A04_01	1.61	5.24	0.26	**9.95**	**0.48**	Detrital		
325	12_A04_02	1.55	14.59	0.33	**19.35**	**0.48**	Cracked		
326	12_A04_03	1.64	15.12	0.37	**19.88**	**0.48**	Overlaps 2		
327	12_A04_04	1.57	17.01	0.33	**21.78**	**0.48**	Mixed		
328	12_A04_05	1.64	15.66	0.41	**20.42**	**0.48**	Mixed		
329	12_A04_06	1.63	17.25	0.42	**22.02**	**0.48**	Mixed		
330	12_A04_07	1.76	15.39	0.28	**20.15**	**0.48**	High Yield		
331	12_A04_08	1.62	7.92	0.37	**12.65**	**0.48**	Mixed		
332	12_A05_01	1.57	6.82	0.29	**11.54**	**0.48**	Mixed		
333	12_A05_02	1.60	10.75	0.50	**15.49**	**0.48**	Mixed		
334	12_A05_03	1.66	13.41	0.32	**18.16**	**0.48**	Mixed		
335	UWQ-1	1.82	7.55						
336	UWQ-1	1.82	7.51						

Analyses #	Sample	^{16}O cps x10^{9}	$\delta^{18}O$ RAW	2 SE	$\delta^{18}O$ VSMOW	2 SD	Comments	µm from DQ	% from DQ
337	UWQ-1	1.80	7.50						
338	UWQ-1	1.79	7.58						
Bracket (309-313, 335-338)		**average**	**7.60**			**2 SD = 0.48**			

Appendix 4: Texas Wilcox SIMS Data

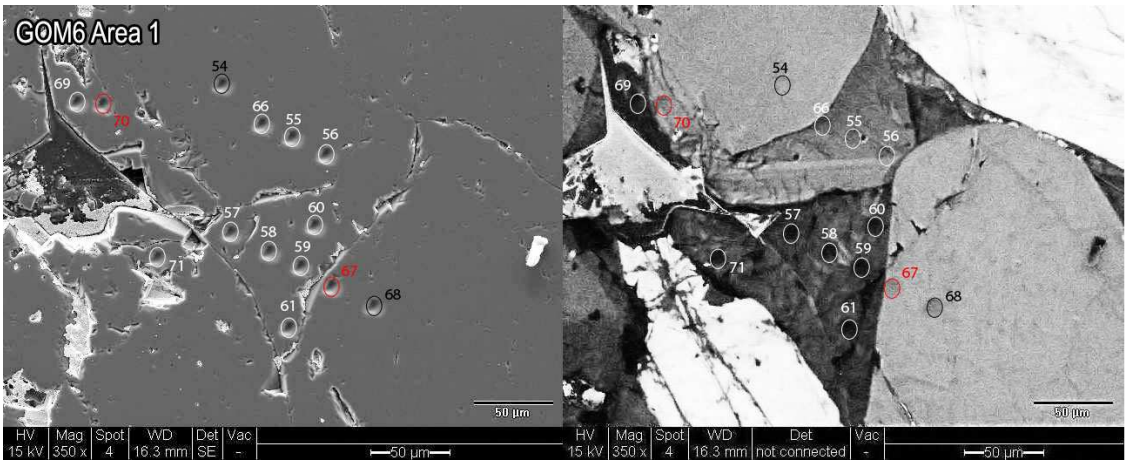

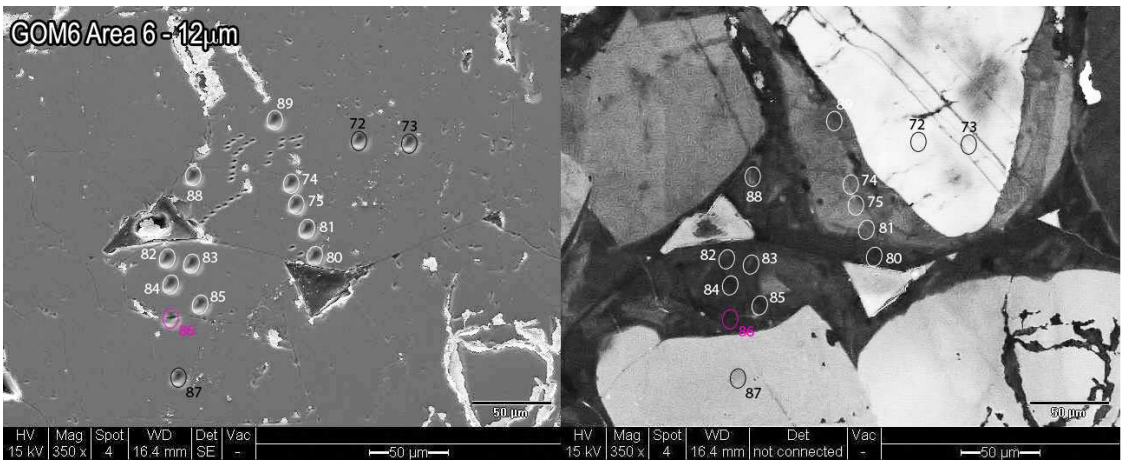

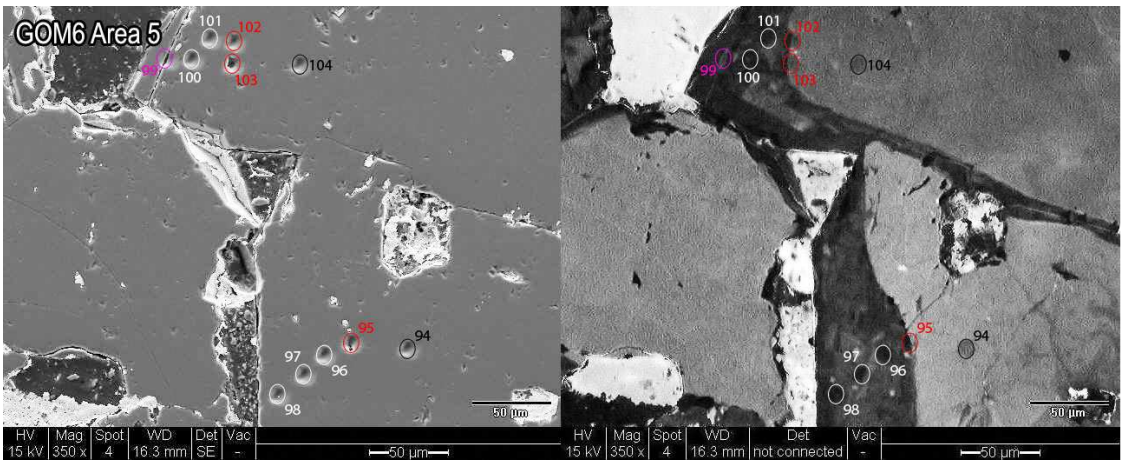

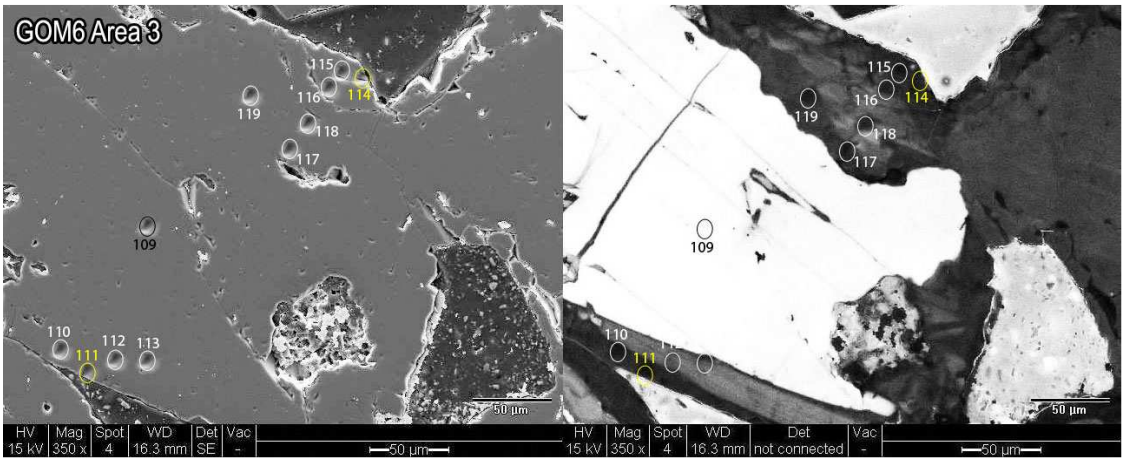
GOM6 Area 3
115
116
114
119
118
117
109
110
112
113
111
50 µm
HV
15 kV
Mag
350 x
Spot
4
WD
16.3 mm
Det
SE
Vac
-
50 µm
115
116
114
119
118
117
109
110
111
50 µm
HV
15 kV
Mag
350 x
Spot
4
WD
16.3 mm
Det
not connected
Vac
-
50 µm

GOM6 (104°C) 12 µm beam, 2.3nA intensity. June 2, 2009.

Analyses #	Sample	^{16}O cps x10^9	$\delta^{18}O$ RAW	2 SE	$\delta^{18}O$ VSMOW	2 SD	Comments	Zone	µm from DQ[a)]	% from DQ [a)]
50	UWQ-1	2.42	6.82	0.27						
51	UWQ-1	2.41	6.76	0.25						
52	UWQ-1	2.37	6.77	0.26						
53	UWQ-1	2.70	6.70	0.29			Cs res.82-89			
54	GOM6 A1_01	2.67	5.29	0.23	10.92	0.19	Detrital			
55	GOM6 A1_02	2.68	21.36	0.24	27.08	0.19	Cement	Grey	23.8	40.8
56	GOM6 A1_03	2.61	21.11	0.17	26.83	0.19	Cement	Grey	45.2	77.6
57	GOM6 A1_04	2.54	18.37	0.24	24.07	0.19	Cement		61.9	78.8
58	GOM6 A1_05	2.49	18.66	0.27	24.37	0.19	Cement		38.1	48.5
59	GOM6 A1_06	2.63	18.48	0.24	24.19	0.19	Cement		16.7	21.2
60	GOM6 A1_07	2.62	18.84	0.24	24.54	0.19	Cement		9.5	13.3
61	GOM6 A1_08	2.60	18.40	0.32	24.10	0.19	Cement		21.4	20.9
62	UWQ-1	2.57	6.62	0.22						
63	UWQ-1	2.50	6.58	0.23						
64	UWQ-1	2.69	6.74	0.18						
65	UWQ-1	2.67	6.56	0.26						
Bracket (50-53, 62-65)		**average**	**6.69**			**2 SD = 0.19**				
66	GOM6 A1_09	2.63	21.17	0.33	26.92	0.18	Cement	Grey	3.6	6.0
67	GOM6 A1_10	2.58	10.42	0.23	16.11	0.18	Mixed			
68	GOM6 A1_11	2.55	9.42	0.26	15.11	0.18	Detrital			
69	GOM6 A1_12	2.75	18.52	0.21	24.26	0.18	Cement		9.5 (5.8)	45.0 (41.7)
70	GOM6 A1_13	2.72	18.04	0.23	23.77	0.18	Mixed			
71	GOM6 A1_14	2.60	18.61	0.21	24.35	0.18	Cement		16.7	38.9
72	GOM6 A6_1	2.59	0.88	0.23	6.52	0.18	Detrital			
73	GOM6 A6_2	2.54	1.73	0.21	7.37	0.18	Detrital			

Analyses #	Sample	^{16}O cps x10^9	$\delta^{18}O$ RAW	2 SE	$\delta^{18}O$ VSMOW	2 SD	Comments	Zone	µm from DQ [a)]	% from DQ [a)]
74	GOM6 A6_3	2.49	21.36	0.24	27.11	0.18	Cement	Grey	16.7	20.0
75	GOM6 A6_4	2.46	21.36	0.16	27.11	0.18	Cement	Grey	23.8	30.0
76	UWQ-1	2.52	6.79	0.26						
77	UWQ-1	2.53	6.59	0.19						
78	UWQ-1	2.52	6.65	0.21						
79	UWQ-1	2.47	6.76	0.14						
Bracket (62-65, 76-79)		**average**	**6.69**			**2 SD = 0.18**				
80	GOM6 A6_5	2.60	17.80	0.20	23.58	0.31	Cement		42.9 (7.0)	85.7 (50)
81	GOM6 A6_6	2.66	21.19	0.20	26.99	0.31	Cement	Grey	31.0	59.1
82	GOM6 A6_7	2.59	17.70	0.23	23.48	0.31	Cement		47.6	80.0
83	GOM6 A6_8	2.60	18.33	0.24	24.12	0.31	Cement		42.9	73.5
84	GOM6 A6_9	2.54	17.94	0.29	23.72	0.31	Cement		31.0	52.0
85	GOM6 A6_10	2.50	18.61	0.20	24.40	0.31	Cement		16.7	28.6
86	GOM6 A6_11	2.58	16.49	0.27	22.26	0.31	Cracked			
87	GOM6 A6_12	2.38	6.25	0.26	11.97	0.31	Detrital			
88	GOM6 A6_13	2.47	18.33	0.27	24.12	0.31	Cement		69.0 (18.6)	74.4 (34)
89	GOM6 A6_14	2.50	21.74	0.27	27.54	0.31	Cement	Grey	7.1	7.7
90	UWQ-1	2.44	6.73	0.22						
91	UWQ-1	2.44	6.50	0.16						
92	UWQ-1	2.55	6.56	0.23						
93	UWQ-1	2.58	6.32	0.21						
Bracket (76-79, 90-93)		**average**	**6.61**			**2 SD = 0.31**				
94	GOM6 A5_1	2.53	5.72	0.27	11.57	0.34	Detrital			
95	GOM6 A5_2	2.57	13.37	0.27	19.27	0.34	Mixed			
96	GOM6 A5_3	2.48	18.34	0.31	24.26	0.34	Cement		19.0	30.8
97	GOM6 A5_4	2.45	18.25	0.32	24.17	0.34	Cement		33.3	53.8
98	GOM6 A5_5	2.40	18.35	0.31	24.27	0.34	Cement		50.0	80.8
99	GOM6 A5_6	2.53	17.76	0.20	23.68	0.34	Cracked			
100	GOM6 A5_7	2.59	18.21	0.24	24.14	0.34	Cement		25.0	45.7

Analyses #	Sample	^{16}O cps x10^9	$\delta^{18}O$ RAW	2 SE	$\delta^{18}O$ VSMOW	2 SD	Comments	Zone	µm from DQ [a)]	% from DQ [a)]
101	GOM6 A5_8	2.53	18.45	0.24	24.37	0.34	Cement		16.7	33.3
102	GOM6 A5_9	2.67	10.12	0.42	15.99	0.34	Mixed			
103	GOM6 A5_10	2.48	12.77	0.19	18.66	0.34	Mixed			
104	GOM6 A5_11	2.42	6.04	0.24	11.89	0.34	Detrital			
105	UWQ-1	2.41	6.54	0.22						
106	UWQ-1	2.55	6.57	0.27						
107	UWQ-1	2.59	6.18	0.18						
108	UWQ-1	2.56	6.42	0.30						
Bracket (90-93, 15-108)		**average**	**6.48**			**2 SD = 0.34**				
109	GOM6 A3_1	2.52	3.98	0.22	9.78	0.37	Detrital			
110	GOM6 A3_2	2.49	18.96	0.23	24.85	0.37	Cement		14.3 (11.6)	57.1 (23.1)
111	GOM6 A3_3	2.29	17.91	0.18	23.78	0.37	Low Yield			
112	GOM6 A3_4	2.44	19.25	0.25	25.14	0.37	Cement	Grey	9.5	36.4
113	GOM6 A3_5	2.52	21.49	0.25	27.39	0.37	Cement	Grey	2.4	9.1
114	GOM6 A3_6	2.22	12.50	0.41	18.35	0.37	Low Yield			
115	GOM6 A3_7	2.54	17.62	0.26	23.50	0.37	Cement		69.0	85.3
116	GOM6 A3_8	2.44	17.99	0.20	23.87	0.37	Cement		57.1	70.6
117	GOM6 A3_9	2.46	18.17	0.33	24.05	0.37	Cement		11.9	14.7
118	GOM6 A3_10	2.39	18.14	0.22	24.02	0.37	Cement		32.1	39.7
119	GOM6 A3_11	2.39	18.51	0.31	24.39	0.37	Cement		21.4	32.1
120	UWQ-1	2.78	6.43	0.22						
121	UWQ-1	2.79	6.79	0.21						
122	UWQ-1	2.78	6.69	0.26						
123	UWQ-1	2.78	6.51	0.34						
Bracket (105-108, 120-123)		**average**	**6.52**			**2 SD = 0.37**				

[a)] Measurements in brackets are exclude grey cement, i.e. measurements are made from the initiation of the darker cement with the grey cement considered as DQ.

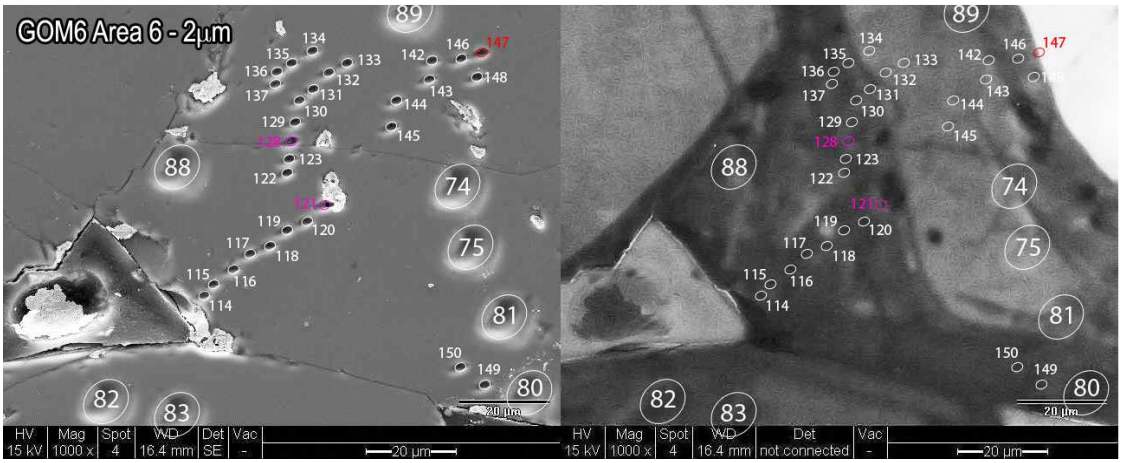
GOM6 Area 6 - 2µm
HV 15 kV | Mag 1000 x | Spot 4 | WD 16.4 mm | Det SE | Vac -
20 µm
HV 15 kV | Mag 1000 x | Spot 4 | WD 16.4 mm | Det not connected | Vac -
20 µm

GOM6 (104°C) 2 µm beam, 2.3nA intensity. June 3, 2009.

Analyses #	Sample	^{16}O cps x10^9	$\delta^{18}O$ RAW	2 SE	$\delta^{18}O$ VSMOW	2 SD	Comments	Zone	µm from DQ [c)]	% from DQ [c)]
110	UWQ-1	29.44	0.24	0.54						
111	UWQ-1	29.99	-0.37	0.61						
112	UWQ-1	29.11	-0.17	0.56						
113	UWQ-1	29.38	0.83	0.56						
114	GOM6.2_A6_01	28.06	12.01	0.75	24.39	0.79	Cement		73.8 (47.4)	93.7 (71.4)
115	GOM6.2_A6_02	29.04	12.03	0.65	24.41	0.79	Cement		71.3 (44.2)	90.5 (80.8)
116	GOM6.2_A6_03	28.15	12.29	0.50	24.67	0.79	Cement		66.3 (36.8)	84.1 (67.3)
117	GOM6.2_A6_04	28.54	12.11	0.60	24.48	0.79	Cement		60.0 (30.5)	76.2 (55.8)
118	GOM6.2_A6_05	28.76	12.64	0.47	25.02	0.79	Cement		56.3 (24.2)	71.4 (44.2)
119	GOM6.2_A6_06	28.55	11.55	0.71	23.92	0.79	Cement		51.3 (14.7)	65.1 (26.9)
120	GOM6.2_A6_07	28.75	12.98	0.52	25.36	0.79	Cement		47.5 (12.6)	60.3 (23.1)
121	GOM6.2_A6_08	32.59	6.09	0.54	18.40	0.79	Cracked			
122	GOM6.2_A6_09	28.34	12.38	0.52	24.77	0.79	Cement		48.8 (14.7)	56.5 (23.3)
123	GOM6.2_A6_10	27.99	12.01	0.55	24.38	0.79	Cement		47.5 (12.6)	54.3(19.7)
124	UWQ-1	28.00	0.48	0.51						
125	UWQ-1	28.09	-0.13	0.63						
126	UWQ-1	27.96	-0.10	0.54			EM HV 3081-3082;			
127	UWQ-1	27.82	-0.01	0.56						
Bracket (110-113, 124-127)		**average**	**0.10**			**2 SD = 0.79**				
128	GOM6.2_A6_11	27.28	12.20	0.58	24.39	0.65	Cracked			
129	GOM6.2_A6_12	27.16	13.27	0.58	25.47	0.65	Cement		42.5 (8.4)	47.9 (12.5)
130	GOM6.2_A6_13	27.17	13.68	0.54	25.88	0.65	Cement		40.0 (5.3)	44.4 (7.7)
131	GOM6.2_A6_14	26.72	16.23	0.58	28.46	0.65	Cement		36.3 (2.1)	40.3(3.1)
132	GOM6.2_A6_15	26.58	15.18	0.62	27.39	0.65	Cement	Grey	25.0	27.8
133	GOM6.2_A6_16	26.39	14.59	0.59	26.81	0.65	Cement	Grey	26.3	29.6
134	GOM6.2_A6_17	26.65	14.29	0.45	26.50	0.65	Cement	Grey	31.3	34.7
135	GOM6.2_A6_18	25.86	14.96	0.62	27.17	0.65	Cement		36.3 (3.2)	40.3 (4.4)

Analyses #	Sample	^{16}O cps x10^9	$\delta^{18}O$ RAW	2 SE	$\delta^{18}O$ VSMOW	2 SD	Comments	Zones	µm from DQ [a)]	% from DQ [a)]
136	GOM6.2_A6_19	24.65	12.35	0.59	24.54	0.65	Cement		40.0 (7.4)	44.4 (10.3)
137	GOM6.2_A6_20	25.10	13.03	0.71	25.23	0.65	Cement		42.5 (10.5)	47.2 (14.7)
138	UWQ-1;	27.80	0.70	0.57			Cs res 131			
139	UWQ-1	27.84	0.56	0.83						
140	UWQ-1	27.70	0.53	0.66			EM HV 3082-3089;			
141	UWQ-1	27.59	0.29	0.58						
Bracket (124-127, 138-141)		**average**	**0.29**	**0.34**		**2 SD = 0.65**				
142	GOM6.2_A6_21	25.03	16.33	0.71	28.25	0.57	Cement	Grey	10.0	11.9
143	GOM6.2_A6_22	26.11	15.64	0.61	27.55	0.57	Cement	Grey	12.5	14.9
144	GOM6.2_A6_23	27.42	14.42	0.54	26.31	0.57	Cement	Grey	21.3	25.4
145	GOM6.2_A6_24	27.20	15.12	0.64	27.02	0.57	Cement	Grey	23.8	28.4
146	GOM6.2_A6_25	26.60	14.88	0.69	26.77	0.57	Cement	Grey	3.8	4.5
147	GOM6.2_A6_26	29.24	5.11	0.66	16.89	0.57	Mixed			
148	GOM6.2_A6_27	29.39	14.78	0.46	26.68	0.57	Cement	Grey	1.3	1.5
149	GOM6.2_A6_28	25.26	14.20	0.57	26.09	0.57	Cement		45.0 (13.7)	87.8 (65.0)
150	GOM6.2_A6_29	26.29	12.61	0.45	24.48	0.57	Cement		42.5 (9.5)	81.0 (45.0)
151	UWQ-1	29.73	0.68	0.46						
152	UWQ-1	29.28	0.29	0.67						
153	UWQ-1	29.52	1.19	0.76			EM HV 3089-3095			
154	UWQ-1	29.16	0.56	0.54						
Bracket (138-141,151-154)		**average**	**0.60**	**0.76**		**2 SD = 0.57**				

[a)] Measurements in brackets are exclude grey cement, i.e. measurements are made from the initiation of the darker cement with the grey cement considered as DQ

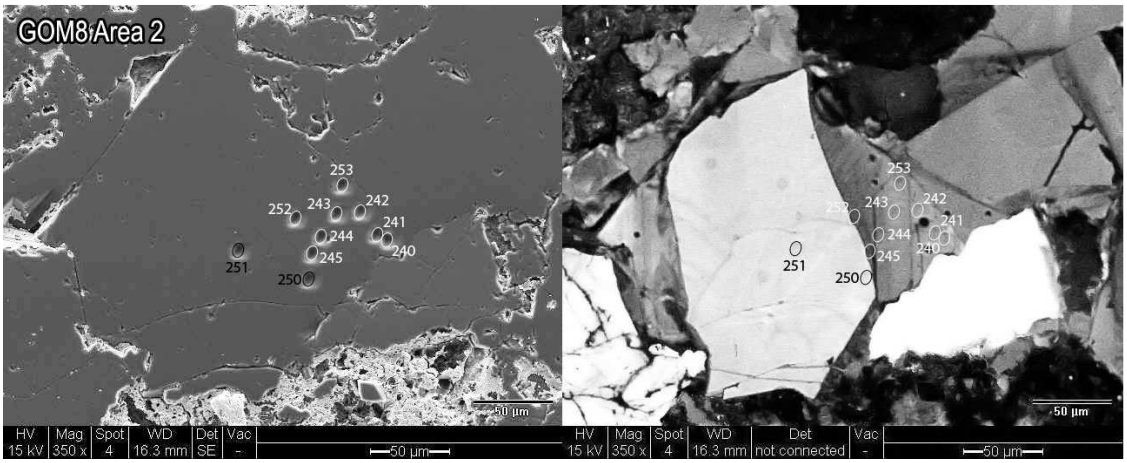
GOM8 Area 2
253
252
243
242
241
244
240
245
251
250
50 µm
HV 15 kV | Mag 350 x | Spot 4 | WD 16.3 mm | Det SE | Vac -
HV 15 kV | Mag 350 x | Spot 4 | WD 16.3 mm | Det not connected | Vac -

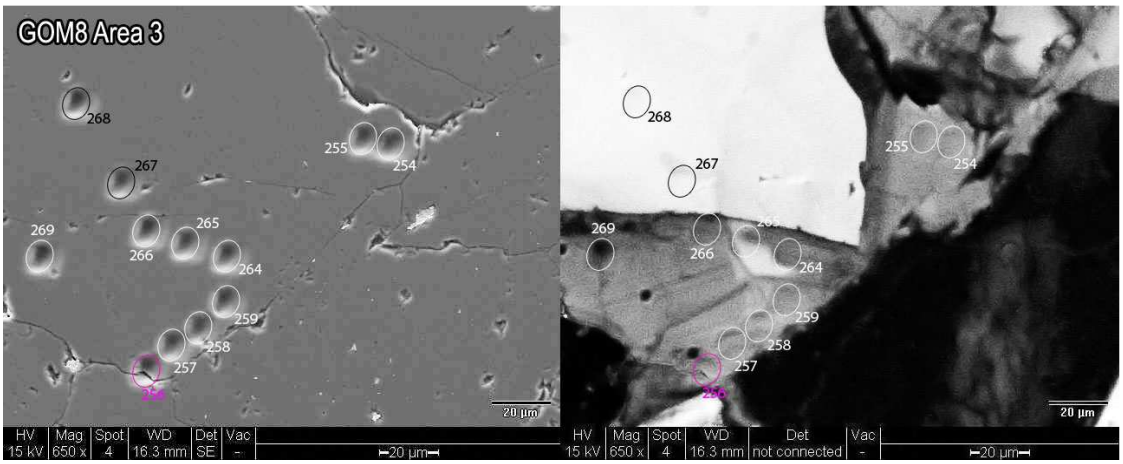
GOM8 Area 3
268
267
255
254
269
265
266
264
259
258
257
20 µm
HV 15 kV | Mag 650 x | Spot 4 | WD 16.3 mm | Det SE | Vac -
HV 15 kV | Mag 650 x | Spot 4 | WD 16.3 mm | Det not connected | Vac -

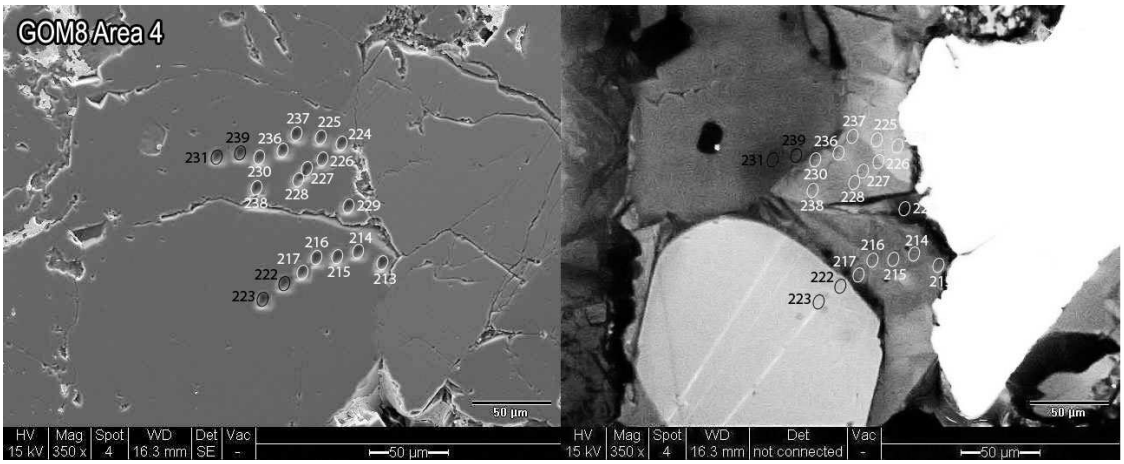
GOM8 Area 4
237
225
239
236
224
231
226
230
227
228
238
229
216
214
217
222
215
213
223
50 µm
HV 15 kV | Mag 350 x | Spot 4 | WD 16.3 mm | Det SE | Vac -
HV 15 kV | Mag 350 x | Spot 4 | WD 16.3 mm | Det not connected | Vac -

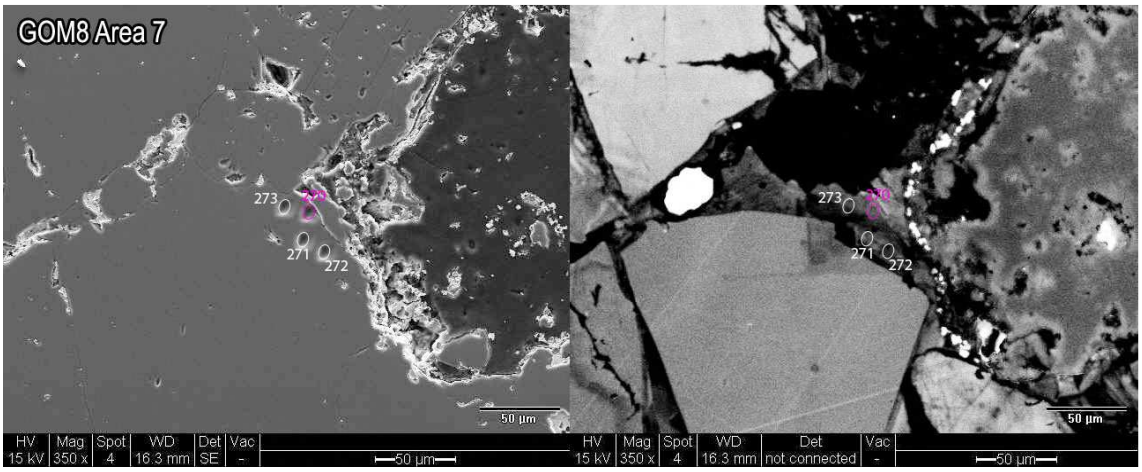
GOM8 Area 7
273
270
271
272
50 µm
HV 15 kV | Mag 350 x | Spot 4 | WD 16.3 mm | Det SE | Vac -
HV 15 kV | Mag 350 x | Spot 4 | WD 16.3 mm | Det not connected | Vac -

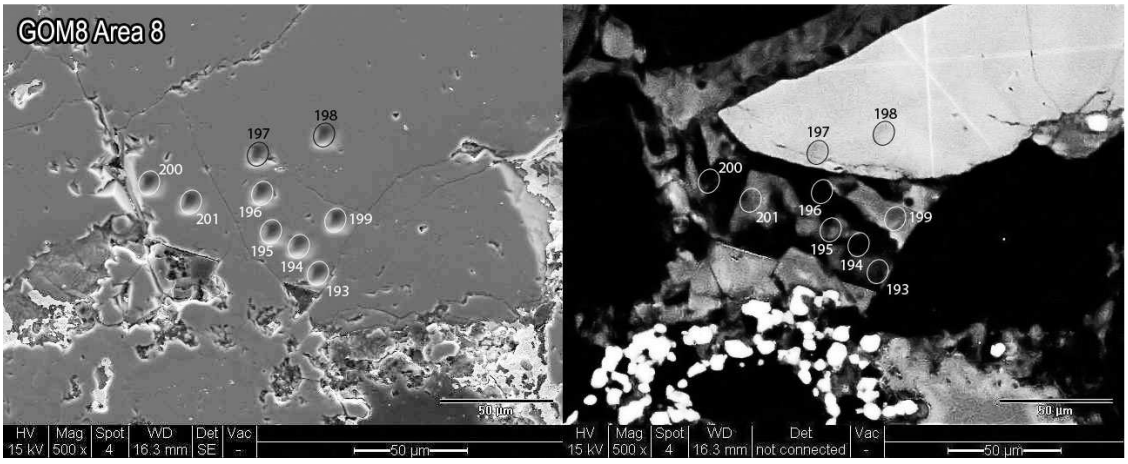
GOM8 Area 8
198
197
200
196
201
199
195
194
193
50 µm
HV 15 kV | Mag 500 x | Spot 4 | WD 16.3 mm | Det SE | Vac -
HV 15 kV | Mag 500 x | Spot 4 | WD 16.3 mm | Det not connected | Vac -

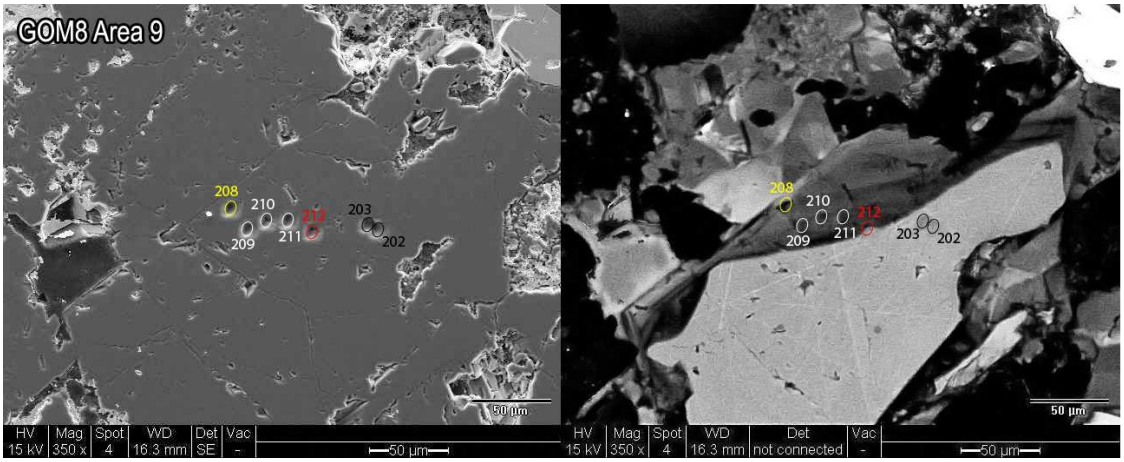
GOM8 Area 9
208
210
212
203
209
211
202
50 µm
HV 15 kV | Mag 350 x | Spot 4 | WD 16.3 mm | Det SE | Vac -
HV 15 kV | Mag 350 x | Spot 4 | WD 16.3 mm | Det not connected | Vac -

GOM8 (143°C) 12 µm beam, 2.3nA intensity. June 2, 2009.

Analyses #	Sample	^{16}O cps x10^9	$\delta^{18}O$ RAW	2 SE	$\delta^{18}O$ VSMOW	2 SD	Comments	µm from DQ	% from DQ
189	UWQ-1	2.39	6.49	0.31					
190	UWQ-1	2.50	6.46	0.18					
191	UWQ-1	2.54	6.36	0.18					
192	UWQ-1	2.56	6.61	0.29					
193	GOM8 A8_1	2.54	13.96	0.23	19.76	0.25	Cement	41.7	83.3
194	GOM8 A8_2	2.55	14.42	0.23	20.23	0.25	Cement	30.0	64.3
195	GOM8 A8_3	2.45	14.36	0.18	20.17	0.25	Cement	26.7	64.0
196	GOM8 A8_4	2.41	15.65	0.24	21.47	0.25	Cement	10.0	27.3
197	GOM8 A8_5	2.41	8.06	0.20	13.84	0.25	Detrital		
198	GOM8 A8_6	2.37	8.08	0.26	13.85	0.25	Detrital		
199	GOM8 A8_7	2.50	14.54	0.19	20.35	0.25	Cement	18.3	57.9
200	GOM8 A8_8	2.48	14.95	0.21	20.76	0.25	Cement	21.7	65.0
201	GOM8 A8_9	2.49	14.54	0.21	20.35	0.25	Cement	21.7	50.0
202	GOM8 A9_1	2.53	4.77	0.18	10.52	0.25	Detrital		
203	GOM8 A9_2	2.58	2.57	0.40	8.31	0.25	Detrital		
204	UWQ-1	2.51	6.61	0.22					
205	UWQ-1	2.37	6.58	0.35					
206	UWQ-1	2.35	6.65	0.25					
207	UWQ-1	2.36	6.77	0.25					
Bracket (189-192, 204-207)		**average**	**6.57**			**2 SD = 0.25**			
208	GOM8 A9_3	2.70	17.07	0.26	22.81	0.25	High Yield		
209	GOM8 A9_4	2.61	18.31	0.19	24.06	0.25	Cement	11.9	31.3
210	GOM8 A9_5	2.65	17.58	0.30	23.33	0.25	Cement	14.3	33.3
211	GOM8 A9_6	2.53	18.82	0.20	24.57	0.25	Cement	11.9	23.8
212	GOM8 A9_7	2.58	11.77	0.70	17.48	0.25	Mixed		
213	GOM8 A4_1	2.47	13.09	0.25	18.81	0.25	Cement	52.4	91.7
214	GOM8 A4_2	2.47	13.94	0.20	19.67	0.25	Cement	42.9	75.0

Analyses #	Sample	^{16}O cps x10^9	$\delta^{18}O$ RAW	2 SE	$\delta^{18}O$ VSMOW	2 SD	Comments	µm from DQ	% from DQ
215	GOM8 A4_3	2.47	14.01	0.25	19.74	0.25	Cement	33.3	60.9
216	GOM8 A4_4	2.45	14.49	0.23	20.22	0.25	Cement	21.4	39.1
217	GOM8 A4_5	2.43	15.23	0.26	20.97	0.25	Cement	9.5	17.4
218	UWQ-1	2.39	6.62	0.18					
219	UWQ-1	2.37	6.53	0.20					
220	UWQ-1	2.34	6.52	0.30					
221	UWQ-1	2.40	6.88	0.30					
Bracket (204-207, 218-221)		**average**	**6.64**			**2 SD = 0.25**			
222	GOM8 A4_6	2.31	7.59	0.19	13.34	0.25	Detrital		
223	GOM8 A4_7	2.28	4.08	0.31	9.80	0.25	Detrital		
224	GOM8 A4_8	2.21	13.20	0.28	18.98	0.25	Cement	38.1	88.9
225	GOM8 A4_9	2.18	14.34	0.26	20.12	0.25	Cement	28.6	66.7
226	GOM8 A4_10	2.15	14.22	0.32	20.00	0.25	Cement	33.3	60.9
227	GOM8 A4_11	2.15	14.42	0.29	20.21	0.25	Cement	33.3	63.6
228	GOM8 A4_12	2.23	12.82	0.21	18.59	0.25	Cement	31.0	59.1
229	GOM8 A4_13	2.60	14.01	0.32	19.79	0.25	Cement	73.8	93.9
230	GOM8 A4_14	2.68	16.27	0.21	22.07	0.25	Cement	2.4	3.7
231	GOM8 A4_15	2.68	5.67	0.24	11.40	0.25	Detrital		
232	UWQ-1	2.57	6.59	0.28					
233	UWQ-1	2.62	6.58	0.23					
234	UWQ-1	2.51	6.48	0.19					
235	UWQ-1	2.51	6.55	0.19					
Bracket (218-221, 232-235)		**average**	**6.59**			**2 SD = 0.25**			
236	GOM8 A4_16	2.63	15.02	0.18	20.84	0.25	Cement	7.1	12.5
237	GOM8 A4_17	2.58	14.81	0.20	20.62	0.25	Cement	9.5	21.1
238	GOM8 A4_18	2.53	14.76	0.21	20.57	0.25	Cracked		
239	GOM8 A4_19	2.51	5.89	0.23	11.65	0.25	Detrital		
240	GOM8 A2_1	2.47	14.04	0.18	19.85	0.25	Cement	50.0	87.5
241	GOM8 A2_2	2.44	12.80	0.22	18.60	0.25	Cement	45.2	79.2

Analyses #	Sample	^{16}O cps x10^9	$\delta^{18}O$ RAW	2 SE	$\delta^{18}O$ VSMOW	2 SD	Comments	µm from DQ	% from DQ
242	GOM8 A2_3	2.37	14.62	0.21	20.43	0.25	Cement	40.5	81.0
243	GOM8 A2_4	2.52	16.68	0.23	22.50	0.25	Cement	26.2	52.4
244	GOM8 A2_5	2.58	17.85	0.18	23.67	0.25	Cement	11.9	22.7
245	GOM8 A2_6	2.53	18.86	0.24	24.69	0.25	Cement	3.6	6.5
246	UWQ-1	2.47	6.81	0.26					
247	UWQ-1	2.46	6.54	0.28					
248	UWQ-1	2.43	6.37	0.24					
249	UWQ-1	2.42	6.62	0.31					
Bracket (232-235, 246-249)		**average**	**6.57**			**2 SD = 0.25**			
250	GOM8 A2_7	2.42	7.86	0.27	13.59	0.27	Detrital		
251	GOM8 A2_8	2.44	4.87	0.23	10.58	0.27	Detrital		
252	GOM8 A2_9	2.41	18.70	0.28	24.49	0.27	Cement	3.6	7.5
253	GOM8 A2_10	2.49	16.08	0.28	21.86	0.27	Cement	38.1	80.0
254	GOM8 A3_1	2.47	14.32	0.25	20.08	0.27	Cement	25.6	73.2
255	GOM8 A3_2	2.50	13.95	0.21	19.71	0.27	Cement	16.3	44.8
256	GOM8 A3_3	2.51	13.47	0.28	19.22	0.27	Mixed		
257	GOM8 A3_4	2.45	15.79	0.31	21.56	0.27	Cement	42.5	79.1
258	GOM8 A3_5	2.40	16.08	0.19	21.85	0.27	Cement	34.4	76.4
259	GOM8 A3_6	2.41	16.07	0.20	21.84	0.27	Cement	23.8	67.9
260	UWQ-1	2.30	6.71	0.33					
261	UWQ-1	2.34	6.63	0.24					
262	UWQ-1	2.48	6.53	0.26					
263	UWQ-1	2.51	6.69	0.25					
Bracket (246-249, 260-263)		**average**	**6.61**			**2 SD = 0.27**			
264	GOM8 A3_7	2.55	17.24	0.24	23.09	0.36	Cement	10.0	28.6
265	GOM8 A3_8	2.55	17.75	0.22	23.60	0.36	Cement	8.1	18.1
266	GOM8 A3_9	2.53	18.76	0.31	24.62	0.36	Cement	5.0	9.3
267	GOM8 A3_10	2.42	3.83	0.32	9.60	0.36	Detrital		
268	GOM8 A3_11	2.51	3.81	0.21	9.58	0.36	Detrital		

Analyses #	Sample	^{16}O cps x10^9	$\delta^{18}O$ RAW	2 SE	$\delta^{18}O$ VSMOW	2 SD	Comments	µm from DQ	% from DQ
269	GOM8 A3_12	2.46	18.16	0.34	24.01	0.36	Cement	15.0	40.0
270	GOM8 A7_1	2.54	13.80	0.25	19.62	0.36	Cracked		
271	GOM8 A7_2	2.50	16.15	0.25	21.99	0.36	Cement	10.6	26.3
272	GOM8 A7_3	2.44	16.24	0.25	22.08	0.36	Cement	8.5	28.6
273	GOM8 A7_4	2.39	15.34	0.25	21.17	0.36	Cement	14.9	70.0
274	UWQ-1	2.37	6.65	0.31					
275	UWQ-1	2.45	6.30	0.24					
276	UWQ-1	2.51	6.23	0.25					
277	UWQ-1	2.49	6.63	0.36					
Bracket (260-263, 274-277)		**average**	**6.55**			**2 SD = 0.36**			

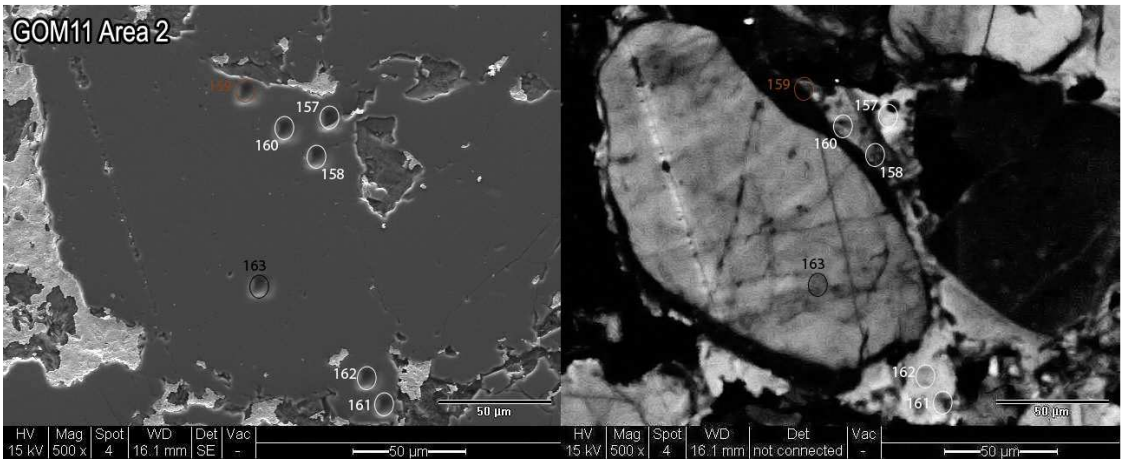
GOM11 Area 2
157
160
158
163
162
161
50 µm
HV 15 kV | Mag 500 x | Spot 4 | WD 16.1 mm | Det SE | Vac -
159
157
160
158
163
162
161
50 µm
HV 15 kV | Mag 500 x | Spot 4 | WD 16.1 mm | Det not connected | Vac -

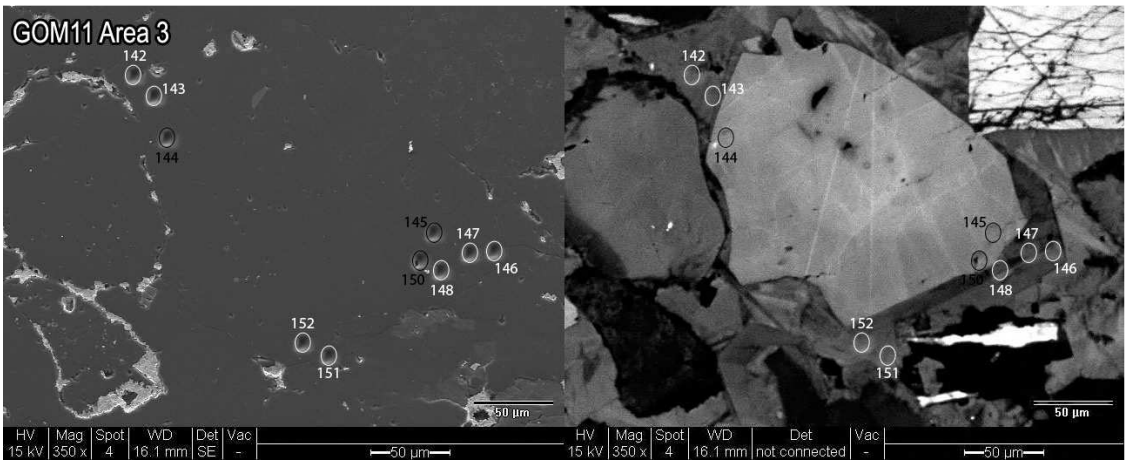
GOM11 Area 3
142
143
144
145
147
146
150
148
152
151
50 µm
HV 15 kV | Mag 350 x | Spot 4 | WD 16.1 mm | Det SE | Vac -
142
143
144
145
147
146
150
148
152
151
50 µm
HV 15 kV | Mag 350 x | Spot 4 | WD 16.1 mm | Det not connected | Vac -

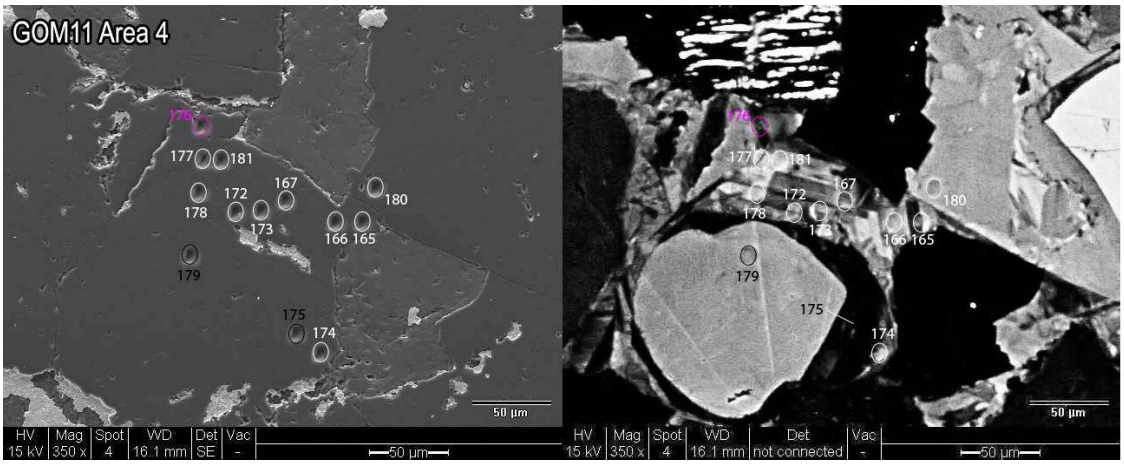
GOM11 Area 4
176
177
181
167
172
178
173
180
166 165
179
175
174
50 µm
HV 15 kV | Mag 350 x | Spot 4 | WD 16.1 mm | Det SE | Vac -
176
177
181
167
172
178
173
180
166 165
179
175
174
50 µm
HV 15 kV | Mag 350 x | Spot 4 | WD 16.1 mm | Det not connected | Vac -

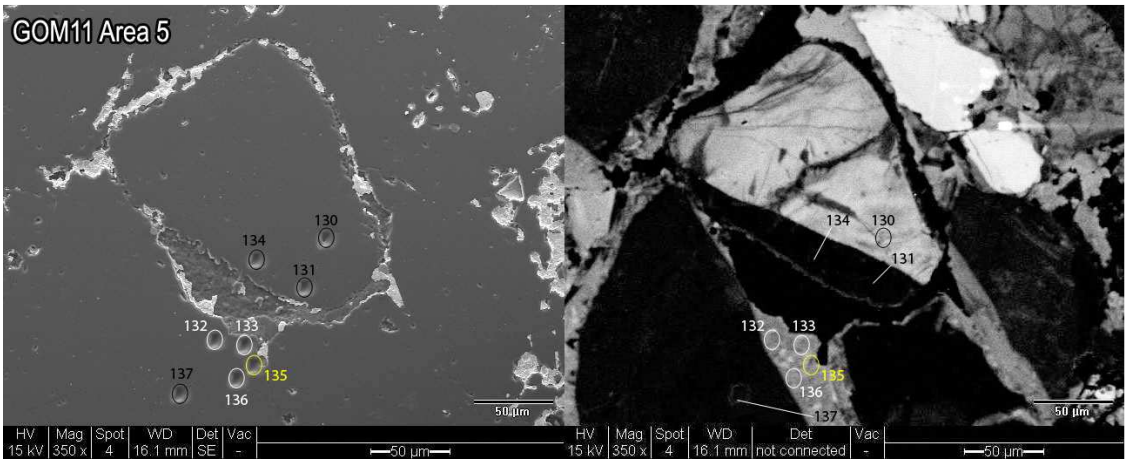
GOM11 Area 5
130
134
131
132
133
135
137
136
50 µm
HV 15 kV | Mag 350 x | Spot 4 | WD 16.1 mm | Det SE | Vac -
50 µm
134
130
131
132
133
135
136
137
50 µm
HV 15 kV | Mag 350 x | Spot 4 | WD 16.1 mm | Det not connected | Vac -
50 µm

GOM11 (185°C) 12 µm beam, 2.3nA intensity. June 2, 2009

Analyses #	Sample	^{16}O cps x10^9	$\delta^{18}O$ RAW	2 SE	$\delta^{18}O$ VSMOW	2 SD	Comments	µm from DQ	% from DQ
126	UWQ-1	2.63	6.65	0.26					
127	UWQ-1	2.55	6.44	0.31					
128	UWQ-1	2.52	6.79	0.24					
129	UWQ-1	2.52	6.75	0.24					
130	GOM11 A5_1	2.49	-1.86	0.26	3.72	0.24	Detrital		
131	GOM11 A5_2	2.57	-1.48	0.23	4.11	0.24	Detrital		
132	GOM11 A5_3	2.57	17.68	0.24	23.37	0.24	Cement	7.1	37.5
133	GOM11 A5_4	2.55	16.52	0.20	22.20	0.24	Cement	22.6	73.1
134	GOM11 A5_5	2.58	-1.24	0.24	4.34	0.24	Detrital		
135	GOM11 A5_6	2.69	15.98	0.22	21.66	0.24	High Yield		
136	GOM11 A5_7	2.49	18.08	0.21	23.77	0.24	Cement	7.1	30.0
137	GOM11 A5_8	2.48	7.92	0.25	13.55	0.24	Detrital		
138	UWQ-1	2.44	6.78	0.23					
139	UWQ-1	2.43	6.66	0.16					
140	UWQ-1	2.39	6.76	0.25					
141	UWQ-1	2.39	6.80	0.25					
Bracket (126-129, 138-141)		**average**	**6.70**			**2 SD = 0.24**			
142	GOM 11A3_1	2.67	15.13	0.22	20.86	0.25	Cement	21.4	56.3
143	GOM 11A3_2	2.75	17.57	0.22	23.31	0.25	Cement	6.0	27.8
144	GOM 11A3_3	2.73	5.79	0.27	11.47	0.25	Detrital		
145	GOM 11A3_4	2.66	5.78	0.17	11.45	0.25	Detrital		
146	GOM 11A3_5	2.62	16.01	0.21	21.74	0.25	Cement	27.4	57.5
147	GOM 11A3_6	2.63	17.27	0.27	23.01	0.25	Cement	13.1	27.5
148	GOM 11A3_7	2.70	17.28	0.26	23.02	0.25	Cement	6.0	13.9
149	GOM 11A3_8	2.61	16.26	0.25	21.99	0.25	Cement		
150	GOM 11A3_9	2.51	6.50	0.22	12.18	0.25	Detrital		
151	GOM 11A3_10	2.53	14.56	0.32	20.28	0.25	Cement	26.2	84.6

Analyses #	Sample	^{16}O cps x10^9	$\delta^{18}O$ RAW	2 SE	$\delta^{18}O$ VSMOW	2 SD	Comments	µm from DQ	% from DQ
152	GOM 11A3_11	2.51	16.22	0.24	21.96	0.25	Cement	9.5	40.0
153	UWQ-1	2.46	6.65	0.25					
154	UWQ-1	2.46	6.50	0.21					
155	UWQ-1	2.56	6.57	0.29					
156	UWQ-1	2.56	6.48	0.22					
Bracket (138-141, 153-156)		**average**	**6.65**			**2 SD = 0.24**			
157	GOM11 A2_1	2.66	13.60	0.14	19.39	0.16	Cement	26.7	64.0
158	GOM11 A2_2	2.56	15.47	0.20	21.26	0.16	Cement	9.2	36.7
159	GOM11 A2_3	2.52	9.19	0.33	14.95	0.16	Detrital		
160	GOM11 A2_4	2.49	14.70	0.30	20.49	0.16	Cement	8.3	31.3
161	GOM11 A2_5	2.41	12.96	0.27	18.74	0.16	Cement	25.0	75.0
162	GOM11 A2_6	2.40	15.51	0.27	21.31	0.16	Cement	11.7	35.0
163	GOM11 A2_7	2.37	5.58	0.30	11.32	0.16	Detrital		
164	GOM11 A2_8	2.64	15.49	0.30	21.28	0.16	?		
165	GOM11 A4_1	2.82	14.61	0.26	20.39	0.16	Cement	42.9	81.8
166	GOM11 A4_2	2.78	13.62	0.22	19.40	0.16	Cement	28.6	54.5
167	GOM11 A4_3	2.73	13.96	0.18	19.75	0.16	Cement	28.6	60.0
168	UWQ-1	2.73	6.53	0.24					
169	UWQ-1	2.74	6.63	0.17					
170	UWQ-1	2.76	6.66	0.36					
171	UWQ-1	2.72	6.69	0.27					
Bracket (153-156, 168-171)		**average**	**6.59**			**2 SD = 0.16**			
172	GOM11 A4_4	2.61	16.48	0.26	22.20	0.28	Cement	7.1	15.0
173	GOM11 A4_5	2.58	15.35	0.18	21.06	0.28	Cement	14.3	30.0
174	GOM11 A4_6	2.51	16.96	0.20	22.68	0.28	Cement	2.4	33.3
175	GOM11 A4_7	2.50	8.35	0.28	14.02	0.28	Detrital		
176	GOM11 A4_8	2.54	14.41	0.15	20.11	0.28	Cracked		
177	GOM11 A4_9	2.60	12.62	0.24	18.31	0.28	Cement	35.7	53.6
178	GOM11 A4_10	2.42	15.80	0.23	21.51	0.28	Cement	14.3	21.4

Analyses #	Sample	^{16}O cps x10^9	$\delta^{18}O$ RAW	2 SE	$\delta^{18}O$ VSMOW	2 SD	Comments	µm from DQ	% from DQ
179	GOM11 A4_11	2.52	4.60	0.28	10.25	0.28	Detrital		
180	GOM11 A4_12	2.56	13.93	0.28	19.63	0.28	Cement	81.0	94.4
181	GOM11 A4_13	2.54	13.93	0.25	19.63	0.28	Cement	35.7	68.2
182	UWQ-1	2.54	6.82	0.35					
183	UWQ-1	2.54	6.68	0.28					
184	UWQ-1	2.53	6.89	0.20					
185	UWQ-1	2.50	6.45	0.25					
Bracket (168-171, 182-185)		**average**	**6.67**			**2 SD = 0.28**			

Appendix 5: North Sea Ness Formation QXRD Results

Well	Temperature (°C)	Depth (m)	Quartz (wt%)	K-feldspar (wt%)	Plagioclase (wt%)	Pyrite (wt%)	Siderite (wt%)	Calcite (wt%)	Dolomite (wt%)
30/9-12	109	2673.3	37.2	6.4	8.1	0.0	2.9	0.2	0.0
30/9-12	109	2674.7	25.7	5.9	0.0	1.3	4.9	0.0	0.0
30/9-12	109	2678.1	32.9	3.1	1.2	0.8	0.0	0.0	0.0
30/9-12	109	2678.8	73.7	5.2	0.4	0.1	1.5	0.0	0.0
30/3-4	118	2831.8	25.9	0.0	0.0	0.0	3.3	0.0	0.0
30/3-4	118	2845.8	44.4	6.3	1.0	0.0	0.0	0.0	0.0
30/3-4	118	2846.1	43.0	9.4	0.9	0.1	0.0	0.0	0.0
211/11a-3	122	3419.9	19.2	2.0	7.0	3.0	2.6	0.0	3.4
211/11a-3	122	3484.8	36.3	0.0	3.6	1.9	0.0	0.0	0.0
211/11a-3	122	3488.7	12.0	12.2	3.4	4.5	0.0	0.0	0.0
211/11a-3	122	3493.0	12.0	11.6	4.1	4.5	0.0	0.0	0.0
25/2-4	137	3818.4	35.3	0.0	0.1	0.0	0.0	2.2	0.0
211/27-A2	133	4292.2	7.2	0.0	0.0	2.6	0.0	0.0	0.0
211/27-A2	133	4292.2	12.6	0.0	0.8	2.7	0.0	0.0	0.0
211/27-A2	133	4292.2	6.1	1.3	0.4	0.0	0.1	0.0	0.0
211/27-A2	133	4311.1	42.0	5.8	0.0	0.0	0.0	0.0	0.0
211/27-A2	133	4319.0	17.3	7.2	0.1	0.0	0.0	0.0	0.0
211/27-A2	133	4337.0	38.1	0.0	0.9	0.0	3.6	0.0	0.0
211/27-A2	133	4342.5	36.6	0.0	1.0	0.0	6.4	0.0	0.0
211/27-A2	133	4343.4	100.0	0.0	0.0	0.0	0.0	0.0	0.0
211/27-A2	133	4344.3	96.2	0.0	0.0	3.0	0.0	0.0	0.0
34/8-7	165	4653.0	14.0	0.0	3.7	2.4	0.0	0.0	0.0
34/8-7	165	4655.9	39.5	0.0	4.0	1.1	0.0	0.0	0.0

Well	Temperature (°C)	Depth (m)	Illite/Musc (wt%)	Montmorillonite (wt%)	Kaolinite (wt%)	Chlorite (wt%)	Illite-smect (wt%)	Clay minerals (wt%)	Total (wt%)
30/9-12	109	2673.3	25.5	0.0	19.6	0.0	0.0	45.1	103.7
30/9-12	109	2674.7	21.4	0.0	24.8	4.5	11.4	62.1	105.4
30/9-12	109	2678.1	20.8	0.0	26.7	4.4	10.0	62.0	97.6
30/9-12	109	2678.8	8.7	0.8	9.5	0.0	0.0	19.1	111.9
30/3-4	118	2831.8	27.7	1.3	21.5	1.9	18.3	70.8	101.0
30/3-4	118	2845.8	24.4	0.0	23.8	0.0	0.0	48.3	98.8
30/3-4	118	2846.1	23.0	5.6	18.0	0.0	0.0	46.6	95.4
211/11a-3	122	3419.9	26.9	0.0	18.0	6.2	11.6	62.7	95.5
211/11a-3	122	3484.8	40.3	0.0	6.0	0.0	12.0	58.2	102.0
211/11a-3	122	3488.7	52.2	0.0	5.6	0.0	10.0	67.8	106.8
211/11a-3	122	3493.0	51.9	0.0	6.0	0.0	9.9	67.9	106.4
25/2-4	137	3818.4	36.8	0.0	21.1	4.5	0.0	62.4	95.0
211/27-A2	133	4292.2	37.6	0.0	39.5	9.7	3.3	90.2	97.0
211/27-A2	133	4292.2	36.1	0.0	33.1	7.1	7.6	83.8	99.2
211/27-A2	133	4292.2	48.3	0.0	32.7	11.1	0.0	92.1	103.5
211/27-A2	133	4311.1	26.9	0.0	25.2	0.0	0.0	52.2	100.1
211/27-A2	133	4319.0	34.7	0.0	36.2	4.4	0.0	75.4	89.6
211/27-A2	133	4337.0	36.4	0.0	18.7	2.3	0.0	57.4	102.9
211/27-A2	133	4342.5	23.9	0.0	27.5	4.7	0.0	56.1	97.9
211/27-A2	133	4343.4	0.0	0.0	0.0	0.0	0.0	0.0	146.7
211/27-A2	133	4344.3	0.0	0.0	0.7	0.0	0.0	0.7	104.7
34/8-7	165	4653.0	69.7	0.0	10.2	0.0	0.0	79.9	98.9
34/8-7	165	4655.9	50.1	0.0	5.3	0.0	0.0	55.4	100.2

North Sea Ness Formation QXRD results normalised to 100%. Total (wt%) column is Fullpat results relative to corundum.

Appendix 6: Texas Wilcox Group QXRD Results

Well	Depth (m)	Temperature (°C)	Quartz (wt%)	K-feldspar (wt%)	Plagioclase (wt%)	Pyrite (wt%)	Siderite (wt%)	Jarosite (wt%)	Calcite (wt%)	Dolomite (wt%)
TOH	324	27	33	0	6	0	9	2	0	0
TOH	412	36	37	2	2	0	0	0	0	0
TOH	482	45	52	6	1	0	0	0	0	0
TOH	483	45	58	8	0	0	1	0	0	0
TOH	714	53	31	1	6	7	6	0	0	0
SL	2734	104	59	0	1	2	2	0	0	0
SL	2734	104	43	0	2	2	2	0	0	0
SL	2734	104	46	0	4	2	2	0	0	0
SL	2735	104	60	1	3	1	0	0	0	0
LC	3497	142	46	0	13	0	2	0	0	0
LC	3500	142	18	6	9	0	1	0	0	0
LC	3500	142	17	3	4	0	0	0	0	0
LC	3504	143	41	1	4	1	1	0	0	0
LC	3506	143	45	1	6	0	0	0	0	0
LC	3511	143	32	6	7	0	0	0	0	0
LC	3512	143	30	3	7	2	13	0	0	0
LC	3513	143	13	4	9	0	0	0	0	0
LC	3518	143	45	0	8	1	0	0	0	0
LC	3527	144	27	2	4	0	0	0	0	0
HA-U	4288	168	31	0	8	0	0	0	0	0
HA-L	4994	186	55	0	11	1	1	0	0	4
HA-L	4998	186	43	0	8	0	1	0	0	0
HA-L	5063	188	30	1	4	0	2	1	0	0
HA-L	5077	188	39	2	5	0	0	0	0	0
CR-U	5813	188	25	0	10	1	0	0	0	0
CR-U	5818	189	51	0	10	0	0	0	0	0
CR-U	5818	189	49	0	12	0	0	0	0	0
CR-U	6375	204	44	1	8	0	2	0	0	0
CR-L	6606	209	51	0	5	0	2	0	0	0
CR-L	6607	210	50	0	6	0	3	0	0	0
CR-L	6608	210	50	0	4	0	1	0	0	0
CR-L	6608	210	47	0	10	0	0	0	0	0

Well	Depth (m)	Temperature (°C)	Illite/Musc (wt%)	Smectite (wt%)	Kaolinite (wt%)	Chlorite (wt%)	I/S (wt%)	K/S (wt%)	C/S (wt%)	Clay Minerals (wt%)	Total (wt%)
TOH	324	27	32	11	6	0	0	0	0	50	118
TOH	412	36	42	8	9	0	0	0	0	59	127
TOH	482	45	12	5	10	1	9	0	2	41	117
TOH	483	45	12	10	11	0	0	0	0	33	108
TOH	714	53	27	0	1	1	20	0	0	49	120
SL	2734	103	31	0	6	0	0	0	0	37	129
SL	2734	103	30	2	5	0	6	5	2	51	132
SL	2734	103	21	0	5	0	8	9	2	45	138
SL	2735	103	22	0	6	0	5	1	1	35	143
LC	3497	142	18	1	5	4	6	5	0	38	97
LC	3500	142	42	0	6	2	10	6	0	66	90
LC	3500	142	45	3	7	0	13	10	0	77	88
LC	3504	143	31	0	2	2	15	2	0	52	103
LC	3506	143	38	0	6	2	3	0	0	49	96
LC	3511	143	41	0	0	8	2	4	0	55	97
LC	3512	143	24	0	9	5	6	0	0	44	98
LC	3513	143	51	1	7	4	10	2	0	75	96
LC	3518	143	25	0	4	4	12	2	0	46	101
LC	3527	144	52	0	6	2	0	7	0	67	90
HA-U	4288	168	54	1	5	0	0	0	0	61	84
HA-L	4994	186	20	0	2	5	0	0	0	27	98
HA-L	4998	186	40	0	0	8	0	0	0	48	95
HA-L	5063	188	59	0	0	3	0	0	0	63	92
HA-L	5077	188	48	0	2	3	0	1	0	53	104
CR-U	5813	188	52	1	3	7	0	0	0	63	100
CR-U	5818	189	26	0	5	7	0	0	0	38	86
CR-U	5818	189	32	0	1	2	0	4	0	39	96
CR-U	6375	204	37	0	0	8	0	0	0	45	94
CR-L	6606	210	30	0	3	8	0	0	0	41	103
CR-L	6607	210	31	0	0	10	0	0	0	41	93
CR-L	6608	210	37	0	4	3	0	0	0	45	87
CR-L	6608	210	42	0	0	1	0	0	0	43	90

Texas Wilcox shale Quantitative X-Ray Diffraction Results. All weights are normalised to 100%. Total (wt%) column is Fullpat results relative to corundum. I/S = illite-smectite, K-S = kaolinite-smectite and C/S = chlorite-smectite.

Well	Depth (m)	Temperature (°C)	Quartz (wt%)	K-feldspar (wt%)	Plagioclase (wt%)	Pyrite (wt%)	Siderite (wt%)	Jarosite (wt%)	Calcite (wt%)	Dolomite (wt%)
SL	2733	103	98	0	0	0	0	0	0	0
LC	3497	142	62	4	11	0	0	0	0	0
LC	3500	142	71	0	16	0	1	0	0	0
LC	3500	142	72	0	16	0	0	0	0	0
LC	3511	143	76	4	8	0	0	0	0	0
LC	3512	143	87	1	4	0	0	0	0	0
LC	3513	143	74	0	16	0	0	0	0	0
LC	3518	143	69	4	8	0	0	0	0	0
LC	3527	144	91	0	8	0	1	0	0	0
LC	3534	144	75	0	17	0	2	0	0	0
HA-U	4278	167	77	2	19	0	1	0	0	0
HA-U	4288	168	85	0	13	0	2	0	0	0
HA-U	4289	168	75	0	17	0	0	0	0	0
HA-L	4983	186	73	0	7	0	1	0	0	0
HA-L	4983	186	71	0	13	0	1	0	0	0
HA-L	4994	186	81	0	10	0	3	0	0	0
HA-L	4998	186	73	0	13	1	3	0	0	0
HA-L	5063	187	86	0	10	1	3	0	0	0
HA-L	5077	188	73	0	5	2	3	0	0	0
CR-U	5798	189	71	0	20	1	3	0	0	0

Well	Depth (m)	Temperature (°C)	Illite/Musc (wt%)	Smectite (wt%)	Kaolinite (wt%)	Chlorite (wt%)	I/S (wt%)	K/S (wt%)	C/S (wt%)	Clay Minerals (wt%)	Total (wt%)
SL	2733	103	0	0	0	0	1	0	0	1	103
LC	3497	142	7	0	1	1	8	2	3	22	120
LC	3500	142	3	1	2	0	5	1	1	12	99
LC	3500	142	3	1	2	0	4	1	1	12	97
LC	3511	143	11	0	0	0	0	0	0	12	104
LC	3512	143	1	0	0	0	6	0	0	7	100
LC	3513	143	8	0	1	0	0	0	0	10	102
LC	3518	143	10	0	8	0	0	0	0	18	99
LC	3527	144	0	0	0	0	0	0	0	0	100
LC	3534	144	2	0	2	1	0	0	0	5	102
HA-U	4278	167	0	0	0	0	0	0	0	0	95
HA-U	4288	168	0	0	0	0	0	0	0	0	109
HA-U	4289	168	5	0	0	0	1	0	0	7	108
HA-L	4983	186	10	0	9	0	0	0	0	19	101
HA-L	4983	186	10	0	0	4	0	0	0	15	98
HA-L	4994	186	4	0	1	0	0	0	0	6	97
HA-L	4998	186	4	0	1	4	1	0	0	10	100
HA-L	5063	187	0	0	0	0	0	0	0	0	100
HA-L	5077	188	14	0	0	3	0	0	0	17	155
CR-U	5798	189	0	0	5	0	0	0	0	5	106

Texas Wilcox sandstone Quantitative X-Ray Diffraction Results. All weights are normalised to 100%. Total (wt%) column is Fullpat results relative to corundum. I/S = illite-smectite, K-S = kaolinite-smectite and C/S = chlorite-smectite.

Appendix 7: North Sea Ness Shale <2 µm Clay Fraction XRD Diffractograms

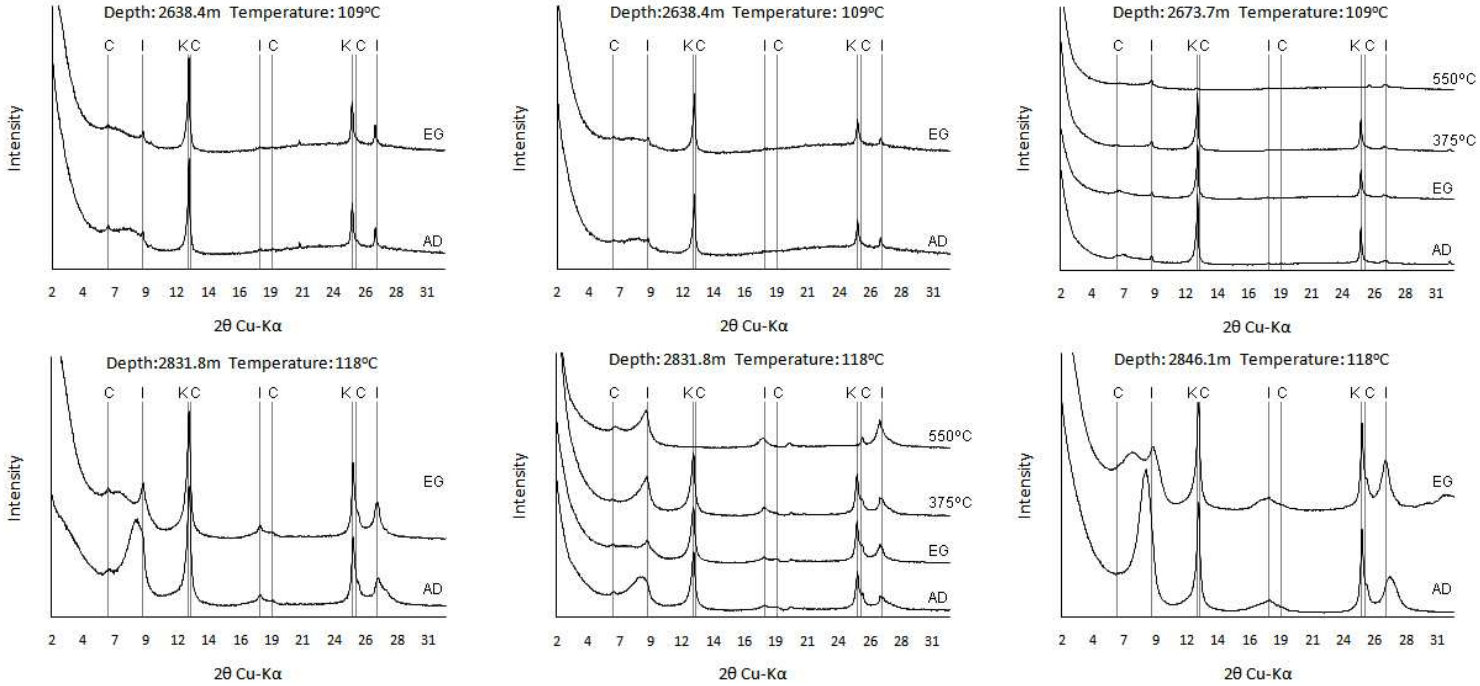

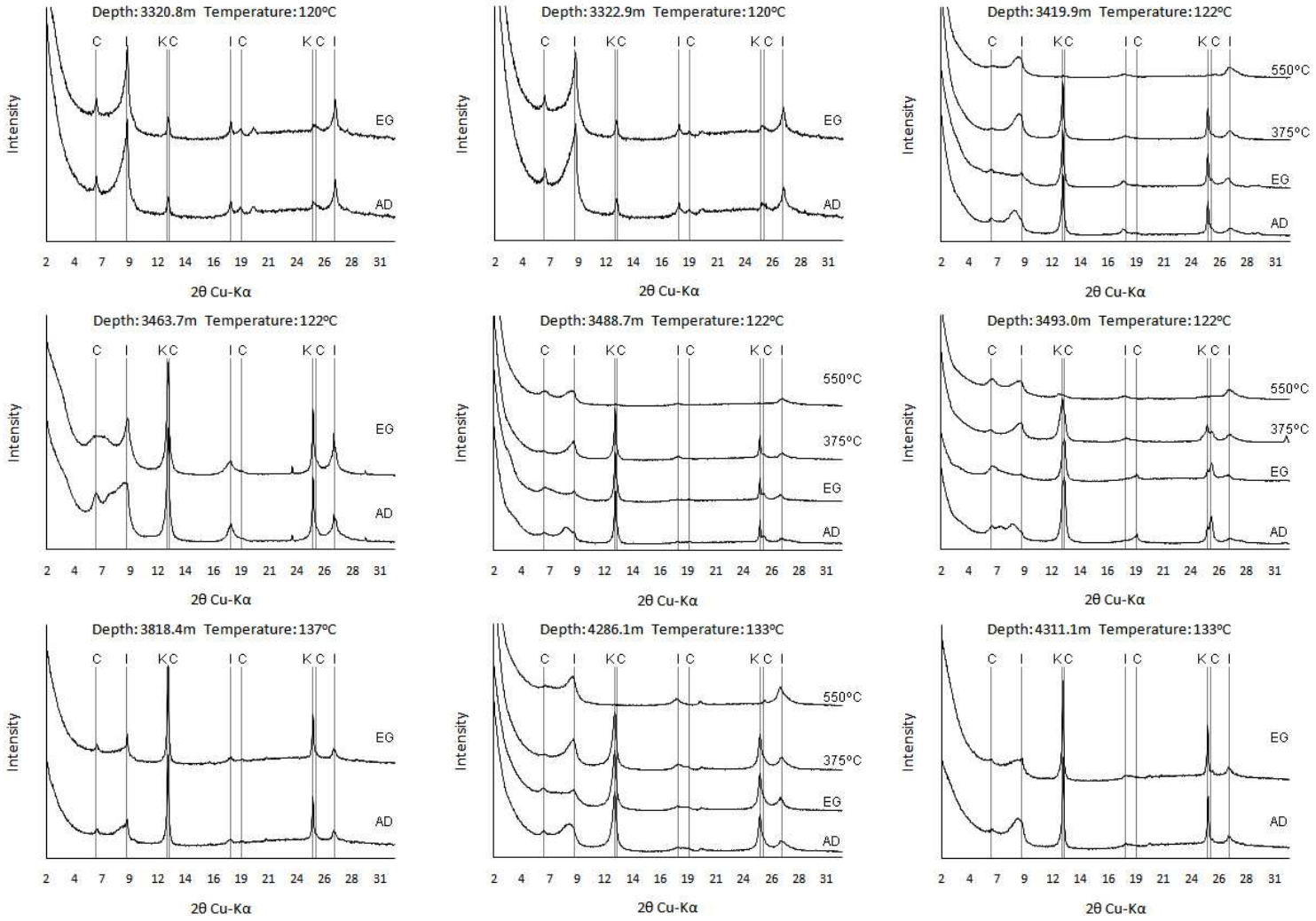
Depth: 3320.8m Temperature: 120ºC
Depth: 3322.9m Temperature: 120ºC
Depth: 3419.9m Temperature: 122ºC
Depth: 3463.7m Temperature: 122ºC
Depth: 3488.7m Temperature: 122ºC
Depth: 3493.0m Temperature: 122ºC
Depth: 3818.4m Temperature: 137ºC
Depth: 4286.1m Temperature: 133ºC
Depth: 4311.1m Temperature: 133ºC
C I KC I C K C I
Intensity
EG
AD
550ºC
375ºC
2 4 7 9 12 14 16 19 21 24 26 28 31
2θ Cu-Kα

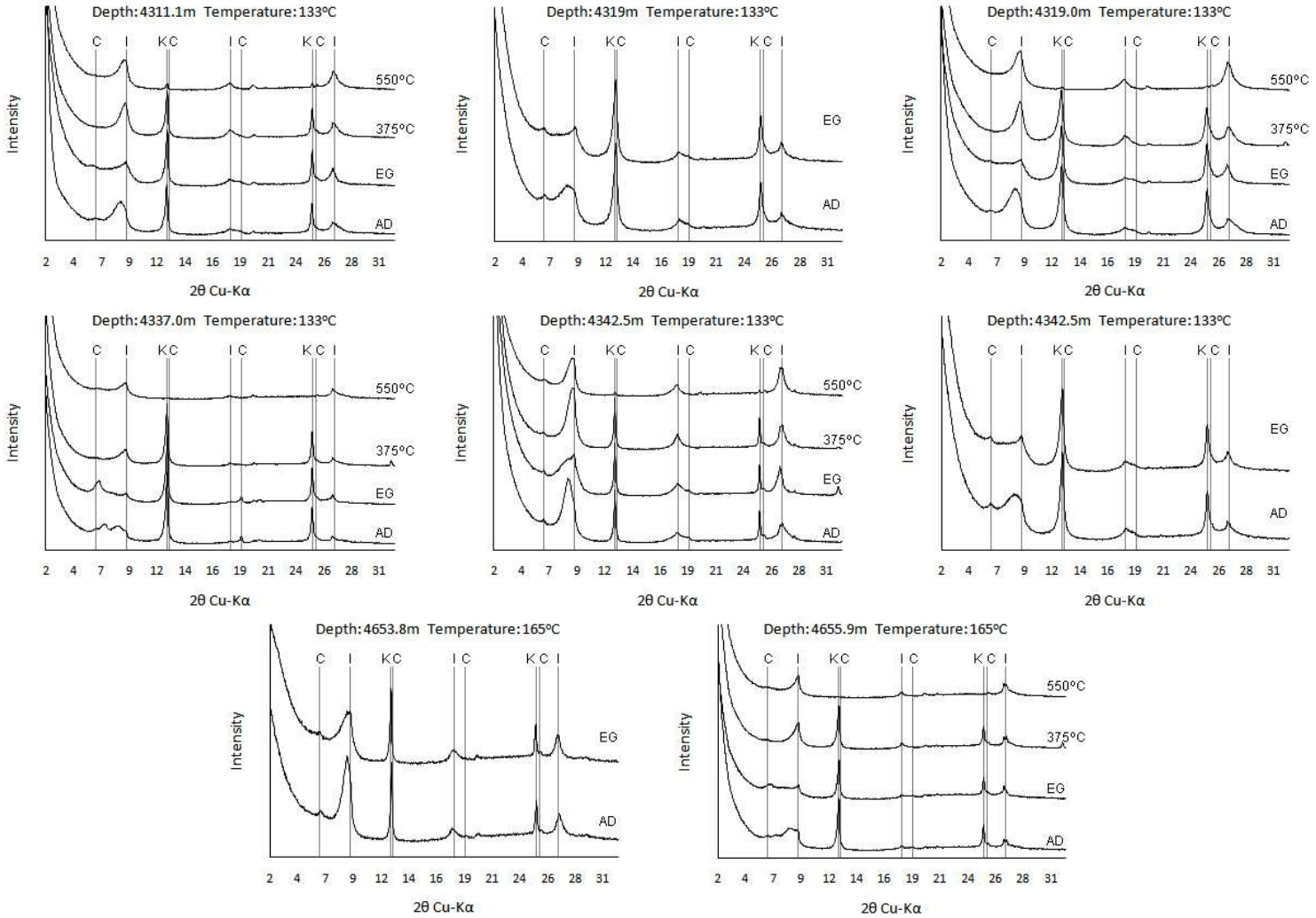
Depth: 4311.1m Temperature: 133ºC
Depth: 4319m Temperature: 133ºC
Depth: 4319.0m Temperature: 133ºC
Depth: 4337.0m Temperature: 133ºC
Depth: 4342.5m Temperature: 133ºC
Depth: 4342.5m Temperature: 133ºC
Depth: 4653.8m Temperature: 165ºC
Depth: 4655.9m Temperature: 165ºC
C I KC I C KC I
550ºC
375ºC
EG
AD
Intensity
2 4 7 9 12 14 16 19 21 24 26 28 31
2θ Cu-Kα

Appendix 8: Texas Wilcox Shale <2 µm Clay fraction XRD diffractograms

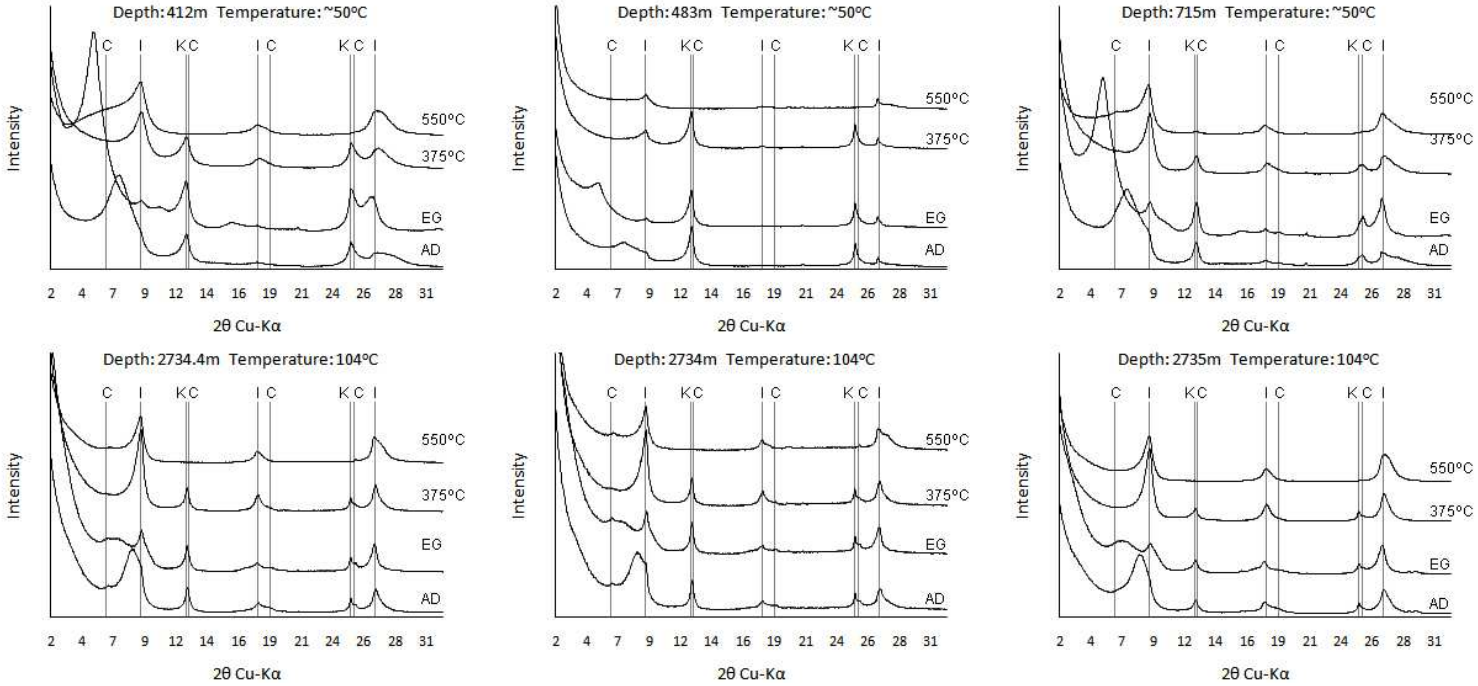

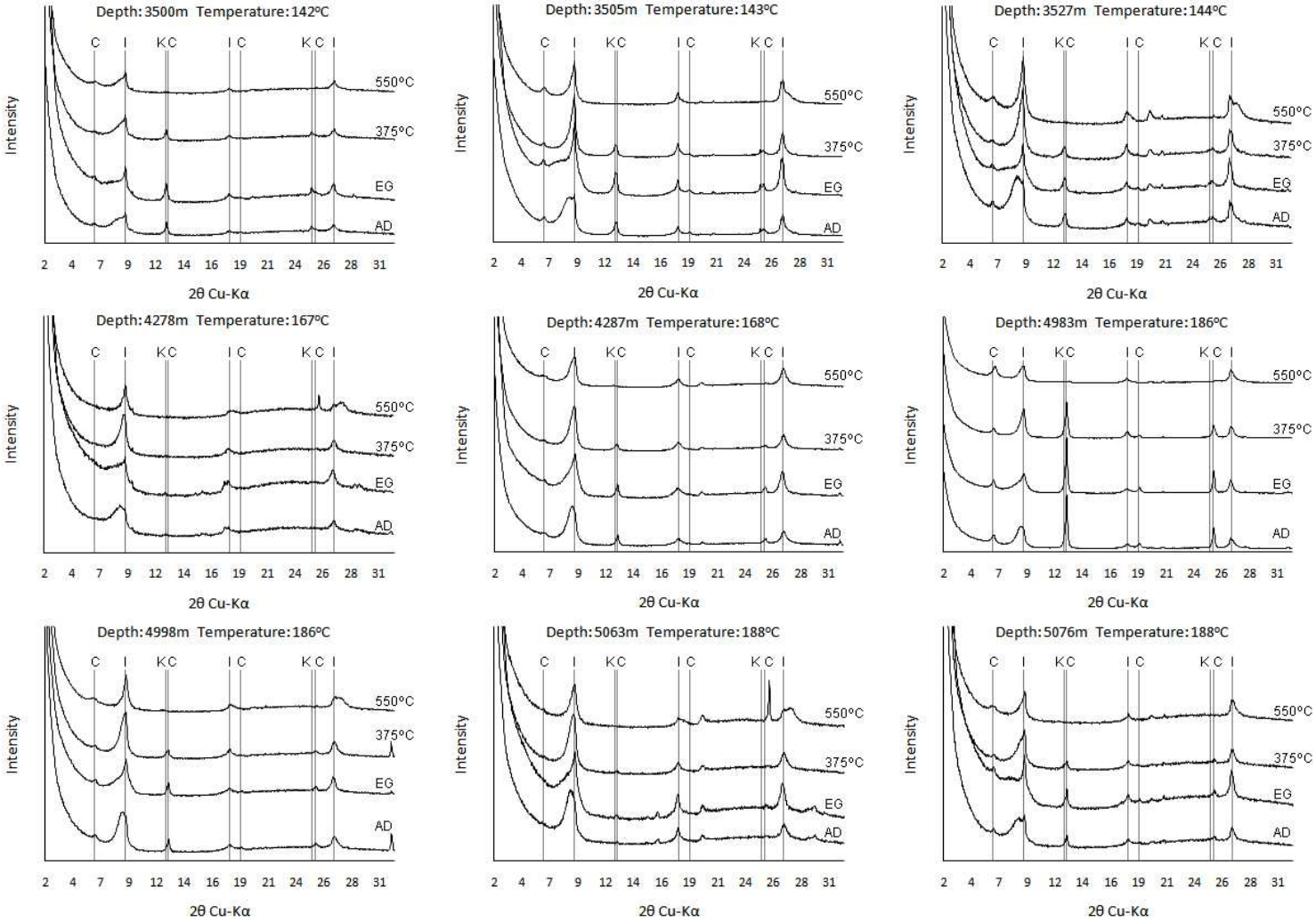
Depth: 3500m Temperature: 142ºC
Depth: 3505m Temperature: 143ºC
Depth: 3527m Temperature: 144ºC
Depth: 4278m Temperature: 167ºC
Depth: 4287m Temperature: 168ºC
Depth: 4983m Temperature: 186ºC
Depth: 4998m Temperature: 186ºC
Depth: 5063m Temperature: 188ºC
Depth: 5076m Temperature: 188ºC
C I KC I C K C I
550ºC
375ºC
EG
AD
Intensity
2 4 7 9 12 14 16 19 21 24 26 28 31
2θ Cu-Kα

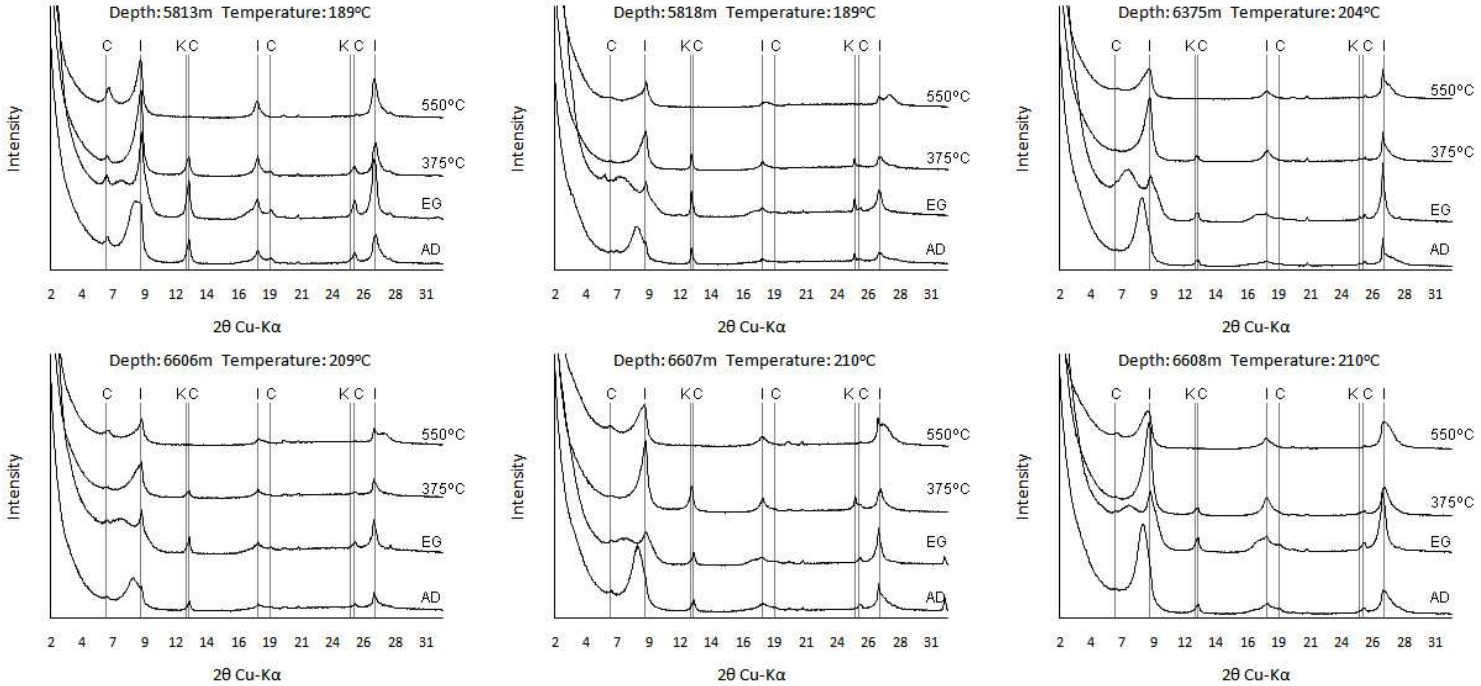
Depth: 5813m Temperature: 189ºC
Depth: 5818m Temperature: 189ºC
Depth: 6375m Temperature: 204ºC
Depth: 6606m Temperature: 209ºC
Depth: 6607m Temperature: 210ºC
Depth: 6608m Temperature: 210ºC
C I KC I C KC I
550ºC
375ºC
EG
AD
Intensity
2 4 7 9 12 14 16 19 21 24 26 28 31
2θ Cu-Kα